Fundamental Physics of Ferroelectrics and Related Materials • 2015

Crowne Plaza, Knoxville, TN
January 25-28 2015

http://www.ferro2015.ornl.gov

Organizing Committee:
Valentino R. Cooper, Oak Ridge National Laboratory
P. Ganesh, Oak Ridge National Laboratory
Haixuan Xu, University of Tennessee

Sponsored by:

Oak Ridge National Laboratory | Center for Nanophase Materials Sciences
Materials Science and Technology Division
UT-Battelle
The University of Tennessee Knoxville

The Fundamental Physics of Ferroelectrics and Related Materials workshop has been held every year since February 1990. The workshop brings together a diverse set of researchers, both theorists and experimentalist, from around the world in order to facilitate the interdisciplinary exchange of ideas. Ferroelectricity is a complex phenomenon, usually, driven by phonon instabilities that give rise to a spontaneous polarization which may exhibit temperature dependent couplings with lattice strains, strain-gradients, and magnetism leading to a wide range of materials such as electrostrictive materials, piezoelectrics, multiferroics, electrocaloric materials and flexoelectrics to name a few. These interactions are strongly affected by external electric/magnetic fields. Understanding the interplay between these different complex interactions that govern material property and its response to fields has been a monumental challenge that has required the combined efforts of theorists and experimentalist in the research community. This workshop series has played a pivotal role in bringing together researchers from different parts of the world, fostering the multi-institutional collaborations necessary for the comprehensive studies devoted to understanding the fundamental physics of this complex phenomenon. At these meetings new advances in experimental and theoretical techniques are also presented. The culture fostered by the regular attendees of this meeting encourages scientific discussions which extend into the breaks and dining periods.

This year the workshop will focus on the following: Multiferroics, Ferroelectrics, Relaxors, Theory and Modeling, Characterization Methods, Domains and Nanostructure, Interfaces and Surfaces, Non-oxide Ferroelectrics, Material Synthesis and Growth, and Phase Transformations.

Invited Speakers:

Paolo Barone - CNR-SPIN, Italy
Laurent Bellaiche – Univ. of Arkansas, USA
Albina Borisevich - ORNL, USA
Gustau Catalan - ICREA, Spain
Hans Christen - ORNL, USA
Brahim Dkhil - CNRS, France
Jirka Hlinka - Acad. Sci. Czech Republic, Czech Republic
Jiawang Hong - ORNL, U.S.A.
Puru Jena - Univ. of Virginia, U.S.A
Anna Kimmel - NPL, U.K.
Jan Musfeldt - Univ. of Tenn., USA
Giovanni Pizzi - EPFL, Switzerland
James Scott - Cambridge University, U. K.
Chi-Shun Tu - Fu Jen Catholic University, Taiwan
Guangyong Xu - BNL, U.S.A.

Ferro 2015 · Daily Agenda

SUNDAY, JANUARY 25TH, 2015

5:00 p.m. – 7:00 p.m. **Reception and Registration (Salon B & C)** – sponsored by the University of Tennessee

MONDAY, JANUARY 26TH, 2015

7:30 a.m. – 8:30 a.m. **Continental Breakfast (Outside of Summit I)**

8:00 a.m. – 8:15 a.m. **Welcome (Summit I) –** Hans Christen, Director, Center for Nanophase Materials Sciences, Oak Ridge National Laboratory

8:15 a.m. – 8:25 a.m. **Opening Remarks (Summit I)** – Valentino Cooper

***Multiferroics and Magnetoelectrics*: 8:25 a.m. – 10:00 a.m. (Summit I)**
Chairperson: Ronald Cohen

8:25 a.m.	J. Scott (Invited) - Dynamics of some nano-ferroelectrics and multiferroics
8:50 a.m.	B. Dkhil (invited) - Strain induced and its consequences in multiferroics
9:15 a.m.	A. Pignolet - The quest for new room temperature multiferroic thin films
9:30 a.m.	S. Ghosh - Design strategy and prediction of new room temperature magnetoelectric multiferroics
9:45 a.m.	O. Udalov - Magnetoelectric coupling in granular multiferroics

10:00 a.m. – 10:30 a.m. **Coffee Break (Outside of Summit I)**

***Growth and Characterization*: 10:30 – 12:10 (Summit I)**
Chairperson: Rama Vasudevan

10:30 a.m.	B. Bein - Novel in-situ X-ray diffraction measurement of ferrroelectric superlattice properties during growth
10:45 a.m.	Z.-G. Ye - New insights into the structure and properties of PZT from mesoscopic to atomic scale
11:00 a.m.	S. Vakhrushev – Lattice modulation and structural instability at ***M***-point in PZT single crystals by X-ray scattering
11:15 a.m.	V. Goian - Demonstration of spin-phonon coupling in infrared and THz spectra of $Sr_{1-x}Ba_xMnO_3$ and $Sr_{1-x}Ba_xMn_{1-y}Ti_yO_3$ ceramics
11:30 a.m.	A. Bussman-Holder - Tiny cause with large effects: The origin of the large magnetoelectric and magnetoelastic effect in $EuTiO_3$
11:45 a.m.	P. Jena (Invited) - Organic metal-free ferroelectric and multiferroic materials

Working Lunch: 12:10 p.m. – 1:40 p.m. (Salon B & C)
Lunch Speaker: A. Borisevich
"*Ferroelectrics in infinite dimensions: beyond order parameter description*"

***Novel Properties I*: 1:40 p.m. – 3:00 p.m (Summit I)**
Chairperson: P. Ganesh

1:40 p.m.	J. Hong (Invited) - Towards a full first-principles theory of flexoelectricity
2:05 p.m.	G. Catalan (Invited) - Flexoelectricity in polar materials
2:30 p.m.	J. Zhang - Pyroelectric and dielectric properties in ferroelectrics with bilayer and compositionally-graded structures
2:45 p.m.	G. Guzman-Verri - Why is the electrocaloric effect so small in ferroelectrics?

3:00 p.m. – 3:30 p.m. **Coffee Break (Outside of Summit I)**

***Novel Properties II*: 3:30 p.m. – 4:55 p.m. (Summit I)**
Chairperson: Nina Balke

3:30 p.m.	C-S. Tu (Invited) – Photovoltaic conversion of rare earth-doped $BiFeO_3$ multiferroic ceramics
3:55 p.m.	F. Wang – Bulk photovoltaic effect enhancement via electrostatic control in layered ferroelectrics
4:10 p.m.	T. Meyer - Superconductivity in over-doped cuprates induced by ferroelectric polarization
4:25 p.m.	B. Mani - Finite-temperature properties of antiferroelectric $PbZrO_3$
4:40 p.m.	H. Fu - Physical constraint and its consequence for hyperferroelectrics

4:55 p.m. – 5:30 p.m. **Summary and Scientific Discussions (Summit I)**

6:00 p.m. – 8:00 p.m. **Poster Session *in lieu of dinner* (Summit II)**

TUESDAY, JANUARY 27TH, 2015

7:30 a.m. – 8:30 a.m. **Continental Breakfast (Outside of Summit I)**

***Nonoxide Ferroelectrics:* 8:00 a.m. – 8:55 a.m. (Summit I)**
Chairperson: Andrew Rappe

8:00 a.m.	P. Barone (Invited) - Ferroelectricity and magnetoelectricity in hybrid organic-inorganic compounds
8:25 a.m.	H. Moriwake - First-principles calculations of the ferroelectric phase transition in pure molecular crystal trichloroacetamide
8:40 a.m.	C. Xu - Prediction of a stable post-post-perovskite structure from first principles

***Relaxors*: 8:55 a.m. – 9:55 a.m. (Summit I)**
Chairperson: Andrew Rappe

8:55 a.m.	A. Bokov – Multiple relaxation and characteristic temperatures in $PbMg_{1/3}Nb_{2/3}O_3$:La relaxor ferroelectric crystals
9:10 a.m.	H. Takenaka - Computational study of real space local structure and diffuse scattering in a relaxor
9:25 a.m.	D. Wang – Fano resonance in lead-free relaxor $Ba(Zr,Ti)O_3$
9:40 a.m.	O. Delaire - Phonons in $SrTiO_3$ and $EuTiO_3$ investigated with neutron scattering

9:55 a.m. – 10:25 a.m. **Coffee Break (Outside of Summit I)**

***Theory*: 10:25 a.m. – 12:00 noon (Summit I)**
Chairperson: David Vanderbilt

10:25 a.m.	G. Pizzi (Invited) - Microscopic description of perovskites near the ferroelectric phase transition
10:50 a.m.	J. Hlinka (Invited) - About the octuplet of symmetry-distinguishable direction indicators
11:15 a.m.	R. Cohen - Absence of ultra-high pressure ferroelectricity in $PbTiO_3$
11:30 a.m.	R. Resta - A fresh look at the position operator (as in polarization, magnetization, and more)
11:45 a.m.	H. Krakauer - Quantum Monte Carlo calculations in solids with downfolded Hamiltonians

Working Lunch: 12:00 noon – 1:30 p.m. (Salon B & C)
Lunch Speaker: L. Bellaiche
"*Novel forms of energy in ferroelectric, antiferroelectric, antiferrodistortive, magnetic and multiferroic materials*"

***New Ferroelectrics*: 1:30 p.m. – 2:45 p.m. (Summit I)**
Chairperson: Hemant Dixit

1:30 p.m.	A. Y. Birenbaum - *Ab initio* analysis of ferroelectric and magnetic properties of potentially multiferroic aurivillius phases
1:45 p.m.	S. Artyukhin - Colossal magnetoelectricity in hexagonal Ni_3TeO_6
2:00 p.m.	S. Disseler - Multiferroicity in bulk and thin-film hexagonal $LuFeO_3$
2:15 p.m.	S. Kamba - Paraelectromagnon in multiferroic $CaMn_7O_{12}$ and hybrid ferroelectric phase transition in multiferroic $Ca_3Mn_2O_7$
2:30 p.m.	D. Saldana-Greco - Magnetic-induced ferroelectric polarization in charge-ordered $CaMn_7O_{12}$ system

2:45 p.m. – 3:15 p.m. **Coffee Break (Outside of Summit I)**

Domains: 3:15 p.m. – 4:55 p.m. (Summit I)
Chairperson: Vincent Garcia

3:15 p.m.	J. Musfeldt (Invited) – Spectroscopic signatures of domain walls in hexagonal $ErMnO_3$
3:40 p.m.	S. Liu – Universal intrinsic origin for ferroelectric domain wall motion
3:55 p.m.	S. Prosandeev – Dynamical magnetoelectric effects associated with ferroelectric domain walls
4:10 p.m.	Z. Hong – PFM-tip induced 90° switching in $Pb(Zr_{0.2}Ti_{0.8})O_3$ thin film: Phase-field modeling
4:25 p.m.	P. Maksymovych – Conductance and electrochemistry of charged domain walls in lead zirconate titanate
4:40 p.m.	N. Barrett – Reversible switching of in-plane polarized ferroelectric domains in $BaTiO_3$(001) with very low energy electrons

4:55 p.m. – 5:30 p.m. **Summary and Scientific Discussions (Summit I)**

Banquet: 6:00 p.m. – 8:00 p.m. (Salon B & C)
Lunch Speaker: H. Christen
"*User Opportunities at the Center for Nanophase Materials Sciences*"

WEDNESDAY, JANUARY 28TH, 2015

7:30 a.m. – 8:30 a.m. **Continental Breakfast (Outside of Summit I)**

***Interfaces/Superlattices/Thin Films*: 8:00 a.m. – 9:00 a.m. (Summit I)**
Chairperson: Ho Nyung Lee

8:00 a.m.	D. Barrionuevo Diestra - Investigations on ferroelectric/multiferroic tunnel junctions for multifunctional applications
8:15 a.m.	V. Garcia - Ferroelectric domains dynamics in memristive tunnel junctions based on super tetragonal $BiFeO_3$
8:30 a.m.	Y. Yang - Room-temperature multiferroic superlattices
8:45 a.m.	M.H. Yusuf - Extrinsic and intrinsic charge trapping at the graphene/ferroelectric interface

***Dopants and Defects*: 9:00 a.m. – 9:55 a.m. (Summit I)**
Chairperson: Ho Nyung Lee

9:00 a.m.	A. Kimmel (Invited) – Defects in ferroelectric oxides and at oxide/ferroelectric interfaces
9:25 a.m.	C. Paillard – Point defects in lead titanate: a first-principles study
9:40 a.m.	T. Granzow - Dopants, defects & domains? Dielectric spectroscopy in $LiNbO_3$

9:55 a.m. – 10:25 a.m. **Coffee Break (Outside of Summit I)**

***$BiFeO_3$*: 10:25 a.m. – 11:20 a.m. (Summit I)**
Chairperson: Veronica Goian

10:25	G. Xu (Invited) – Spin and lattice dynamics in multiferroic $BiFeO_3$
10:50	H. Dixit – Stabilization and switchability of weak ferromagnetism in epitaxially strained $BiFeO_3$
11:05	F. Vidal – Spin-orbit coupling effects in multiferroic Bi_2FeCrO_6

11:20 a.m. – 11:40 a.m. **Closing Remarks (Summit I)**

12:00 noon **Bus leaves for Tour of ORNL (Main Lobby)**

Ferro 2015 · Posters

Listed in alphabetical order

1. Saad Binomran - Application of the Wang-Landau algorithm applied to ferroelectrics
2. Annette Bussmann-Holder - Revisiting the phase transition in $SrTiO_3$: type of transition and precursor effects
3. Xiaoxing Cheng - Influence of coherent twin grain boundary on domain configuration in PZT
4. Omar Chmaissem - Structural and magnetic properties of the novel $Sr_{1-x}Ba_xMnO_3$ multiferroics
5. Bogdan Dabrowski - Multiferroic $Sr_{1-x}Ba_xMnO_3$ perovskite with a huge magnetoelectric coupling
6. Jelle Dionot - Surface polarization, rumpling, and domain ordering of strained ultrathin $BaTiO_3$(001) films with in-plane and out-of-plane polarization
7. Simon Divilov - Role of interface termination in $SrRuO_3/PbTiO_3/SrRuO_3$ capacitors under epitaxial strain
8. Tamotsu Hashimoto - Piezoelectric constants of $KNbO_3$ by molecular dynamics simulations using a shell model
9. Christopher Hendriks - *Ab initio* phonon calculations in metallic and insulating VO_2
10. Ryan Herchig - Tailored polarization reversal and terahertz frequency dynamics in ferroelectric nanowires
11. Brian Holinsworth - Direct band gaps in multiferroic *h*-$LuFeO_3$
12. Hsiang-Chun Hsing - Electrical transport and magnetic properties of $PbTiO_3/SrRuO_3$ superlattices
13. Jiamian Hu - Purely electric-field-driven perpendicular magnetization reversal
14. Alexander Lebedev - Ferroelectric phase transitions in stressed $SrTiO_3$ thin films
15. Hee Young Lee - Magnetoelectric properties of ferrite-PZT multilayer thin films
16. Shinbuhm Lee - Growth control of metal-insulator transition and oxygen stoichiometry in VO_{2-x} epitaxial thin films
17. Lydie Louis - Structural and dielectric properties of the Ruddlesden-Popper Ba_2ZrO_4 structure from first-principles
18. Chengtao Luo - Enhanced piezoelectric response near the morphotropic phase-boundary in lead-free $(Na,Bi)TiO_3$-$BaTiO_3$
19. Subhasish Mandal - Many body effects on the formal charge of 3*d*-transition metal doped $BaTiO_3$
20. Yousra Nahas - Skyrmionic state in ferroelectric nanocomposites
21. John Nichols - Tuning the physical properties in strontium iridate heterostructures
22. Takeshi Nishimatsu - Direct molecular dynamics simulation of thermal conductivity in ferroelectrics
23. Javier Nossa - Effects of Mn addition and compensating oxygen vacancies on the ferroelectric properties of $BaTiO_3$

24. Charles Paillard - Tuning the electron-skyrmion interaction: topological Hall effect and beyond
25. Jonathan Petrie - Strain control of electronic structure in epitaxial $LaNiO_3$
26. Daniel Phelan - Revisiting the structural evolution in powders and single crystals of PMN-xPT
27. Sergei Prokhorenko - Vortex lines at the intersection of domain walls in ferroelectrics
28. Aldo Raeliarijaona - Influence of vacancies on polarization and polarization switching from first-principles.
29. Harold Robinson - ONR's research program on acoustic transduction materials and devices
30. Xuan Shen - Interfacial structure in epitaxial perovskite oxides on (001) Ge crystal
31. Irina Sluchinskaya - Local structure and oxidation state of Ni impurity in $SrTiO_3$, $BaTiO_3$, and $PbTiO_3$
32. Oleg Udalov - Electron transport properties of composite ferroelectrics
33. Rajasekarakumar Vadapoo - High pressure synthesis and characterization of predicted oxynitride perovskite: Yttrium silicon oxynitride ($YSiO_2N$)
34. Raymond Walter - Revisiting galvanomagnetic effects in conducting ferromagnets through electromagnetic field angular momentum density and magnetic moment coupling
35. Bin Xu - Finite-temperature properties of rare-earth-substituted $BiFeO_3$ multiferroic solid solutions and superlattices
36. Tiannan Yang - Phase-field modeling on the elastically coupled magnetic and ferroelectric domains
37. Meng Ye - Magnetic charge and the magnetoelectricity in hexagonal manganites $RMnO_3$ and ferrites $RFeO_3$
38. Michael Yokosuk - Magnetoelectric coupling in Ni_3TeO_6
39. Lipeng Zhang - Oxygen vacancy diffusion in bulk $SrTiO_3$ from density functional theory
40. Fan Zheng - First-principles calculation of bulk photovoltaic effect in $CH_3NH_3PbI_3$ and $CH_3NH_3PbI_{3-x}Cl_x$
41. Houlong Zhuang - Metal-insulator transition in nanostructured $SrTiO_3/LaAlO_3$

Multiferroics and Magnetoelectrics

Dynamics of some Nano-Ferroelectrics and Multiferroics

J. F. Scott,[1] S. E. Rowley,[1] Yi-sheng Chai,[2] R. S. Katiyar,[3] D. Sanchez,[3] Nora Ortega,[3] A. Kumar[4], R. Ahluwalia,[5] Nathaniel Ng,[5] I. Luk'yanchuk,[6] A. Gruverman[7]

[1] Cavendish Laboratory, Cambridge Univ., Cambridge, U.K.
[2] Institute of Physics, Chinese Academy of Sciences, Beijing, China
[3] Dept. Physics, University of Puerto Rico, San Juan, P.R.(USA)
[4] National Physical Laboratory, Delhi, India
[5] IHPC, Singapore
[6] Univ. Picardie, Amiens, France
[7] Univ. Nebraska, Lincoln, NE (USA)

In this talk I will briefly discuss three experiments for which conventional DFT calculations fail due to the dominance of aperiodic boundary conditions: (1) High-symmetry faceting instabilities in low-symmetry crystals[1] with macroscopic demonstration examples ("toys"); (2) Faceting oscillations due to electrical charging of nano-disks, with a highly accurate simulation[2,3] relating the faceting with internal atomic-scale domain realignment; (3) Cylinder stress in nano-crystals.[4] However most of the talk will be devoted to new work on ferroelectric quantum critical points (QCPs). Very recently we presented[5] studies of the quantum critical point (QCP) in the uniaxial ferroelectric tris-sarcosine calcium bromide, which has critical dimensionality d(eff) = d + z + 1 = 5, in contrast to d(eff) = d + z = 4 in $SrTiO_3$ [Fig.1]. We showed that the theoretical prediction of Khmelnitskii[6] that critical exponent for isothermal susceptibility gamma = 3 is violated, and that gamma = 2, due to ultra-weak polarization (its Curie constant C is proportional to Tc, so that both drop to zero at T=0).

More recently we extended these studies to $(Ba,Sr)Fe_{12}O_{19}$ (M-type hexaferrite) with data down to 300 mK.[7] This material, unlike $BiFeO_3$, exhibits a strong ferromagnet moment, with ferrimagnetic ordering of its Fe^{+3} spins. Unlike other ferroelectric QCPs, it is ferroelectric above its incipient QCP (which like $SrTiO_3$ or $KTaO_3$ extrapolates to tens of degrees below T=0). Due to the fact that the $(Ba,Sr)Fe_{12}O_{19}$ crystal used is quite some distance away from the quantum critical point, neither of these exponents were

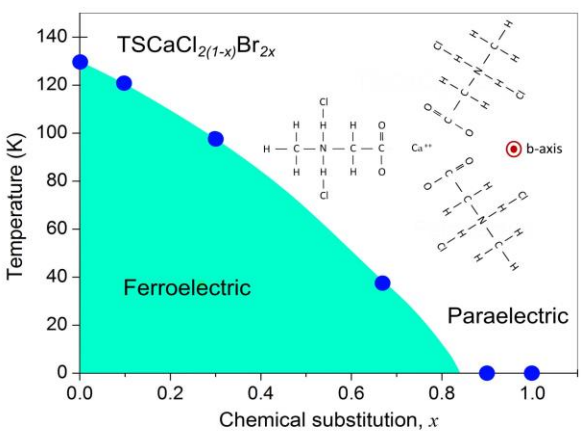

observed. We find two unexpected results: (1) below 5K the dependence of dielectric constant e'(T) is not monotonic and resembles that in $SrTiO_3$ and $KTaO_3$; we interpret this as arising from coupling of the soft mode to acoustic phonons; (2) the critical exponent gamma that describes the divergence of e'(T) above 4K describes a power-law dependence with gamma = 1.5+/-0.1, which differs significantly from both the value 2.0 for quasi-cubic materials with d+1 = 4 and from Khmelnitskii's theory for anisotropic uniaxial

ferroelectrics with d+1 = 5 and gamma = 3. It displays the non-monotonic dip in reciprocal dielectric constant below ca. 5K ("Rowley dip") seen in other QCP systems due to electrostriction. A model for this is presented that is an extension of the phenomenological Barrett Equation, related to work by Tokunaga[8])]. We show however that the form of the dielectric function of this quantum paraelectric (it has a fairly large optical gap frequency of 42 cm^{-1} at q=0 and at T = 6K) may still be well described by the self-consistent phonon model, even under the approximation of a wavevector-independent soft mode frequency (the Einstein approximation); this involves a carefully justified extension of the Barrett Equation.

Dome-shaped phases in the graphs of T versus X in superconductors and magnets, where X is pressure, or magnetic field, or percentage concentration of some constituent element, are also phenomena of great current interest. Interesting states of matter and unusual physical properties often are often found near these phase boundaries. However, such dome-shaped phases are highly unusual if not unique in (T,E) phase diagrams in ferroelectrics. Here we look (unsuccessfully!) for the presence of such domes in both lead iron niobate ($PbFe_{1/2}Nb_{1/2}O_3$) and lead iron tantalate ($PbFe_{1/2}Ta_{1/2}O_3$) mixed into single chemical phase compounds with lead zirconate titanate ($PbZr_{0.47}Ti_{0.53}O_3$) to produce high-temperature magnetoelectric multiferroics (PFNZT and PFTZT). Each dome-shaped phase has been predicted by Glinchuk et al.[9] to exhibit a quantum critical point (QCP) -- a phase transition at T=0 -- at ca. 5% and 20% Fe^{+3}-ion B-site occupancy (four QCPs in all in the two materials PFNZT and PFTZT). The experimental data do NOT however reveal dome-shaped phases in the T vs. %Fe phase diagram, nor any QCPs, but are compared with the general theoretical predictions of Das and others[10-13] and with experiments by Kim et al.[14,15] Finally we note that these $PbFe_{1/2}Nb_{1/2}O_3$-PZT materials are indeed single-phase crystals and not nano-composites; this is proved by the fact that the *B*-site Fe,Nb,Ti,Zr occupancy ratios are not static but change dynamically with temperature, as shown by the NMR studies of Raevski et al.[16]

References

[1] I. Luk'yanchuk et al., *Condmat arXiv* 1309.0291 (2013)
[2] J. F. Scott and A. Kumar, *Appl. Phys. Lett.* **105**, 052902 (2014)
[3] R. Ahluwalia, N. Ng et al (in press)
[4] J. F. Scott, *J. Phys. Cond. Mat.* **26**, 212202 (2014)
[5] S. E. Rowley et al., *arXiv condmat* (12 Oct 2014)
[6] D. E. Khmelnitskii, *JETP* **118**, 133 (2014)
[7] S. E. Rowley, J. F. Scott, Yi-sheng Chai (in press)
[8] M. Tokunaga, *J. Phys. Soc. Jpn.* **57**, 4275 (1988)
[9] M. Glinchuk et al., *J. Appl. Phys.* **106**, 054101(2014)
[10] N. Das et al., *Mod. Phys. Lett.* **28**, 1450167 (2014)
[11] N. Das et al., *Int. J. Mod. Phys.* **27**, 1350028(2013)
[12] N. Das et al., *Phys. Lett.* **A376**, 40 (2012)
[13] N. Das et al., *J. Phys. Cond. Mat.* **21**, 095901 (2009)
[14] J. W. Kim et al., *Proc. US Nat. Acad. Sci.* **106**, 15573 (2009)
[15] J. W. Kim et al., *Nat. Commun.* **5**, 4419 (2014)
[16] I. Raevski et al., *J. Mater. Sci.* **49**, 6459 (2014)

Strain induced and its consequences in multiferroics

B. Dkhil[1], P. Ruello[2], L. Bellaiche[3,4], A. Barthélémy[5], M. Bibes[5]

[1]Laboratoire Structures, Propriétés et Modélisation des Solides
UMR8580 CNRS – Ecole Centrale Paris, 92290 Châtenay-Malabry, France
[2]Institut des Molécules et Matériaux du Mans, UMR CNRS 6283, Université du Maine, Av. O. Messiaen, 72085 Le Mans, France
[3]Physics Department, University of Arkansas, 72701 Fayetteville, AR, USA
[4]Institute for Nanoscience and Engineering, University of Arkansas, 72701 Fayetteville, AR, USA
[5]Unité Mixte de Physique CNRS / Thales & Université Paris-Sud
1 av. Fresnel, 91767 Palaiseau & 91405 Orsay, France

Strain is a powerful tool for tuning physical properties of functional perovskite oxides like polar and/or magnetic orders in multiferroics. This parameter can be generated using various paths including external hydrostatic pressure, biaxial and uniaxial stresses. In case of the model multiferroic $BiFeO_3$ (BFO), the structure i.e. polar atomic shifts and oxygen octahedra tilts which is closely linked to its ferroelectric and magnetic properties shows pressure instabilities [1]. We took advantage of this strain sensitivity to study how coherent acoustic phonons can be generated by a ultrafast pulsed laser which can be seen in somehow as a "uniaxial pressure" [2]. We also used biaxial stresses through various substrates to tune the whole properties of BFO showing how misfit strain can 1) affect BFO phases allowing original mixed-phase state [3]; 2) tune the critical temperatures of antiferromagnetic and ferroelectric transitions [4]; 3) modify the ferroelectric, dielectric and piezoelectric properties [5]; and 4) control the magnetic properties and spin arrangements [6]. Finally, we will also show results in hybrid or artificial multiferroics i.e. heterostructures made of magnetic and ferroelectric materials. In these systems, the so-called magnetoelectric coupling can be mediated at the interface through strain. Here, we showed how the magnetic (AntiFerroMagnetic and FerroMagnetic) states of a FeRh film can be controlled through strain by applying an electric field on an underlying $BaTiO_3$ ferroelectric substrate [7]. In this talk, I will illustrate these remarkable features by stressing the key role of the strain.

References

[1] M. Guennou et al., *Phys.Rev B* **84**, 174107 (2011)
[2] M. Lejman et al. *Nature Comm.* **5**, 4301 (2014)
[3] I.C Infante et al., *Phys. Rev. Lett*. **105**, 057601 (2010)
[4] I.C Infante et al., *Phys. Rev. Lett*. **107**, 2376011 (2011)
[5] C. Daumont et al., *J. Phys. : Condens. Matter* **24**, 162202 (2012)
[6] D. Sando et al., *Nature Materials* **12**, 641 (2013)
[7] R.O. Cherifi et al., *Nature Materials* **13**, 345 (2014)

The Quest for new Room Temperature Multiferroic Thin Films

A. Pignolet[1], L. Corbellini[1], T. Hajlaoui[1], C. Harnagea[1], C. Lacroix[2], D. Menard[3]

[1]Centre Énergie Matériaux Télécommunications, Institut National de la Recherche Scientifique (INRS), Varennes, Québec, Canada
[2]Department of Electrical Engineering, Polytechnique Montréal, Montréal, Québec, Canada
[3]Department of Engineering Physics, Polytechnique Montréal, Québec, Canada

Multiferroic materials that exhibit both ferroelectric and magnetic properties continue to generate great interest for a variety of applications. However, obtaining materials with ferroelectric and magnetics properties that are sufficiently strong and robust at or above room temperature for potential integration into novel devices remain elusive. In addition, novel integrated devices stipulate that these materials be produced in the form of thin films of high quality. Fortunately thin films, in particular when synthesized via deposition processes far from equilibrium, do provide for a number of parameters controlling the synthesis, such as, strain engineering for epitaxial films, which plays an important role and provides a convenient parameter to tune the properties and enable the existence of otherwise metastable phases. As a result, several strategies have been pursued in the quest of thin films of novel multiferroic materials with good multiferroic properties at room temperature.

Replacing every second atom of Fe with an atom of Cr in $BiFeO_3$ (BFO) - until recently the only single phase material known to be multiferroic at room temperature - changes the weak ferromagnetism of BFO stemming from slightly canted spins antiferromagnetically coupled, into ferrimagnetic Bi_2FeCrO_6 (BFCO) with order of magnitude larger magnetic properties without affecting much its ferroelectric properties. The recent developments in the growth and characterization of BFCO epitaxial thin films[1,2] as well as our current understanding of their properties will be briefly presented[3].

Composite materials with one component ferroelectric and a second component magnetic above room temperature is another route to engineer a material that exhibit multiferroic properties at room temperature. The coupling is ten mostly elastically mediated at the boundaries between the two phases. An example of such a system is the maghemite(γ-Fe_2O_3)/BFO composite epitaxial films spontaneously forming when synthesized in the right conditions. Another similar system spontaneously forming a multiferroic composite in the bulk is the tetragonal tungsten bronze $Ba_2LnFeNb_4O_{15}$ (TTB-Ln) / $BaFe_{12}O_{19}$ / $LnNbO_4$, with Ln = Nd, Sm and Eu[4].

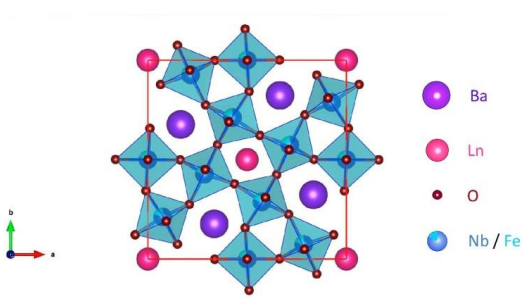

Figure 1 Crystal structure of $Ba_2Ln\ Fe_4O_{15}$

Using TTB-Ln bulk ceramic as targets, epitaxial thin films of $Ba_2LnFeNb_4O_{15}$ (Ln = Eu, Sm, and Nd) have been successfully obtained on $SrTiO_3$(100), MgO(100) and $Gd_3Ga_5O_{12}$(100), and the optimum conditions of deposition established. A structural analysis shows that the lattice parameters are slightly smaller than those observed in the bulk[1], indicative of a compressive stress buildup in the films during the deposition. Ferroelectric macroscopic P-E hysteresis loops as well as microscopic electromechanical behavior probed by piezoelectric force microscopy have demonstrated the existence of a spontaneous polarization at room temperature in TTB-Ln thin films.

A third system that is magnetoelectric and potentially multiferroic at room temperature is ε-Fe_2O_3 (epsilon ferrite), a metastable phase of iron (III) oxide with orthorhombic structure, intermediate between maghemite (γ-Fe_2O_3) and hematite (α-Fe_2O_3). Epsilon ferrite is ferrimagnetic (T_C = 510 K). It exhibits a

polar distortion (non-centrosymmetric space group $Pna2_1$,) and a large magnetic anisotropy at room temperature, as well as a magnetoelectric coupling[5-7]. Moreover, the material is characterized by a ferromagnetic resonance (FMR) frequency in the THz range in the absence of magnetic field and at room temperature, which is of interest for short-range wireless communications (e.g. 60GHz WiFi) and ultrafast computer non-volatile memories[8-10]. It has been recently shown that thin films of metastable ε-Fe_2O_3 can be stabilized by epitaxial strains.[11]

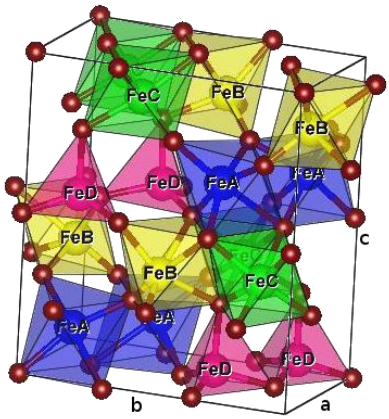

Figure 2 Crystal structure of ε-Fe_2O_3

Epitaxial thin films of ε-Fe_2O_3 and ε-$Al_xFe_{2-x}O_3$ grown by Pulsed Laser Deposition on different single crystalline substrates have been investigated, in order to understand the role of the Al-doping and of the compressive epitaxial strain in the epsilon phase stabilization as well as on the ferroelectric and magnetic properties. While detailed X-ray diffraction studies evidence multiple growth orientations, piezoelectric and ferroelectric properties were analyzed both at the macroscopic level and locally at the nanoscale by Piezoresponse Force Microscopy (PFM) and magnetic properties were characterized using a Vibrating Sample Magnetometer (VSM) and Magnetic force Microscopy (MFM), verifying that the synthesized epitaxial thin films indeed exhibit a high magnetic anisotropy.

References

[1] R. Nechache, C. Nauenheim, U. Lanke, A. Pignolet, F. Rosei and A. Ruediger, J. Phys. Condensed Matter **24**, 142202 (2012).
[2] R. Nechache, C. Harnagea and A. Pignolet, J. Phys.: Condensed Matter **24**, 096001 (2012).
[3] R. Nechache, C. Harnagea, S. Li, L. Cardenas, W. Huang, J. Chakrabartty and F. Rosei, Nature Photonics (2014), doi:10.1038/nphoton.2014.255
[4] M. Josse, O. Bidault, F. Roulland, E. Castel, A. Simon, D. Michau, R. Von der Muhll, O. Nguyen, M. Maglione, Solid State Sciences **11**, 1118 (2009).
[5] S. Ohkoshi *et al.*, Angew. Chem. Int. Ed. **46**, 8392 (2007);
[6] E. Tronc *et al.*, J. Solid State Chem. **139**, 93 (1998);
[7] M. Gich *et al.*, Nanotechnology **17**, 687 (2007);
[8] M. Nakajima, A. Namai, S. Ohkoshi, T. Suemoto, Optics Express **18**, 18260 (2010);
[9] H.C. Siegmann *et al.*, J. Magn. Magn. Mater. **151**, L8 (1995);
[10] C.H. Back *et al.*, Science **285**, 864 (1999);
[11] M. Gich *et al.*, Appl. Phys. Lett. **96**, 112508 (2012).

Design Strategy and Prediction of New Room Temperature Magnetoelectric Multiferroics

Saurabh Ghosh[1], Hena Das[1], Tanusri Saha-Dasgupta[2] and Craig. J. Fennie[1]

[1]School of Applied & Engineering Physics, Cornell University, Ithaca, NY 14853, USA
[2]S.N. Bose National Centre for Basic Sciences, Kolkata 700098, INDIA

Perovskite ABO_3 oxides display many promising functional properties including ferroelectricity and magnetism. An ongoing challenge has been to design and synthesize materials in which ferroelectric and magnetic orderings not only coexist in a single phase above room temperature, but also are nontrivially coupled. Such a cross coupling between these different ferroic orderings could lead to many novel applications, in particular, involving electrical control of magnetism that is required in case of MERAMs or magnetic capacitors.

Taking advantage of a newly developed mechanism to induce ferroelectricity - "*hybrid improper ferroelectricity*"[1-4] and supported by first-principles density functional theory (DFT) calculations, we will discuss and outline strategies where electric field control of magnetism can be possible in systems consisting of ABO_3 building blocks. First, we take the example of ABO_3 / $A'BO_3$ superlattices, which may be amenable to advanced oxide thin film growth techniques, and second, bulk $AA'BB'O_6$ double perovskites which can be realized by synthetic chemical route.

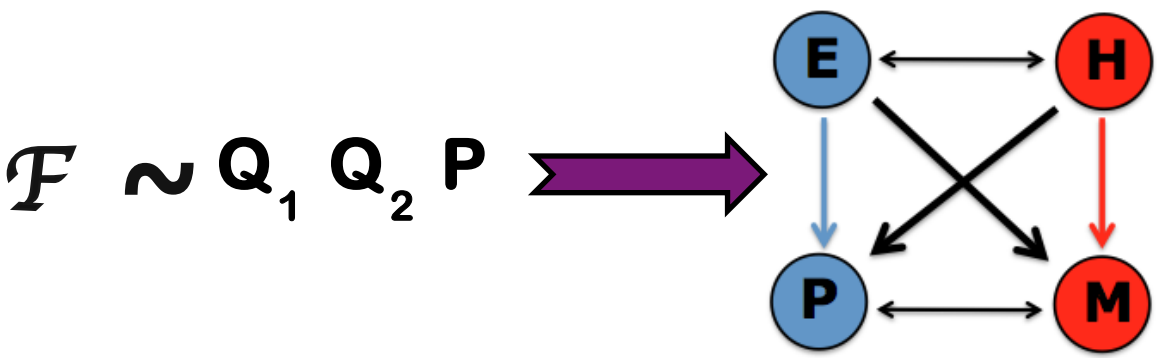

Figure: Hybrid improper ferroelectricity: route to create new room temperature magnetoelectric multiferroics, here, switchable polarization P is driven by two primary order parameters Q_1 and Q_2. Individually, Q_1 and Q_2 can drive weak magnetization as well as linear magnetoelectric coupling, which is promising for electric field control of magnetism.

ABO_3 / $A'BO_3$ Superlattice: We show that in $(LnFeO_3)_m$ / $(Ln'FeO_3)_n$ digital superlattices (Ln, Ln' = lanthanide or Y, and both *m*, *n* are odd integers) constructed from *Pnma* perovskites, BO_6 octahedral rotations induce a spontaneous electrical polarization. Furthermore, this rotation pattern is shown to induce linear magnetoelectricity and weak-ferromagnetism, much like the recently

discussed '327' manganite Ruddlesden-Popper [2]. In these ferrite superlattices, however, it is clear that both the ferroelectric and magnetic ordering temperatures should occur above room temperature. We discuss how the Ln/Ln' cation radius mismatch controls the magnitudes of the induced polarization and magnetization, as well as the barrier to switch the polarization. Finally, we suggest that these systems represent a practice way to realize a linear magnetoelectric effect at room temperature. To help in identifying a successful design strategy we have also addressed the governing factors that determine the strength of the linear magnetoelectric coupling.

$AA'BB'O_6$ Bulk Double Perovksites: Ordered double perovskite materials with general chemical formula $A_2BB'O_6$ (where A is an alkaline-earth or rare earth ion, BB' are transition-metal ions) exhibit rare combination of ferromagnetic/ferrimagnetic-insulating properties above or near room temperature. Here, the high magnetic T_c is due the complex interplay between B and B' transitions metal cations arranged in rock salt manner. Three types of AA' orderings are possible in $AA'BB'O_6$, namely, layer, rock salt and columnar. Symmetry arguments show that layer and rock salt orderings can have spontaneous polarization induced due to *hybrid improper* mechanism. Thus, this family of materials can be promising for investigation of electric field control of magnetism. We take up the case of Sr_2CrOsO_6, which is a ferrimagnetic insulating double perovskite with $T_c \sim$ 725K [5], the highest known T_c for a magnetic insulator with appreciable uncompensated magnetic moment among the oxide family [6]. In $AA'CrOsO_6$ systems, we proposed a chemical route to stabilize the layered AA' phase. We have also identified new multiferroic materials in layer $AA'CrOsO_6$ with low switching barriers and with strong magnetoelectric coupling, expected above room temperature. Our study, which includes an extensive choice of A and A' cations should form the platform for checking feasibility of synthesizing them and verifying our proposal.

We believe that the general conception and design strategy for room temperature electrical control of magnetism by considering ABO_3 perovskite oxides as building blocks will motivate further experimental and theoretical investigation in this direction.

References:

1. E. Bousquet, M. Dawber, N. Stucki, C. Lichtensteiger, P. Hermet, S. Gariglio, J.-M. Triscone, and P. Ghosez, Nature **452**, 732 (2008)
2. N. A. Benedek and C. J. Fennie, Phys. Rev. Lett. **106**, 107204 (2011)
3. J. M. Rondinelli and C. J. Fennie, Advanced Materials **24**, 1961 (2012)
4. A. T. Mulder, N. A. Benedek, J. M. Rondinelli, and C. J. Fennie, Advanced Functional Materials **23**, 4810 (2013)
5. Y. Krockenberger, *et.al*. Phys. Rev. B, **75**, 020404 (2007)
6. Hena Das, P. Sanyal, T. Saha-Dasgupta and D.D. Sarma, Phys. Rev. B **83**, 104418 (2011)

Email: sg827@cornell.edu

Magneto-electric coupling in granular multiferroics

Oleg Udalov[1], N.M. Chtchelkatchev[2], I.S. Beloborodov[1]

[1] Department of Physics and Astronomy, California State University Northridge, Northridge, CA 91330, USA

[2] Institute for Physics of Microstructures, Russian Academy of Science, Nizhny Novgorod, 603950, Russia

Currently composite materials with combined magnetic and electric degrees of freedom attract much of attention for their promise to produce new effects and functionalities[1,2]. The idea of using ferromagnetic and ferroelectric properties in a single phase multiferroics was developing since seventeenths. However, in bulk homogeneous materials this coupling is weak due to relativistic parameter v/c, with v and c being the electron velocity and the speed of light, respectively. Only recently the new classes of two-phase multiferroic materials such as single domain multiferroic nanoparticles[3], laminates[4], and epitaxial multilayers[5] and granular materials[6] were discovered giving a new lease of life to this field. So far, the interface strain generated by the ferroelectric layer was considered as the promising mechanism for strong enough magneto-electric coupling in two-phase multiferroic materials. This strain modifies the magnetization in the magnetic layer and the magnetic anisotropy energy.

We propose a different mechanism for magneto-electric coupling emerging at the edge of strong long-range electron interaction, ferroelectricity, and magnetism[7]. In composite multiferroics - materials consisting of metallic ferromagnetic grains embedded into ferroelectric (FE) matrix, the origin of this coupling is twofold: i) Strong influence of FE matrix on the Coulomb gap depending the electron localization length and the overlap of electron wave functions, and therefore controlling the exchange forces. ii) Dependence of the long-range part of Coulomb interaction, and thus the exchange interaction, on the dielectric permittivity of the FE matrix.

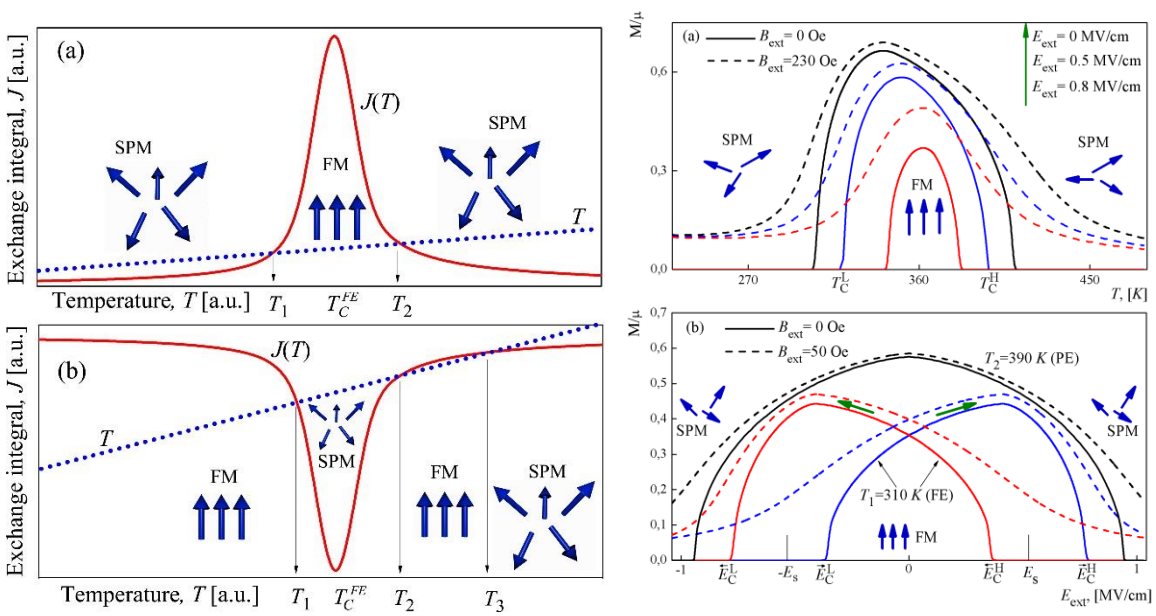

Figure 1. Left panel is the dependence of intergrain exchange constant in granular multiferroic on temperature. (a) and (b) correspond to granular systems with different parameters. Dotted line shows temperature. T^{FE}_C is the FE Curie temperature. Right panel shows magnetization of granular multiferroic as a function of temperature (a) and external electric field (b). SPM denotes superparamegnetic state of the multiferroic, FM denotes ferromagnetic state. B_{ext} and E_{ext} are external magnetic and electric field, correspondingly.

We show that the effective ferromagnetic exchange constant J between the ferromagnetic grains strongly depends on temperature near the ferroelectric Curie temperature in granular multiferroics due to the above mentioned mechanisms. This give rise to unusual magnetic phase diagram of composite multiferroics (see Fig. 1, left panel). The transition temperature between ordered and disordered magnetic states can be found approximately using the equation $J(T) = T$. FM state corresponds to $J(T) > T$. If mechanism (i) is the strongest, the FM state appears at higher temperatures than the disordered SPM state. This is known as an inverse phase transition.

We study magnetization of composite multiferroic as a function of temperature and external electric field (see Fig. 1, right panel). The FM state exists at finite temperature range around the FE phase transition point. Outside this region the superparamagnetic phase appears. Both the magnetic phase transition temperature and the magnitude of magnetization are strongly electric field dependent. In addition, the magnetic phase transition can be drive by the external electric field. The magnetic state of the system depends on the mutual orientation of external electric field and polarization of FE matrix. The ferromagnetic and ferroelectric degrees of freedom are coupled due to the influence of FE substrate on the screening of intragrain and intergrain Coulomb interaction.

Acknowledgements The work was supported by NSF under Cooperative Agreement Award EEC-1160504 and NSF Award DMR-1158666

References

[1] W. Eerenstein, N. D. Mathur, and J. F. Scott, *Nature* **442**, 759 (2006).
[2] R. Ramesh and N. A. Spaldin, *Nature Mat.* **6**, 21 (2007).
[3] N. Mathur, *Nature* **454**, 591 (2008).
[4] N. Cai, C.-W. Nan, J. Zhai, and Y. Lin, *Appl. Phys. Lett.* **84**, 3516 (2004).
[5] S. Mukherjee, A. Roy, S. Auluck, R. Prasad, R. Gupta, and A. Garg, *Phys. Rev. Lett.* **111**, 087601 (2013).
[6] X. L. Zhong, J. B. Wang, M. Liao, G. J. Huang, S. H. Xie, Y. C. Zhou, Y. Qiao, and J. P. He, *Appl. Phys. Lett.* **90**, 152903 (2007).
[7] O. G. Udalov, N. M. Chtchelkatchev, and I. S. Beloborodov, *Phys. Rev. B* **89**, 174203

Growth and Characterization

Novel in-situ X-ray diffraction measurement of ferroelectric superlattice properties during growth[a)]

Benjamin Bein,[1, b)] Hsiang-Chun Hsing,[1] Sara J Callori,[1, c)] John Sinsheimer,[1, d)] and Matthew Dawber[1, e)]
Dept of Physics and Astronomy Stony Brook University, Stony Brook, NY 11794-3800 USA

Ferroelectric domains, surface termination, average lattice parameter and bilayer thickness were monitored by in-situ x-ray diffraction during the growth of $BaTiO_3/SrTiO_3$ (BTO/STO) superlattices by off-axis RF magnetron sputtering. A new x-ray diffraction technique was employed which makes effective use of the custom growth chamber, pilatus detector and synchrotron radiation available at beamline X21, NSLS, BNL. The technique allows for scan times substantially faster than the growth of a single layer of material, allowing continuous monitoring of multiple structural parameters as the film grows. The effect of electric boundary conditions was investigated by growing the same superlattice alternatively on STO substrates and 20nm SRO thin films grown on STO substrates. The growth rate was calibrated using X-ray reflectivity like in[2].

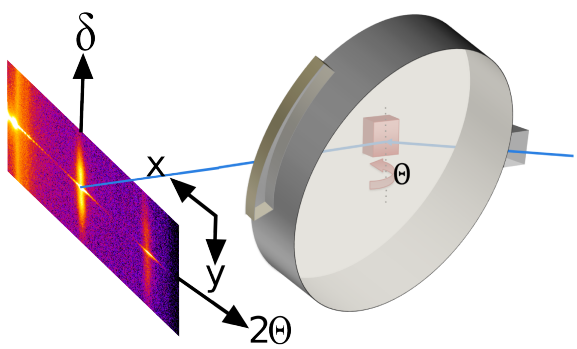

FIG. 1. The figure shows a schematic of the experimental setup and the diffractometer angles. The detector is represented by a snapshot of the data together with the detector coordinate system.

To increase the scan speed to be faster than the growth of one single unit cell layer of material a new scanning technique was employed. The angular integration mode from SPEC called powder mode is used to integrate over the rocking curve of a single crystal. This allows to integrate the exposure of the detector while the θ angle is rocked. An example of the taken data is shown in Fig. 2. One can see one single image taken during the experiment and labels of the observed features. These can be assembled into continuous *movies* which allow the observation of the evolution of diffraction features during the growth.

Area scans can be split into two main line scans. The first scan is along the q_z direction which is a horizontal line in Fig. 2. A plot along this line together with a fit to the data and basic superlattice X-ray diffraction analyzes is shown in Fig. 3. Fitting for superlattice X-ray diffraction is described in[3]. From the fit one can determine surface termination, average lattice parameter $\bar{c}$ and bilayer thickness. Fig. 4 shows a plot of $\bar{c}$ against the total superlattice thickness. One can see that all superlattices show a larger tetragonality than one would expect from the known elastic constants for BTO and STO if the samples are paraelectric. This could be explained if the sample is ferroelectric with a out-of-plane component. Furthermore $\bar{c}$ is larger for the sample grown on a SRO bottom electrode which would suggests a larger polarization of the superlattice grown on a SRO bottom electrode.

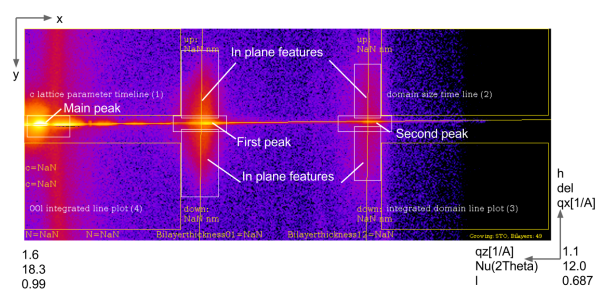

FIG. 2. One single detector image is shown with explanations of the main features one can observe in each scan.

The second line scan is along the q_x direction which is vertical in Fig 2. The most interesting line for q_x is in the region where one can observe diffuse scattering. This diffuse scattering is a sign of periodic in-plane features. For ferroelectrics one possible explanation would be stripe domains. This diffuse scattering is shown in Fig. 5, as a vertical cut through the first superlattice peak. The shown data was rescaled to be able to compare the shape of the diffuse scattering for the early stage(7 bilayers) and the end stage(25 bilayers). The rescaling was done by dividing the data by the peak diffuse scattering intensity.

This shows that diffuse scattering gets more intense while the superlattice grows but the average domain size does not change with the square root of the total super-

[a)] This work was supported by NSF DMR1055413
[b)] benjamin.bein@stonybrook.edu
[c)] Now at: Bragg Institute, ANSTO, New Illawarra Road, Lucas Heights NSW 2234,Australia.
[d)] Now at: Brookhaven National Laboratory, Upton, New York 11973-5000, USA.
[e)] matthew.dawber@stonybrook.edu

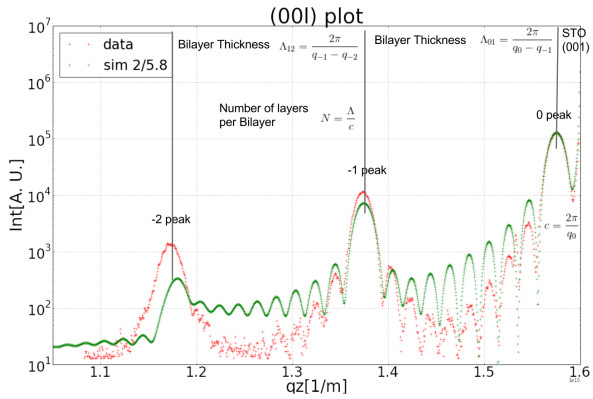

FIG. 3. The figure shows a CTR along (0,0,l) and basic superlattice X-ray diffraction analysis. Furthermore a fit to the superlattice is shown. The fit is used to determine the superlattice characteristics.

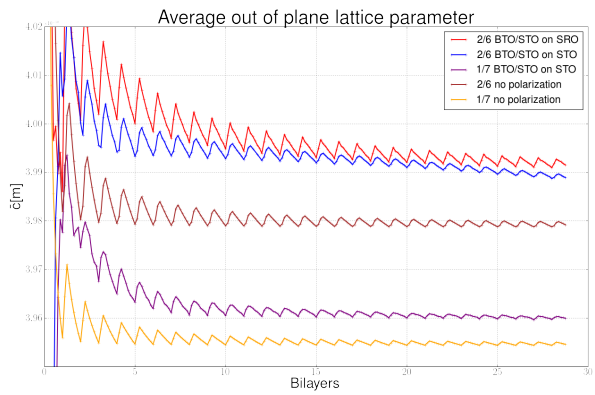

FIG. 4. This plot shows the average out of plane lattice parameter $\bar{c}$ of the superlattice. The blue curve is $\bar{c}$ for a 2/6 BTO/STO grown on STO and the red curve is the same superlattice grown on a SRO electrode. The sample grown on SRO has a larger $\bar{c}$ which suggests a larger polarization. The brown curve would be the expected $\bar{c}$ for a 2/6 BTO/STO superlattice without any polarization. The purple curve shows $\bar{c}$ for a 1/7 BTO/STO superlattice grown on STO and the yellow curve is the expected $\bar{c}$ for the same superlattice without any polarization.

lattice thickness. This suggests that the polarization in the sample is not homogeneously polarized in the out of plane direction. This could be due to closur domains, which are predicted for ultrathin BTO/SRO capacitors[1]. One can write and read domains on the sample using Piezo force microscopy (PFM) which suggests that there is still some cross talk between the different BTO layers. This means that the samples have most likely a mixed stated between closure and stripe domains where the out of plane polarization in the STO is smaller than in BTO. Fig. 6 shows a schematic of the mixed domain state. A similar behavior was found for PTO/STO superlattices with only 3 or 4 unit cell layers of PTO per bilayer[4].

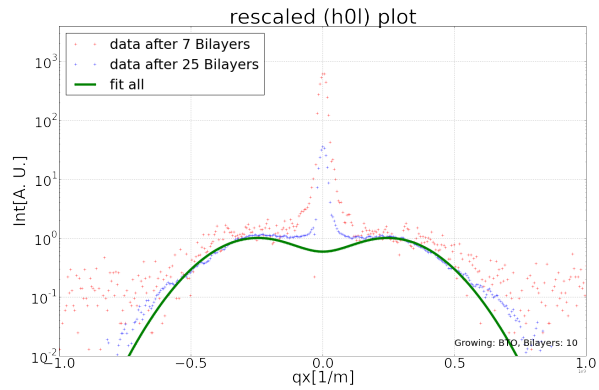

FIG. 5. In the figure one can see a cut along the h direction through the first superlattice peak for two different superlattice thicknesses. The data was rescaled using the domain peak intensity to show that only the absolute intensity of the diffuse scattering changes with time but the distribution does not change. This means that the domain size does not change with thickness.

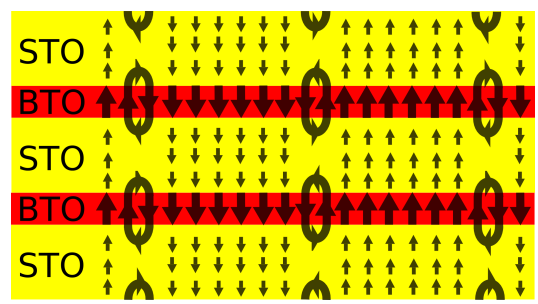

FIG. 6. schematic of ferroelectric domains inside the BTO/STO superlattices.

Besides the fundamental knowledge gained from these studies, being able to monitor the structural parameters of a growing ferroelectric superlattice at this level of detail provides numerous insights which can guide the growth of higher quality ferroelectric superlattices in general.

[1]Pablo Aguado-Puente and Javier Junquera. Ferromagneticlike closure domains in ferroelectric ultrathin films: First-principles simulations. *PHYSICAL REVIEW LETTERS*, 100(17), MAY 2 2008.

[2]Priya V. Chinta, Sara J. Callori, Matthew Dawber, Almamun Ashrafi, and Randall L. Headrick. Transition from laminar to three-dimensional growth mode in pulsed laser deposited BiFeO3 film on (001) SrTiO3. *APPLIED PHYSICS LETTERS*, 101(20), NOV 12 2012.

[3]EE FULLERTON, IK SCHULLER, H VANDERSTRAETEN, and Y BRUYNSERAEDE. STRUCTURAL REFINEMENT OF SUPERLATTICES FROM X-RAY-DIFFRACTION. *PHYSICAL REVIEW B*, 45(16):9292–9310, APR 15 1992.

[4]P. Zubko, N. Jecklin, A. Torres-Pardo, P. Aguado-Puente, A. Gloter, C. Lichtensteiger, J. Junquera, O. Stephan, and J. M. Triscone. Electrostatic Coupling and Local Structural Distortions at Interfaces in Ferroelectric/Paraelectric Superlattices. *NANO LETTERS*, 12(6):2846–2851, JUN 2012.

New Insights into the Structure and Properties of PZT from Mesoscopic to Atomic Scale

Zuo-Guang Ye, Nan Zhang, Yujaun Xie, and Alexei A. Bokov

Department of Chemistry and 4D LABS, Simon Fraser University,
Burnaby, British Columbia, V5A 1S6, Canada

Lead zirconate-titanate solid solution, $PbZr_{1-x}Ti_xO_3$ (PZT), has been studied extensively over the past decades for both industrial applications and fundamental research, but almost exclusively in the forms of ceramics and thin films because of the difficulties encountered in the growth of PZT single crystals. On the other hand, the mesoscopic domains, the microstructure and the atomistic mechanisms that cause the outstanding piezoelectric performance of this class of materials near the morphotropic phase boundary (MPB) remain poorly understood. Therefore, it is of particular interest to grow large single crystals of PZT, which are not only necessary for thorough characterization of the anisotropic properties of this prototype ferroelectric solid solution system, but are also expected to exhibit superior piezo- and ferroelectric performance over the PZT ceramics, and a higher depoling temperature (T_d) and higher coercive field (Ec) (than the relaxor-based PMN-PT and PZN-PT single crystals), which are required for a broader range of advanced applications. The objective of this work is to synthesize the PZT single crystals and to characterize their domain structures, phase transitions, local structure, and micro polar structures in order to provide a better understanding of the structure-property relations.

Recently, thanks to the capability to grow PZT single crystals and the availability of advanced characterization and analytical techniques, such as piezoresponse force microscopy (PFM), spherical aberration-corrected transmission electron microscopy, high-resolution neutron total scattering and diffuse scattering, and pair-distribution function analysis, we have gained new insights into the complex local structure, atomic scale polarization rotation, nano-scale domain structure, intricate phase transition and critical behaviour, and tri-critical points in PZT. These results have provided a better understanding of the relationship between micro-/nano-scopic structure and macroscopic functional properties for this important material, but also for the piezo-/ferroelectric materials in general.

In this paper, we present our successful growth of $PbZr_{1-x}Ti_xO_3$ single crystals with a wide composition range across the morphotropic phase boundary (MPB) ($0.20 \leq x \leq 0.65$) by a top-seeded solution growth (TSSG) technique. The systematic characterization of the grown PZT single crystals by a variety of techniques, such as dielectric and piezo-/ferroelectric measurements, polarized light microscopy, piezoresponse force microscopy and transmission electron microscopy, has allowed us to discover a series of new physical phenomena in this important family of piezo-materials.

The crystal growth conditions are optimized in terms of the chemical, thermodynamic and kinetic parameters. The growth temperature is found to be a key factor for controlling the composition of the grown crystals. PZT crystals with composition from x = 0.42 to x = 0.47 show characteristic ferroelectric-to-ferroelectric phase transitions due to the presence of a curved MPB. The crystals of MPB composition, x = 0.46, are found to exhibit the best properties, with a piezoelectric coefficient d_{33} = 1223 pC/N, an electromechanical coupling factor k_{33} = 80%, a large coercive field E_c= 7 kV/cm and a high Curie temperature T_C = 386 ℃, potentially useful for high temperature and high power electromechanical transducer applications.

The studies of the mesoscopic domain structure [1], local polar domain structure and phase transition behaviour of PZT single crystals suggest that quenched random fields play an important role in the formation of nanodomain state in PZT, which is discussed in the framework of the behaviour and mechanisms of relaxor ferroelectrics [2].

Pair Distribution Function (PDF) analysis and Rietveld refinement have been carried out to study both the short- and long-range orders in the Zr-rich rhombohedral region of the PZT phase diagram. The nature of the monoclinic phase across the Zr-rich and morphotropic phase boundary area of PZT is clarified. Evidence is found that long-range average rhombohedral and both long- and short-range monoclinic regions coexist at all compositions. In addition, a boundary between one type of monoclinic (M_A) structure and another monoclinic (M_B) structure has been found. The general advantage of a particular monoclinic distortion (M_A) for high piezoactivity is discussed from a spatial structural model of susceptibility to stress and electric field, which is applicable across the wide field of perovskite materials science [3].

The atomic structure of PZT crystals with x=0.42 is imaged by means of high-resolution TEM. The accurate Pb displacements and their directions are successfully determined relative to the centre of the four B-cations, on the <110> monoclinic mirror plane. The orientation and distribution of local polarizations indicate a mixture of rhombohedral, tetragonal and monoclinic local symmetry, providing the atomistic evidence of the monoclinic phase.

The work was supported by the U.S. Office of Naval Research (Grant No. N00014-12-1-1045) and the Natural Science & Engineering Research Council of Canada (NSERC).

References:

[1] A. A. Bokov, X. Long, and Z.-G. Ye, *Phys. Rev. B*, **81**(17), 172103/1-4 (2010)..

[2] D. Phelan, C. Stock, J. A. Rodriguez-Rivera, S. Chi, J. Leão, X. Long, Y. Xie, A. A. Bokov, Z.-G. Ye, P. Ganesh, and P. M. Gehring, *Proc. Natl. Acad. Sci. U.S.A.*, **111**(5)，1754 – 1759 (2014).

[3] N. Zhang, H. Yokota, A. M. Glazer, Z. Ren, D. A. Keen, D. S. Keeble, P. A. Thomas and Z.-G. Ye, *Nat. Commun.* **5**, Article #5231 [DOI: 10.1038/ncomms6231] (*2014*).

Lattice modulation and structural instability at M-point in PZT single crysatls by X-ray scattering

S.Vakhrushev[1,2], D.Andronikova[2], A. Bosak[3], Yu. Bronwald[2], R. Burkovsky[2], D. Chernyshov[4], I.N. Leontyev[5], Z.-G. Ye[6]

1- Ioffe Institute, 26 Politekhnicheskaya, St.-Petersburg, 194021 Russia
2- St.Petersburg State Polytechnical University, St.-Petersburg, Russia
3- European Synchrotron Radiation Facility, Grenoble, France
4- Swiss-Norwegian Beamlines at ESRF, Grenoble, France
5- LE STUDIUM®, Loire Valley Institute for Advanced Studies Orleans&Tours, France
6 - Simon Fraser University, V5A 1S6, Burnaby, Canada.

In recent years the revival of the interest to the physics of $(PbZrO_3)_{1-x}(PbTiO_3)_x$ (PZT) solid solution is observed. To large extent this revival is related to development in the single crystal growth and to the new experimental possibilities in studying the extremely small single crystals using high-flux synchrotron radiation sources.

Already the structure of pure lead zirconate crystal $PbZrO_3$ (PZO) is extremely complicated. In the Ref.1 it is mentioned that the lattice distortion in PZO is described as a sum of 6 different frozen "modes". The major role is played by the Σ_3 and R_{25} components. Ab-initio calculations of Ph. Gosez et al., demonstrated instability of the Last-type Γ_{15} TO mode and completely flat M-R branch related to the oxygen octahedra tilts. In recent paper [3] it was shown that antiferroelectric transition in PZO can be described by the softening of Γ_{15} mode with Σ_3 order parameter being the result of the flexoelectric TO - TA coulpling and R_{25} order parameter appeared due to the Holakovsky mechanism.

However even in pure PZO intermediate phase (presumably ferroelectric) characterized by the M-type superstructure exists. In PZO this phase is observed only in very narrow temperature region but it becomes stable at 0<x<~6% [4]. The structure of the phase is still under discussion and we will abbreviate it as F.

Until now most of the measurements of this intermediate phase were done using ceramic samples. Single crystal measurements were carried out only using electron diffraction and electron microscopy techniques.

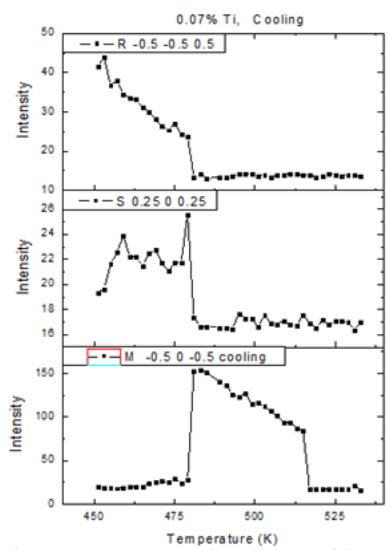

Figure 1 Temperature dependences of the intensity of the superstructure peaks in PZT07

In this report we are going to present the results of the study of PZT single crystals with lead titanate concentrations from 0.7% to 20% (x=0.7%, 1.5%, 3.3%, 6% 20%). To explore the structural changes and critical phenomena in the mentioned single crystals we have used a combination of the X-ray diffraction, diffuse and inelastic X-ray scattering techniques. Diffraction and DS measurements were carried out at Swiss-Norwegian Beam Lines (SNBL) at ESRF using the KUMA (Oxford Diffraction) diffractometer with PILATUS position sensitive detector. Inelastic X-ray measurements were performed at ID28 ESRF beamline.

In the present report we will mostly concentrate on the study of the phase transition from cubic paraelectric to the intermediate phase manifesting itself by M-type (h+½ k+½ l) superstructure peaks.In agreement with earlier published data we have observed a sequence of phase transitions from cubic phase (C) to phase F and then to the orthorhombic AFE phase Figure 1 demonstrates temperature

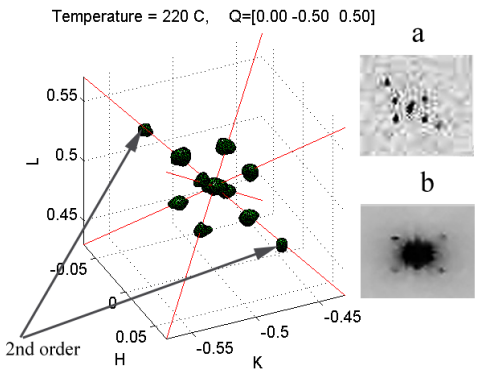

Figure 2 M-superstructure and satellites

evolution of the intensity of the superstructure peaks in PZT07 (x=0.7%). It is clearly seen that C - F and F - AFE transitions are of the first order and F phase is stable in the broad temperature range.

It was shown before (see e.g. [4]) that M-peaks have complicated "fine structure". Electron diffraction experiments demonstrated existence of additional satellites around the M-peaks. Neither X-ray nor neutron scattering experiments confirmed this observation before. In our measurements we have found fine satellite structure for all studied compositions except 20%PT. Superstructure peaks observed in PZT07 are shown in the Figure 2. In the main panel 3-d distribution of the scattering intensity is shown, panel ***a*** demonstrates 2-d map around M position and panel ***b*** 2-d map around "major" Bragg peak. Our observations can be summarized as follows:

- no extinction rules exist. This fact indicates that the M-superstructure is not determined by the oxygen octahedra tilts;
- each M peak is surrounded by 8 1-st order {δδδ} satellites δ≈0.018a*;
- around some of the M peaks second order satellites shifted for 2δ are observed. These satellites usually occur only one of 4 equivalent {111} directions (main panel and panel ***a*** Figure 2);
- In addition to the satellites around M-peaks additional weak spikes were found around major Bragg peaks (panel ***b*** Figure 2);

Both 1-st and 2-nd order satellites around M-peaks can be described in the frames of antiphase domains but we cannot at the moment explain 2-nd order spikes around major Bragg peaks.

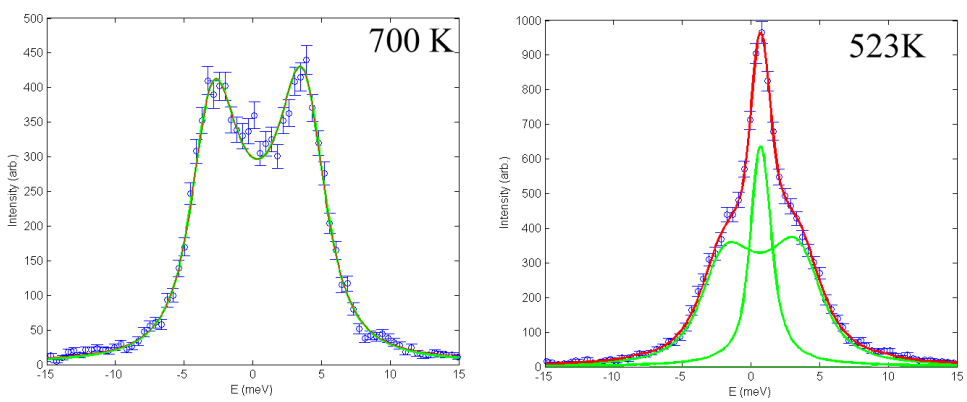

To elucidate the microscopic origin of the C - F phase transition we have carried out IXS measurements. Phonon dispersion for in-plane polarized modes was determined and its temperature evolution was traced. Very flat dispersion of the TA branch similar to that in pure PZO was found with weak anomaly around $\boldsymbol{q}_{\Sigma}$=(¼¼0). However no frequency lowering at around M-point was found. Instead on approaching the transition temperature from above strong central peak aroused (Figure 3). At the moment we cannot say if this CP is related to the critical relaxational degree of freedom relevant to the C - F transition or it results from the coupling of the relevant phonon mode to some dynamic disorder (lead rattling ?).

References

[1] E. Cockayne, K.M. Rabe, *J. of Phys. Chem. Sol*. **61** 305, (2000)

[2] Ph. Gosez et al., Phys. Rev. B 60,836, (1999)

[3] A. K. Tagantsev et al., *Nature communications*, vol.4, 2229, (2013).

[4] G. Ricote et al., *J. Phys.: Condens. Matter*, **10**, 1767, (1998).

Demonstration of spin-phonon coupling in infrared and THz spectra of $Sr_{1-x}Ba_xMnO_3$ and $Sr_{1-x}Ba_xMn_{1-y}Ti_yO_3$ ceramics

V. Goian[1], M. Savinov[1], V. Bovtun[1], C. Kaldec[1], F. Kadlec[1], M. Kempa[1], D. Nuzhnyy[1], B. Dabrowski[2], and S. Kamba[1]

[1] Institute of Physics, Czech Academy of Sciences, Prague, Czech Republic
[2]Department of Physics, Northern Illinois University, DeKalb, IL, USA

e-mail: goian@fzu.cz

Spin-phonon coupling has been investigated in several materials because it is used to probe and design new multiferroics.[1] Importance of the spin-phonon coupling was emphasized for example in $EuTiO_3$ where ferroelectricity and ferromagnetism have been induced in epitaxial strained thin films,[1,2] although the bulk $EuTiO_3$ is a quantum paraelectric antiferromagnet. Recent first principles calculations predicted a large spin-phonon coupling in various manganites, chromides and ferrites with perovskite structure,[3] so these materials can theoretically become new bulk multiferroics with appropriate doping or as thin films under strain.

In this work, we focus on polycrystalline $Sr_{1-x}Ba_xMnO_3$ (x=0, 0.4, 0.43 and 0.45) and $Sr_{1-x}Ba_xMn_{1-y}Ti_yO_3$ (x=0.5 and 0.6 and y=0.06 and 0.1) perovskites for which we demonstrate phonon anomalies near ferroelectric and antiferromagnetic phase transitions. Pure $SrMnO_3$ crystallizes in cubic perovskite $Pm\bar{3}m$ crystal structure and exhibits magnetic phase transition to antiferromagnetic G-type phase near 230 K.[4] Close to this temperature, the 23% hardening of the lowest-frequency phonon was revealed in the IR spectra due to spin-phonon coupling.[5] Although $SrMnO_3$ is paraelectric down to liquid He temperatures, recent first principles calculations predicted that system can become ferroelectric and even ferromagnetic under a biaxial strain.[6] Neither strain-induced ferroelectricity nor ferromagnetism have been confirmed experimentally in $SrMnO_3$ thin films but Sakai et al.[7] expanded the $SrMnO_3$ lattice with Ba substitution and successfully induced ferroelectricity in $Sr_{1-x}Ba_xMnO_3$ ($x \geq 0.45$) crystals at $T_C \approx 400$ K while Néel temperature of $T_N \approx 180$ K is the same. Important fact is that in this case the large spontaneous polarization ($P_S \approx 13$ μC/cm^2) is driven by displacement of magnetic Mn^{4+} cations, so exceptionally strong magnetoelectric coupling is expected and should be verified.

Initially we performed low frequency (100 Hz – 1 MHz) and microwave (1 MHz – 1.8 GHz) dielectric studies on $Sr_{1-x}Ba_xMnO_3$ ceramics (x=0.4, 0.43 and 0.45). Unfortunately, leakage current strongly influenced the dielectric measurements and therefore a giant permittivity was observed in these compounds above 100 K. Conductivity was strongly reduced in THz and completely suppressed in IR spectra. THz permittivity exhibits a step up on cooling below T_N confirming the strong spin-phonon coupling in these ceramics. Moreover, IR spectra of $Sr_{0.55}Ba_{0.45}MnO_3$ reveal phonon anomalies near 350 K supporting ferroelectric phase transition observed already in structural studies with X-ray and neutron diffractions.[7,8]

Hopping conductivity is expected to be strongly reduced by Ti doping. For that reason we investigated $Sr_{1-x}Ba_xMn_{1-y}Ti_yO_3$ (SBMTO) samples. Dielectric spectra in the kHz range still show a giant permittivity in paramagnetic phase, but decrease by several orders of magnitude was observed in conductivity and permittivity of SBMTO at Néel temperature near 170 K. Microwave permittivity and conductivity remains influenced by hopping conductivity, nonetheless permittivity of $Sr_{0.4}Ba_{0.6}Mn_{0.94}Ti_{0.06}O_3$ exhibits a peak at ferroelectric phase transition near 400 K. Ferroelectric phase transition is seen as well in phonon permittivity (see Figure 1) obtained from fits of the THz and IR reflectivity spectra. Moreover, phonon permittivity exhibits significant increase on cooling below T_N, evidencing the presence of spin-phonon coupling. Spectra of $Sr_{0.5}Ba_{0.5}Mn_{0.9}Ti_{0.1}O_3$ did not reveal a ferroelectric phase transition, however the manifestation of spin-phonon coupling was still present in phonon permittivity near T_N. No change of

THz permittivity of $SrMnO_3$ and $Sr_{0.4}Ba_{0.6}Mn_{0.94}Ti_{0.06}O_3$ ceramics was observed in external magnetic field up to 7 T. It indicates that magnetodielectric effect is quite small for the G-type antiferromagnetic phase despite of huge spin-phonon coupling present in investigated ceramics.

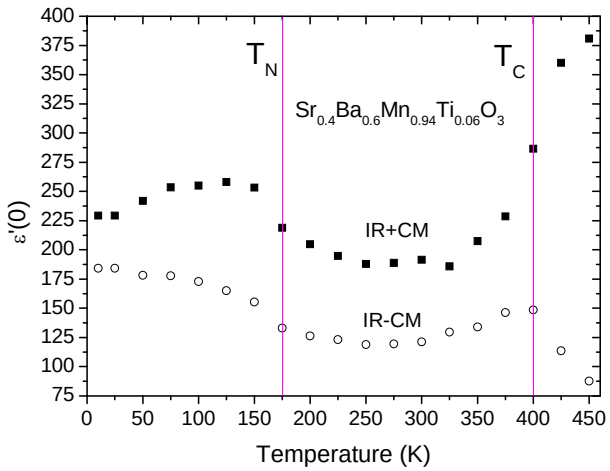

Figure.1 Temperature dependence of static permittivity of $Sr_{0.4}Ba_{0.6}Mn_{0.94}Ti_{0.06}O_3$ obtained from the fits of phonon spectra measured in THz and IR range. Dielectric relaxation of central mode (CM) presented below phonon frequencies comes from lattice anharmonicity as well as from hopping conductivity mostly at higher temperatures.

[1] C. J. Fennie and K. Rabe, *Phys. Rev. Lett.*, **97**, 267602 (2006).
[2] J. H. Lee *et al.*, *Nature*, **466**, 954 (2010).
[3] J. Hong *et al.*, *Phys. Rev. B* **85**, 054417 (2012).
[4] O. Chmaissem *et al.*, *Phys Rev. B*, **64**, 134412 (2001).
[5] S. Kamba *et al.*, *Phys. Rev. B*, **89**, 064308 (2014).
[6] J.-H. Lee and K.M. Rabe, *Phys. Rev. Lett.* **104**, 207204, (2010).
[7] H. Sakai *et al.*, *Phys. Rev. Lett.* **107**, 137601 (2011).
[8] D. K. Pratt *et al.*, *Phys. Rev. B*, **90**, 140401(R) (2014).

Tiny cause with large effects: the origin of the large magnetoelectric and magnetoelastic effect in $EuTiO_3$

Annette Bussmann-Holder, Max-Planck-Institute for Solid State Research, Heisenbergstr. 1, D-70569 Stuttgart, Germany

The magnetoelectric coupling in the perovskite oxide $EuTiO_3$ (ETO) is analyzed within a spin-phonon coupled Hamiltonian. It is shown that the *tiny* magnetostriction which accompanies the onset of antiferromagnetic order at T_N=5.7K induces a *substantial* hardening in the soft optic mode and a drop in the dielectric constant. The reduction of magnetostriction with increasing magnetic field reverses this behavior. While for small fields ferromagnetic order rapidly sets in accompanied by a volume expansion, this is destroyed with increasing fields and a strange paramagnetic state obtained. This exotic observation can be understood as stemming from the interplay between the enhanced oxygen p Ti d dynamical covalency which alters the crystal field at the Eu site and inhibits the virtual transition from $4f^7$ to $4f^65d$ responsible for ferromagnetic order.

In addition, it is shown that new thermal expansion experiments at high temperatures are an excellent tool to detect the structural instability in ETO since a pronounced anomaly takes place here. Also this feature is well explained within the polarizability model and evidences that a single model is well suited in describing the exotic behavior of ETO.

Finally, new μSR measurements are described which clearly demonstrate that magnetic domains (most likely fluctuating) exist in ETO at temperatures exceeding the structural instability. From these data a new temperature scale is defined where the fluctuations become more correlated and an increase in their correlation length sets in.

Organic Metal-free Ferroelectric and Multiferroic Materials

P. Jena
Physics Department, Virginia Commonwealth University, Richmond, VA 23284
pjena@vcu.edu

Ferroelectric materials, possessing spontaneous electric polarizations that are switchable under an external electric field, have a wide range of applications in electronics, micro-mechatronics, and electro-optics. Most of the current ferroelectric materials are based on inorganic elements. Using density functional theory we show that graphene based materials, functionalized with hydroxyl groups, constitute a class of multifunctional, lightweight, and nontoxic organic ferroelectric and multiferroic materials. For example, the polarizations of semi-hydroxylized graphane and graphone, as well as fully hydroxylized graphane, are much higher than any organic ferroelectric materials known to date. Further, hydroxylized graphene nanoribbons with proton vacancies at the end can have much larger dipole moments. They may also be applied as high-capacity cathode materials with a specific capacity that is six times larger than lead-acid batteries and five times that of lithium-ion batteries. Density functional theory has also been used to design of a variety of organic ferroelectric and multiferroic materials by functionalizing crystallized transition-metal molecular sandwich nanowires with chemical groups such as F, Cl, CN, NO_2, O, and OH. Such functionalized polar wires exhibit molecular reorientation in response to an electric field.

Novel Properties I

Towards a full first-principles theory of flexoelectricity

Jiawang Hong[1], Olivier Delaire[1], Gustau Catalan[2,3], Emilio Artacho[4,5] and David Vanderbilt[6]

[1] Materials Science and Technology Division Division, Oak Ridge National Laboratory, Oak Ridge, TN, USA
[2]ICN2–Institut Catala de Nanociencia i Nanotecnologia, Campus UAB, 08193 Bellaterra (Barcelona), Spain
[3]ICREA - Institucio Catalana de Recerca i Estudis Avanc ̸ats, 08010 Barcelona, Spain
[4]Theory of Condensed Matter, Cavendish Laboratory, University of Cambridge, Cambridge, CB3 0HE, UK
[5]Nanogune and DIPC, Tolosa Hiribidea 76, 20018 San Sebastia ́n, Spain
[6]Department of Physics and Astronomy, Rutgers University, Piscataway, New Jersey 08854-8019, USA

Flexoelectricity is the electromechanical coupling effect between strain gradient and electronic polarization. It is always allowed by symmetry because a strain gradient automatically breaks inversion symmetry. This is unlike the case of piezoelectricity, which can only occur in noncentrosymmetric materials. Flexoelectricity can have a significant effect on the functional properties of dielectric nanostructures due to the much larger strain gradient at the nanoscale than at macroscopic scales. The possibility of large effects at the nanoscale, with application to functional nanodevices, has triggered a recent increase of interest in flexoelectricity. [1-12] The development of nanoscience and nanotechnology requires a better understanding of flexoelectricity, and a better ability to utilize flexoelectric effects for a variety of purposes. Despite growing experimental interest, there have been relatively few theoretical studies of flexoelectricity, especially in the context of first-principles calculations. This is in part due to challenges in treating strain gradients in the calculations.

Direct first-principles calculations of flexoelectricity require the use of supercells with periodic boundary conditions, whereas a strain gradient, by definition, results in an inhomogeneous distribution of lattice parameters and thus a breaking of the lattice periodicity. We introduce an "accordion" supercell in which the strain gradient is itself periodic, thus allowing the recovery of the periodic boundary condition (Fig.1). We calculate the longitudinal flexoelectric response in rhombohedral $BaTiO_3$ and tetragonal $SrTiO_3$ perovskites at constant electric displacement boundary condition. [4] Based on this approach, the calculation of the transverse flexoelectric response was recently developed. [7, 12] This method is applicable even to low-symmetry systems. It offers a promising approach to determine the full flexoelectric tensor components for dielectric materials from first principles. However, the origin of the flexoelectrity and the surface role is unclear from this direct first-principles method.

In order to understand the origin of the flexoelectricity, we developed a complete first-principles theory of flexoelectric tensors, formulated in such a way that the tensor elements can be computed directly in the context of density-functional calculations. [6, 10] We reveal that the origin of flexoelectricity is from the electronic contribution due to octupoles ($Q^{(3)}$) and the lattice contribution due to the interaction between effective charges ($Q^{(1)}$) and the atomic displacements induced by the strain gradient (N), as well as the interaction between quadrupoles ($Q^{(2)}$) and the displacements induced by the strain (Γ), as can be seen in Eq. (1). We find that surfaces have contributions to the total flexoelectric response, which is related to dependence of the surface work function on local strain. We propose a method to calculate the flexoelectric coefficients in supercells with different orientations by using first-principles methods (Fig.2), including lattice and electronic contributions, under fixed E or fixed D electric boundary conditions in different parts of the procedure.

$$\mu_{\alpha\beta\gamma\delta} = V_c^{-1}\sum_{I\tau} Q^{(1)}_{I\alpha\tau} N_{I\tau\beta\gamma\delta} - \frac{1}{4}V_c^{-1}\sum_{I\tau}\left(Q^{(2)}_{I\alpha\tau\delta}\Gamma_{I\tau\beta\gamma} + Q^{(2)}_{I\alpha\tau\gamma}\Gamma_{I\tau\beta\delta}\right) + \frac{1}{6}V_c^{-1}\sum_{I} Q^{(3)}_{I\alpha\beta\gamma\delta} \qquad (1)$$

For the time being, it is still challenging for both theory and experiment to obtain the full flexoelectric tensor components for even the simplest cubic crystal. Combining the first-principles calculations and experiment to obtain the full flexoelectric tensor will be discussed.

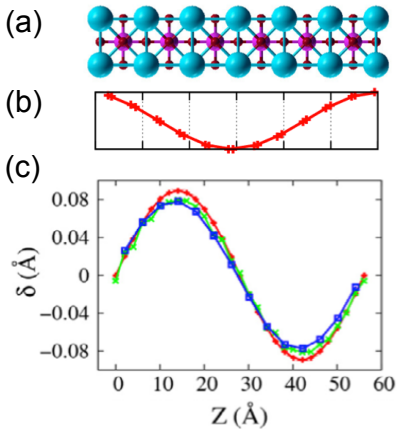

Fig.1 (a) Supercells for direct first-principles calculations without strain gradient; (b) strain gradient profile in the supercells; (c) the atomic displacement after relaxation (atom Ba is fixed, red) in $BaTiO_3$ (green:O, blue:Ti).

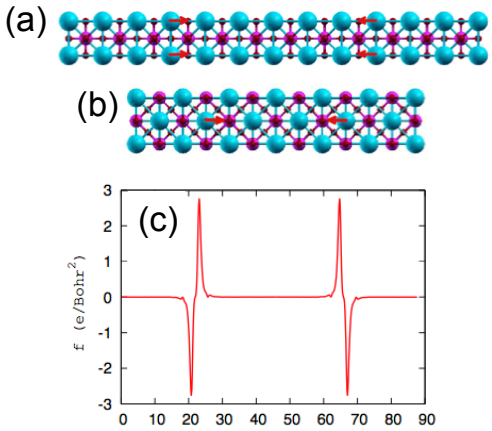

Fig.2 Original (a) and 45o-rotated (b) supercell for first-principles calculation; (c) change of charge-density distribution (a) in SrTiO3 supercell (original frame) at fixed *D*.

Acknowledgements This work was supported by EPSRC, ONR Grant No. N00014-05-1-0054 and N00014-12-1-1035 and ORNL "Next Big Ideas" awards. Computations were done at the Cambridge's CamGRID and the Center for Piezoelectrics by Design. J.H. thanks China's Scholarship Council for its support for visiting the University of Cambridge.

References

[1] L. E. Cross, J. Mater. Sci. **41**, 53 (2006).
[2] P. Zubko, G. Catalan, and A. K. Tagantsev, Annu. Rev. Mater. Res., **43**, 387 (2013).
[3] P. V. Yudin and A. K. Tagantsev, Nanotechnology **24**, 432001 (2013).
[4] J. Hong, G. Catalan, J. F. Scott, and E. Artacho, J. Phys.: Condens. Matter **22**, 112201 (2010).
[5] R. Resta, Phys. Rev. Lett. **105**, 127601 (2010).
[6] J. Hong and D. Vanderbilt, Phys. Rev. B **84**, 180101 (2011).
[7] I. Ponomareva, A. K. Tagantsev, and L. Bellaiche, Phys. Rev. B **85**, 104101 (2012).
[8] H. Zhou, J. Hong, Y. Zhang, F. Li, Y. Pei, and D. Fang, Physica B: Condensed Matter 407, 3377 (2012).
[9] H. Zhou, J. Hong, Y. Zhang, F. Li, Y. Pei, and D. Fang, EPL (Europhysics Letters) 99, 47003 (2012).
[10] J. Hong and D. Vanderbilt, Phys. Rev. B 88, 174107 (2013).
[11] M. Stengel, Phys. Rev. B **88**, 174106 (2013).
[12] T. Xu, J. Wang, T. Shimada, and T. Kitamura, J. Phys.: Condens. Matter **25**, 415901 (2013).

FLEXOELECTRICITY IN POLAR MATERIALS

Gustau Catalan

ICREA-Institucio Catalana de Recerca i Estudis Avançats, Barcelona, Spain

ICN2-Insitut Catala de Nanociencia i Nanotecnologia, Campus UAB, Bellaterra, Barcelona, Spain.

Flexoelectricity is a linear coupling between polarization and strain gradients that is allowed in any material. Naturally, it is most tempting to exploit such "universality" in order to elicit polarization out of non-polar materials. However, the best flexoelectric materials tend to be ferroelectrics, and moreover even formally non-polar materials such as $SrTiO_3$, or relaxors, or ferroelectrics in the paraelectric phase can nevertheless display built-in polarity in their behaviour [1]. It is therefore essential that we understand the interplay between flexoelectric polarization and pre-existing polarization.

In this talk I would like to discuss several ideas and results concerning the two-way interaction between flexoelectricity and ferroelectricity. We already know that flexoelectricity can be used to modify ferroelectricity (e.g., strain gradient engineering or flexoelectric switching [2]) and, conversely, that pre-existing polarization affects apparent flexoelectricity (e.g. apparently "giant" flexoelectricity [3]). Less is known, and this is something that I will discuss, about the effect of existing or induced polarization on converse flexoelectricity. Yet a third aspect that I will also cover is how the interaction between flexoelectricity and piezoelectricity affects, and is affected by, other material properties such as toughness and conductivity [4].

1. A. Biancoli et al, Nature Materials doi:10.1038/nmat4139 (2014).
2. Catalan et al, Nature Materials 10, 963–967 (2011); Lu et al, Science 336, 59–61 (2012).
3. Narvaez&Catalan, Appl. Phys. Lett. 104, 162903 (2014).
4. Abdollahi, Catalan, Arias (unpublished); Narvaez&Catalan (unpublished).

Pyroelectric and Dielectric Properties in Ferroelectrics with Bilayer and Compositionally-Graded Structures

Jialan Zhang[1], Anoop R. Damodaran[2], and Lane W. Martin[2]

[1]Department of Physics and Astronomy, Rutgers University, Piscataway, NJ, USA
[2]Department of Materials Science and Engineering, University of California, Berkeley, California, USA

Ferroelectrics represent a group of functional materials with spontaneous polarization dependent of temperature, electric field, and strain. The pyroelectric and dielectric properties of ferroelectrics can be exploited for technological use in electronic devices, microsystems, computer memories, infrared detection, imaging, refrigeration, and power conversion. For these applications, ferroelectrics are usually integrated into thin film structures. Compared with bulk and homogeneous ferroelectric films, ferroelectric superlattices and compositionally-graded ferroelectrics show distinctive physical properties.

In this work, we focus on the ferroelectric/non-ferroelectric bilayer and compositionally-graded ferroelectric films. The computations are performed using nonlinear thermodynamic models based on Ginzburg-Landau-Devonshire theory by taking into account appropriate mechanical boundary conditions, and electrostrictive coupling of in-plane strains and polarization. In particular, we will take $BaTiO_3$ as the model ferroelectric layer in our studies on ferroelectric/non-ferroelectric bilayer. We will explore the phase diagram of the ferroelectrics under as a function of (1) in-plane misfit strain; (2) temperature; and (3) elastic properties, and (4) relative layer thickness of the non-ferroelectric layer. We will also take several scandate substrates as the model non-ferroelectric layer to discuss the roles of these four factors on polarization, pyroelectric coefficient and dielectric responses in $BaTiO_3$. Furthermore, we will describe the total free energy density in (001)-oriented, compositionally graded, and monodomain $Ba_{1-x}Sr_xTiO_3$ ferroelectric films including the relative contributions and importance of flexoelectric, gradient, and depolarization energy terms. We will discuss the effects of these energies on the evolution of the spontaneous polarization, the pyroelectric coefficient and dielectric permittivity as a function of position throughout the film thickness, temperature, and epitaxial strain. Overall, this work illustrates how temperature, strains, composition, and mechanical boundary conditions can be adjusted to deterministically control and engineer ferroelectrics with multilayer and compositionally-graded structures.

Why is the electrocaloric effect so small in ferroelectrics?

G. G. Guzmán-Verri[1], P. B. Littlewood[1,2]
[1] *Argonne National Laboratory, Argonne, IL 60439*
[2] *James Franck Institute, University of Chicago, Chicago, IL 60637*

Ferroelectrics are attractive candidate materials for environmentally friendly solid state refrigeration free of greenhouse gases. Their thermal response upon variations of external electric fields is largest in the vicinity of their phase transitions, which may occur near room temperature. The magnitude of the effect, however, is too small for useful cooling applications even when they are driven close to dielectric breakdown. Insight from microscopic theory is therefore needed to characterize materials and provide guiding principles to search for new ones with enhanced electrocaloric performance. Here, we derive from well-known microscopic models of ferroelectricity meaningful figures of merit which provide insight into the relation between the strength of the effect and the characteristic interactions of ferroelectrics such as dipole forces. We find that the long range nature of these interactions results in a small effect. A strategy is proposed to make it larger by shortening the correlation lengths of fluctuations of polarization.

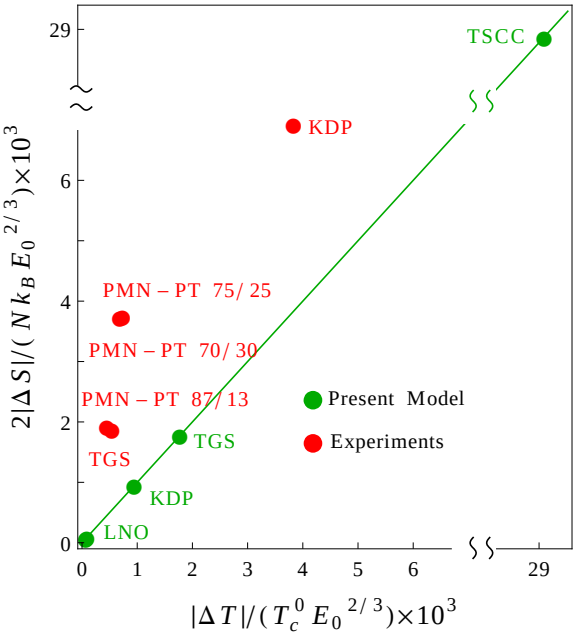

FIG. 1. Figure of merit at the paraelectric-to-ferroelectric transition for several ferroelectrics. Axes are in units of $(\text{statvolt/cm})^{2/3}$. Here, TSCC = $(CH_3NHCH_2COOH)_3CaCl_2$, KDP = KH_2PO_4, TGS = $(NH_2CH2COOH)_3 \cdot H_2SO_4$, LNO = $LiNbO_3$, and PMN-PT $1-x/x = (PbMg_{1/3}Nb_{2/3}O_3)_{1-x}$-$(PbTiO_3)_x$. Data taken from Refs. [2, 5, 6].

The thermal changes that occur in ferroelectric (FE) materials upon the application or removal of electric fields are known as the electrocaloric effect (ECE).[2–4] The effect is the electric analogue of the magnetocaloric effect, which is commonly used to reach temperatures in the milliKelvin range. The ECE is the result of entropy variations with polarization, e.g., isothermal polarization of a ferroelectric reduces its entropy while depolarization increases it. It is parametrized by isothermal changes in entropy ΔS and adiabatic changes in temperature ΔT and it is strongest near the ferroelectric transition.

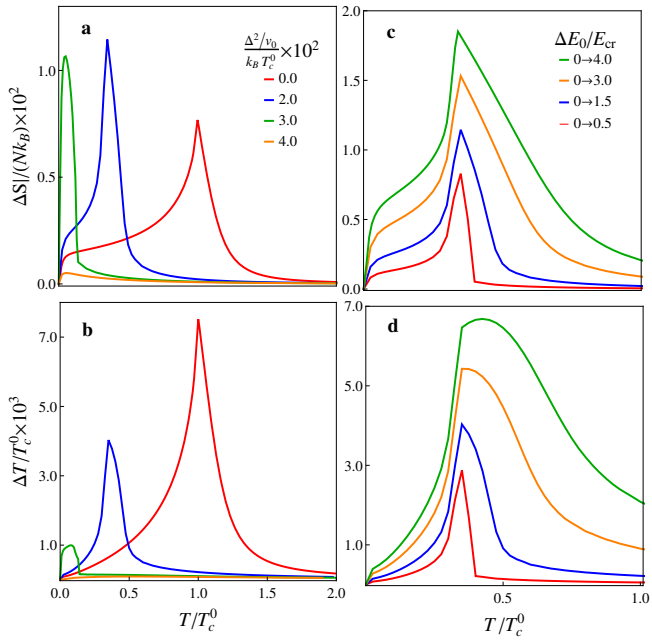

FIG. 2. (a)-(b) Calculated dependence of the ECE with compositional disorder for strong changes in the electric field $\Delta E_0/E_{cr} = 0 \rightarrow 1.5$. (c)-(d) Calculated ECE of a FE with moderate compositional disorder for several electric field strengths.

It has been recently pointed out that insight from microscopic theory into the ECE may contribute to characterize known materials and provide guiding principles to search for new ones with enhanced electrocaloric performance.[2] Here, we provide such insight by deriving meaningful figures of merit from well-known microscopic models of ferroelectricity. Our figure of merit allow us to set trends across different classes of FE materials (see Fig. 1) and provides insight into the relation between the magnitude of the ECE and the characteristic interactions of FEs (e.g. dipolar and strain). We find that the long-range nature of these interactions produces trade-offs in the ECE: while

they can give rise to high transition temperatures (i.e., comparable to room temperature), they concomitantly give rise to long correlation lengths of polarization at finite electric fields, which, as we show here, result in a small effect. We make contact with well-known results derived from Ginzburg-Landau (GL) theory[7] and those from heuristic arguments.[8] Based on these findings, we then study the effects of compositional disorder. The purpose of this is twofold: to propose a strategy to increase the magnitude of the ECE and to model the ECE of relaxor ferroelectrics (see Fig. 2).[9–11] We find that the commonly observed broad peak in the ECE of relaxors is expected in any ferroelectric that is deep in the supecritical region of their phase diagram. Our results also bring into question the common practice of defining the electrocaloric strength of a material as the ratio of the entropy or temperature changes over the change in applied electric field.

Work at Argonne National Laboratory is supported by the U.S. Department of Energy, Office of Basic Energy Sciences under contract no. DE-AC02-06CH11357.

[1] G. G. Guzmán-Verri and P. B. Littlewood, arXiv: 1411.1326.
[2] X. Moya, S. Kar-Narayan, and N. D. Mathur, Nat. Mater. **13**, 439 (2014).
[3] M. Valant, Prog. Mater. Sci. **57**, 980 (2012).
[4] J. Scott, Annu. Rev. Mater. Res. **41**, 229 (2011).
[5] R. Mackeviciute, M. Ivanov, J. Banys, N. Novak, Z. Kutnjak, M. Wenka, J. F. Scott, J. Phys. Condens. Matter **25**, 212201 (2013).
[6] B. A. Strukov, Sov. Phys.-Crystallography **11** 757 (1967).
[7] M. E. Lines and A. M. Glass, *Principles and Applications of Ferroelectrics and Related Materials* (Clarendon Press, Oxford, 1977).
[8] R. Pirc, Z. Kutnjak, R. Blinc, and Q. M. Zhang J. Appl. Phys. **98**, 021909 (2011).
[9] A. S. Mischenko, Q. Zhang, R. W. Whatmore, J. F. Scott, and N. D. Mathur, Appl. Phys. Lett. **89**, 242912 (2006).
[10] T. M. Correia, J. S. Young, R. W. Whatmore, J. F. Scott, N. D. Mathur, and Q. Zhang, Appl. Phys. Lett. **95**, 182904 (2009).
[11] J. Peräntie, H. N. Tailor, J. Hagberg, H. Jantunen, and Z.-G Ye, J. Appl. Phys. **114**, 174105 (2013).

Novel Properties II

Photovoltaic conversion of rare earth-doped $BiFeO_3$ multiferroic ceramics

Chi-Shun Tu[1], Li-Yun Chang[1], Chun-Yen Lin[1], V. H. Schmidt[2]

[1]Department of Physics, Fu Jen Catholic University, New Taipei City 24205, Taiwan

[2]Department of Physics, Montana State University, Bozeman, MT 59717, USA

Large photovoltaic (PV) open-circuit voltage, short-circuit current density, and power-conversion efficiencies under illumination of λ=405 nm have been observed in the heterostructures of indium tin oxide (ITO)/$(Bi_{1-x}R_x)FeO_3$ ceramic/Au (R=La, Nd, Sm, Eu, Gd, and Dy) for x=0.0-0.07. $(Bi_{1-x}R_x)FeO_3$ ceramics were prepared by the solid state reaction method. ITO and Au films were deposited using sputtering deposition. The PV effects and power-conversion efficiency strongly depend on doping concentration, illumination intensity, and ceramic thickness. For instance, the maximal open-circuit voltages (V_{oc}) and short-circuit current densities (J_{sc}) in ITO/$(Bi_{0.95}Nd_{0.05})FeO_3$ ceramic/Au can reach 0.8-0.92 V and 1-5 A/m^2. The maximal power-conversion efficiency (PCE) and external quantum efficiencies (EQE) in the ITO/$(Bi_{0.95}Nd_{0.05})FeO_3$/Au structure reach respectively 0.82% and 1.4% under illumination of λ=405 nm. The light-to-electric PCE is calculated as PCE=P_{out}/P_{in}, where $P_{out}=J_L\times V_L$ is the photovoltaic output power density (W/m^2) and P_{in} is the illumination intensity. J_L and V_L are respectively load current density and load voltage under illumination. The maximal PCE in the ITO/$(Bi_{0.95}Nd_{0.05})FeO_3$/Au under standard solar irradiation is about 0.025%, which is larger than 0.005% in $(La_{0.7}Sr_{0.3})MnO_3/(Pb_{0.97}La_{0.03})(Zr_{0.52}Ti_{0.48})O_3$/Nb-$SrTiO_3$ films under sunlight [1], 0.0025% in graphene/ polycrystalline BFO/Pt films under AM 1.5 irradiation [2], and 0.01% in ITO/BFO/$BiCrO_3$/$CaRuO_3$/ $LaAlO_3$ films under a solar simulator [3].

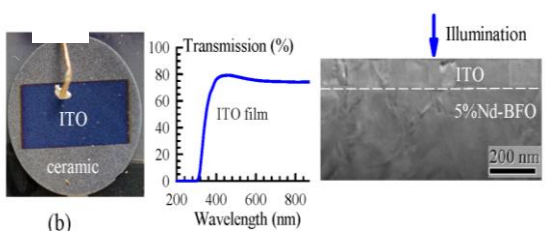

Figure 1 Ceramic disk with ITO electrode, optical transmission of ITO, and TEM image near the interface between ITO and ceramic.

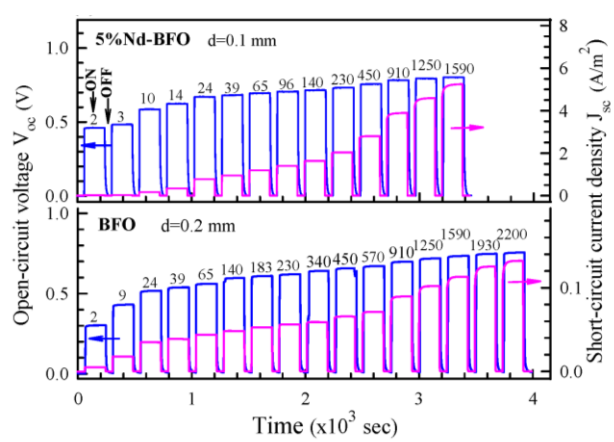

Figure 2 Open-circuit voltage V_{oc} and short-circuit current density J_{sc} as light was switched on and off with increasing incident intensity (in unit of W/m^2) [1]labeled above the tops of illumination plateaus.

The characteristic curves (current i vs. voltage V) in the dark can be expressed as

$$i_d = i_o\{\exp[q(V - i_d R_d)/\xi kT] - 1\}. \quad (1)$$

where i_d, R_d and ξ are the diode current, diode resistance, and diode-quality factor. The asymmetrical characteristic curves suggest that the heterojunction between ITO film and $(Bi_{1-x}R_x)FeO_3$ ceramics is responsible for the photovoltaic responses.

To determine the oxidation states of Fe and Bi ions in $(Bi_{1-x}R_x)FeO_3$ perovskite, Fe K-edge and Bi L_{III}-edge X-ray absorption near-edge structure (XANES) spectra were measured. The results reveal that the valences of Fe and Bi ions in BFO and $(Bi_{1-x}R_x)FeO_3$ are +3 and also rules out the presence of the other bismuth ferrite secondary phases. The $k^2\chi(k)$ spectra of BFO and $(Bi_{1-x}R_x)FeO_3$ are similar and suggest that A-site R^{3+} substitution does not affect structural order. The Fourier transforms of extended X-ray absorption fine structure (EXAFS) spectra were also studied to identify interatomic distances of F–O and Bi–O bonds in $(Bi_{1-x}R_x)FeO_3$ compounds.

The micro-Raman spectra were obtained to identify rare earth doped effects of atomic vibrations. The Raman active modes of rhombohedral R3c for $BiFeO_3$ can be summarized as the following irreducible representation: $\Gamma=4A_1+9E$ [4,5]. Bi atoms participate mainly in the low-frequency modes below 170 cm^{-1} and Fe atoms involve in the vibration modes in the region of 150-270 cm^{-1}. Oxygen motions strongly dominate in modes above 260 cm^{-1}. The four lowest and strongest vibrations can be attributed to $E(1)$ mode near 67 cm^{-1}, E(LO2) mode near 130 cm^{-1}, A_1(LO1) mode near 170 cm^{-1}, and A_1(LO2) mode near 220 cm^{-1}. The atomic vibrations near 220 cm^{-1} are mainly originated from the A_1 tilt mode of FeO_6 oxygen octahedral.

References:

[1] M. Qin, K. Yao, and Y. C. Liang, *Appl. Phys. Lett.* **93**, 122904 (2008).

[2] Y. Zang, D. Xie, X. Wu, Y. Chen, Y. Lin, M. Li, H. Tian, X. Li, Z. Li, H. Zhu, H. T. Ren, and D. Plant, *Appl. Phys. Lett.* **99**, 132904 (2011).

[3] J. Chakrabartty, R. Nechache, S. Li, M. Nicklaus, A. Ruediger, and F. Rosei, *J. Am. Ceram. Soc.* **97**, 1837 (2014).

[4] P. Hermet, M. Gofinet, J. Kreisel, and Ph. Ghosez, *Phys. Rev. B* **75**, 220102(R) (2007).

[5] J. Bielecki, P. Svedlindh, D. T. Tibebu, S. Cai, and S.-G. Eriksson, *Phys. Rev. B* **86**, 184422 (2012).

Bulk photovoltaic effect enhancement via electrostatic control in layered ferroelectrics

Fenggong Wang, Steve M. Young, Fan Zheng, Ilya Grinberg, and Andrew M. Rappe*

The Makineni Theoretical Laboratories, Department of Chemistry,

University of Pennsylvania, Philadelphia, PA 19104–6323

The power conversion efficiency (PCE) of conventional solar cells based on $p-n$ junctions is limited by the Shockley-Queisser limit [1]. Ferroelectrics provide an alternative way to separate charge by the internal depolarization field or by the bulk photovoltaic effect (BPVE). In the BPVE, the electrons are continuously excited to a quasiparticle coherent state that has an intrinsic momentum, generating a spontaneous direct short-circuit photocurrent. Besides, BPVE is able to create an open-circuit photovoltage that is above materials' band gap, potentially enabling higher PCE. Although it has been shown that BPVE arises in noncentrosymmetric materials through the "shift current" mechanism [2–5], the effects of materials' structure and electronic structure remain unclear, and this hinders the use and optimization of bulk photovoltaics. Furthermore, ferroelectric oxides usually possess wide band gaps, which allow absorption of only a small proportion of the solar irradiation [6].

Here, we choose a recently designed visible-light-absorbing ferroelectric $Pb(Ni_xTi_{1-x}O_{3-x}$ (Ni-PTO) [7] whose electronic states near the band gap possess a diverse character that enhances the physical and chemical tunabilities, and engineer its BPVE performance via electrostatic control. We construct the Ni-PTO solid solutions as layered systems by substituting Ni for Ti and then removing the O atom that is adjacent to the Ni atom at its apical position. We show that the shift current yield of this layered material can be greatly enhanced by increasing the number of layers. This shift current enhancement is accomplished through electrostatic control of electron density delocalization. The change of covalent orbital character not only enhances the shift vector magnitude, but also changes its sign, highlighting the importance of consistency in direction of shift current from different regions of the Brillouin zone. This system can be viewed as a nanoscale composite with alternating photocurrent generating layers and insulating layers, ideal for a BPVE device. This is helpful for optimizing the performance of photovoltaics.

ACKNOWLEDGMENTS

F. W. was supported by the National Science Foundation. S. M. Y. was supported by the Department of Energy Office. F. Z. was supported by the Air Force Office Scientific Research. I. G. and A. M. R were supported by the Office of Naval Research. Computational support was provided by the High-Performance Computing Modernization Office of the Department of Defense.

[1] W. Shockley and H. Queisser, J. Appl. Phys. **32**, 510 (1961).

[2] A. M. Glass, D. von der Linde, and T. J. Negran, Appl. Phys. Lett. **25**, 233 (1974).

* rappe@sas.upenn.edu

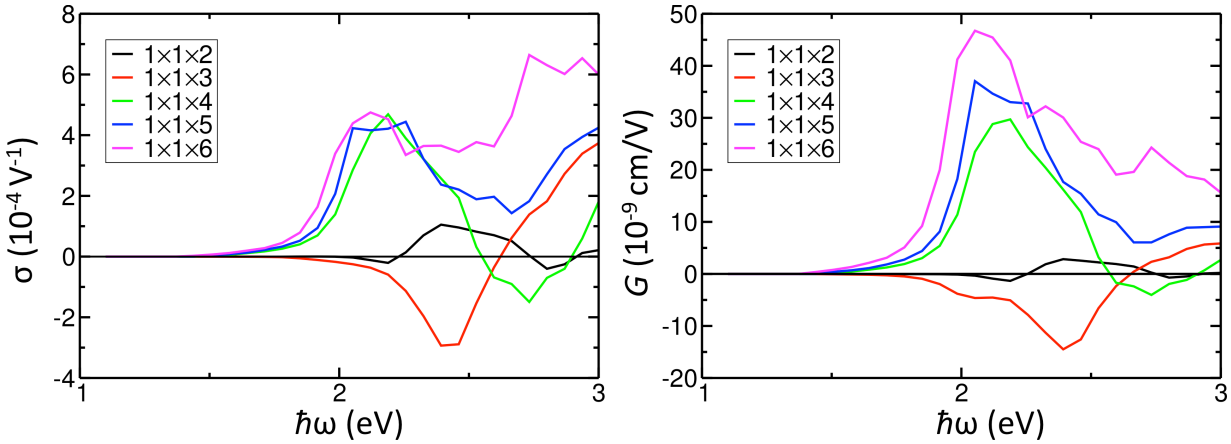

FIG. 1: (Color online) The (left) shift current susceptibilities (σ_{xxZ}) and (right) Glass coefficients (G_{xxZ}) of the layered Ni-PTO with varying superlattice periodicity.

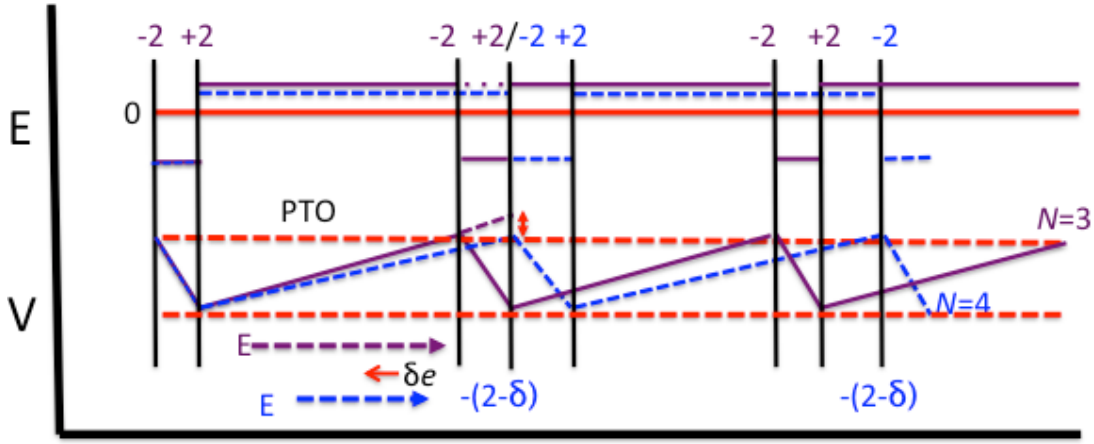

FIG. 2: (Color online) The electric field and potential inside Ni-PTO for N =3 and 4. The Ni-V_{O} substitution results in adjacent planes of charge. As layers increase, stronger screening over a greater distance is required to minimize the potential changes introduced by this charge separation.

[3] W. Kraut and R. von Baltz, Phys. Rev. B **19**, 1548 (1979).

[4] A. G. Chynoweth, Phys. Rev. **102**, 705 (1956).

[5] S. M. Young and A. M. Rappe, Phys. Rev. Lett. **109**, 116601 (2012).

[6] I. Grinberg, D. V. West, M. Torres, G. Gou, D. M. Stein, L. Wu, G. Chen, E. M. Gallo, A. R. Akbashev, P. K. Davies, J. E. Spanier, and A. M. Rappe, Nature **503**, 509 (2013).

[7] J. W. Bennett, I. Grinberg, and A. M. Rappe, J. Am. Chem. Soc. **130**, 17409 (2008).

Superconductivity in over-doped cuprates induced by ferroelectric polarization

Tricia Meyer[1], Lu Jiang[2], Shinbuhm Lee[1], John Freeland[2], Takeshi Egami[1,3], Ho Nyung Lee[1]

[1]Materials Science and Technology Division, Oak Ridge National Laboratory, Oak Ridge, TN, USA
[2]Advanced Photon Source, Argonne National Laboratory, Lemont, IL, USA
[3]Department of Physics and Department of Materials Science and Engineering, University of Tennessee, Knoxville, TN, USA

The structure-property relationships in oxide films have traditionally been focused on their "bulk" phenomena. Recently, several studies have determined that the interfacial properties contain a wide breadth of new physics and chemistry on a length scale not observable in the bulk of the film. Several examples of these phenomena include the discovery of 2-dimensional electron gas behavior at the $LaAlO_3/SrTiO_3$ interface, superconductivity existing between two non-superconducting cuprates, and electric field control of spin polarization between ferroelectric and ferromagnetic layers.[1–3] In many applications such as non-volatile memory, ferroelectric tunnel junctions or GMR heterostructures, this interfacial behavior is the key to developing novel materials and devices with greatly improved performance.

Previously, our group has explored the ferroelectric field effect in $PbZr_{0.2}Ti_{0.8}O_3$ (PZT)/$La_{1-x}Sr_xMnO_3$ (LSMO) heterostructures as a means to control the hole concentration in the ultrathin LSMO layer (5 nm) by switching the ferroelectric polarization.[4,5] Confirmation of this phenomenon was revealed by a drastic modification of the electronic and magnetic ground states depending upon the direction of the polarization. A large enhancement in the Curie temperature and decreased resistivity, indicative of hole accumulation at the interface, were clearly observed. Thus, it is clear that the ferroelectric control of various physical order parameters is a viable approach.

Here, we show another example of the ferroelectric field effect control of electronic ground states in $La_{2-x}Sr_xCuO_4$ (LSCO). LSCO exhibits a complex phase diagram which includes metallic and insulating regions separated by a superconducting dome with a maximum critical temperature, T_c, of 40 K at $x = 0.15$ as shown in Figure 1.[6] The wide range of the physical properties offered in LSCO is the result of increased hole-doping with substitution of lower valent Sr^{2+} for La^{3+}. It is well known that the origin of the superconductivity in LSCO relates to the CuO_2 plane; thus the amount of charge carriers within the CuO_2 plane is an important control parameter for observing superconductivity. We believe that such behavior can be influenced by electrostatic doping, similar to that of LSMO due to the short length scale. Additionally, previous studies on the YBCO-$BiFeO_3$ interface has demonstrated that electrostatic control of the superconducting, critical temperature is possible.[7]

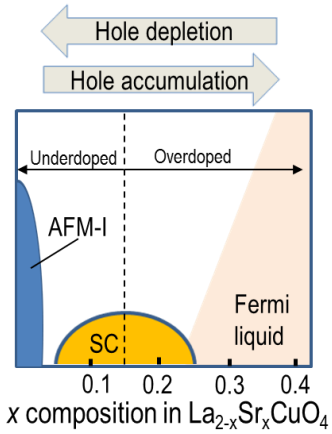

Figure 1. Phase diagram of $La_{2-x}Sr_xCuO_4$ illustrating wide-range of properties with hole-doping.

In this presentation, we report recent results on the electronic behavior of pulsed laser deposited $La_{1.6}Sr_{0.4}CuO_4$ epitaxial films capped with a highly polar ferroelectric PZT layer. We have determined from *dc* transport measurements that the over-doped cuprates, which are nominally non-superconducting, can become superconductors by effective hole depletion via the ferroelectric field effect as demonstrated in Figure 2. A downward polarization of the PZT layer was confirmed by piezoresponse force microscopy, which corresponds to hole depletion at the interface. We provide further evidence of the hole depletion by studying the O K-edge prepeak region from X-ray absorption spectra of $La_{1.6}Sr_{0.4}CuO_4$ films with and without a PZT overlayer. Through the various characterization techniques, we show that the field effect can take advantage of the cuprate's inherent sensitivity to hole doping. Therefore, it is possible to create superconducting "switches" by the formation of a charge accumulation or depletion layer at the interface between LSCO and PZT. These results strongly suggest that electrostatic control of the interfacial state has the ability to mimic the effect of chemical substitution in the LSCO phase diagram and turn on superconductivity in conventionally non-superconducting $La_{1.6}Sr_{0.4}CuO_4$.

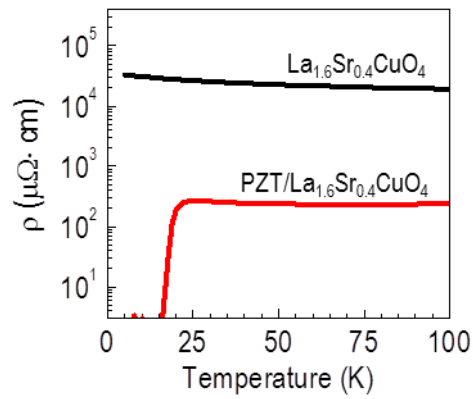

Figure 2: Resistivity of PZT-capped and as-grown 20 nm thick over-doped $La_{1.6}Sr_{0.4}CuO_4$ on $LaAlO_3$-001.

Acknowledgements The work was supported by the U.S. Department of Energy, Basic Energy Sciences, Materials Sciences and Engineering Division. Use of the Advanced Photon Source was supported by the U. S. Department of Energy, Office of Science, under Contract No.DE-AC02-06CH11357.

References

[1] A. Ohtomo and H.Y. Hwang, Nature **427**, 423 (2004).

[2] A. Gozar, G. Logvenov, L.F. Kourkoutis, A.T. Bollinger, L.A. Giannuzzi, D.A. Muller, and I. Bozovic, Nature **455**, 782 (2008).

[3] V. Garcia, M. Bibes, L. Bocher, S. Valencia, F. Kronast, a Crassous, X. Moya, S. Enouz-Vedrenne, a Gloter, D. Imhoff, C. Deranlot, N.D. Mathur, S. Fusil, K. Bouzehouane, and a Barthélémy, Science **327**, 1106 (2010).

[4] L. Jiang, W. Seok Choi, H. Jeen, T. Egami, and H. Nyung Lee, Appl. Phys. Lett. **101**, 042902 (2012).

[5] L. Jiang, W.S. Choi, H. Jeen, S. Dong, Y. Kim, M. Han, Y. Zhu, S. V Kalinin, E. Dagotto, T. Egami, and H.N. Lee, Nano Lett. **13**, 5837 (2013).

[6] J. Tarascon, L. Greene, and W. McKinnon, Science **235**, 1373 (1987).

[7] A. Crassous, R. Bernard, S. Fusil, K. Bouzehouane, D. Le Bourdais, S. Enouz-Vedrenne, J. Briatico, M. Bibes, A. Barthélémy, and J.E. Villegas, Phys. Rev. Lett. **107**, 247002 (2011).

Finite-Temperature Properties of Antiferroelectric $PbZrO_3$

B. K. Mani and I. Ponomareva

Department of Physics, University of South Florida, Tampa, Florida 33620, USA
e-mail: bmani@usf.edu

The antiferroelectric $PbZrO_3$ exhibits several characteristic properties, such as the electric-field induced phase transition from antiferroelectric (AFE) to ferroelectric (FE) phase, large electrostriction coefficients, and giant electrocaloric effects. Thanks to these attractive functionalities, there is an increased interest for the use of this material in the several key technological applications [1, 2]. Below $T_c = 505$ K $PbZrO_3$ develops an antiferroelectric orthorhombic distorted structure with an associated space group *Pbam*.

Several density functional theory (DFT) studies investigated the structural and electronic properties of $PbZrO_3$ [3–5]. However, most of these studies are limited to zero temperature. As a result, some finite temperature properties such as temperature evolution of AFE and antiferrodistortive (AFD) order parameters, lattice distortion, and double hysteresis loops are less understood. Furthermore, the possible existence of an intermediate FE phase between high temperature paraelectric and low temperature AFE phases is under debate.

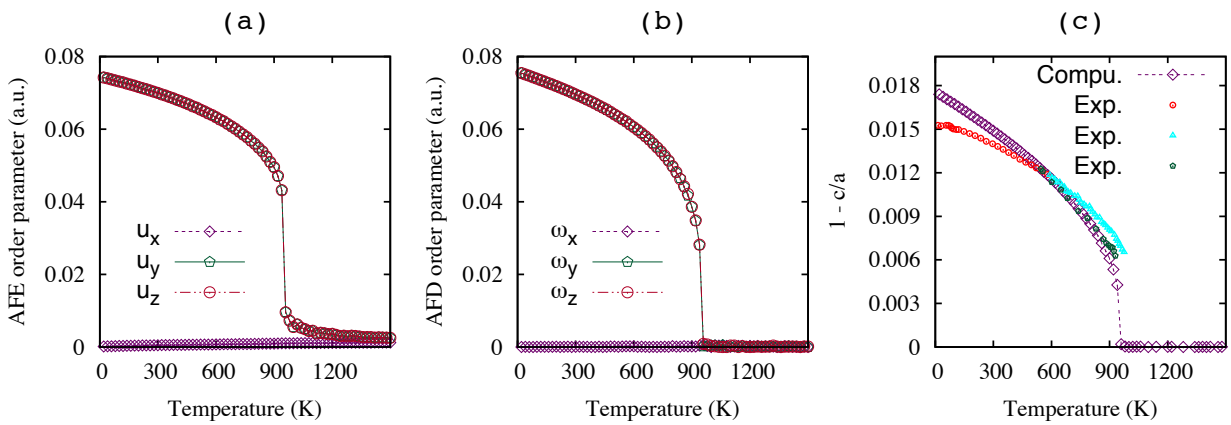

FIG. 1: Dependence of the AFE order parameter (a), the AFD order parameter (b), and the lattice distortion $1 - c/a$ (c) on the temperature. Experimental data (are rescaled to match the T_c) in the panel (c) are from the Refs. [6–8].

We develop a first-principles-based effective Hamiltonian for $PbZrO_3$ that allows computation of properties at finite temperatures. The degrees of freedom for the Hamiltonian are the local modes that are proportional to the dipole moment of a unit cell, the AFD local modes that are responsible for the oxygen octahedron rotation, and the strain variables which describe local structural deformations [9, 10]. The parameters in the effective Hamiltonian are derived from the local density approximation based DFT calculations. Next, we use this effective Hamiltonian in Monte Carlo (MC) simulations to investigate the properties of $PbZrO_3$ in a wide range of temperatures. Simulations are done using 16x16x16 supercell with periodic boundary conditions applied along all three directions to simulate a bulk system. For each temperature we used 40,000 MC sweeps.

Our computations predict that, in agreement with both experiments and first-principles calculations, the ground state structure of $PbZrO_3$ is an AFE orthorhombic structure with a tilting of the oxygen octahedron about the [110] axis. As evident from the Figs. 1(a)-(b),

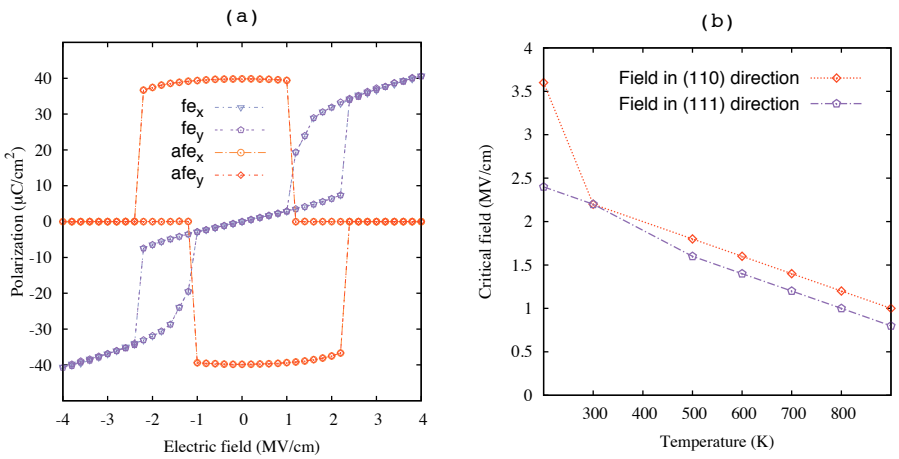

FIG. 2: (a) The electric-field induced double hysteresis loops. (b) Dependence of the critical field on the temperature.

there is a single transition from a paraelectric cubic phase to an AFE orthorhombic phase at 940±20 K. The overestimation of T_c is attributed to the over binding of structure by DFT. We also find that, in agreement with the experimental findings, an application of electric field induces a AFE to FE transition through a double hysteresis loops (see Fig. 2(a)). Our study further shows that the critical field, required to induce such a transition, decreases with the temperature (see Fig. 2(b)). We will report our findings about the temperature evolution of the structural distortion and electric properties and discuss the possibilities of finding the intermediate ferroelectric phase.

This work is supported by the U.S. Department of Energy, Office of Basic Energy Sciences, Division of Materials Sciences and Engineering under grant DE-SC0005245. This research used resources of the National Energy Research Scientific Computing Center, which is supported by the Office of Science of the U.S. Department of Energy under Contract No. DE-AC02-05CH11231.

---

[1] H. Liu and B. Dkhil, J. Kristallog **226**, 163 (2011).
[2] X. Tan, C. Ma, J. Fredrick, S. Beckman, and K. G. Webber, J. Am. Ceram. Soc. **94**, 4091 (2011).
[3] D. J. Singh, Phys. Rev. B. **52**, 12559 (1995).
[4] R. Kagimura and D. J. Singh, Phys. Rev. B. **77**, 104113 (2008).
[5] M. D. Johannes and D. J. Singh, Phys. Rev. B. **71**, 212101 (2005).
[6] H. Fujishita and S. Tanaka, Ferroelectrics **258**, 37 (2001).
[7] R. W. Whatmore and A. M. Glazer, J. Phys. C **12**, 1505 (1979).
[8] E. Sawaguchi, J. Phys. Soc. Jpn. **7**, 110 (1952).
[9] W. Zhong, D. Vanderbilt, and K. M. Rabe, Phys. Rev. B **52**, 6301 (1995).
[10] D. Vanderbilt and W. Zhong, Ferroelectrics **206**, 181 (1998).

Physical constraint and its consequence for hyperferroelectrics

Huaxiang Fu
Department of Physics, University of Arkansas, Fayettville, Arkansas 72701, USA

Hyperferroelectricity (HyFE) is a new phenomenon of fundamental importance since hyperferroelectric solids are capable of developing ferroelectricity under an open-circuit boundary condition, despite the existence of strong depolarization fields.[1] Unlike *improper* ferroelectrics (in which the dominating soft mode is nonpolar, and the polarization results from the polar-nonpolar mode coupling),[2–7] HyFEs are *proper* ferroelectrics with a dominating polar instability and a strong polarization.

For decades it has been known that proper ferroelectrics (FE) exhibit ferroelectric phase transition and mono-domain polarization only when the depolarization field is sufficiently screened, e.g., under the short-circuit boundary condition or surrounded by metallic electrodes[8]. When the depolarization field is not screened, FE polarization tends to form multi-domains along the direction of the depolarization field.[9] Another possibility is that proper FEs may undergo a different phase transition by forming vortex.[10] However, the recent discovery showed that HyFE solids defy the accepted belief by being able to retain a mono-domain polarization even under the open-circuit boundary condition,[1] opening a new field of ferroelectric physics[11]. Furthermore, HyFE solids are technologically important since, by forming interface with other functional materials such as semiconductors, strongly-correlated oxides, or multiferroics, the polarization retained in HyFEs can effectively control and/or tune the materials properties across the interface.

However, HyFEs remain mystic, and so far were found only in some uncommon semiconductors LiZnAs, LiBeSb, and LiBeBi.[1] Many key questions of general interest remain to be answered. For example, what is the criterion, if any, that a hyperferroelectric must satisfy? Is there any law governing the magnitude of polarization to be retained by a HyFE under the open-circuit boundary condition? Furthermore, one may wish some intuitive knowledge that may guide the designing of new HyFEs. Obviously the lack of sufficient understanding hampers the searching for other HyFE materials.

In this study, based on a fourth-order Ginzburg-Landau theory[12], we formulate a physical constraint that a HyFE must satisfy. The constraint leads to a nonzero polarization under the open-circuit boundary condition as well as a stable electric state as the minimum of the free energy. The theory further reveals a guide principle on the search for new hyferroelectrics, i.e., they need to have a deep potential well and a small zero-field polarization. In addition, we show that an unstable longitudinal optical phonon is a natural consequence of the constraint. Prototypical ferroelectric $BaTiO_3$, $PbTiO_3$, and $KNbO_3$ do not meet the physical constraint, and are not hyperferroelectrics.

This work was supported by the Office of Naval Research.

[1] K.F. Garrity, K.M. Rabe, and D. Vanderbilt, Phys. Rev. Lett. **112**, 127601 (2014).
[2] C.J. Fennie and K.M. Rabe, Phys. Rev. B **72**, 100103 (2005).
[3] E. Bousquet, M. Dawber, N. Stucki, C. Lichtensteiger, P. Hermet, S. Gariglio, J.-M. Triscone, and P. Ghosez, Nature (London) **452**, 732 (2008).
[4] N. Sai, C.J. Fennie, and A.A. Demkov, Phys. Rev. Lett. **102**, 107601 (2009).
[5] N.A. Benedek and C.J. Fennie, Phys. Rev. Lett. **106**, 107204 (2011).
[6] J.M. Rondinelli and C.J. Fennie, Adv. Mater. **24**, 1961 (2012).
[7] M. Stengel, C.J. Fennie, and P. Ghosez, Phys. Rev. B **86**, 094112 (2012).
[8] J. Junquera and P. Ghosez, Nature (London) **422**, 506 (2003).
[9] C. Thompson, D.D. Fong, R.V. Wang, F. Jiang, S.K. Streiffer, K. Latifi, J.A. Eastman, P.H. Fuoss, and G. Stephenson, Appl. Phys. Lett. **93**, 182901 (2008).
[10] I.I. Naumov, L. Bellaiche, and H. Fu, Nature (London) **432**, 737 (2004); I. Naumov and H. Fu, Phys. Rev. Lett. **98**, 077603 (2007).
[11] N.A. Benedek and M. Stengel, Physics **7**, 32 (2014).
[12] L.D. Landau and E.M. Lifshitz, *Statistical Physics*, (Butterworth-Heinemann, Oxford, 2000).

Nonoxide Ferroelectrics

Ferroelectricity and magnetoelectricity in hybrid organic-inorganic compounds

Paolo Barone

CNR-SPIN, UOS L' Aquila, Italy

Ferroelectric materials have a wide range of applications in device electronics. In the last decade, materials displaying the coexistence of two or more ferroic orders in the same material, i.e., multiferroicity, have attracted a lot of interest due to their potential applications in devices exploiting cross-coupling phenomena such as the magnetoelectric effect. Most of the known ferroelectric and multiferroic materials are inorganic compounds, being typically transition-metal oxides. However, in recent years the search for new multiferroic materials has been extended to hybrid organic-inorganic compounds such as metal-organic frameworks (MOFs) [1,2]. MOFs are porous crystalline compounds consisting of networks of metal ions connected by coordinating organic linkers, whose cavities can be filled by organic cations. Magnetism can be brought in by the metal framework, whereas novel functional properties can be tailored by suitably choosing the organic building blocks which enter the cavities. The hybrid character of MOFs, therefore, may lead to novel mechanisms by which ferroelectric, magnetic and magnetoelectric properties can be realized and tuned. In this respect, computational approaches based on density functional theory represent a valuable tool for identifying such mechanisms and for devising promising candidates in a material-design approach. Some representative examples in the class of MOFs with perovskite structure will be discussed, highlighting the role of organic cations and of their interplay with the metal framework in mediating ferroelectricity and magnetoelectricity [3-7].

References:

[1] R. Ramesh, Nature 461, 1218 (2009).
[2] G. Rogez, N. Viart and M. Drillon, Angew. Chem. Int. Ed. 49, 1921 (2010).
[3] A. Stroppa, P. Jain, P. Barone, M. Marsman, J. M. Perez- Mato, A. K. Cheetham, H. W. Kroto and S. Picozzi, Angew. Chem. Int. Ed. 50 , 5847 (2011).
[4] A. Stroppa, P. Barone, P. Jain, J. M. Perez-Mato and S. Picozzi, Adv. Mater. 25, 2284 (2013).
[5] D. Di Sante, A. Stroppa, P. Jain and S. Picozzi, J. Am. Chem. Soc. 135, 18126 (2013).
[6] Y. Tian, A. Stroppa, Y. Chai, L. Yan, S. Wang, P. Barone, S. Picozzi and Young Sun, Sci. Rep. 4, 6062 (2014).
[7] Y. Tian, A. Stroppa, Y. Chai, P. Barone, J. M. Perez-Mato, S. Picozzi and Y. Sun, Phys. Status Solidi RRL. doi: 10.1002/pssr.201409470 (2014)

First-Principles Calculations of the Ferroelectric Phase Transition in Pure Molecular Crystal Trichloroacetamide

Hiroki MORIWAKE[1], Ayako KONISHI[1], Takafumi OGAWA[1], Craig A. J. FISHER[1], Akihide KUWABARA[1], Noriko OTANI[1], Chikako MORIYOSHI[2], Yoshihiro KUROIWA[2]

[1] Nanostructures Research Laboratory, Japan Fine Ceramics Center, Nagoya, Aichi, JAPAN
[2] Department of Science, Hiroshima University, Saijyo, Hiroshima, JAPAN

Trichloroacetamide (TCAA) forms a monoclinic molecular crystal within non-centrosymmetric space group $P2_1$ below 355 K that exhibits ferroelecticity. A single TCAA molecule has a dipole-moment, but the unit cell contains two crystallographically independent molecules, labelled A and B in figure 1, aligned anti-parallel to one another. The alignment is imperfect, however, so that a small polarization exists parallel to the *b* axis ($\boldsymbol{P}_s$ = 0.2 μC/cm^2). Experimentally, TCAA crystals have been found to transform to a paraelectric phase with space group symmetry $P2_1/c$ above 355 K [1], and this is attributed to rotation of the trichloromethyl (Cl_3) groups relative to one another [2]. Up to 150 K, with the crystal in its ferroelectric form, the Cl_3 groups are essentially "frozen" in position, but above 150 K the Cl_3 group of molecule B begins to rotate in an oscillatory manner, the magnitude of the rotation increasing until a temperature of around 350 K is reached. Above 355 K, the Cl_3 groups in both types of molecule rotate completely, cancelling each other's dipole moment [2]. Here we report the first theoretical study of the ferroelectric phase transition behavior of this system based on first-principles total-energy minimization and first-principles molecular dynamics (FPMD) techniques. Calculations were performed using the projector augmented wave method of density functional theory. The molecule rotation behavior obtained from FPMD simulations at different temperatures is summarized in fig. 2. We show that the simulations reproduce the experimental features of the intramolecular order-disorder phase transition well.

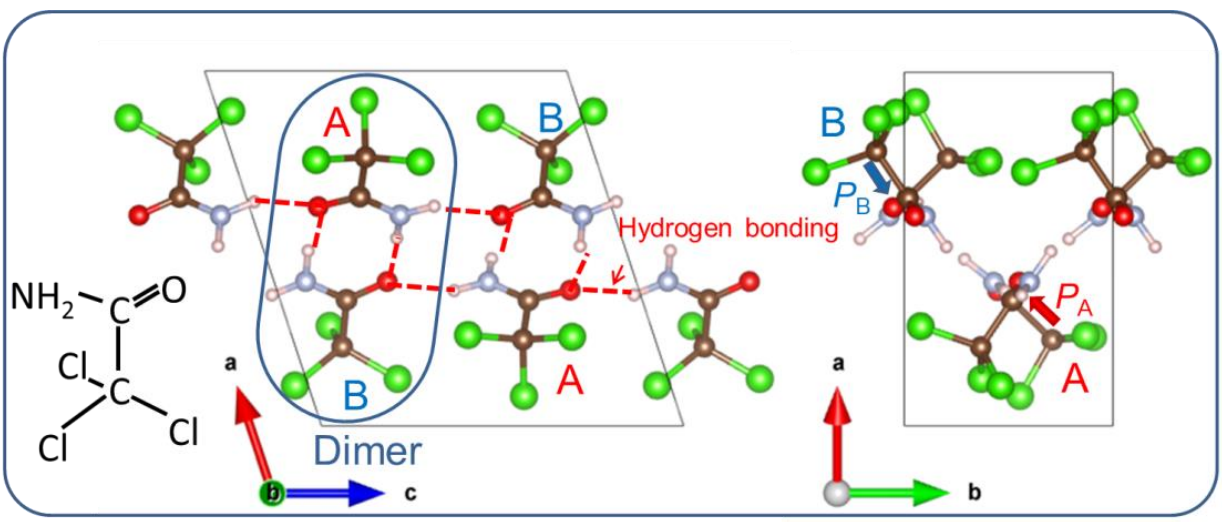

Fig. 1 Structure of a TCAA crystal. The unit cell contains two crystallographically independent TCAA molecules, labelled A and B. Each molecule has a dipole moment, *P*, and pairs of molecules (dimers) are aligned anti-parallel to one another.

References
[1] Y. Kamishina: J. Phys. Soc. Jpn. **60** 2147 (1991).
[2] K. Saito, et al.: CrystEngComm **13** 2693 (2011).

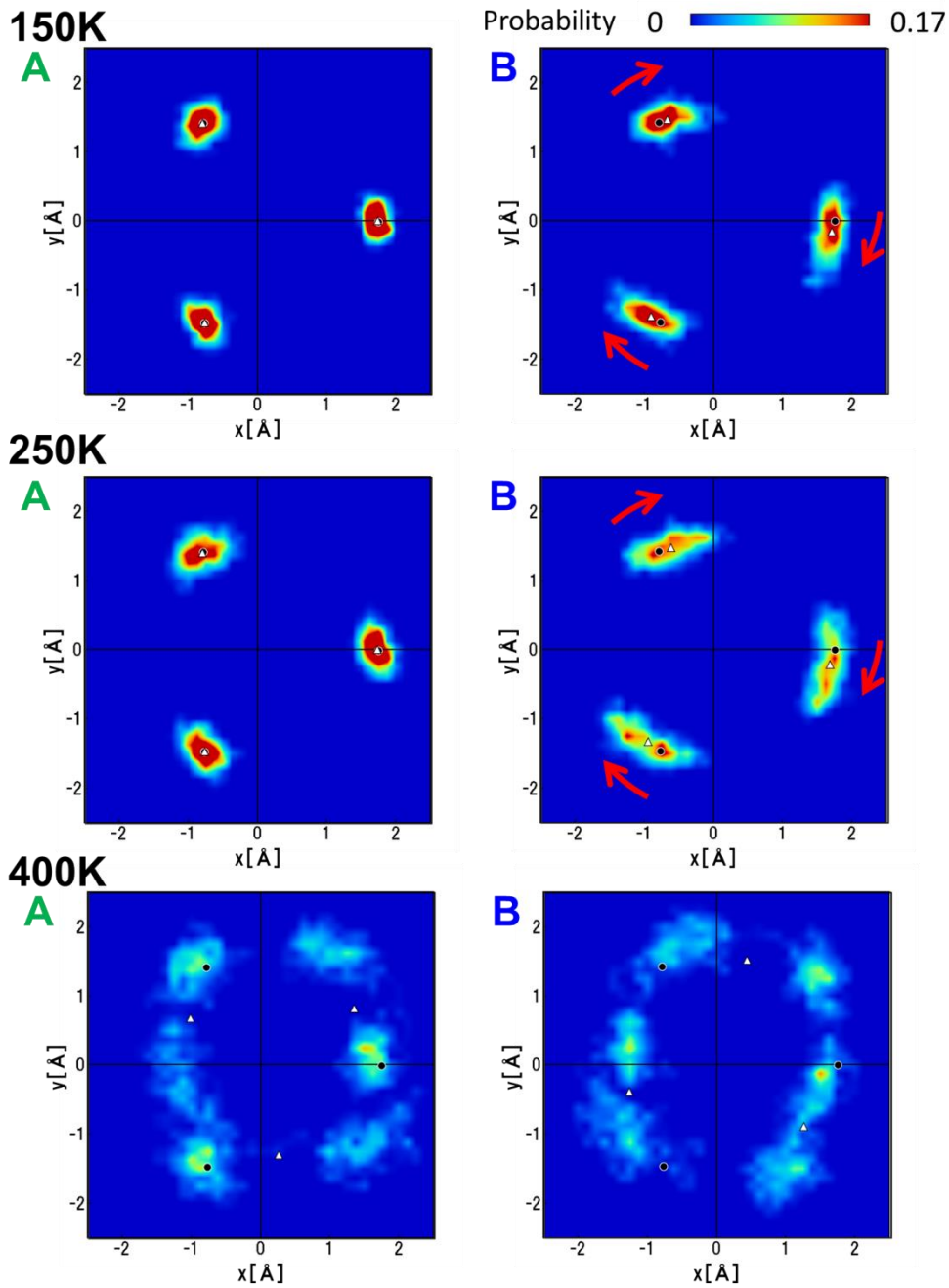

Fig. 2 Probability plots of positions of atoms in the trichloromethyl (Cl_3) group about the C-C axis in TCAA molecule types A and B at 150 K, 250 K and 400 K according to first-principles molecular dynamics simulations. The Cl positions at 0 K are indicated by black circles and the mean positions at each temperture are indicated by white triangles. At 150 K, only Cl atoms in molecule B have begun to rotate. The rotation angle increases with temperature.

Prediction of a Stable Post-Post-Perovskite Structure from First Principles

Changsong Xu[1, 2], Bin Xu[2], Yurong Yang[2], Huafeng Dong[3], Artem R. Oganov[3, 4, 5], Shanying Wang[1], Wenhui Duan[1,6], Binglin Gu[6], and L. Bellaiche[2]

[1]State Key Laboratory of Low-Dimensional Quantum Physics and Collaborative Innovation Center of Quantum Matter, Department of Physics, Tsinghua University, Beijing 100084, China
[2]Physics Department and Institute for Nanoscience and Engineering, University of Arkansas, Fayetteville, Arkansas 72701, USA
[3]Department of Geosciences, Center for Materials by Design and Institute for Advanced Computational Science,State University of New York, Stony Brook, NY 11794, USA
[4]Moscow Institute of Physics and Technology, 9 Institutskiy Lane, Dolgoprudny City, Moscow Region 141700, Russia
[5]School of Materials Science, Northwestern Polytechnical University, Xi'an 710072, China
[6]Institute for Advanced Study, Tsinghua University, Beijing 100084, China

ABX_3 perovskites (Pv) form an important class of crystal structures for which A and B are cations and X is typically the oxygen or fluorine anion. Perovskites display a wealth of phenomena, such as ferroelectricity, magnetism, multiferroicity, piezoelectricity, magnetoelectricity, charge and orbital orderings, superconductivity, etc.... As a result, they constitute a rich playground for research and are important for various technologies, which explains the flurry of activities that have been devoted to them. Interestingly, recent works have shown that applying a hydrostatic pressure in some ABX_3 materials can result in the transformation from the Pv structure to the so-called “post-perovskite” (pPv) structure, which can have important physical consequences [1-3]. For instance, the pPv structure discovered in $MgSiO_3$ explains the existence of anisotropic features in the D" layer of Earth. Moreover, CaRhO3 was recently found to adopt a polymorph that was described as being an intermediate phase between perovskite and post-perovskite [4]. Based on these discoveries as well as recent findings of new high-pressure phases in ABO_3 and ABF_3 systems [5], one may wonder if there is another crystal structure for which Pv or pPv materials can evolve to under hydrostatic pressure. As demonstrated in Ref. [6] and as detailed here, the answer is positive.

More precisely, in this work, a novel stable crystallographic structure is discovered in a variety of ABO_3, ABF_3 and A_2O_3 compounds, via the use of first principles (VASP+USPEX [7]). This novel structure appears under hydrostatic pressure, and can be considered to be a post-post-perovskite (ppPv) phase. It provides a successful solution to experimental puzzles in important systems, and is characterized by one-dimensional chains linked by group of two via edge-sharing oxygen/fuorine octahedra. Such organization automatically results in anisotropic elastic properties and new magnetic arrangements. Depending on the system of choice, this post-post-perovskite structure also possesses electronic band gaps ranging from zero to about 10 eV being direct or indirect in nature, which emphasizes its potential to have striking, e.g., electrical or transport phenomena.

We hope that our work can encourage researchers to confirm the predictions presently reported and to determine properties associated with such novel crystal structure.

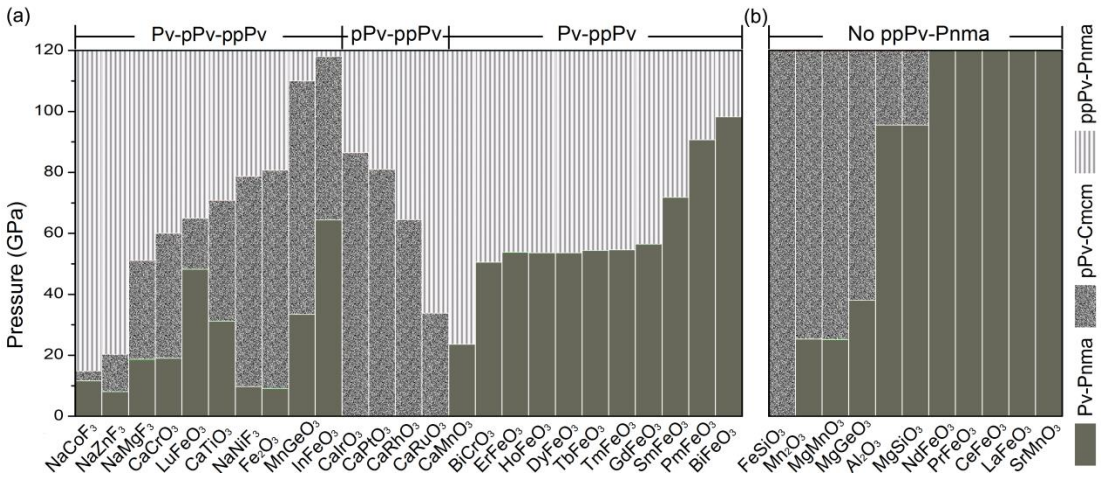

FIG. 1. Pressure range of stability of the Pv, pPv and ppPv phases in the ABX_3 and A_2O_3 materials under study. Panels (a) and (b) report materials possessing or missing, respectively, the presently discovered ppPv structure for pressure up to 120 GPa.

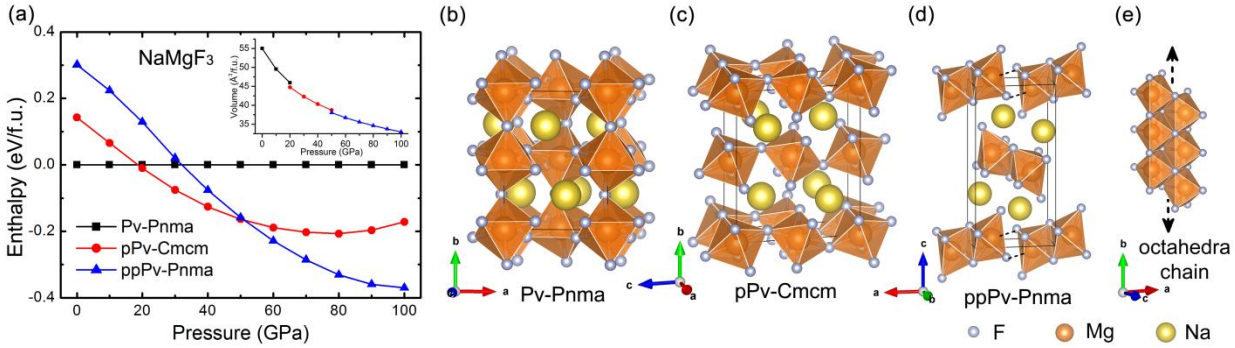

FIG. 2. Pressure dependence of the enthalpy of the Pv, pPv and ppPv phases of $NaMgF_3$ (Panel (a)), along with the schematization of (b) the Pv, (c) pPv and (c) and (d) ppPv crystallographic structures. Note that the enthalpy of the Pv phase has been set to be zero for any pressure in Panel (a), and that the inset of Fig. 2a displays the behavior of the volume versus pressure in the Pv, pPv and ppPv phases.

Acknowledgements This work is financially supported by the Department of Energy, Office of Basic Energy Sciences, under contract ER-46612 (B.X.) and ONR Grant N00014-12-1-1034 (Y.Y.). It is also supported by the Ministry of Science and Technology of China (Grant No.2011CB606405) and National Natural Science Foundation of China (Grant No. 11174173).

References

[1] M. Murakami, K. Hirose, K. Kawamura, N. Sata, and Y. Ohishi, *Science* **304**, 855 (2004).
[2] A. R. Oganov, and S. Ono, *Nature* **430**, 445 (2004).
[3] K. Umemoto, R. M. Wentzcovitch, and P. B. Allen, *Science*, **311**, 983 (2006).
[4] Y. Shikaro et al, *American Mineralogist* **97**, 159 (2012).
[5] C. D. Martin, W. A. Crichton, H. Liu, V. Praparkenka, J. Chen, and J. B. Parise, *Geophys. Res. Lett.* 33, L11305 (2006).
[6] C. Xu, B. Xu, Y. Yang, H. Dong, A. R. Oganov, S. Wang, W. Duan, B. Gu, L. Bellaiche arXiv:1410.5030
[7] A. R. Oganov et al, *J. Chem. Phys.* **124**, 244704 (2006); *Comput. Phys. Commun.* **184**, 1172-1182 (2013); *Acc. Chem. Res.* **44**, 227 (2011); *Rev. Mineral. Geochem.* **71**, 271 (2010)

Relaxors

Multiple relaxation and characteristic temperatures in $PbMg_{1/3}Nb_{2/3}O_3$:La relaxor ferroelectric crystals

Alexei A. Bokov[1], Džiugas Jablonskas[2], Robertas Grigalaitis[2], Jūras Banys[2], Zuo-Guang Ye[1]

[1]Department of Chemistry and 4D LABS, Simon Fraser University, Burnaby, British Columbia, Canada
[2]Faculty of Physics, Vilnius University, Vilnius, Lithuania

Unusual relaxation is a basic property of relaxor ferroelectrics which distinguish them from other ferroic materials. Several relaxation processes typically contribute to the dielectric spectra of a relaxor and their deconvolution is always a challenging task. The distribution of relaxation times function is used to adequately describe the entire spectrum, which provides restricted opportunities to determine the parameters of the constituent relaxation processes. A remarkable feature of relaxors is that different relaxation contributions to the dielectric response can appear or disappear at specific temperatures not related to structural phase transitions. It is known, in particular, that a high-frequency relaxation (central mode) emerges upon cooling at the Burns temperature, T_B and the characteristic relaxation time of the low-frequency part of the spectrum diverges at the freezing temperature $T_f << T_B$. However, at another characteristic temperature known as T^* ($T_f < T^* < T_B$), no evident anomalies have been observed in dielectric relaxation spectra.

In this work we analyze the dielectric relaxation spectra of $PbMg_{1/3}Nb_{2/3}O_3$ relaxor ferroelectric crystals doped with ~2 at.% La^{+3} (PMNL) in a wide frequency range between 10^{-2} Hz and 5×10^{10} Hz. These crystals are characterized by the enhanced degree of compositional order as compared to pure PMN. Previous investigations of relaxation in these crystals by means of dielectric spectroscopy at low-frequencies $f < 1$ MHz[1] and Brillouin scattering[2] showed that La impurity influences little the relaxation times and the width of the relaxation spectrum, but decreases significantly the magnitude of dielectric constant facilitating the measurements in the microwave range.

Our results indicate that two low-frequency relaxation processes which are usually believed to be related to flipping and "breathing" of polar nanoregions (PNRs), respectively, actually appear only below the T^*, but not below T_B, as believed earlier.[3] An additional strong relaxation process is discovered which provides the main contribution to the dielectric response at $T \sim T^*$. It was confirmed that the dielectric spectra of pure and La-doped crystals are qualitatively similar.

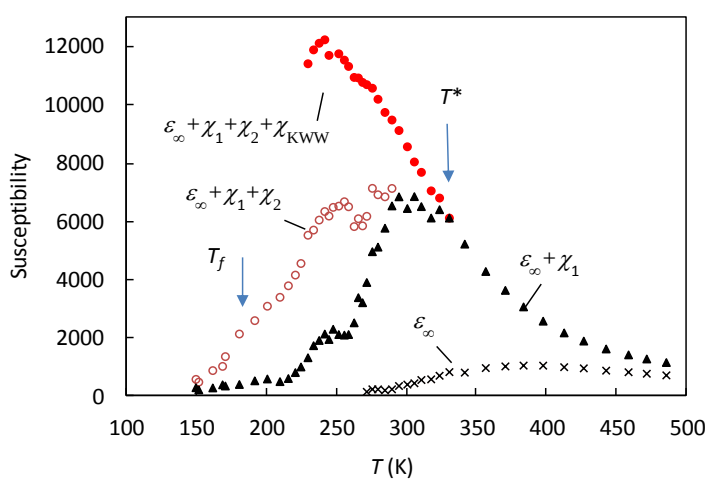

Figure 1 Structure of the dielectric spectrum in PMNL crystal. Static susceptibilities associated with different contributions to the dielectric response are shown as a function of temperature.

To determine the parameters of different relaxations the spectra were least-squares fitted to a multi-relaxation model in which the complex dielectric permittivity was represented as a sum of susceptibilities related to different polarization mechanisms: $\varepsilon^*(f) = \varepsilon_\infty + \sum \chi_k^*(f)$, where the susceptibilities χ_1^* and χ_2^* are represented by the Cole-Cole relaxation function, $\chi_3^* \equiv \chi_{KWW}^*$ is

represented by the Kohlrausch-Williams-Watts (KWW) relaxation function, $\chi_4^* \sim f^{n-1}$ is the "universal" relaxation which appeared in the low-frequency part of the spectrum due to the mobile charge carriers and the constant ε_∞ describes the contributions of electrons, phonons and the fast component of central mode which is known to exist in PMN and PMNL in the THz frequency range.[2,3.]

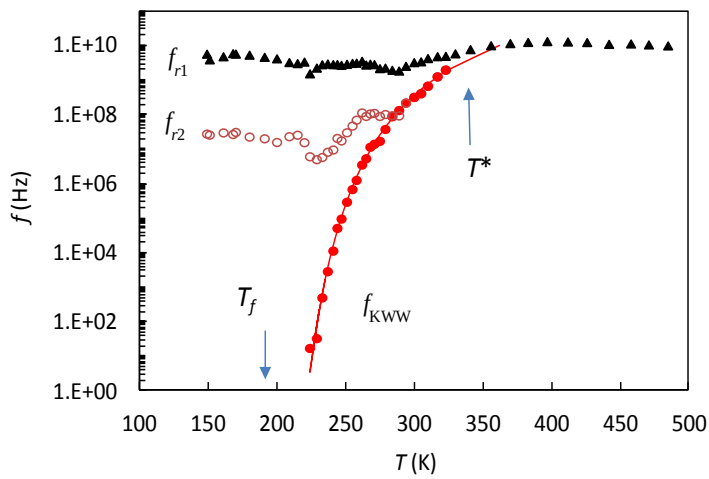

Figure 2 Temperature dependencies of characteristic relaxation frequencies of three relaxation processes observed in PMNL crystal. Solid line is the fit to Vogel-Fulcher law.

The temperature dependences of selected relaxation parameters extracted from the fitting model are shown in Figs. 1 and 2. At temperatures above $T^* \approx 340$ K only one relaxation process is resolved, which fits the Debye function (the Cole-Cole parameter $\alpha \approx 0$) whose relaxation frequency, f_{r1}, is practically temperature-independent. The relaxation strength of this process, χ_1, peaks at ~ 300 K and decreases upon further cooling. At $T<T^*$ a new relaxation contribution appears whose relaxation spectrum fits the KWW pattern, the characteristic relaxation frequency obeys the Vogel-Fulcher law, $f_{KWW} = f_0 \exp[-E_a/(T-T_f)]$ with T_f =185 K, E_a=1100 K and f_0=4.8×10^{12} Hz, while the shape parameter follows the similar law $\beta = \beta_0 \exp[-E_\beta/(T-T_f)]$. This dielectric contribution is usually believed to result from thermally-activated reorientations of PNRs.[3] The last relaxation mechanism with the intermediate relaxation frequency f_{r1} is developed at comparatively low temperatures. Its relaxation time distribution increases dramatically (i.e. α increases) on cooling, resulting in frequency–independent loss at $T< T_f$. This mechanism is presumably attributed to the motion of PNRs boundaries (breathing).[3]

The work was supported by the U.S. Office of Naval Research (Grants No. N00014-11-1-0552 and No.N00014-12-1-1045).

References

[1] X. Long, A. A. Bokov, Z.-G. Ye, W. Qu and X. Tan, *J. Phys.; Condens. Matter* **20**, 015210, (2008).
[2] J.-H. Ko, T. H. Kim, S. Kojima, X. Long, A. A. Bokov and Z.-G. Ye, *J. Appl. Phys.* **107**, 054108, (2010).
[3] V. Bovtun, S. Veljko, S. Kamba, J. Petzelt, S. Vakhrushev, Y. Yakymenko, K. Brinkman and N. Setter, *J. Eur. Ceram. Soc.* **26**, 2867, (2006).

Computational Study of Real Space Local Structure and Diffuse Scattering in a Relaxor

Hiroyuki Takenaka[1], Ilya Grinberg[1], Andrew M. Rappe[1]

[1]Department of Chemistry, University of Pennsylvania, Philadelphia, Pennsylvania, USA

Relaxor ferroelectrics are attractive materials due to a strong piezoelectric effect, a high permittivity value over a broad temperature range, and a unique dielectric response with strong frequency dispersion with the diffuse phase transitions.[1-3] Currently, the relaxor phase transitions are described by the widely-accepted polar nanoregions (PNR) in a matrix model. At the Burns temperatures (T_b) above the Curie-Weiss temperatures (T_c), spherical polar nanoregions (PNRs) appear in a non-polar matrix and the material undergoes a phase transition from the paraelectric phase to the dynamic relaxor phase. As the temperature is lowered further, the size of PNRs and interactions between PNRs grow and strengthen, and the local distortions appear at the intermediate temperature (T^*). When the system is cooled down to T_f, the growth of PNRs stops and their dynamics freeze as the system undergoes a transition from the dynamic relaxor phase to the frozen relaxor phase.

Investigations of local structure play a crucial role in understanding how the important properties of relaxors arise from their composition. While the real space local structure motifs are poorly understood due to the complexity of relaxor materials, experimental diffuse scattering (DS) studies have clear demonstrated that relaxor behavior is related to the appearance of local disorder in the ionic displacements. Recent diffuse scattering studies have questioned the PNR model[4] and the DS intensity patterns are reported in $Pb(Zr,Ti)O_3$ near T_c.[5]

In this work, we study how local Pb dipoles give rise to the observed DS patterns using bond-valence (BV) model molecular dynamics simulations of a 46656-atom supercell of the $0.75PbMg_{1/3}Nb_{2/3}O_3$-$0.25PbTiO_3$ (PMN-PT) relaxor ferroelectric with the random site rocksalt *B*-site cation arrangement.[6,7]

Our computational DS results reproduce the butterfly shape and exhibit a similar trend to the experimental results on cooling (Figure 1). We find that the magnitude of local displacements directly influences the extent of the DS pattern. To analyze the local structure, we examine the Pb displacement angle autocorrelation and the angles between the local time averaged Pb off-center displacements. We find that the time-averaged Pb displacement autocorrelation angle is small but greater than zero. This indicates that even in the the Pb dipoles are not frozen but rather rotate slowly. At low temperature, the angles between the local Pb dipoles are small up to Pb-Pb separation of 30-40Å, and increase dramatically to approximately70 degrees for larger Pb-Pb separation (Figure 2). This indicates that the frozen phase is a multidomain state with 71 degree domain walls separating small 3~nm sized ferroelectric like domains. The domain walls are centered on Pb atom with several Mg neighbors; such atoms display fast dynamics even in the frozen phase. Simulations of the DS pattern with model structures shows that it is this multidomain structure that gives rise to the butterfly shape observed in diffuse scattering. Thus, the butterfly shape is a signature of the formation of the multidomain state. Using an analogy with water,[8] the dynamic phase can be thought of as hydrogen-bonded liquid water while the frozen phase is consists of small ferroelectric regions separated by domain walls with fast dynamics analogous to a slushy mixture of ice and water.

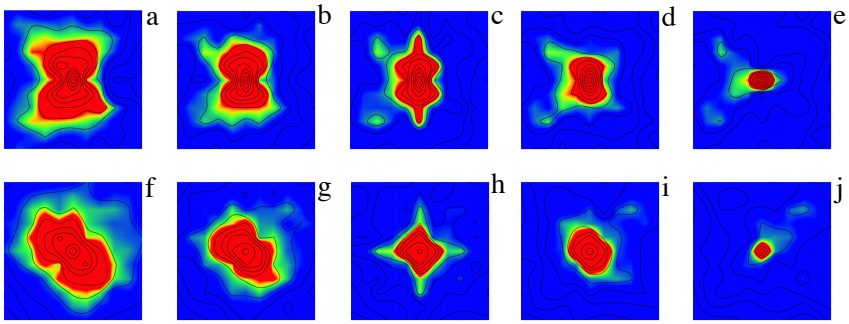

Figure 1 Diffuse scattering intensity on (*hk0*) plane. The intensities around *(100)* at 100K (a), 300K (b), 400K (c), 500K (d), and 600K (e) in upper panel. In lower panel, the intensities around *(110)* at 100K (f), 300K (g), 400K (h), 500K (i), and 600K (j).

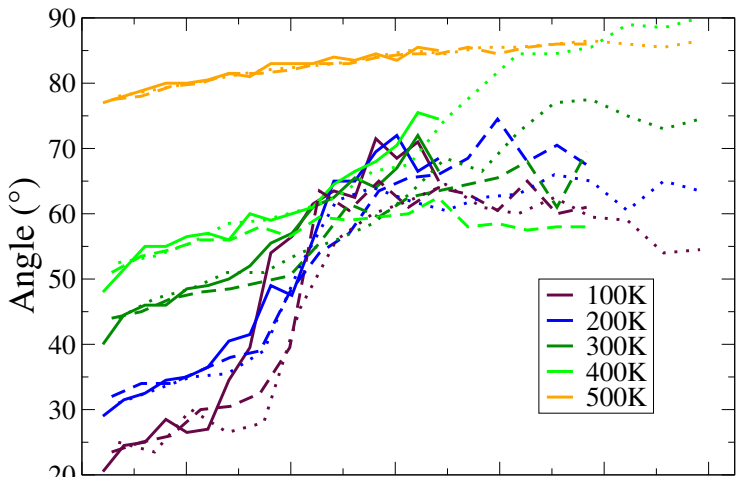

Figure 2 The peak height positions of the time-averaged angle correlations as a function of Pb atoms distance with various temperature. The solid lines are for *n00*, dashed line for *nn0*, and dotted lines for *nnn*.

In conclusion, the computational DS patterns exhibit evidence of local distortions around T^* similar to the experimental observations. The butterfly shape arises from the "slush" multidomain structure of the relaxor phase. One significant consequence of the slush structure is the extremely high non-180 degrees domain wall density, which is favorable for large piezoelectric response. Thus our results show how local structure gives origin to the diffuse scattering, phase transitions and the ultra-high piezoelectric response of relaxor materials.

Acknowledgements This work was supported by the Office of Naval Research under grant N00014-12-1-1033, the US DOE under grant DE-FG02-07ER46431. the NSF under grant DMR11-24696, and the NSF under grant CMMI-133241. Computational support was provided by a Challenge Grant from the HPCMO of the U.S. Department of Defense.ere appropriate.

References

[1] S.-E. Park, T.R. Shrout, *J. Appl. Phys.* **82**, 1804, (1997).
[2] Z. Kutnjak, J. Petzelt, and R. Blinc, *Nature.* **441**, 956, (2006).
[3] E.V. Colla, N.K. Yushin, and D. Vieland, *J. Appl. Phys.* **83**, 3298, (1998).
[4] A. Bosak, D. Chernyshov, S. Vakhrushev, and M. Krischa, *Acta Cryst. Appl.* **A64**, 117, (2012).
[5] G. Burkovsky, Yu. A. Bronwald, A. V. Filimonov, A. I. Rudskoy, D. Chernyshov, A. Bosak, J. Hlinka, X. Long, Z.-G. Ye, and S. B. Vakhrushev, *Phys. Rev. Lett.* **109**, 097603, (2012).
[6] Y.-H. Shin, V.R. Cooper, I. Grinberg, and A.M. Rappe, *Phys. Rev. B* **71**, 054104, (2005).
[7] S. Liu, I. Grinberg, H. Takenaka, and A.M. Rappe, *Phys. Rev. B* **88**, 104102, (2013).
[8] H. Takenaka, I. Grinberg, and A.M. Rappe, *Phys. Rev. Lett.* **110**, 147602, (2013).

Fano resonance in lead-free relaxor Ba(Zr,Ti)O_3

D. Wang,[1] J. Hlinka,[2] A. A. Bokov,[3] Z.-G. Ye,[3,1] P. Ondrejkovic,[2] J. Petzelt,[2] and L. Bellaiche[4]

[1]*Electronic Materials Research Laboratory–Key Laboratory of the Ministry of Education and International Center for Dielectric Research, Xi'an Jiaotong University, Xi'an 710049, China*

[2]*Institute of Physics, Academy of Sciences of the Czech Rep., Na Slovance 2, CZ-182 21 Praha 8, Czech Republic*

[3]*Department of Chemistry and 4D LABS, Simon Fraser University, Burnaby, British Columbia V5A 1A6, Canada*

[4]*Physics Department and Institute for Nanoscience and Engineering, University of Arkansas, Fayetteville, Arkansas 72701, USA*

In many different physical systems, the interference of a discrete state with a continuum of states results in a Fano resonance. Here, we use an *ab-initio* molecular dynamic scheme to reveal such resonance between the bare optical phonon mode of the Zr sublattice (the discrete state) and the bare optical phonon mode of the Ti sublattice (the continuum of states) in disordered lead-free Ba(Zr,Ti)O_3 relaxor [1]. In addition, a terahertz relaxation mode reflecting reorientations of Ti dipoles and showing an Arrhenius-like behavior is predicted, in agreement with experiments.

Canonical relaxor ferroelectrics are a special class of material that have broad dielectric response over a large temperature range, which are also strongly frequency dependent. Because of their large dielectric permittivity, property measurements in their GHz–THz range are challenging and, as a result, very few data are currently available for this frequency range [2–6]. Here, we investigate, analyze and compare with experiments the complex dielectric response of disordered lead-free Ba(Zr,Ti)O_3 (BZT) relaxor numerically obtained in the terahertz regime, via a combination of a first-principles-based effective Hamiltonian [7–9] and a molecular dynamics (MD) technique [10, 11]. One particular feature of BZT is that it is also experimentally known [6] to demonstrate a separate relaxation mechanism at the frequencies that are in the order of a few cm^{-1}, which are accessible by the present simulations. BZT has also been selected here because recent simulations [7–9] did reveal the importance of polar nanoregion (PNRs, inside which Ti dipoles are parallel to each other) and the existence of all three known characteristic temperatures of relaxors (i.e., the Burns temperature $T_{\rm B} \simeq 450$ K, $T^{*} \simeq 240$ K, and the freezing temperature $T_{\rm f} \simeq 130$ K).

The studied material is made of 50% of Zr and Ti ions that are randomly distributed inside a $12\times12\times12$ supercell (8,640 atoms). The latter is periodic along the x-, y- and z-axes, which lie along the pseudocubic [100], [010] and [001] directions, respectively. We perform effective-Hamiltonian-based MD simulations [10, 11] to obtain complex dielectric responses of the disordered BZT for temperatures between 10 K to 1000 K. The complex electric susceptibility $\chi_{\alpha\beta}(\nu)$, can be obtained using the following equation:

$$\chi_{\alpha\beta}(\nu) = \frac{1}{\varepsilon_0 V k_B T}\left[\left\langle d_\alpha(t) d_\beta(t)\right\rangle + i2\pi\nu\int_0^\infty dt e^{i2\pi\nu t}\left\langle d_\alpha(t)\, d_\beta(0)\right\rangle\right] \quad (1)$$

where ν is the frequency while α and β define Cartesian components, V is the volume of the chosen supercell and ε_0 is the vacuum permittivity. $\boldsymbol{d}(t)$ is the electric dipole moment of the system at time t, and $\langle ... \rangle$ represents thermal averages. Due to the complexity of the system, the total dielectric response of BZT is rather challenging to fit. To solve this problem, we use the fact that the total electric dipole moment, $\boldsymbol{d}$, of the system in Eq. (1) consists of two parts $\boldsymbol{d} = \boldsymbol{d}^{\rm Zr} + \boldsymbol{d}^{\rm Ti}$, where $\boldsymbol{d}^{\rm Zr}$ (respectively, $\boldsymbol{d}^{\rm Ti}$) is the dipole moment originating from the electric dipoles centered on Zr (respectively, Ti) sites, to obtain and fit the constitutional dielectric responses, $\chi^{\rm Zr,Zr}_{\alpha\beta}$, $\chi^{\rm Ti,Ti}_{\alpha\beta}$, which represent the "sole" contributions of the Zr-centered and Ti-centered sites, respectively, and $\chi^{\rm Ti,Zr}_{\alpha\beta}$ that quantifies the role of the correlations between the Zr and Ti-centered sites in that total response.

We first concentrate on the MD data for the imaginary part of these different dielectric responses at $T = 900$ K. Figure 1 shows that the imaginary part of $\chi^{\rm Zr,Zr}$ consists of a single narrow peak centered around 155 cm^{-1}, while Im($\chi^{\rm Ti,Ti}$) appears to have two (rather than one) significant broad peaks centered around 130 cm^{-1} and 250 cm^{-1}, respectively. However, it is known that there is no PNR at 900 K [7], which implies that the anisotropy of PNRs can *not* be the cause of the two peaks seen in Im($\chi^{\rm Ti,Ti}$). To search for the mechanism that is responsible for the occurrence of these two peaks, we consider two linearly *coupled* damped harmonic oscillators (DHO) – one of them (with bare frequency $\nu_{\rm Ti,0}$, bare damping constant $\Gamma_{\rm Ti,0}$, and bare plasma frequency $\Omega_{\rm Ti,0}$) representing the intrinsic, bare dynamical response of the Ti sublattice, the other (with $\nu_{\rm Zr,0}$, $\Gamma_{\rm Zr,0}$, and $\Omega_{\rm Zr,0}$) representing the intrinsic, bare dynamical response of the Zr sublattice. Application of this coupled model to the simulated dielectric response at 900 K is shown in Fig. 1. We find that: (i) the bare Zr oscillator is described by $\Omega_{\rm Zr,0} = 450$ cm, $\nu_{\rm Zr,0} = 170\,{\rm cm}^{-1}$, and $\Gamma_{\rm Zr,0} = 19\,{\rm cm}^{-1}$; (ii) the bare Ti oscillator is described by $\Omega_{\rm Ti,0} = 1250\,{\rm cm}^{-1}$, $\nu_{\rm Ti,0} = 193\,{\rm cm}^{-1}$, and $\Gamma_{\rm Ti,0} = 205\,{\rm cm}^{-1}$; and (iii) the coupling constants are $\Delta_{\rm Ti,Zr} = -8435\,{\rm cm}^{-1}$ and $\Gamma_{\rm Ti,Zr} = -41\,{\rm cm}^{-1}$. The resulting

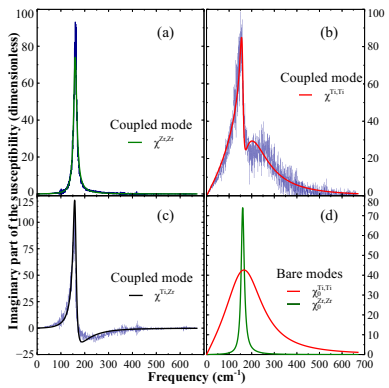

FIG. 1 . Imaginary part of different dielectric responses of BZT is shown as a function of frequency at $T = 900$ K.

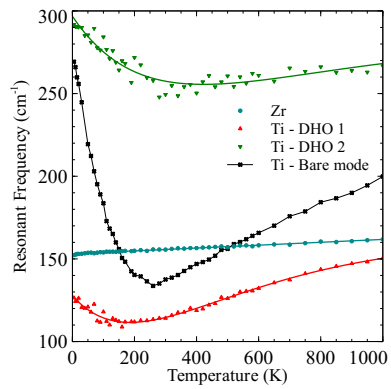

FIG. 2 . Resonant frequencies of the DHO modes associated with the Zr and of Ti sublattices, as a function of temperature.

bare dielectric response, $\chi_0^{\mathrm{Zr,Zr}}$ and $\chi_0^{\mathrm{Ti,Ti}}$, associated with these parameters, are shown in Fig. 1(d). It is important to realize that the bare Ti oscillator is clearly much more damped than the Zr one and that these two oscillators overlap in frequency. As a result, it is clear that the mechanism we are looking for is the so-called Fano resonance, for which the broad bare Ti response provides the background component while the sharp bare Zr response provides the discrete state (that are the two ingredients for the Fano resonance). To further demonstrate that the proposed Fano resonance exists in BZT relaxors, we performed additional MD simulations in which the resonance of $\chi^{\mathrm{Zr,Zr}}$ is artificially tuned to 450 cm^{-1}, that is far away from the (bare) resonance of $\chi_0^{\mathrm{Ti,Ti}}$. In such a case, we numerically found that, e.g., $\chi^{\mathrm{Ti,Ti}}$, has now only *one* (broad) peak rather than two, which confirms the adequacy of the Fano interference in our investigated system. Moreover, Figure 2 reports the temperature evolution of the resonant frequencies of all the DHO modes associated with the Zr and Ti dielectric responses, as well as the bare resonant frequency $\nu_{\mathrm{Ti},0}$ associated with $\chi_0^{\mathrm{Ti,Ti}}$ (note that the bare resonant frequency $\nu_{\mathrm{Zr},0}$ associated with $\chi_0^{\mathrm{Zr,Zr}}$ is very similar to $\nu_{\mathrm{Zr\text{-}Zr}}$, and not shown for clarity). Interestingly, the characteristic temperatures of BZT, T_{f}, T_{B} and T^*, reveal themselves in Fig. 2, either as the crossing of bare frequencies or the temperature at which $\nu_{\mathrm{Ti},0}$ hits its minimum. However, whether this is a coincidence for BZT or a general feature of relaxors needs further investigation.

In addition to the Fano resonance, our simulations also predict a thermally activated THz relaxation mode, in agreement with experiment [6], which follows an Arrhenius law above the freezing temperature. Finally, if time allows, we will show that our computations can naturally reproduce and explain at a microscopic level the frequency dependence of the peak in the dielectric response of BZT, which is often taken as the defining property of a relaxor.

This work is financially supported by the NSF grant DMR-1066158 and ONR grant N00014-12-1-1034 (D.W. and L.B.). P.O., J.P. and J.H. acknowledge the support from the Czech Science foundation (Project 13-15110S). Z.G.Y. and A.A.B. thank the support from the NSERC. Z.G.Y also acknowledges the support from ONR grant N00014-12-1-1045, and the International Science & Technology Cooperation Program of China (Grant No. 2011DFA51880), the NSFC grants 50728201 and 90923001, and the 'Qianren Program'. D.W also acknowledges the support from the NSFC grant 51390472 and the 111 Project (B14040). Some computations were made possible thanks to the grants 0722625, 0959124, and 0918970 from NSF.

[1] D. Wang, J. Hlinka, A.A. Bokov, Z.-G. Ye, P. Ondrejkovic, J. Petzelt, and L. Bellaiche, *Nat. Commun.* **5**, 5100 (2014).
[2] D. Nuzhnyy, *et al., Phys. Rev. B* **86**, 014106 (2012).
[3] W. Dmowski, *et al., Phys. Rev. Lett.* **100**, 137602 (2008).
[4] H. Takenaka, I. Grinberg, and A. M. Rappe, *Phys. Rev. Lett.* **110**, 147602 (2013).
[5] A. Bokov, M. Maglione, and Z.-G. Ye, *J. Phys.: Condens. Matter* **19**, 092001 (2007).
[6] J. Petzelt, *et al*, *Ferroelectric* **469**, 14 (2014).
[7] A. R. Akbarzadeh, S. Prosandeev, Eric J. Walter, A. Al-Barakaty, and L. Bellaiche, *Phys. Rev. Lett.* **108**, 257601 (2012).
[8] S. Prosandeev, D. Wang, A. Akbarzadeh, B. Dkhil, and L. Bellaiche, *Phys. Rev. Lett.* **110**, 207601 (2013).
[9] S. Prosandeev, D. Wang, and L. Bellaiche, *Phys. Rev. Lett.* **111**, 247602 (2013).
[10] I. Ponomareva, L. Bellaiche, T. Ostapchuk, J. Hlinka, and J. Petzelt, *Phys. Rev. B* **77**, 012102 (2008).
[11] D. Wang, D., J. Weerasinghe, A. Albarkati, and L. Bellaiche, *Inter. J. Mod. Phys. B* **27**, 1330016 (2013).

Phonons in $SrTiO_3$ and $EuTiO_3$ investigated with neutron scattering

Olivier Delaire[1], Jiawang Hong[1], Huibo Cao[2], Jiaqiang Yan[1],

Barry Winn[2], Songxue Chi[2], G. Ehlers[1], Lynn Boatner[1], Brian Sales[1]

[1]Materials Science and Technology Division, Oak Ridge National Laboratory, Oak Ridge, TN, USA
[2]Quantum Condensed Matter Division, Oak Ridge National Laboratory, Oak Ridge, TN, USA

$SrTiO_3$ (STO) is an incipient ferroelectric material, whose phonons have been studied in seminal works [1-5]. While the zone-center transverse optic (TO) mode softens with decreasing temperature, the ferroelectric transition is suppressed by quantum fluctuations [6]. Another distortion, corresponding to alternative tilts of oxygen octahedra, causes a stronger instability and result in a transition from cubic perovskite to an antiferrodistortive (AFD) tetragonal phase at Tc=105K. The AFD transition involves the softening of the R_{25} phonon mode at the R-point. The temperature dependence of both the zone-center TO and the R_{25} mode can be understood in principle on the basis of anharmonic interatomic potentials. However, a more detailed understanding of anharmonic effects is still lacking, in particular for the renormalization of phonon frequencies at finite temperature. In addition, recent re-examination of the dynamics of STO have emphasized the competition between FE and AFD instabilities [7], but a full understanding of coupled instabilities has not yet emerged.

$EuTiO_3$ (ETO) presents a number of similarities with STO, with the cubic to tetragonal AFD distortion occurring at Tc=280K [8,9]. ETO is also unique owing to the presence of magnetic Eu ions. By applying a tuning parameter, such as bi-axial tension, ETO can be turned into a ferroelectric ferromagnet, the ideal multiferroic. [10] However, in unstrained ETO, the ferroelectric TO mode does not exhibit as much softening as in STO, and its frequency remains above ~10meV at all temperatures, precluding the formation of the desired ferroelectric state. The origin of this behavior remains an open question, and both quantum fluctuations or spin-phonon interactions could be involved.

We will present results of extensive lattice dynamics measurements in single crystals with inelastic neutron scattering (INS), on single crystals of STO and ETO (synthesized with ^{153}Eu), highlighting similarities and differences. In addition, we present results of first-principles computations of the dynamical structure factor, S(**Q**,E), including anharmonic effects stabilizing the cubic phase at finite temperature in both STO and ETO.

Acknowledgements We acknowledge funding from the DOE Office of Science, Basic Energy Science.

References

[1] R. A. Cowley, Phys. Rev. **134**, A981 (1964).
[2] R. A. Cowley, *et al.*, Solid St. Commun. **7**, 181 (1969)
[3] G. Shirane and Y. Yamada, Phys. Rev. **177**, 858 (1969)
[4] S. M. Shapiro, J. D. Axe, G. Shirane, and T. Riste, Phys. Rev. B **6**, 4332–4341 (1972).
[5] P. A. Fleury and J. M. Worlock, Phys. Rev. **174**, 613 (1968)
[6] K. A. Müller and H. Burkard, Phys. Rev. B **19**, 3593 (1979)
[7] U. Aschauer and N. Spaldin, J. Phys.: Condens. Matter **26**, 122203 (2014)
[8] D. S. Ellis *et al.*, Phys. Rev. B **86**, 220301(R) (2012)
[9] A. Bussmann-Holder *et al.*, Phys. Rev. B **83**, 212102 (2011)
[10] J. H. Lee, et al., *Nature* **466**, 954 (2010).

Theory

Microscopic description of perovskites near the ferroelectric phase transition

Giovanni Pizzi[1], Andrea Cepellotti[1], Samed Halilov[2], Boris Kozinsky[3], Marco Fornari[4], Nicola Marzari[1]

[1]Theory and Simulation of Materials (THEOS) and National Center for Computational Design and Discovery of Novel Materials (MARVEL), École Polytechnique Fédérale de Lausanne (EPFL), Lausanne, Switzerland
[2]Department of Materials Science and Engineering (DMSE), Massachusetts Institute of Technology (MIT), Cambridge (MA), USA
[3]Robert Bosch LCC Research and Technology Center, Cambridge (MA), USA
[4]Department of Physics, Central Michigan University, Mount Pleasant (MI), USA

Ferroelectric materials like $BaTiO_3$ have been used for decades in a broad range of technological applications (capacitors, gate dielectrics, IR detectors, holographic memories, …). However, there is still significant debate concerning the microscopic behavior of these materials, in particular near the paraelectric–ferroelectric phase transition. In $BaTiO_3$, Ti displacements with respect to the center of the oxygen cage create local dipole moments that are at the origin of the finite polarization in the ferroelectric state. However, these perovskites display a complex energy landscape. In order to clarify the microscopic behavior of these materials, we perform ab-initio molecular dynamics calculations to assess the driving mechanisms for the formation of the different phases. We then run a high-throughput study of the cubic phase on a set of representative ABO_3 insulating perovskites, to systematically and automatically explore their energy landscape and understand how the behavior depends on the different materials. We first use spacegroup techniques to systematically analyze all possible local displacement patterns that are compatible with a net paraelectric phase. Then, we run total-energy DFT calculations to assess the energetics and the stability of these patterns in the different perovskites. Using this technique, we are able to identify the different classes of models underlying the perovskite systems.

For the symmetry analysis of crystal structures, we used the tools from SPGLib [1] and the Bilbao Crystallographic Server [2], together with custom scripts written by us. DFT calculations are run using Quantum ESPRESSO [3], and all calculations are managed, run, parsed and stored in a database by means of our high-throughput platform AiiDA [4].

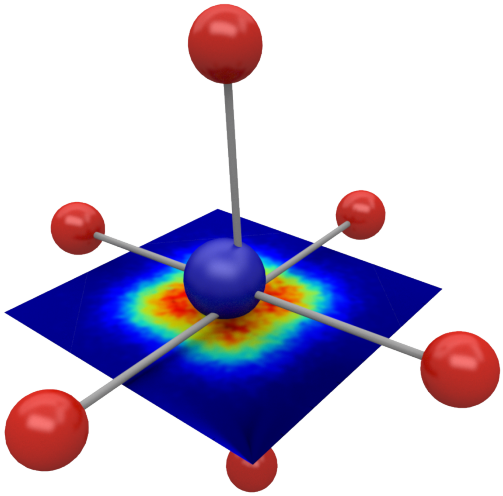

Figure 1 – Oxygen atoms (red) around a Ti atom (blue) in a $BaTiO_3$ cubic crystal at finite temperature (extracted from a snapshot of a MD simulation on a cubic 4x4x4 supercell). The color plot represents the projection on a plane of the statistical distribution of the Ti atoms with respect to the center of the respective oxygen octahedral cage, integrated over 30 ps of Car-Parrinello MD, and it shows the complex energy landscape for the Ti atoms.

References

[1] http://spglib.sourceforge.net
[2] M. I. Aroyo et al., Bulg. Chem. Commun. **43** 183 (2011), http://www.cryst.ehu.es
[3] P. Giannozzi et al., J. Phys. Cond. Matt **21**, 395502 (2009)
[4] http://www.aiida.net

About the octuplet of symmetry-distinguishable direction indicators

Jiri Hlinka

Department of Dielectrics, Institute of Physics, Czech Academy of Scinces, Prague, Czech Republic

Physical quantities defined by a magnitude and an oriented axis in 3D space are often represented by three-component Euclidean vectors. Frequently, polar and axial (or pseudo-) vectors are distinguished, depending on whether they change their sense or not, respectively, upon the operation of spatial inversion (parity operation).[1–4] For classification of temporal processes or magnetic phenomena of vectorial nature, the action of the time-inversion operator (1′) can be used.

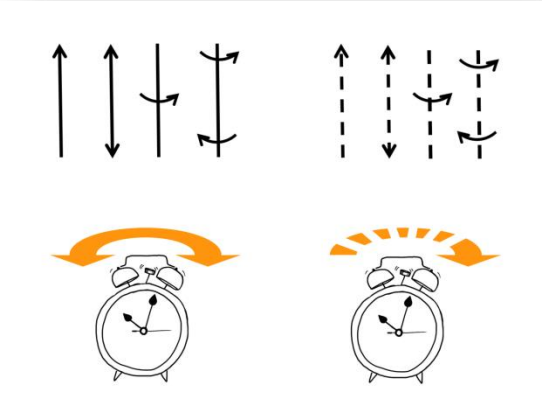

Figure 1 Pictograms providing intuitive definition of the octuplet of the symmetry-distinct vector-like quantities: vectors and bidirectors.

For example, magnetization M and magnetic field vector H are ”time-odd axial” vectors electric polarization P or electric field E are ”time-even polar” vectors, while other quantities like velocity v or toroidal moment T are ”time-odd polar” vectors.[1–6] The two inversion operations generate an Abelian (commutative) group of 4 elements with 4 one-dimensional irreducible representations; the symmetry operations this group allow to classify these vectors into 4 categories (see Table I).[1–4]

1	$\bar{1}$	1′	$\bar{1}'$	vectorial quantity	symbol
1	1	1	1	electric toroidal moment	**G**
1	-1	1	-1	electric dipole moment	**P**
1	1	-1	-1	magnetic dipole moment	**M**
1	-1	-1	1	(magnetic) toroidal moment	**T**

TABLE I: Action of space ($\bar{1}$) and time (1′) inversion operations on selected examples of vectorial quantities: 1 stands for the invariance, -1 stands for the sign-reversal.[3, 9, 12]

The aim of this contribution is to emphasize that there are another four types of quantities, which are also defined by a magnitude, an axis and a geometrical sign, and which are also often associated with three-component Euclidean vectors, but which possess a different spatiotemporal symmetry than the examples given in Table I): two kinds of chiral "bidirectors" C and F (associated with the so-called true and false chirality, resp.) and still another two "bidirectors" N and L, achiral ones, transforming as the nematic liquid crystal order parameter and as the antiferromagnetic order parameter of the hematite crystal α-Fe_2O_3, respectively. List of all kinds of the symmetry-distinct “vectorlike” quantities is given below and also illustrated in Fig. 1. Application of this classification to several selected issues discussed or cited in [7-13] will be given for illustration of the concept and the notation proposal.

		$\bar{1}$	$1'$	$m_{\parallel}$	limiting group
G	time-even axial	1	1	−1	$\infty/m.\mathbf{1}'$
P	time-even polar	−1	1	1	$\infty m.\mathbf{1}'$
M	time-odd axial	1	−1	−1	∞/mm'
T	time-odd polar	−1	−1	1	$\infty/m'm$
N	time-even neutral	1	1	1	$\infty/mm.\mathbf{1}'$
C	time-even chiral	−1	1	−1	$\infty 2.\mathbf{1}'$
L	time-odd neutral	1	−1	1	∞/mm
F	time-odd chiral	−1	−1	−1	$\infty/m'm'$

Acknowledgements It is a real pleasure to acknowledge Václav Janovec for his valuable suggestions related to this work, financially supported by the Czech Science Foundation (Project 13-15110S).
.

References

[1] F. Author, S. Author and T. Author, *J. Sig. Res.* **Vol**, Page, (Year).
[1] R. R. Birss, *Symmetry and Magnetism* (North-Holland, Amsterdam, 1964).
[2] H. Grimmer, *Ferroelectrics* **161**, 181 (1994).
[3] E. Ascher, *Int. J. Magnetism* **5**, 287 (1974).
[4] V. Kopsky, *Z. Krystallogr.* **221**, 51 (2006).
[5] Yu. Sirotin and M. P. Shaskolskaya, *Osnovy Kristallophiziki* (In Russian, Moscow: Nauka, 1975); [Engl. transl: Fundamentals of Crystal Physics (Moscow: Mir. 1982)].
[6] V. M. Dubovik and V. V. Tugushev, *Physics Reports* **187**, 145 (1990).
[7] V. K. Wadhawan, *Introduction to Ferroic Materials* (Gordon and Breach, New York, 2000).
[8] A.S. Borovik-Romanov and H. Grimmer, in *International Tables for Crystallography*, edited by A. Authier (Kluwer Academic, Dordrecht, 2003), Vol. D, p. 137.
[9] D. B. Litvin, *Acta Cryst.* **A64**, 316 (2007).
[10] I. S. Zheludev, *Fizika kristallov i simmetria* (Nauka, Moscow, 1987).
[11] I. S. Zheludev, *Acta Cryst.* **A42**, 122 (1986).
[12] V. M. Dubovik, S. S. Krotov, and V. V. Tugushev, *Kristallograya* **32**, 540 (1987).
[13] J.Hlinka, *Phys.Rev.Lett.* **113** (2014).

Absence of ultra-high pressure ferroelectricity in $PbTiO_3$

R.E. Cohen[1,2], Muhtar Ahart[1], Subhasish Mandal[1,3], Javier Nossa[1], P. Ganesh[4], Ivan Naumov[1], Alexander F. Goncharov[1], Stanislav V. Sinogeikin[5], and Russell J. Hemley[1]

[1]Geophysical laboratory, Carnegie institution of Washington, Washington, DC 20015, USA
[2]Department of Earth Sciences, University College London, WC1E 6BT, London, UK
[3]Department of Applied Physics, Yale University, New Haven, Connecticut, USA
[4]Oak Ridge Natl. Lab., Ctr. Nanophase Mat. Sci., Oak Ridge, TN 37830 USA
[5]High Pressure Collaborative Access Team, Geophysical Laboratory, Carnegie Institution of Washington, Advanced Photon Source, Argonne National Laboratory, Argonne, IL 60439, USA

Ferroelectricity was long thought to disappear at high pressures, but density functional (DFT) calculations showed reentrant ferroelectricity at high pressures in perovskites such as $BaTiO_3$ and $PbTiO_3$ (PTO). Our second-harmonic generation measurements, however show no evidence of ferroelectricity at ultra-high pressures (above 20 GPa) in PTO. Our DFT computations confirm an absolute static ferroelectric ground state for pressures up to at least 100 GPa. However, the ferroelectric well is very shallow, and we find that PTO is most likely a quantum paraelectric at high pressures with a distorted perovskite crystal structure. This settles a long-time problem in understanding ferroelectric behaviour.

For many years it was thought that ferroelectricity (FE) was squeezed out at high pressures. Room temperature Raman measurements showed a soft mode with increasing pressure that goes to zero at a pressure Pc, with no first-order Raman above this pressure [1-3]. However, first-principles Density Functional Theory (DFT) computations for $PbTiO_3$ showed a series of high pressure phase transitions to other polar phases rather than a simple tetragonal ferroelectric to cubic paraelectric transition [4]. This was confirmed by Raman and micro-x-ray studies that agreed well with experiments at cryogenic temperatures [5]; the earlier observed transition at room temperature is not the ground state. The Ahart et al. study also showed that the low temperature transitions are like the morphotropic phase boundary in $PbTiO_3$-$PbZrO_3$ (PZT) and other ferroelectric solid solutions, but in a pure material, and supported the role of polarization rotation for large piezoelectric response in relaxor ferroelectrics [6]. Theoretical study of perovskite ferroelectrics was pushed to higher pressures, and showed reentrant ferroelectric to ultrahigh pressures [7-9]. This was a surprising result, since in the ferroelectric state atoms move closer together, and the repulsive forces should increase rapidly with density, so that one would expect ferroelectric distortions to be unstable at high pressures, rather than showing increasing instability as predicted by Kornev et al. within DFT. This prediction of ultrahigh pressure ferroelectricity is addressed here using experiments and theory.

To clarify whether the high-pressure ferroelectricity exists or not in PT, we performed Second Harmonic Generation (SHG) measurements (Fig. 1). The second nonlinear harmonic of the dielectric permittivity is finite only if the crystal symmetry is broken such that the crystal does not possess a center of symmetry [26]. The relative intensity at each pressure is obtained by normalizing the integral intensity to the intensity obtained at ambient pressure, during the same time interval. All three runs of experiments (single crystals and powder samples) show consistent results. The SHG signal decreases with pressure almost linearly in the interval between 0 and 12 GPa, but remains almost same above 12 GPa up to 100 GPa with low intensity.

To better understand the discrepancy between DFT computations and our SHG measurements we have performed a large number of DFT computations using different codes, pseudopotentials, and compared also with all-electron computations performed with the WIEN2K code. All static computations are consistent with a ferroelectric ground state, as in previous computations. All these computations cannot prove that there is not a lower static energy structure. For example, there could be a larger unit cell with antiferroelectric (AFE) distortions that would have off-centering, but in an alternating pattern with zero polariza-

tion [10]. We searched for such structures, but exhaustive searching was not able to find a more stable centrosymmetric structure.

A FPMD simulation at 100 GPa seems to give a disordered perovskite structure. Averaging atomic positions over several ps gives a structure that cannot be mapped onto any structure with symmetry greater than P1. This indicates unit cell disorder in polarization direction, consistent, with the low energy barriers for polarization rotation or displacement direction. To confirm this, we computed the Berry's phase polarization and obtained zero polarization, consistent with the SHG measurements.

Our cryogenic SHG measurements also show no signal at high pressures, suggesting that quantum fluctuations also play a role. To test this we mapped the double well from R-3c to R3c at fixed volume, where the central R-3c point at 0 is at 100 GPa. We treat this as a quantum anharmonic oscillator. The zero point energy computed for this oscillator is comparable to the enthalpy difference between R3c and R-3c at 100 GPa. So we expect quantum fluctuations to average over the double well. So our results are consistent with the ground state of ultrahigh pressure PTO being a quantum paraelectric, consistent with experiment.

Acknowledgements This work is supported by ONR grants N00014-12-1-1038 and N00014-14-1-0561, by the ERC Advanced grant ToMCaT, and by CDAC-NNSA (DE-NA- 000006).

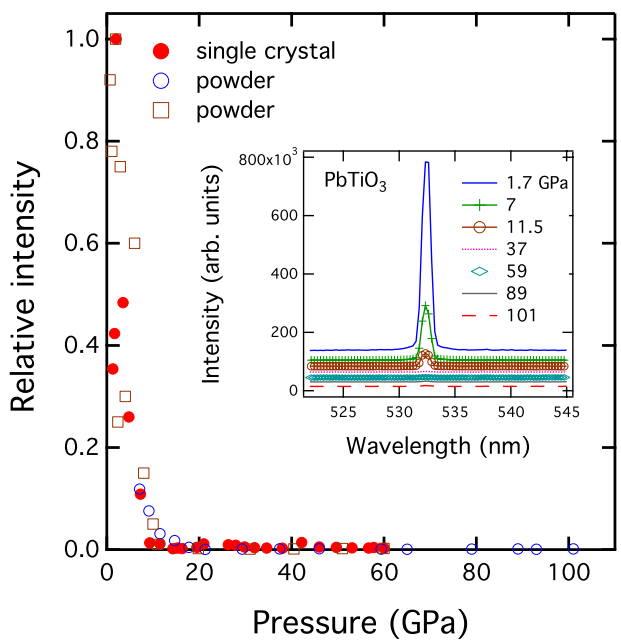

Figure 1. Pressure dependence of the integrated intensity of SHG. We normalize the integrated intensity with the intensity obtained at ambient pressure. We performed three experimental runs: first run, solid circle (red) marks, neon pressure medium; second run, open circle (blue), single crystal, neon pressure medium; third run, solid square (green) marks, neon pressure medium. The SHG spectrum of the $PbTiO_3$ single crystal at selected pressures. The wave length of the incident light is 1064 nm, so the SGH signals appear at 532 nm.

References

[1] G. Burns and B. A. Scott, Phys. Rev. Lett. **25**, 1191 (1970).
[2] J. Sanjurjo, E. López-Cruz, and G. Burns, Phys. Rev. B **28**, 7260 (1983).
[3] D. L. Decker and Y. X. Zhao, Phys. Rev. B **39**, 2432 (1989).
[4] Z. Wu and R. Cohen, Physical Review Letters **95** (2005).
[5] M. Ahart *et al.*, Nature **451**, 545 (2008).
[6] H. X. Fu and R. E. Cohen, Nature **403**, 281 (2000).
[7] I. Kornev, L. Bellaiche, P. Bouvier, P. E. Janolin, B. Dkhil, and J. Kreisel, Physical Review Letters **95** (2005).
[8] I. A. Kornev and L. Bellaiche, Phase Transitions **80**, 385 (2007).
[9] P. Ganesh and R. E. Cohen, J. Phys.: Condens. Matter, 064225 (2009).
[10] K. M. Rabe, in: Functional Metal Oxides: New Science and Novel Applications, 221 (2013).

A fresh look at the position operator (as in polarization, magnetization, and more)

Raffaele Resta
Dipartimento di Fisica, Università di Trieste, Italy,

Macroscopic polarization, orbital magnetization, and related quantities have a trivial expression for a molecule or for a finite crystallite, where the wavefunction is square-integrable: so-called "open" boundary conditions (OBCs). In condensed matter physics it is instead necessary to adopt periodic boundary conditions (PBCs): what makes life difficult is the unbounded position operator $\mathbf{r}$, which is *not* a legitimate operator within PBCs.

Solutions to this problem are known since the early 1960s, when the first expressions for computing the dielectric polarizability of a solid where proposed. Other solutions, to be applied to different problems, appeared over the years. Invariably, bulk properties of a crystalline system are cast as Brillouin zone (BZ) integrals, where the integrand is expressed in terms of Bloch orbitals. We have therefore two expressions—one a $\mathbf{k}$-space integral within PBCs, the other an $\mathbf{r}$-space integral within OBCs—for the same physical property. What is disturbing is that the two expressions do not bear any apparent relationship.

Here I am going to show that the OBCs and PBCs expressions for a given property are essentially the same when expressed in terms of the *projected* position operator $\tilde{\mathbf{r}}$, defined below. While some of the results presented here are known, some are not: in particular, the expression for orbital magnetization given below is new.

For noninteracting electrons (either Hartree-Fock or Kohn-Sham) the ground state is uniquely determined by the projector P over the occupied electronic states; in the large system limit, P is the same within either OBCs or PBCs. We define as Q the complementary projector over the unoccupied states, and we define the *Hermitian* operator $\tilde{\mathbf{r}} = P\mathbf{r}Q + Q\mathbf{r}P$, i.e. $\mathbf{r}$ minus its occupied-occupied and unoccupied-unoccupied components. In a crystalline system $\tilde{\mathbf{r}}$ is a lattice-periodical operator, and is expressed as a BZ integral. The physical properties of interest will be expressed as traces per unit volume involving $\tilde{\mathbf{r}}$. The novel compact formulation applies to both OBCs and PBCs; it even applies to noncrystalline systems, where $\tilde{\mathbf{r}}$ is no longer lattice-periodical, but is nonetheless a regular operator.

In the following the symbol "Tr" means trace per unit volume; it becomes the trace per cell in the crystalline case. The expressions are given for "spinless electrons"; trivial factors of 2 are not included.

Polarization. When an insulating system is adiabatically transformed between an initial and a final state the (electronic) polarization difference is

$$\Delta \mathbf{P}_{\text{electronic}} = -e \int_0^1 d\lambda \ \text{Tr} \ \left\{ \frac{\partial P}{\partial \lambda} \tilde{\mathbf{r}} \right\}.$$

Quadratic spread. The gauge-invariant quadratic spread, as it enters the Marzari-Vanderbilt theory of maximally localised Wannier functions, is

$$\Omega_{\text{I}} = V_{\text{cell}} \text{Tr} \ \{ P \, \tilde{\mathbf{r}} \cdot \tilde{\mathbf{r}} \},$$

where V_{cell} is the cell volume. When used for a molecule within OBCs, the analogous formula yields the gauge-invariant spread of Boys' orbitals.

Orbital magnetization. The new formula for insulating materials is

$$M_\gamma = -\frac{ie}{2\hbar c} \epsilon_{\gamma\alpha\beta} \text{Tr} \ \{ |H - \mu| \, \tilde{r}_\alpha \tilde{r}_\beta \},$$

where μ is the Fermi level. We stress that this applies to both a finite crystallite within OBCs, and to a crystalline system within PBCs. When the operator $\tilde{\mathbf{r}}$ is expressed as a BZ integral, we recover the known $\mathbf{k}$-space formula of the modern theory of magnetization. The present formula, as given, holds for Chern insulators as well.

Chern number. We switch here to a two-dimensional system, and we redefine "Tr" as the trace per unit area. The Chern number is

$$C = -2\pi i \text{Tr} \ \{ P[\tilde{x}, \tilde{y}] \}.$$

If the formula is adopted for a finite flake within OBCs the total trace vanishes; nonetheless the trace per unit area evaluated in an inner region of the flake provides the Chern number.

Acknowledgments
Work supported by the ONR Grant No. N00014-11-1-0145.

Quantum Monte Carlo calculations in solids with downfolded Hamiltonians

Henry Krakauer
Department of Physics, College of William and Mary, Williamsburg, VA 23187.

A systematic downfolding many-body approach for extended systems is presented [1, 2]. Many-body calculations operate on a simpler Hamiltonian which retains material-specific properties. The Hamiltonian is systematically improvable and allows one to dial, in principle, between the simplest model and the original Hamiltonian. As a by-product, pseudopotential (PSP) errors are essentially eliminated using a frozen-core (FC) treatment. The cost of the calculation is dramatically reduced without sacrificing accuracy. We use the auxiliary-field quantum Monte Carlo (AFQMC) method [3–7] to solve the downfolded Hamiltonian. This approach greatly extends the reach of general, *ab initio* many-body calculations in materials. We illustrate the approach [1] by obtaining accurate equilibrium properties in a range of solids, including semiconductors, ionic insulators, and metals. We then show that the present approach can describe BN, with an accurate EOS extending to high pressures, without resorting to all-electron calculations [8]. Finally, the spin gap in strongly correlated NiO is accurately determined and compared with experiment.

The most fundamental issue in computations of electron correlation effects is accuracy. For QMC calculations, the fermion sign problem must be controlled with an approximation. The AFQMC framework, by carrying out the random walks in non-orthogonal Slater determinant space, has shown to lead to an approximation which is more accurate and less dependent on the trial wave function (see Ref. 5 and references therein). Our approach treats downfolded Hamiltonians expressed with respect to a truncated basis set of mean-field orbitals of the target system, using AFQMC. The simplification, often with drastic reduction in computational cost, can extend the reach of *ab initio* computations to more complex materials. A large gain in statistical accuracy often results as well, because of the smaller range of energy scales (or many fewer degrees of freedom) which need to be sampled stochastically in the downfolded Hamiltonian.

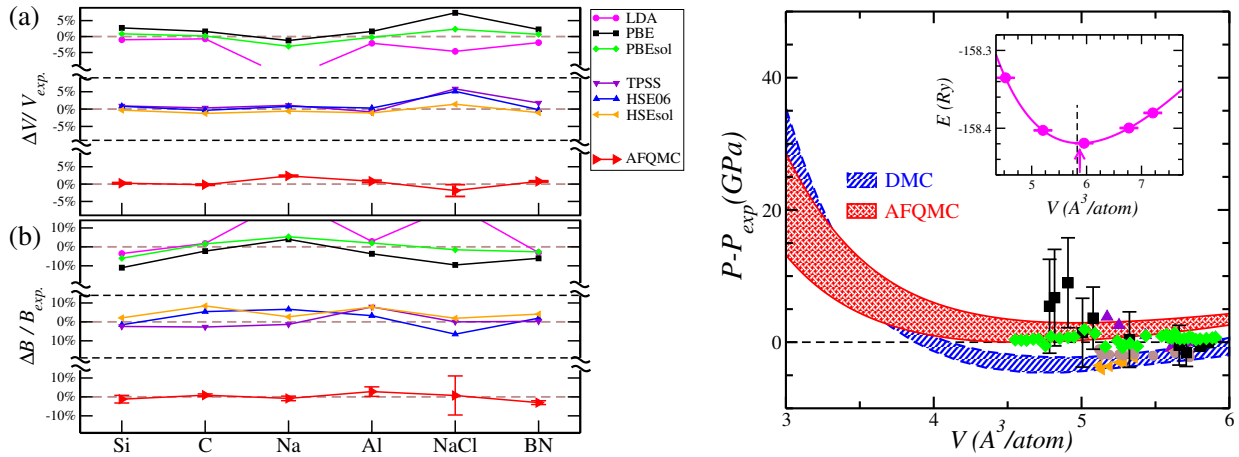

FIG. 1: Left panel: Calculated equilibrium volumes (a) and bulk moduli (b), as relative errors from experiment. Selected DFT results are also shown. Right panel: Pressure calibration and EOS in cubic BN. The main graph displays the calculated pressure vs. volume at room-temperature, using the fitted experimental curve of Datchi et al. [8] (green diamond symbols) as a pressure reference. Different symbols are from different experiments. The shading gives the overall statistical uncertainties. The all-electron DMC results are from Ref. 8. The inset shows the $T = 0\,\mathrm{K}$ EOS near equilibrium from AFQMC. The calculated equilibrium position is shown by the arrow. The vertical line indicates the experimental value.

The left panel in Figure 1 summarizes the calculated equilibrium properties and compares them with experiment. Calculations for metallic bcc Na and fcc Al used twist averaging over 90 random **k**-points. He-core PSPs were used for Na and Al, together with the FC treatment. This makes a major difference in both NaCl and Na. With a Ne-core PSP, the equilibrium volume is underestimated by $\sim 30\%$ in Na, for example. The error is eliminated by the FC approach, which allows the semi-core $2s$ and $2p$ electrons to fully relax in the *target environment of the solid* at the DFT-level, before freezing them in the corresponding KS orbitals in the many-body calculation. In a more demanding test, we apply downfolding AFQMC to obtain the EOS of cubic BN for pressures up to 900 GPa ($V \sim 0.5\,V_{eq}$). This system has been identified as a promising material for an ultra-high pressure calibration scale [8]. A recent DMC study stressed the need for all-electron (AE) calculations in order to obtain reliable results at high pressures

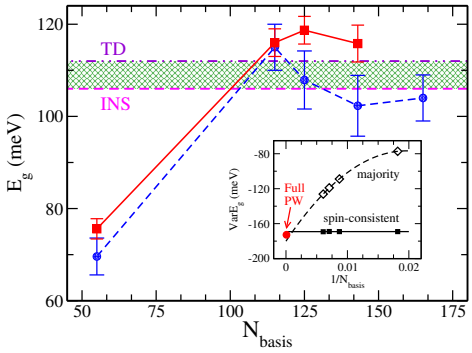

FIG. 2: AFQMC spin gap in NiO and comparison with experiment: thermodynamic measurements (TD; top line) and inelastic neutron scattering (INS; bottom line). Blue circles used averaging over only two **k**-points and confirm convergence with respect to $N_{\rm basis}$. Calculations averaging over a $4 \times 4 \times 4$ **k** grid (red squares) are used to obtain the final results. The inset illustrates the much faster convergence enabled by using a spin-consistent basis set [1] than using the KS orbitals from the majority spin.

[8]. The difficulty underscores the PSP transferability problem and is exacerbated by the need to apply a locality approximation in DMC to treat non-local PSPs. The AE treatment would be difficult to realize for heavier atoms. Our calculations freeze the $1s$ electrons in their KS orbitals in the supercell at each volume, using extremely hard "zero-electron-core" PSPs for B and N in the downfolding procedure [1]. In most cases ~ 55 states/atom were used, but larger $N_{\rm basis}$ calculations were done at selected volumes to extrapolate the EOS to the complete basis set limit. As seen in the right panel Fig. 1, the calculated EOS at low pressures is in excellent agreement with experiments (see Ref. 8). At high pressures, the two QMC results are in good agreement, providing a consistent *ab initio* pressure calibration.

As a final application, we determine the spin gap between the ferromagnetic (FM) state and the antiferromagnetic (AFM-II) ground state in NiO (Fig. 2). Understanding and predicting magnetic properties of transition-metal oxides epitomizes the challenge of computations in quantum matter. NiO is a prototypical system for strong electron correlations. Many-body calculations of the spin gap have been limited, and DFT-based methods have yielded widely varying values [1]. We use Ne-core and He-core PSPs for Ni and O, respectively. The downfolded Hamiltonian treats the Ni $3s$, $3p$, $3d$, $4s$ and O $2s$, $2p$ electrons. A rhombohedral supercell with a lattice constant of 4.17 $\mathring{A}$ containing two formula units is used. To reduce one-body finite-size effects, we used twist-averaging with a $4 \times 4 \times 4$ **k** grid. (A recent study [9] by full configuration-interaction QMC and coupled-cluster methods, with calculations at $\mathbf{k} = \Gamma$, obtained a gap value $\sim 0.96\, eV$.) One- and two-body finite-size corrections [10] are then applied to the many-body results (two-body finite-size effects are greatly reduced by cancellation, because the two phases share the same supercell). In the inset in Fig. 2, the variational gap value from the single-determinant trial wave functions is shown vs. the number of basis functions, for both the spin-consistent basis set and one which uses truncated KS orbitals of the majority spin. Both converge to the same infinite basis-set limit, as expected, but the former greatly accelerates convergence. Note that the variational gap is actually negative, i.e., the trial wave functions identify the incorrect phase for the ground state. The AFQMC calculations correctly recovers from these, and yield a final estimate of the gap of 116(3) meV, in good agreement with experiments [1].

The downfolding approach can be generalized to carry out excited state and many-body band structure calculations, which was recently formulated [11] in planewave AFQMC. A large number of applications are possible within the present form. Further improvements, for example by using localized virtual states or optimizing the orbitals with respect to the environments, will lead to even more general and powerful approaches.

Acknowledgments: Work done in collaboration with Fengjie Ma, Wirawan Purwanto, and Shiwei Zhang; supported by ONR, DMR, and NSF. Calculations used the SciClone cluster at the College of William and Mary.

[1] S. Zhang, F. Ma, W. Purwanto, and H. Krakauer, http://arXiv.org/abs/1412.0322.
[2] W. Purwanto, S. Zhang, and H. Krakauer, J. Chem. Theory Comput. **9**, 4825 (2013).
[3] S. Zhang and H. Krakauer, Phys. Rev. Lett. **90**, 136401 (2003).
[4] W. A. Al-Saidi, S. Zhang, and H. Krakauer, J. Chem. Phys. **124**, 224101 (2006).
[5] S. Zhang, *Emergent Phenomena in Correlated Matter: Modeling and Simulation*, Vol. 3, Ed. E. Pavarini, E. Koch, and U. Schollwöck (Verlag des Forschungszentrum Jülich, 2013).
[6] Y. Virgus, W. Purwanto, H. Krakauer, and S. Zhang, Phys. Rev. Lett. **113**, 175502 (2014).
[7] W. Purwanto, H. Krakauer, and S. Zhang, arXiv:1410.3505.
[8] K. P. Esler, R. E. Cohen, B. Militzer, J. Kim, R. J. Needs, and M. D. Towler, Phys. Rev. Lett. **104**, 185702 (2010).
[9] G. H. Booth, A. Gruneis, G. Kresse, and A. Alavi, Nature **493**, 365 (2013).
[10] F. Ma, S. Zhang, and H. Krakauer, Phys. Rev. B **84**, 155130 (2011).
[11] F. Ma, S. Zhang, and H. Krakauer, New J. Phys. **15**, 093017 (2013).

Novel forms of energy in ferroelectric, antiferroelectric, antiferrodistortive, magnetic and multiferroic materials

L. Bellaiche[1,2], S. Bhattacharjee[1,2], X. M. Chen[3], H. Fu[1], Z. Gui[1,2], J. Iniguez[4], I. Kornev[5], A.-J. Mao[6], A. Raeliarijaona[1], W. Ren[7], S. Singh[1], M. Viret[8], R. Walter[1,2], D. Wang[9], Y. Yang[1,2] and H. J. Zhao[1,2,3]

[1]*Physics Department, University of Arkansas, Fayetteville, Arkansas 72701, USA*
[2]*Institute for Nanoscience and Engineering, University of Arkansas, Fayetteville, Arkansas 72701, USA*
[3]*Laboratory of Dielectric Materials, Department of Materials Science and Engineering, Zhejiang University, Hangzhou 310027, China*
[4]*Institut de Ciencia de Materials de Barcelona (ICMAB-CSIC), Campus UAB, 08193 Bellaterra (Barcelona), Spain*
[5]*Laboratoire Structures, Proprietes et Modelisation des Solides, Ecole Centrale Paris, CNRS-UMR8580, Grande Voie des Vignes, 92295 Chatenay-Malabry Cedex, France*
[6]*Institute of Atomic and Molecular Physics, Sichuan University, Chengdu 610065, China*
[7]*Department of Physics, Shanghai University, 99 Shanghai Road, Shanghai 200444, China*
[8]*Service de Physique de l'Etat Condense, CEA Saclay, DSM/IRAMIS/SPEC, URA CNRS 2464, 91191 Gif-Sur-Yvette Cedex, France*
[9]*Electronic Materials Research Laboratory, Key Laboratory of the Ministry of Education and International Center for Dielectric Research, Xi'an Jiaotong University, Xi'an 710049, China*

Discovering new energy terms in materials is obviously of fundamental interest and may lead to the understanding of complex phenomena. Discovery of such terms may also help us design materials with novel or optimized properties, and thus lead to new devices and advances in technology.

The aim of this talk is to report and discuss novel energy terms that have been recently proposed to exist in a variety of materials and their fundamental and practical implications:

- (1) A rather simple energy term containing four different macroscopic terms was suggested in Ref. [1] to explain and understand coupled magnetic orders (and the directions of the simultaneously-occurring ferromagnetic and/or antiferromagnetic vectors) in terms of anti-phase and/or in-phase oxygen octahedra tiltings, in magnetic and multiferroic perovksites. This energy is derived from a suggested simple microscopic formula, and takes its root in the Dzyaloshinsky-Moriya interaction. Comparison with data available in the literature and with first-principles calculations confirms the validity of such simple energy term quite generally for any tested structural paraelectric and even ferroelectric phase, and for any chosen direction of any selected primary magnetic vector.

- (2) Two elemental interatomic couplings that control the collaborative (as opposed to competing) interaction between the O_6 octahedral rotations (usually called antiferrodistortive or AFD modes) and the antiferroelectric (AFE) displacement patterns of the A-site cations in oxides with the ABO_3 perovskite structure were identified in Ref. [2]. Straightforward analytical derivations allowed us to reproduce and explain the origin of various long-range AFE orders that have been previously found in different phases of several perovskite compounds, all possessing simple or even complex long-range

AFD patterns. Our analysis also predicts new peculiar combinations of AFD and AFE orders that are waiting to be observed. Interestingly, the generalization of these two elemental interatomic couplings to superlattices made of paraelectric perovskites is straightforward [3] and it allows not only to understand the so-called hybrid improper ferroelectricity [4-7], but also to design near room-temperature multiferroics with tunable ferromagnetic and electrical properties [8].

- (3) An novel energy involving trilinear coupling between polarization, octahedral tilting and an antiferroelectric distortion was found in Ref. [9] for some structural phases. The existence of this energy combined with that indicated in item (1) results in the emergence of a novel magnetoelectric effect that makes it possible to control magnetism with an electric field via a two-step process.

- (4) Starting from the known control of magnetic vortices by the cross-product of electric and magnetic fields [10-13], Ref. [14] demonstrated that the angular momentum density associated with an electromagnetic field can directly couple with magnetic moments to produce a physical energy. Remarkably, this new form of energy was further found to reproduce in a straightforward manner and to naturally explain many complex effects. Examples include the spin-current model in multiferroics [14], the anomalous Hall effect [15], and the anisotropic magnetoresistance and the planar Hall effect in ferromagnets [16]. This energy also led to the prediction of novel spintronic effects [17] that bear resemblance to the so-called inverse Rashba-Edelstein effect.

These works are supported by ONR Grant N00014-12-1-1034, the Department of Energy, Office of Basic Energy Sciences, under contract ER-46612, the ARO grant W911NF-12-1-0085 and NSF grant DMR-1066158. Some computations were made possible thanks to the MRI grant 0722625 from NSF, the ONR grant N00014-07-1-0825 (DURIP) and a Challenge grant from the Department of Defense.

References:

[1] L. Bellaiche, Zhigang Gui and Igor A. Kornev, J. Phys.: Condens. Matter 26 24, 312201(2012).
[2] L. Bellaiche and Jorge Iniguez, Phys. Rev. B 88, 014104 (2013).
[3] Hong Jian Zhao, Jorge Iniguez, Wei Ren, Xiang Ming Chen and L. Bellaiche, Phys. Rev. B 89, 174101 (2014).
[4] N.A. Benedek and C.J. Fennie, Phys. Rev. Lett. 106, 107204 (2011).
[5] J.M. Rondinelli and C.J. Fennie, Adv. Mater 24, 1961 (2012).
[6] J. Young and J.M. Rondinelli, Chem. Mater. 25, 4545 (2013).
[7] A. Mulder, N A. Benedek, J. M. Rondinelli, and C. J. Fennie, Adv. Funct. Mater. 23, 4810 (2013).
[8] Hong Jian Zhao, Wei Ren, Yurong Yang, Jorge Iniguez, Xiang Ming Chen and L. Bellaiche, Nature Communications 5, 4021 (2014).
[9] Yurong Yang, Jorge Iniguez, Ai-Jie Mao and L. Bellaiche, Phys. Rev. Lett. 112, 057202 (2014).
[10] H. Schmid, Ferroelectrics 252, 41 (2001).
[11] C. Ederer and N.A. Spaldin, Phys. Rev. B 76, 214404 (2007).
[12] V. M. Dubovik and V. V. Tugushev, Physics Reports 187, 145 (1990).
[13] A. A. Gorbatsevich, Yu.V. Kopaev, and V.V. Tugushev, Zh. Eksp. Teor. Fiz. 85, 1107 (1983) [Sov. Phys. JETP 58, 643 (1983)].
[14] Aldo Raeliarijaona, Surendra Singh, Huaxiang Fu, and L. Bellaiche, Phys. Rev. Lett. 110, 137205 (2013).
[15] L. Bellaiche, Wei Ren and Surendra Singh, Phys. Rev. B 88, 161102(R) (2013).
[16] R. Walter, M. Viret, Surendra Singh and L. Bellaiche, J. Phys.: Condens. Matter 26, 432201 (2014).
[17] S. Bhattacharjee, S. Singh, D. Wang, M. Viret and L. Bellaiche, J. Phys.: Condens. Matter 26, 315008 (2014).

New Ferroelectrics

Ab Initio Analysis of Ferroelectric and Magnetic Properties of Potentially Multiferroic Aurivillius Phases

Axiel Yaël Birenbaum, Jan van den Broek, and Claude Ederer
Materials Theory, ETH Zürich, Switzerland

Multiferroic materials combining magnetic properties with electric polarization in the same phase, are promising for novel applications in electronic devices. [1] However, these combined properties are typically exhibited at low temperatures. Novel ways to integrate ferroelectricity with long-range magnetic order above room temperature are therefore of high relevance.

We focus on the Aurivillius family of naturally-layered perovskite-related materials, which combine well-established high temperature ferroelectric properties [2, 3] with a layered structure that allows for systematic introduction of various magnetic ions. The structure consists of m perovskite layers $(A_{m-1}B_mO_{3m+1})^{2-}$, stacked along the [001] direction, and separated by fluorite-like $(Bi_2O_2)^{2+}$ layers (see Figure 1a).

To exhibit robust multiferroic properties, the Aurivillius phases need to satisfy two criteria: i) maintain ferroelectricity despite the introduction of magnetic cations, and ii) form long-range magnetic order from magnetically dilute compositions. The simplest case that has been explored as potential multiferroic is $Bi_5FeTi_3O_{15}$. However, no well-established value exists for its spontaneous electric polarization, with reports varying from $3.5\mu C/cm^2$ to $\sim 30\mu C/cm^2$. [4, 5] Similarly, an antiferromagnetic Néel temperature of 80 K has been reported [6], in contradiction with other studies observing paramagnetic behavior with no magnetic long-range order even at very low temperatures. [4, 7–9]

To provide clarification as well as guideline for future studies, we first establish the intrinsic properties of $Bi_5FeTi_3O_{15}$ using first-principles electronic structure calculations and symmetry mode analysis. These results are then generalized to other Aurivillius phases. We also perform Monte Carlo simulations to assess the possibility of long-range magnetic order and estimate the corresponding ordering temperature.

For the case of $Bi_5FeTi_3O_{15}$, we find a slight preference of the Fe^{3+} cation to occupy the "inner" site within the perovskite-like layers, consistent with recent experimental observations. [10] This site-preference can be tuned by applying epitaxial strain and we observe a transition to an "outer"-site preference under strong in-plane tensile strain. The calculated value for the spontaneous electric polarization of $Bi_5FeTi_3O_{15}$ is $\sim 55\mu C/cm^2$, and can also be tuned by applying epitaxial strain (see Figure 1b). We obtain very strong antiferromagnetic coupling for Fe^{3+} in nearest-neighbor positions ($\sim$ 40 meV), but rather weak coupling ($\sim$ 1-2 meV) at next-nearest neighbor distances and beyond, consistent with the Goodenough-Kanamori rules for superexchange.

To clarify whether magnetic long range order can occur in $Bi_5FeTi_3O_{15}$and similar systems, despite the low concentration of magnetic cations and the short range of the magnetic superexchange interaction, we perform Monte Carlo simulations for an appropriately chosen Heisenberg model. We find that the critical temperature for magnetic long-range order depends crucially on the rather weak next-to-nearest neighbor coupling. On the other hand, the also very weak interlayer-coupling (i.e. across the fluorite layer) is less crucial as long as the coupling within the perovskite layers is sufficiently strong. We discuss possible strategies to obtain Aurivillius phases with high magnetic ordering temperatures.

Finally, in order to better understand the mechanism for ferroelectricity in $Bi_5FeTi_3O_{15}$ and other Aurivillius phases, we examine different 2-layered systems, based on the well-studied reference system $SrBi_2Ta_2O_9$ [11], where we systematically substitute the nominally "ferroelectrically-active" cations (Bi^{3+} and Ta^{5+}) by "non-ferroelectrically-active" cations (La^{3+} and Sb^{5+}). In total we consider 9 different compositions by also substituting Ta^{5+} with Nb^{5+} and Sr^{2+} with Ba^{2+} and Ca^{2+}. Strikingly, we find a spontaneous polarization of $\sim 15\mu C/cm^2$ even in the case of $SrLa_2Sb_2O_9$, with no nominally ferroelectrically-active cations. We discuss these results in light of the tri-linear coupling between soft and hard modes demonstrated for $SrBi_2Ta_2O_9$ [11] and the general concept of "hybrid improper ferroelectricity". [12]

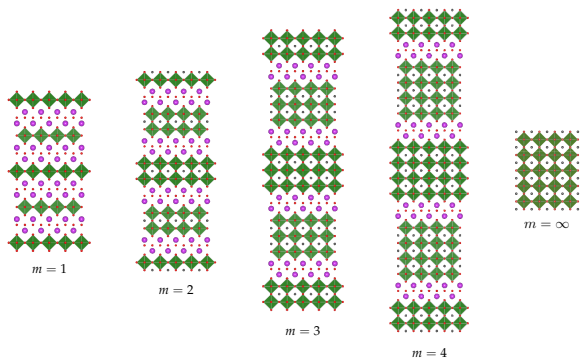

(a) The Aurivillius family of layered-perovskite related materials. m denotes the number of perovskite layers, recovering bulk at ∞.

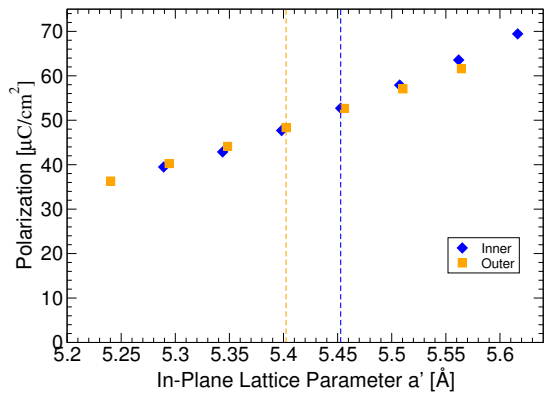

(b) Polarization as a function of bi-axial in-plane strain. "Outer" denotes Fe^{3+}as B-cation of a perovskite next to the (Bi_2O_2) layer, "Inner" denotes Fe^{3+}as B-cation of a perovskite surrounded by perovskites.

Figure 1: The Aurivillius family as robust ferroelectric materials.

References

[1] N. A. Spaldin, S-W. Cheong, R. Ramesh, *Physics Today* **63**, 38 (2010)

[2] C. A-Paz de Araujo, J. D. Cuchiaro, L. D. McMillan, M. C. Scott, and J. F. Scott, *Nature* **374**, 627-629, (1995).

[3] B. H. Park, B. S. Kang, S. D. Bu, T. W. Noh, J. Lee, and W. Jo, *Nature* **401**, 682-684, (1999).

[4] W. Bai, J. Y. Zhu, J. L. Wang, T. Lin, J. Yang, X. J. Meng, X.D. Tang, Z. Q. Zhu, and J. H. Chu, *Journal of Magnetism and Magnetic Materials* **324**, 2265, (2012).

[5] X. Y. Mao, W. Wang, H. Sun, Y. Lu, and X. Chen, *Journal Material Science* **47**, 2960, (2012).

[6] A. Srinivas, S. V. Suryanarayana, G. S. Kumar, and M. Mahesh Kumar, *Journal of Physics: Condensed Matter* **11**, 3335, (1999).

[7] X. W. Dong, K. F. Wang, J. G. Wan, J.S. Zhu, and J.M. Liu, Journal Applied Physics **103**, 094101, (2008).

[8] E. Jartych, T. Pikula, M. Mazurek, A. Lisinska-Czekaj, D. Czekaj, K. Gaska, J. Przewoznik, C. Kapusta, and Z. Surowiec, *Journal of Magnetism and Magnetic Materials* **342**, 27, (2013).

[9] G. Chen, W. Bai, L. Sun, J. Wu, Q. Ren, W. Xu, J. Yang, X. Meng, X. Tang, C. G. Duan, and *et. al*, *Journal Applied Physics* **113**, 034901, (2013).

[10] N. A. Lomanova, V. G. Semenov, V. V. Panchuk, and V. V. Gusarov, *Journal of Alloys and Compounds* **528**, 103, (2012).

[11] J. M. Perez-Mato, M. Aroyo, A. Garcia, P. Blaha, K. Schwarz, J. Schweifer, and K. Parlinski, *Physical Review B* **70**, 214111, (2004).

[12] N. A. Benedek, C. J. Fennie, *Physical Review Letters* **106**, 107204, (2011).

Colossal magnetoelectricity in hexagonal Ni_3TeO_6

Sergey Artyukhin[1], Yoon Seok Oh[1], Jun Jie Yang[2], Vivien Zapf[3], Jae Wook Kim[3], Sang-Wook Cheong[1,2] and David Vanderbilt[1]

[1]*Department of Physics & Astronomy, Rutgers University, Piscataway, NJ 08854, USA*

[2]*Laboratory for Pohang Emergent Materials, Pohang University of Science and Technology, Pohang 790-784, Korea*

[3]*Los Alamos Natl Lab, Natl High Magnet Field Lab, Los Alamos, NM 87545 USA*

Multiferroic and magnetoelectric (ME) materials, with their coexisting magnetic and ferroelectric orders, are of pressing interest for spintronics and information storage technology. Several ways to enhance the magnetoelectric effect were proposed, such as driving the ferroelectric modes to low frequency ("structural softness") by applying strains to thin films [1]. Recent discovery of the colossal magnetoelectric effect at the spin-flop transition in the hexagonal Ni_3TeO_6 offered an alternative approach, in which the responses are enhanced due to the soft magnon mode in the vicinity of the magnetic critical point, cf. Fig. 1. This material, showing the largest known to date ME coefficient, has a peculiar second-order spin-flop transition, separating the antiferromagnetic and canted phases. Heisenberg exchange striction couples magnetic ordering to the pyroelectric polarization, giving rise to the polarization

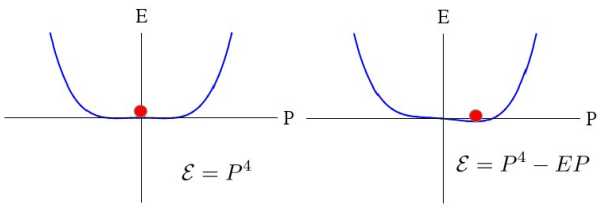

Fig. 1. At the second-order phase transition the flat free energy landscape gives rise to large responses.

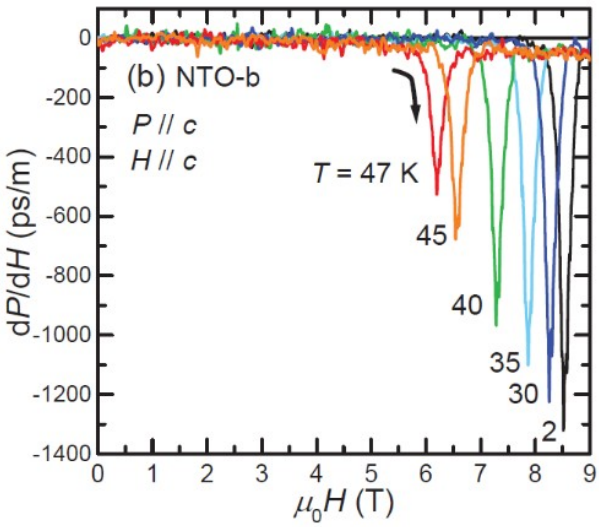

Fig. 2. The experimentally measured linear magnetoelectric coefficient increases as the temperature is decreased, suggesting that the effect is controlled by the quantum critical point.

change across the transition. This enables one to cross the transition boundary by applying magnetic or electric fields, and the linear ME coefficient as large as 1400 ps/m at 2K, to our best knowledge, the largest observed to date [2], cf. Fig. 2. While the phenomenological Landau-type theory describes the essential physics of the ME effect, it does not explain another transition at higher magnetic fields, that was recently discovered. The latter transition at round H=52 T is accompanied by an even larger polarization change, and shows strong dependence on the magnetic field direction, seen in Fig. 4. Using a microscopic Hamiltonian with the parameters determined from DFT calculations, we model the whole phase diagram of this material and obtain the insights into how the competition of exchange interactions and exchange anisotropies gives rise to the rich phase diagram, observed experimentally.

[1] J. C. Wojdel, J. Iniguez, PRL **105**, 037208 (2010).

[2] Y. S. Oh, S. Artyukhin, J. J. Yang, V. Zapf, J. W. Kim, D. Vanderbilt, S.-W. Cheong, Nature Communications **5**, 3201 (2014).

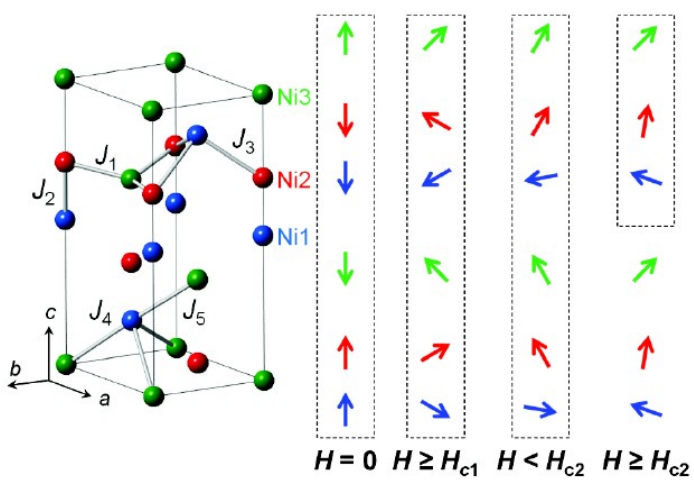

Fig. 3. The nearest-neighbor exchange interactions, included in the model, shown in the hexagonal crystallographic unit cell and various magnetic field-induced spin configurations shown in the rhombohedral magnetic unit cell.

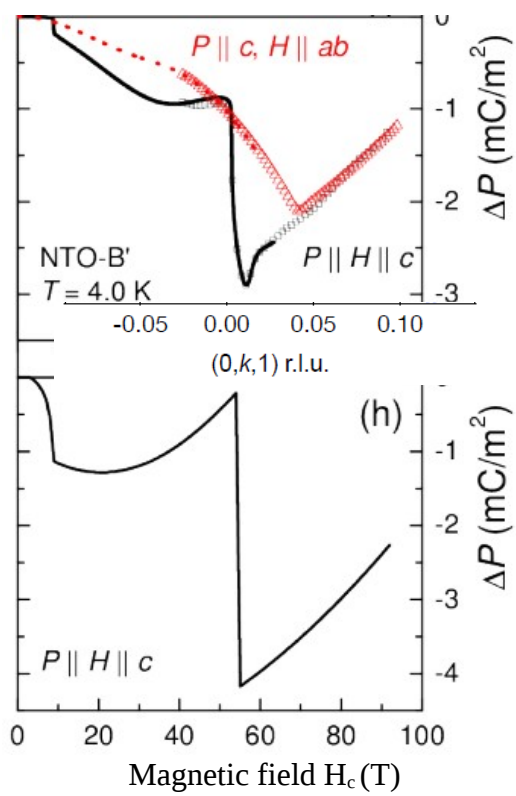

Fig. 4. The polarization dependence on the magnetic field, measured in the experiment (top panel) and calculated from the model with parameters extracted from DFT.

Multiferroicity in Bulk and Thin-Film Hexagonal $LuFeO_3$

Steven Disseler[1], Xuan Luo[2], Yoon Seok Oh[3], Rongwei Hu[3], June Lau[1], Rick Paul[1], Jeffrey W. Lynn[1], Sang-Wook Cheong[2,3], Julie A. Borchers[1], Charles M. Brooks[4], Julia A. Mundy[5], Jarrett A. Moyer[6], D. A. Hillsberry[7], E. L. Thies[7], D. A. Tenne[7], John Heron[4], James D. Clarkson[8], Gregory M. Stiehl[9], Peter Schiffer[6], David A. Muller[5,10], Darrell G. Schlom[4,10],William Ratcliff II[1],

[1]NIST Center for Neutron Research, National Institute of Standards and Technology, Gaithersburg, Maryland 20899, USA
[2]Laboratory for Pohang Emergent Materials, Pohang University of Science and Technology, Pohang 790-784, Korea
[3]Rutgers Center for Emergent Materials and Department of Physics and Astronomy, Rutgers University, Piscataway, New Jersey 08854, USA
[4]Department of Materials Science and Engineering, Cornell University, Ithaca, New York 14853, USA
[5]School of Applied and Engineering Physics, Cornell University, Ithaca, New York 14853, USA
[6]Department of Physics and Frederick Seitz Materials Research Laboratory, University of Illinois at Urbana-Champaign, Urbana, Illinois 61801, USA
[7]Department of Physics, Boise State University, Boise ID 83725
[8]Department of Materials Science and Engineering, University of California, Berkeley, California 94720, USA
[9]Department of Physics, Cornell University, Ithaca, New York 14853, USA
[10]Kavli Institute at Cornell for Nanoscale Science, Ithaca, New York 14853, USA

The hexagonal manganites such as $LuMnO_3$ are prototypical examples of type-I multiferroics, where ferroelectricity stems from a structural distortion at high temperatures (T_{FE} ~ 1000 K) with antiferromagnetic order occurring only at a much lower temperature (T_N ~ 100K). The isostructural hexagonal $LuFeO_3$ is a promising candidate for enhancing many of the magnetic properties of this system, including the ordering temperature, as the isovalent Fe exhibits a larger spin relative to Mn as well as the potential for enhanced super-exchange interactions. Interest in this material has been bolstered by recent first-principles calculations predicting an enhanced ferromagnetic moment parallel to the ferroelectric moment as well as a mechanism for establishing robust magnetoelectric coupling[1]. However, detailed studies of this material have been lacking to date due in large part to the instability of the hexagonal phase of $LuFeO_3$ in bulk, which instead forms in the orthorhombically distorted perovskite structure. In light of this, we have performed an extensive study of this material in two forms: (1) pure hexagonal $LuFeO_3$ thin-films grown by molecular beam epitaxy, and (2) bulk polycrystalline and single crystals stabilized by Mn-substitution on the Fe-site. We use a variety of techniques in to study these samples including magnetometry, neutron scattering, Raman spectroscopy, STEM and PFM. Through these, we find that both films and bulk samples are ferroelectric at room temperature and order magnetically with an enhanced T_N relative to $LuMnO_3$. However, despite recent claims of room temperature magnetic order[2], we find that the maximum intrinsic ordering temperature for hexagonal $LuFeO_3$ is only 150 K. A weak ferromagnetic moment is observed along the *c*-axis of thin-films and bulk samples that vanishes rapidly with increasing Mn concentration, consistent with theoretical predictions. Lastly, we will discuss how our determination of the magnetic phase diagram as a function of temperature and Mn concentration provide insight into microscopic models put forth to explain the various transition and spin-reorientations in this family of compounds.

Acknowledgements Work at Rutgers University was supported by the DOE under Grant No. DE-FG02-07ER46382, and at Cornell University through DMR 1120296, NSF IMR-0417392, and DE-SC0002334.

References

[1] H. Das, A. L. Wysocki, Y. Geng, W. Wu, and C. J. Fennie, *Nat. Commun.* **5**, 2998 (2014).

[2] Wenbin Wang, Jun Zhao, Wenbo Wang, Zheng Gai, Nina Balke, Miaofang Chi, Ho Nyung Lee, Wei Tian, Leyi Zhu, Xuemei Cheng, David J. Keavney, Jieyu Yi, Thomas Z. Ward, Paul C. Snijders, Hans M. Christen, Weida Wu, Jian Shen, and Xiaoshan Xu, Phys. Rev. Lett. **110** 237601 (2013).

Paraelectromagnon in Multiferroic $CaMn_7O_{12}$ and Hybrid Ferroelectric Phase Transition in Multiferroic $Ca_3Mn_2O_7$

S. Kamba,[1] F. Kadlec,[1] V. Goian,[1] C. Kadlec,[1] C. Adamo,[2] H. Zhang,[3] K. Smith,[3] R. Beanland,[3] A.S. Gupta,[4] V. Gopalan,[4] J. Drahokoupil,[1] P. Vaněk,[1] M. Svatuška,[1] H. Seiner,[5] L. Palatinus,[1] M. Klementová,[1] N.A. Benedek,[6] I. Reaney,[7] K. Maca,[8] C.J. Fennie[2] and D.G. Schlom[2,9]

[1] Institute of Physics, Czech Academy of Sciences, Prague, Czech Republic
[2] Cornell University, Ithaca, New York, USA
[3]University of Warwick, Gibbet Hill Road, Coventry, UK
[4]Pennsylvania State University, University Park, Pennsylvania, USA
[5] Institute of Thermomechanics, Czech Academy of Sciences, Prague, Czech Republic
[6]Materials Science and Eng. Program, The University of Texas at Austin Texas, USA
[7]University of Sheffield, Sheffield, UK
[8]Brno University of Technology, Brno, Czech Republic
[9] Kavli Institute at Cornell for Nanoscale Science, Ithaca, New York, USA
e-mail: kamba@fzu.cz

Electromagnons are collective spin excitations occurring in magnetic phases of many magnetoelectric multiferroics. They contribute not only to the magnetic susceptibility but, due to dynamic magnetoelectric coupling, also to the off-diagonal components of the magnetoelectric susceptibility tensor. For that reason electromagnons are frequently considered as electrically active magnons. In the first part of this contribution we will show that electromagnons can persist in a paramagnetic phase, if there are short-range magnetic correlations. In analogy with paramagnons we propose to call such spin excitations *paraelectromagnons*.

We investigated spin and lattice dynamics of $CaMn_7O_{12}$ ceramics using infrared (IR), THz and inelastic neutron scattering (INS) spectroscopies in the temperature range 2 to 590 K, and, at low temperatures, in applied magnetic fields of up to 12 T.[1] Ferroelectric polarization in $CaMn_7O_{12}$, which appears at the antiferromagnetic phase transition, is the highest among all spin-induced ferroelectrics.[2] In the two antiferromagnetic phases below T_{N1}=90 K and T_{N2} = 48 K, several IR-active excitations emerge below 90 cm^{-1}. Their frequencies correspond to the maxima in the magnon density of states obtained by INS. At the magnetic phase transitions, these modes display strong anomalies and, for some of them, a transfer of dielectric strength from the higher-frequency phonons is observed. We propose that these modes are electromagnons. Remarkably, at least one of these modes lying near 50 cm^{-1} remains IR active in the paramagnetic phase; for this reason, we call it a paraelectromagnon. This mode becomes overdamped above 150 K, but it remains in the spectra at least up to 300 K. In accordance with this observation, quasielastic neutron scattering revealed short-range magnetic correlations persisting within temperatures up to 500 K above T_{N1}.

The second part of our contribution concerns our theoretical and experimental studies of $Ca_3Mn_2O_7$. Based on *ab initio* calculations, a new type of ferroelectric phase transition has been proposed in this material.[3] Supposedly, the ferroelectricity would be induced by freezing of two nonpolar phonons from the Brillouin zone boundary. If these modes of X_2^+ and X_3^- symmetries freeze simultaneously, the *I4/mmm* phase transforms to an $A2_1am$ orthorhombic structure; this phase transition would be called hybrid improper ferroelectric. If the modes freeze sequentially, the paraelectric *I4/mmm* phase should transform to an intermediate *Cmcm* or *Cmca* one

(depending on if the X_3^- or the X_2^+ mode freezes first); after freezing of the other order parameter, the ferroelectric *A2₁am* orthorhombic structure would finally appear. The same calculations have shown in $Ca_3Mn_2O_7$ films subjected to a biaxial compressive strain, switching of the polarization by the electric field should cause a 180°-flip of the magnetic moments by reversing the octahedral tilt.[3]

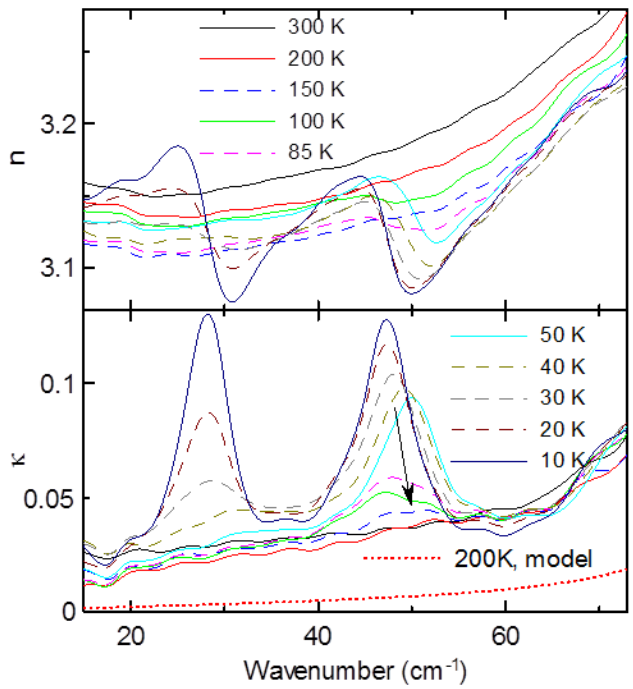

Fig. 1. Real and imaginary parts of the complex refractive index obtained by THz spectroscopy. The red dotted line in $\Bbbk(\omega)$ spectra shows the low-frequency wing from the phonons at frequencies above 90 cm^{-1}, obtained from fits. A heavily damped electromagnons (marked by arrow) is needed for the fit of experimental spectra above T_{N1}.

Thus, it is still an open question whether $Ca_3Mn_2O_7$ undergoes one hybrid or two successive phase transitions. Therefore we performed measurements using x-ray and electron diffraction, second harmonic generation (SHG), heat capacity, resonant ultrasound (RUS), and IR spectroscopy. We investigated bulk ceramics, unstrained and strained thin films. The thin films were deposited using MBE on (110) $YAlO_3$ and (110) $LuAlO_3$ single-crystal substrates.

The room-temperature electron and x-ray diffraction studies revealed the polar *A2₁am* crystal structure, but a rather high conductivity of the ceramics did not allow us to perform measurements of FE hysteresis loops nor a *T*-dependence of the radio-frequency permittivity. X-ray diffraction revealed an abrupt change in the lattice parameter near 670 K and the thermal expansion exhibited an anomaly around 630 K. Near 690 K, high-temperature selective-area electron diffraction and large-angle convergent-beam electron diffraction experiments found a single structural phase transition to the *I4/mcm* structure, but the polar clusters (probably with an *A2₁am* symmetry) persisted up to 900 K in approximately 1 volume percent of the sample. RUS experiment revealed two anomalies near 650 and 800 K. The first one can be explained by the structural phase transition and the second one by the disappearance of polar clusters (Burns temperature). Phonon anomalies seen in the IR spectra of ceramics and thin films supported a single structural change near 700 K. The square root of the SHG signal, which is proportional to the spontaneous polarization, linearly increased on cooling, which is typical for improper ferroelectrics. Thus, our data confirm the scenario of a hybrid ferroelectric phase transition in $Ca_3Mn_2O_7$.

[1] F. Kadlec, V. Goian, C. Kadlec, M. Kempa, P. Vaněk, J. Taylor, S. Rols, J. Prokleška, M. Orlita and S. Kamba, *Phys. Rev*. B **90** 054307 (2014).

[2] R. D. Johnson, L. C. Chapon, D. D. Khalyavin, P. Manuel, P. G. Radaelli and C. Martin, *Phys. Rev. Lett.* **108** (2012).

[3] N. A. Benedek and C. J. Fennie, *Phys. Rev. Lett*. **106** (2011).

Magnetic-induced ferroelectric polarization in charge-ordered $CaMn_7O_{12}$ system

Diomedes Saldana-Greco, Jin Soo Lim, and Andrew M. Rappe

The Makineni Theoretical Laboratories, Department of Chemistry, University of Pennsylvania, Philadelphia, PA 19104-6323, USA

The electronic properties of $CaMn_7O_{12}$ yield to interesting physical phenomena including charge-ordering [1], non-collinear magnetism [2], and improper ferroelectricity [3]. The charge-ordered $CaMn_7O_{12}$ is a complex, distorted quadruple perovskite whose chemical formula could be rewritten in the form of $(AA'_3)(B_4)O_{12}$ as $(CaMn_3^{3+})(Mn_3^{3+}Mn^{4+})O_{12}$ where three Mn^{3+} are on the A-site (Mn1), three Mn^{3+} on the B-site (Mn2), and one Mn^{4+} on the B-site (Mn3). Three parallel c-chains with alternating Mn1 and Mn2 form a Kagome lattice with either Mn3 or Ca at the center of the hexagonal rings. The crystal structure of this material is shown in Fig. 1a and the computed electronic structure shows a ≈0.2 eV band gap for the charge-ordred structure, shown in Fig. 1b. The non-collinear magnetic ground state, shown in Fig. 1c and 1d, consists of spin moments lying on the ab-plane, forming a helical pattern along the c-axis. Antiferromagnetic and ferromagnetic interactions among these c-chains cause spin frustration, leading to 120° alignment of these spin moments. Our DFT+U+J study shows that the Mn3 spins at the center adopt (30°,90°) magnetic configuration with respect to the surrounding (Mn1,Mn2) spins, breaking the inversion symmetry and generating a Berry-phase computed ferroelectric polarization of 2975 $\mu C/m^2$ along the c-axis (Fig. 1d). Our computed ferroelectric polarization is in close agreement with experimental measurements of 2870 $\mu C/m^2$ [3]. When the magnetic helicity of the system is reversed, the ferroelectric polarization flips, reinforcing that it is a magnetic-driven process. This study aims to explore how the electronic and magnetic properties are intertwined to give rise to a multiferroic, charge-ordered state.

This work was supported by the US Office of Naval Research under Grant No. N00014-11-1-0664. Computational support was provided by the High Performance Computing Modernization Office of the US Department of Defense, and the National Energy Research Scientific Computing Center of the US Department of Energy.

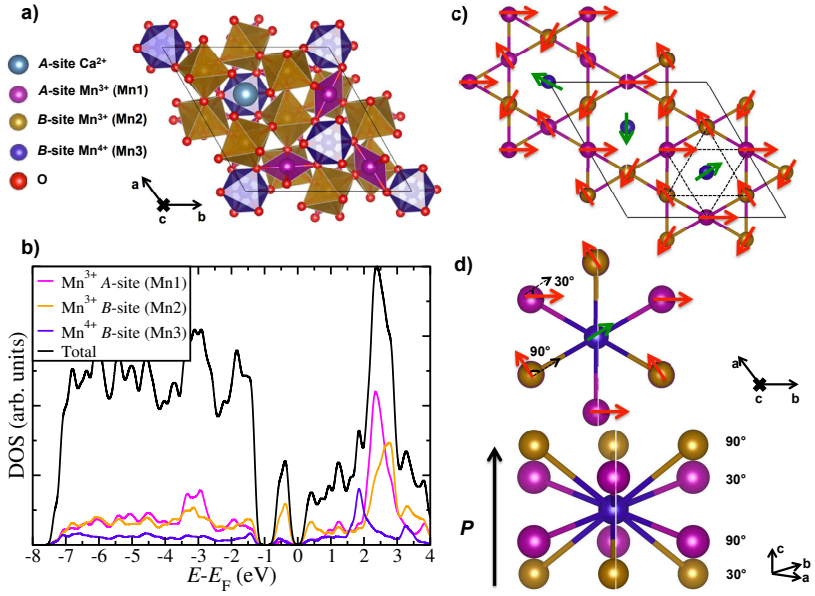

FIG. 1. Structural, electronic and magnetic properties of $CaMn_7O_{12}$. a) The crystal structure of the lowest energy and charge-ordered $CaMn_7O_{12}$ in the rhombohedral $R\bar{3}$ phase. The system has three different Mn atoms, Mn^{3+} on the A-site (Mn1), Mn^{3+} on the B-site (Mn2), and Mn^{4+} on the B-site (Mn3). b) Projected density of states shows a ≈0.2 eV band gap. The charge density is projected to Mn atomic orbitals indicating their differences in bonding character. c) Non-collinear magnetic configuration shows red arrows to represent the spin moments of either Mn1 or Mn2 and green arrows to represent the spin moments of Mn3. The dashed black lines show the Mn1 and Mn2 surrounding the Mn3. d) Top panel shows a top view of the Mn3 spins at the center within the (30°,90°) magnetic configuration with respect to the surrounding (Mn1,Mn2) spins. Bottom panel shows a side view indicating the direction of the ferroelectric polarization.

---

[1] I. O. Troyanchuk, L. S. Lobanovsky, N. V. Kasper, M. Hervieu, A. Maignan, C. Michel, H. Szymczak, and A. Szewczyk, Phys. Rev. B **58**, 14903 (1998).

[2] R. B. P. Bo, D. Wardecki, W. S. B. Dski, I. Sosnowska, and L. Keller, Physica B: Condensed Matter **428**, 27 (2013).

[3] R. D. Johnson, L. C. Chapon, D. D. Khalyavin, P. Manuel, P. G. Radaelli, and C. Martin, Phys. Rev. Lett. **108**, 067201 (2012).

Domains

Spectroscopic signatures of domain walls in hexagonal $ErMnO_3$

Jan Musfeldt
Department of Chemistry, University of Tennessee, Knoxville, Tennessee 37996 USA

We investigated the spectroscopic response of stripe- and vortex-containing $ErMnO_3$ in order to uncover the dynamic signatures of the domain walls. We quantify Born effective charge and polarization differences using the lattice behavior, analyze the local rare earth environment from the *f*-manifold excitations, and reveal how shifts in the charge transfer excitations impact the band gap. These findings are unified with a discussion of hybridization and domain wall density effects.

Mesoscopic stripe and vortex domains in h-$ErMnO_3$ along with the crystal structure and vibrational response. We use the spectral contrast to reveal Born charge and polarization differences.

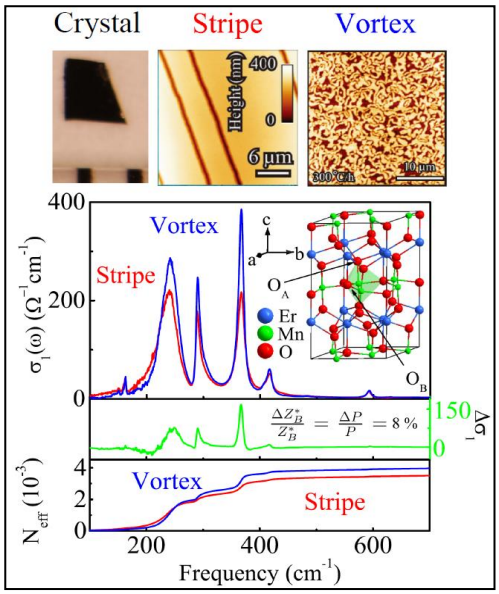

Universal intrinsic origin for ferroelectric domain wall motion

Shi Liu, Ilya Grinberg, and Andrew M. Rappe
The Makineni Theoretical Laboratories, Department of Chemistry, University of Pennsylvania, Philadelphia, PA, 19104-6323

The existence of domain walls in ferroelectric materials can have a profound influence on the properties of ferroelectrics.[1] We explored the dynamics of the 90° domain walls in $PbTiO_3$ (FIG. 1) with molecular dynamics (MD) simulations[2] under a wide range of temperatures and electric fields. We found an intrinsic "creep-depinning" transition for the temperature- and field-dependence of the wall velocity, resulting from the nucleation-and-growth mechanism. MD simulations reveal a diamond-like nucleus exhibiting a diffusive boundary with a gradual polarization change at the domain boundary (FIG 2). By mapping non-180° domain walls to a 180° domain wall, we proposed an analytical model that is able to quantify the dynamics of all types of domain walls in various ferroelectrics, enabling rapid estimation of finite-temperature coercive fields with first-principles inputs. This work offers a unified picture for domain wall motion and an efficient framework for computational optimization of ferroelectrics.

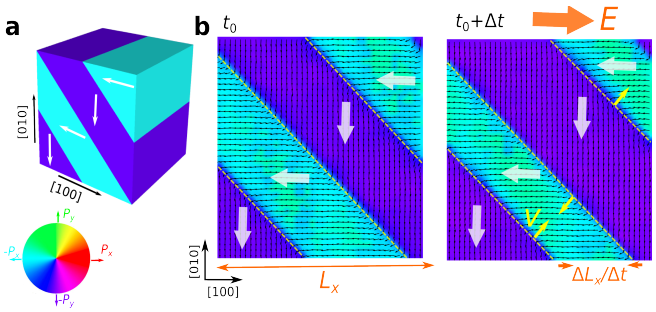

FIG 1. ***Large-scale molecular dynamics simulations of 90° domain wall motions. a****. Schematic diagram of a 40×40×40 supercell with 90° domain walls used in molecular dynamics simulations. The colors of the domains correspond to the polarization wheel shown at the bottom.* ***b****. Simulated domain evolution under [100]-oriented electric field. The electric field is turned on at t_0.*

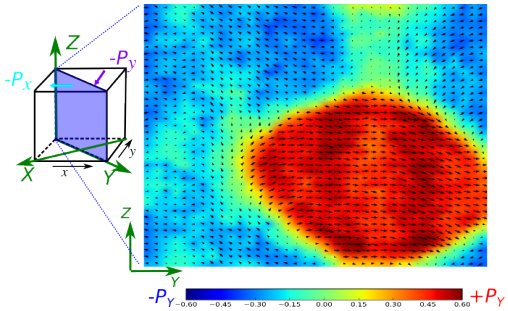

FIG 2. ***Nucleation at the 90° domain wall obtained from MD simulations.*** *The black arrows scale with the local dipole magnitudes of each unit cell at the domain wall. The background of each arrow is colored based on the magnitude of the local dipole.*

Funding: NSF, DOE, ONR

Reference

[1] Seidel, J., J. Phys. Chem. Lett. **3**, 2905 (2012).
[2] S. Liu, I. Grinberg, H. Takenaka, and A. M. Rappe, Phys. Rev. B **88**, 104102 (2013).

Dynamical magnetoelectric effects associated with ferroelectric domain walls

Sergey Prosandeev[1,2], Andrei Malashevich[3], Igor P. Raevski[2], L. Bellaiche[1]

[1]*Institute of nanoscience physics and Physics department of University of Arkansas, Fayetteville 72701, AR2*

[2]*Institute of Physics and Physics Department of Southern*

Federal University, Rostov-na-Donu 344090, Russia

[3]*Department of Applied Physics, Yale University, New Haven,*

Connecticut 06520, USA

It was recently found [1] that a magnetization naturally exists in systems possessing a finite time-derivative of the electric toroidal moment. Interestingly, the ferroelectric domain walls (FDW) separating the nanoscale domains recently observed in ferroelectric ultrathin films [2] can exhibit a non-zero electric toroidal moment. It is thus legitimate to wonder if the *motion* of such FDW can affect their electric toroidal moment and therefore lead to the creation of a magnetization – which would constitute a novel dynamical magnetoelectric effect (ME).

In order to resolve such issue, Molecular dynamics simulations [3] using a first-principles-derived effective Hamiltonian [4] are conducted for lead zirconium titanate (PZT) ultrathin films possessing nanoscale ferroelectric domains and being under GHz electric field. As shown in Fig. 1, pulses of magnetization are indeed predicted in this system, when sudden changes of morphology of these nanodomains occur.

A simple equation relating the magnetization and product between the electrical polarization and its time derivative is further derived from a simple model (via the relation between the magnetization and time derivative of the electrical toroidal moment). This equation explains our numerical findings, as well as ME effects that have been observed 30 years ago in moving ferroelectric domain walls/phase boundaries in ferroelectric $BaTiO_3$ and $Gd_2(MoO_4)_3$ thin films [5-7].

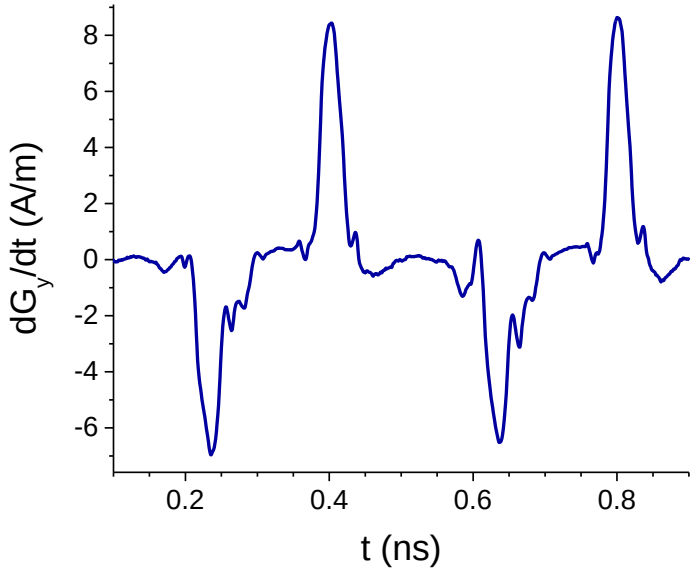

Figure 1. Predicted Time-dependency of the time derivative of the electric toroidal moment in the studied PZT film being under a GHZ electric field.

This work is financially supported by ONR Grant N00014-12-1-1034. I.P.R. appreciates Grant 14-02-90438 Ucr of the Russian Foundation for Basic Research. Some computations were also made possible thanks to the MRI grant 0722625, MRI-R2 grant 0959124, and CI-TRAIN grant 0918970 from NSF.

References:

1. S. Prosandeev, A. Malashevich, Z. Gui, L. Louis, R. Walter, I. Souza, and L. Bellaiche, Phys. Rev. B **87**, 195111 (2013).
2. D. D. Fong *et al*, Science **304**, 1650 (2004).
3. I. Ponomareva, L. Bellaiche, T. Ostapchuk, J. Hlinka and J. Petzelt, Phys. Rev. B **77**, 012102 (2008).
4. L. Bellaiche, A. García, and D. Vanderbilt, Phys. Rev. Lett. **84**, 5427 (2000); Ferroelectrics **266**, 41 (2002).
5. S. A. Flerova and O. E. Bochkov, JETP Lett. **33**, 34 (1981).
6. S. A. Flerova and O. E. Bochkov, Soviet Phys. Cryst. **27**, 122 (1982).
7. S. A. Popov, N. A. Tikhomirova, and S. A Flerova, Soviet Phys. Cryst. **30**, 354 (1985).

PFM-tip induced 90° switching in $Pb(Zr_{0.2}Ti_{0.8})O_3$ thin film: Phase-field modeling

Zijian Hong[1,*], Jason Britson[1], Jia-Mian Hu[1], Long-Qing Chen[1]

[1] *Department of Materials Science and Engineering, The Pennsylvania State University, University Park, Pennsylvania 16802, USA.*

Ferroelectric thin films have been extensively studied in the past few decades due to their multifunctionality and applications in nonvolatile dynamic random access memory, microelectromechanical systems, microelectronic and sensing applications. Among them, $Pb(Zr_xTi_{1-x})O_3$ **(**PZT) thin films are perhaps the most well studied systems due to their large piezoelectric and pyroelectric responses. Under external stimuli, the bending or moving of 90° domain walls, across which the polarization directions change by 90°, will give rise to extra "extrinsic" contributions to the local displacements, thus to the electromechanical responses.

Piezoresponse Force Microscopy (PFM) has emerged as a powerful tool in domain imaging, domain patterning, domain dynamics and domain switching spectroscopy. Many attempts have been made to visualize and even artificially control the prototype ferroelectric domains with PFM. In general, an applied voltage is applied through a conductive tip with the piezoelectric responses of the surface detected by the vibration of a PFM cantilever. Thus, images of ferroelectric domains can be obtained. Moreover, by applying a DC voltage through the tip, the local polarization can be switched at the nanoscale, i.e., "writing" of a ferroelectric domain.

Previously, Chen *et al.* showed in experiments that the 180° switching could be stabilized by the existence of newly-formed surrounding *a*-domains which form to release elastic energy

during electric loading. Meanwhile, both experiments and theoretical analysis indicate that the newly-formed less mobile 90° domain wall cannot be fully switched back by a reverse electric field, which could lead to the so called “fatigue behavior”. So in both senses, understanding the dynamics of 90° switching during the local 180° switching is of fundamental importance to the future applications of the ferroelectric /ferroelastic thin films.

Herein, we extend the phase-field model with a semi-implicit Fourier transform scheme to investigate the ferroelectric switching in ferroelectric/ ferroelastic PZT epitaxial thin films under applied bias through PFM tip. 90° switching during local 180° switching is observed, in good agreement with experimental observations. The coherency strain and applied bias effects will be discussed. Different switching patterns are observed under different strain and applied bias conditions. With decreasing magnitude of compressive strain, higher ratios of *a*-domains are favored which lowers the voltage bias for 90° switching. Under low to medium bias, 90° switching is favored due to a huge release of elastic energy, while for high applied bias 180° switching dominates with a large electric energy decrease.

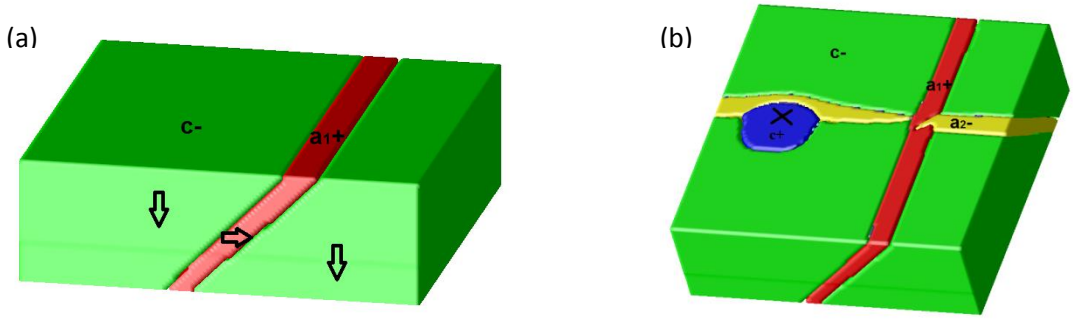

Fig 1(a) Initial *a*/*c* domain configuration, arrows indicate the polarization direction. (b) Equilibrium domain configurations with applied bias of -2.2V at the location indicated by black cross, showing the 90° switching along with the local 180° switching.

Conductance and Electrochemistry of Charged Domain Walls in Lead Zirconate Titanate

Petro Maksymovych[1], Ye Cao[1], Rama Vasudevan[1], Gabriel Vellarde[2], Simon Kelly[1], Anna Morozovska[3], Lane W. Martin[2], Pu Yu[4], Ramamoorthy Ramesh[4], Sergei V. Kalinin[1]

[1]Center for Nanophase Materials Sciences, Oak Ridge National Laboratory, Oak Ridge, TN, 37831
[2]Department of Materials Science and Engineering, University of Illinois Urbana-Champaign, Urbana, IL 61801
[3]Institute of Semiconductor Physics, National Academy of Science of Ukraine, Kyiv, Ukraine
[4]Department of Materials Science and Engineering, University of California Berkeley, Berkeley, CA 94720

The discovery of conducting domain walls in $BiFeO_3$ in early 2008 ignited the effort to understand conduction phenomena in ferroelectric films and their coupling to the ferroic order parameters. Despite numerous cases where conducting domain walls has subsequently been observed, the basic phenomena underlying these mechanisms are still elusive. Most interpretations lean toward modification of the Schottky barrier at the film's interfaces by electric field and/or vacancy accumulation due to domain walls. Our effort in this direction has brought out the importance of charged domain walls, wherein the conductivity is mediated by the compensating mechanism of polarization charges at the domain wall. In this way, the domain wall can genuinely modify electronic conduction through the bulk of the ferroelectric film, rather than merely its interfaces. And only in such geometries one expects to achieve substantial electronic conductivity, far in excess of limited picoSiemens range that is frequently observed. Conceptually dynamic polarization distortions are very different from electroresistance effects in complex oxides, calling for new advances in both theory and experiments.

The involvement of charge domain walls or domain wall junctions in conduction phenomena has been motivated by three observations: (1) dynamic and hysteretic conductivity of domain walls in bismuth ferrite [1]; (2) anisotropic conductance of domain walls in $BiFeO_3$, as a function of their orientation to the in-plane polarization vector [2]; (3) an insulator-metal transition in lead zirconate [3], which is observed any time a ferroelectric nanodomain (with the radius of < 10 nm) is created by localized electric fields. Here electronic conductance locally increases by 4-6 orders of magnitude – one of the largest effects reported so far.

In the case of lead zirconate titanate, we recently compared a variety of compositions of epitaxial PZT films, intentionally chosen with different growth conditions. The variability primarily manifested in the overall magnitude of local current, which ranged by orders of magnitude between different films. However, even for the most insulating lead zirconate films, ferroelectric nanodomains exhibited small thermal activation barriers of only ~ 50 meV. In contrast, leakage through the bulk would occur with barriers as high as 0.9 eV. Based on the I-V characteristics, the mechanism most compatible with these results involves tunneling into a highly conducting state in the bulk of the film, therefore implying a heavily doped or metallic state associated with tilted and charged domain boundaries of the nanodomains.

The experiments with scanning probe microscopy provide only indirect evidence that the conductance is controlled by charged walls. We turned to modeling of the morphology of ferroelectric nanodomains and the respective charge compensating mechanisms via solutions of Landau-Ginzburg-Devonshire (LGD) theory for ferroelectric semiconductors with analytical and phase-field methods. Analytical calculations in a reduced 1D geometry predicted up to 3 orders higher local density of compensating charges at tilted domain walls compared to background density

due to ionized dopants and intrinsic carriers, depending on the domain wall tilt [3]. At the same time, both holes and electrons can be accumulated, depending on the tilting direction relative to the polar axis. These calculation imply that a charged domain wall in a ferroelectric semiconductor acts as a heavily doped n- or p-channel, and a metal-insulator transition can occur *within* a domain wall itself. Phase-field modeling extended these calculations onto more realistic 3D geometry. The simulations clearly indicate that the [00-1] domain is nucleated under the tip, continues to grow in cone-shape (Fig. 1a), and forms positively charged head-to-head tilted domain walls (Fig. 1b) with wall segregated compensating electrons. Under certain bias condition, the nucleus and tilted domain walls are stabilized with electronic screening. Experiments to test some of the detailed results are currently on-going [4].

Finally, we will discuss the possibility of electrochemical effects caused by local ferroelectric switching. Specifically, we have explored the regime of few hundred thousand switching cycles, finding significant changes in local topography and conductivity (Fig. 1c,d). LGD simulations reveal that even with efficient compensation, charged domain walls still develop large local electric fields due to finite Debye screening length. Presumably these fields are responsible for creation/and or motion of charged vacancies inside the material. Altogether these studies pave way to better understanding of coupled transport phenomena in ferroelectric films and novel approaches to control ferroelectric switching toward desired properties.

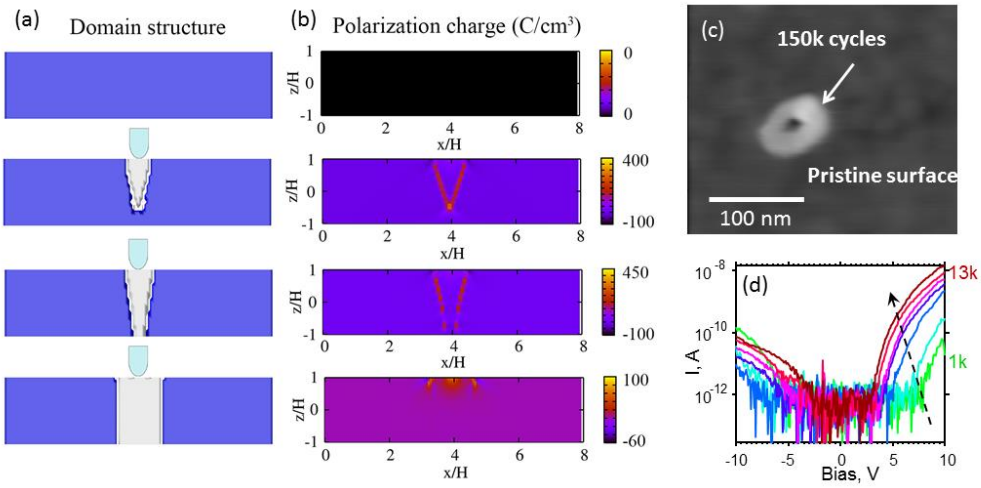

Figure 1. Phase-field simulation of 180° domain switching in PZT (a) domain switching; (b) polarization charge evolution showing tilted domain walls under certain conditions; (c) Surface topography change following 150 thousand consecutive local switching cycles; (d) Local conductance progressively increases with repeated switching.

Microscopy experiments were carried out at the Center for Nanophase Materials Sciences, Oak Ridge National Laboratory. Research supported in part by the Center for Nanophase Materials Sciences, sponsored at Oak Ridge National Laboratory by the Scientific User Facilities Division, Office of Basic Energy Sciences, US Department of Energy. Research supported in part by US Department of Energy, Basic Energy Sciences, Materials Sciences and Engineering Division.

[1] Maksymovych et al., Nano Lett. (2011), 11, 1906; [2] Vasudevan et al., Nano Lett. (2012), 12, 5524; [3] Maksymovych et al., Nano Lett. (2012) 12, 209. [4] Ye et al., to be published.

Reversible switching of in-plane polarized ferroelectric domains in BaTiO3(001) with very low energy electrons

N. Barrett[1], J.E. Rault[2], T.O. Mentes[1], A. Locatelli[2]

[1]CEA, DSM/IRAMIS/SPEC, F-91191 Gif-sur-Yvette Cedex, France.
[2]Synchrotron-SOLEIL, BP 48, Saint-Aubin, F-91192 Gif sur Yvette CEDEX, France
[2]Elettra-Sincrotrone Trieste S.C.p.A.. Strada Statale 14 - km 163, 5 in AREA Science Park 34149 Basovizza, Trieste, Italy,

Polarization switching by an applied field depends on the initial domain ordering, defect concentration, electrical boundary conditions and charge screening. In Merz's original theory of domain formation and switching, the application of an electric field gives rise to a transient current due to displacement of the polarization charge[1]. Therefore the injection of free charge might also switch the polarization. Electron beams can lead to specimen charging, setting up a potential difference and generating an internal electric field large enough to switch polarization[2] However, high energy e-beam switching is generally irreversible because of radiation damage.

We use a low energy electron microscope (LEEM) to simultaneously switch and observe in-plane polarized FE domains of a $BaTiO_3$ single crystal[3]. At very low electron kinetic energy (KE), called mirror electron microscopy (MEM), electrons are reflected without penetrating the sample surface[4]. At higher KE, the electrons penetrate the surface. In between, the reflectivity gives measure of the local work function or surface potential[5].

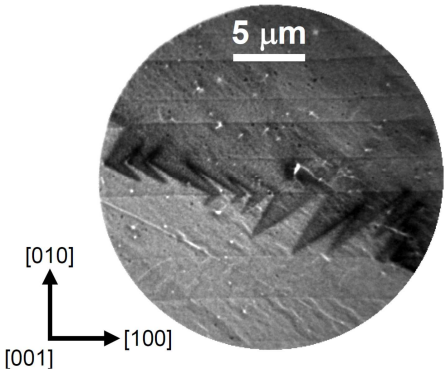

Figure 1 Electron image of the surface 1.3 seconds after the start voltage has been switched from 1 to 5 eV.

Figure 1 shows the electron image of the surface during switching in a 30 μm field of view (FoV). Nine domain boundaries (thin horizontal lines) are visible. At t = 0 the SV is increased from 1 to 5 eV and the polarization switches. The switching proceeds in a zig-zag around the direction [0-10]. It starts from discrete points at an upper domain wall and propagates as rather broad needles until reaching the opposite domain wall. Then, the needles expand until the polarization is switched in the entire domain. In a fourth step, switching then continues in the next domain but at an angle of 90° with respect to the previous one and so on, until the polarization in the entire FoV has been switched.

Figure 2c shows the normalized intensity profile across the domain wall before switching. The profile obtained across each domain wall is the same. The intensity asymmetry results from the electrons being deflected by the electric field due to the domain wall dipole along [0-10]. Figure 2d shows the intensity profiles across the same wall after polarization switching. The intensity asymmetry across the domain

wall is reversed, showing that the dipole is now along [010]. The profiles across successive domain walls have the same shape, showing that the overall macroscopic polarization is indeed along [010] before and [0-10] after switching.

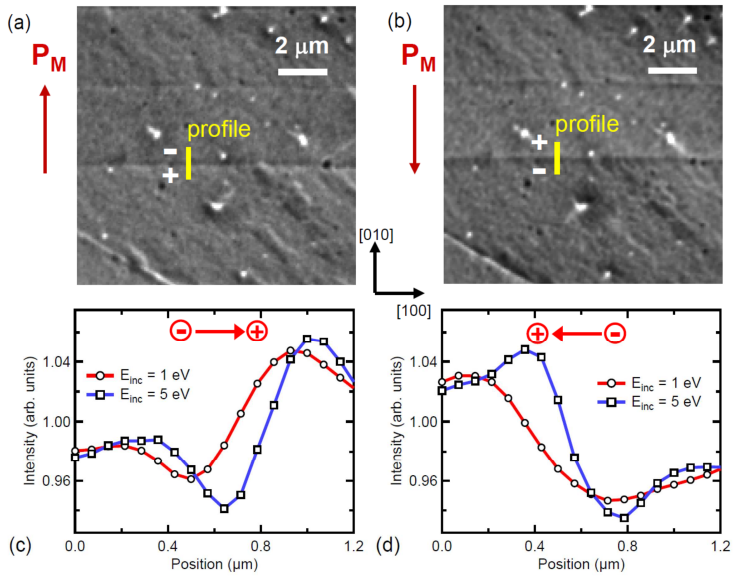

Figure 2 LEEM images of sample surface before (a) and after (b) switching, the field of view is 30 µm. Intensity profiles extracted from LEEM images acquired using 1 eV (round, red symbols) and 5 eV (square, black symbols) along [0-10] across a domain wall before (c) and after (d) switching. The dipole across the wall is shown by the plus/minus signs.

The switched state is therefore a steady state resulting from the balance between the equilibrium domain pattern and the injection of negative charge. The current density required to switch the in-plane polarization is 0.26 mA/cm^2. This scales to 1 pA for a 10 µm long domain of the same width (3 µm) as in our experiment. Tuning the electron energy allows to increase the switching speed by orders of magnitude. Low energy electrons switch the polarization without the collateral radiation damage which occurs with high energy electrons. Switching by charge injection adds a new dimension to the multifunctionality of ferroic oxides.

Acknowledgements J.E.R. was funded by CEA and by the Labex PALM APTCOM project. We thank ELETTRA (Trieste) for provision of synchrotron radiation facilities. We gratefully acknowledge funding from the Agence National de la Recherche project ANR-12-IS04-0001-01 CHEM-SWITCH.

References

[1]W.J. Merz, *Phys. Rev.* **95** (1954).
[2]D.B. Li, D.R. Strachan, J.H. Ferris and D.A. Bonnell, *J. Mat. Res.* **21**, 935–940 (2006).
[3]J. E. Rault, T. O. Menteş, A. Locatelli, N. Barrett *Scientific Reports* **4**, 6792 (2014)
[4]N. Barrett et al., *J. Appl. Phys.* **113**, 187217 (2013).
[5]J. Rault et al. *Phys. Rev. Lett.* **109**, 267601 (2012).

Interfaces / Superlattices / Thin Films

Investigations on Ferroelectric/Multiferroic tunnel junctions for multifunctional applications

D. Barrionuevo[1], Le Zhang[2], N. Ortega[1], A. Sokolov[2,3], and R. S. Katiyar[1]

[1] Department of Physics and Institute of Functional Nanomaterials, University of Puerto Rico, San Juan, Puerto Rico 00931-3343 USA.
[2] Department of Physics and Astronomy, University of Nebraska-Lincoln, Lincoln, Nebraska 68588-0299 USA
[3] Nebraska Center for Materials and Nanoscience, University of Nebraska-Lincoln, Lincoln, Nebraska 68588-0298 USA

A ferroelectric tunnel junction (FTJs) consists of a few unit cells of a ferroelectric material sandwiched between two electrodes where interplay of ferroelectricity and electron tunneling occurs[1]. This is possible since ferroelectricity can be retained in perovskite oxides films with thickness of the order of a few nanometers[2-3]. FTJ may exhibit a tunneling electroresistance (TER) effect associated with the polarization switching of the ferroelectric barrier layer, leading to a change in resistance of the junction[4]. FTJ devices have the potential to function as nanometer scale non-volatile memory devices, operating with low power consumption. We demonstrate room temperature polar switching and tunneling in $PbZr_{0.52}Ti_{0.48}O_3$ (PZT) ultra-thin films of thickness 3-7 nm, sandwiched between platinum metal and ferromagnetic $La_{0.67}Sr_{0.33}MnO_3$ (LSMO) layers, which also shows magnetic field dependent tunnel current switching in Pt/$PbZr_{0.52}Ti_{0.48}O_3$/$La_{0.67}Sr_{0.33}MnO_3$ heterostructures. The oxide PZT/LSMO heterostructure films were synthesized on $(LaAlO_3)_{0.3}(Sr_2AlTaO_6)_{0.7}$ (LSAT) using a pulsed laser deposition (PLD) technique. The epitaxial nature, surface quality and ferroelectric switching of heterostructured films were examined with the help of X-ray diffraction (XRD) patterns, atomic force microscopy (AFM), and piezoresponse force microscopy (PFM), respectively. The capacitance versus voltage graphs show butterfly loop above the coercive field (> ±3 V) of PZT for small probe area (~16 μm^2). The effect of ferroelectric switching was observed in current density versus voltage curves with a large variation in high-resistance/low-resistance (HRS/LRS) ratio (2:1 to 100:1), however, these effects were more prominent in the presence of in-plane external magnetic field.

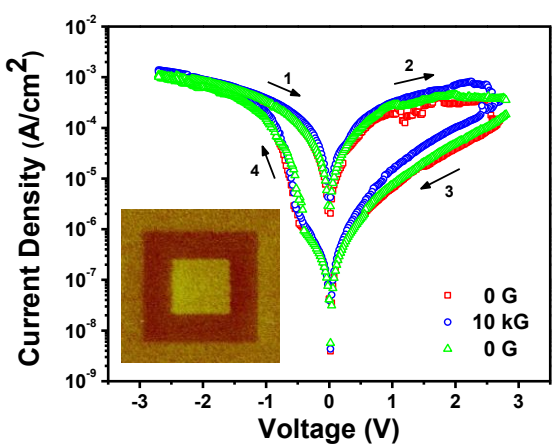

Figure 1 Current density versus voltage curve of the sample 7 nm showing the effect of applied 10 kG magnetic field. Inside picture on left down show the switching polarizations.

We show the effect of magnetic field along the in-plane direction; it was observed when 10 kG was applied to the junction during current versus voltage measurements, the resistance is decreased only in the positive voltage range (controlled by the LSMO electrode), while no significant change was observed in the negative voltage range (controlled by the Pt electrode). This is reasonable considering that LSMO becomes more metallic in its ferromagnetic state. For this junction the resistance switching between LRS and HRS became sharper, and the HRS/LRS ratio values at zero bias was between ~60 (at 0 G) and 110 (at 10 kG); the maximum value of HRS/LRS ratio was obtained in presence of a magnetic field (see Figure 1). The conductance is fitted with Brinkman's model, and the parabolic conductance upon bias voltage implies electron tunneling governs the transport[5].

Another interesting topic is multiferroic tunnel junction (MFTJ) that consists of metal or ferromagnetic electrodes separated by a ferroelectric (FE) or single-phase multiferroics barrier. MFTJ device displays four non-volatile resistance states due to the coexistence of tunneling magnetoresistance and tunneling electroresistance effects, which makes them very promising for the application in memory devices. $Pb(Zr_{0.53}Ti_{0.47})_{0.60}(Fe_{0.5}Ta_{0.5})_{0.40}O_3$ (PTZFT) is a single-phase multiferroic material, exhibiting remanent polarization of ~14 μC/cm^2 in bulk, remanent magnetization ~0.024 emu/g and, low loss ~ 0.06-10 kHz and a magnetoelectric coupling coefficients ~ 1x10^{-7} s/m at room temperature[6-7]. In order to study thickness effect on electrical and magnetic properties from thicker to ultrathin films, we have grown films with thicknesses from 4 to 80 nm of PZTFT on LSMO/$(LaAlO_3)_{0.3}(Sr_2AlTaO_6)_{0.7}$ (LSMO/LSAT) (001) substrate deposited by pulsed laser deposition technique. The X-ray diffraction patterns of the heterostructures show only (00*l*) reflections corresponding to the LSAT substrate, PZTFT and LSMO layers. The Atomic force microscopy of PZTFT/LSMO/LSAT heterostructures showed that the average surface roughness decreases from 1.5 to 0.4 nm for PZTFT films with thickness from 80 to 4 nm respectively. Well saturated ferroelectric loops were observed for PZTFT films with a remanent polarization of 60, 35 and 10 μC/cm^2 for films with thicknesses of 80, 50 and 20 nm respectively (see Figure 2). An enhanced saturated magnetization (M_s) was observed with increased of PZTFT layer thickness in PZTFT/LSMO structures. The average M_s values for PZTFT/LSMO heterostructures were 65, 50, and 40 emu/cm^3 for 80, 50, and 20 nm respectively, at 300 K.

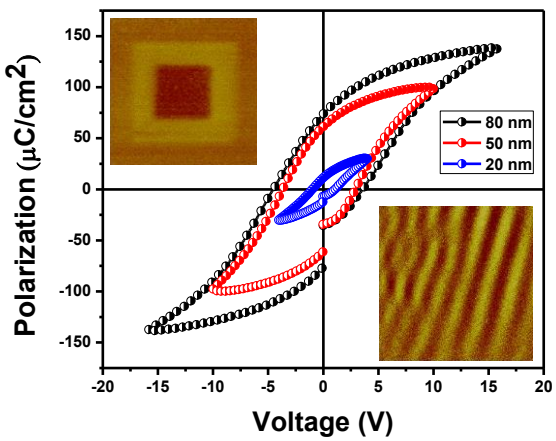

Figure 2 Well saturated ferroelectric loops were observed for PZTFT films. Inside pictures on left up and on right down show the ferroelectric and magnetic nature of PZTFT-7 nm.

Enhancement in magnetization with increase in PZTFT thickness may be due to the interface effect between PZTFT/LSMO layers. Piezo force microscopy measurements for 4, 5, and 7 nm ultrathin PZTFT films showed a clear and reversible out-of-plane phase contrast above ± 4 V, which indicates the ferroelectric character of ultra-thin films. Magnetic force microscopy shows a clear magnetic domain patterns. Stripe domains were present, typical of systems with perpendicular magnetic anisotropy. The effect of PZTFT film thickness on temperature dependent dielectric properties will be discussed.

Acknowledgements This work was supported by the DOE grant (No. DE-FGD2-08ER46526). Acknowledgement is also due to NSF Grant EPS-01002410 for providing fellowships to D. Barrionuevo.

References

[1] L. Esaki, R. B. Laibowitz, P. J. Stiles, *IBM Tech. Discl. Bull*. **1971**, 13, 2161

[2] E. Y. Tsymbal, H. Kohlstedt, *Science* **2006**, 313, 181.

[3] D. Barrionuevo, N. Ortega, A. Kumar, R. Chatterjee, J. F. Scott, R. S. Katiyar, *J. Appl. Phys*. **2013**, 114, 234103.

[4] A. Gruverman, D. Wu, H. Lu, Y. Wang, H. W. Jang, C. M. Folkman, M. Ye. Zhuravlev, D. Felker, C. B. Etom, E. Y. Tsymbal, *Nano Lett.* **2009**, 9, 3539.

[5] D. Barrionuevo, Le Zhang, N. Ortega, A. Sokolov, A. Kumar, Pankaj Misra, J. F. Scott, R. S. Katiyar. *Nanotechnology.* **25**, 495203 (2014).

[6] D.M. Evans, A. Schilling, Ashok Kumar, D. Sanchez, N. Ortega, M. Arredondo, R.S. Katiyar,J.M. Gregg & J.F. Scott *Nat. Commun.* **4**, 1534 (2013).

[7] Dilsom A. Sanchez, N. Ortega, A. Kumar, G. Sreenivasulu**,** Ram S. Katiyar, J. F. Scott, Donald M. Evans, Miryam Arredondo-Arechavala, A. Schilling, and J. M. Gregg. *J. Appl. Phys.* (2013).

Ferroelectric Domains Dynamics in Memristive Tunnel Junctions based on Super-Tetragonal $BiFeO_3$

V. Garcia[1], S. Boyn[1], S. Fusil[1], M. Marinova[2], H. Yamada[1], A. Chanthbouala[1], S. Collin[1], C. Deranlot[1], C. Carrétéro[1], A. Gloter[2], J. Grollier[1], M. Bibes[1], A. Barthélémy[1]

[1]Unité Mixte de Physique CNRS/Thales, 1 Av. A. Fresnel, 91767 Palaiseau, France
[2]Laboratoire de Physique des Solides, Université Paris Sud XI, 91405 Orsay, France

Ferroelectric tunnel junctions (FTJs) [1] consist of an ultrathin ferroelectric film sandwiched between two electrodes. The information is encoded through the non-volatile ferroelectric polarization than can be switched with an electric field. The tunneling current is influenced by the ferroelectric polarization direction, enabling a simple non-destructive readout of the polarization state [2].

Following our previous work with $BaTiO_3$-based FTJs [3, 4], we recently focused our attention to FTJs based on super-tetragonal $BiFeO_3$ (T-BFO), a material with a very large polarization. We will present results from scanning transmission electron microscopy which reveal that these ultrathin T-BFO films have a large tetragonality and a native ferroelectric polarization pointing toward the bottom electrode of $(Ca,Ce)MnO_3$ [5]. FTJs based on ultrathin T-BFO films show fast, stable and repeatable switching with very high resistance ratios of up to four orders of magnitude [6, 7]. Moreover, quasi-continuous resistance variations can be achieved depending on the amplitude and time of voltage excitations. Thus, FTJs behave as memristors [4] that could be implemented as nano-synapses in neuromorphic architectures. Combined piezoresponse force microscopy (PFM) and electrical measurements give a clear correlation between ferroelectric domain configurations and multiple resistance states. As a consequence, the memristive response of the FTJ provides insights into the switching dynamics of ferroelectric domains in response to trains of nanosecond pulses. We will show recent experiments on cumulative pulses dynamics using both transport measurements and PFM imaging, with possible interpretations considering nucleation of ferroelectric domains with limited propagation as well as Monte Carlo simulations [8].

(We acknowledge financial support from the European Research Council (ERC Advanced Grant FEMMES, No. 267579))

References

[1] V. Garcia & M. Bibes, *Nature Comm.* **5**, 4289 (2014)
[2] V. Garcia et al., *Nature* **460**, 81-84 (2009); P. Maksymovych et al., *Science* **324**, 1421–1425 (2009); A. Gruverman et al., *Nano Lett.* **9**, 3539–3543 (2009)
[3] A. Chanthbouala, V. Garcia et al., *Nature Nanotech.* **7**, 101-104 (2012)
[4] A. Chanthbouala, V. Garcia et al., *Nature Mater.* **11**, 860-864 (2012)
[5] M. Marinova, V. Garcia et al. (in preparation)
[6] H. Yamada, V. Garcia et al., *ACS Nano* **7**, 5385-5390 (2013)
[7] S. Boyn, V. Garcia et al., *Appl. Phys. Lett.* **104**, 052909 (2014)
[8] S. Boyn, V. Garcia et al. (in preparation)

Room-temperature multiferroic superlattices

L. Bellaiche[1], Xiang Ming Chen[2], Jorge Íñiguez[3],
Wei Ren[4], Yurong Yang[1] and Hongjian Zhao[1,2]

[1]*Physics Department & Institute for Nanoscience and Engineering, University of Arkansas, Fayetteville, Arkansas 72701, USA*
[2]*Laboratory of Dielectric Materials, Department of Materials Science and Engineering, Zhejiang University, Hangzhou 310027, China*
[3]*Institut de Ciència de Materials de Barcelona (ICMAB-CSIC), Campus UAB, 08193 Bellaterra, Spain*
[4]*Department of Physics, Shanghai University, 99 Shangda Road, Shanghai 200444, China*

Discovering multiferroic materials having an electrical polarization and being strongly ferromagnetic near room-temperature is a long-time-sought quest, due to the promise of novel spintronic devices. Strikingly, it appears that these two desired features are rather difficult to simultaneously co-exist. Using first-principle and Monte Carlo calculations, we demonstrate that two kinds of multiferroic superlattices do possess these two desired features [1,2].

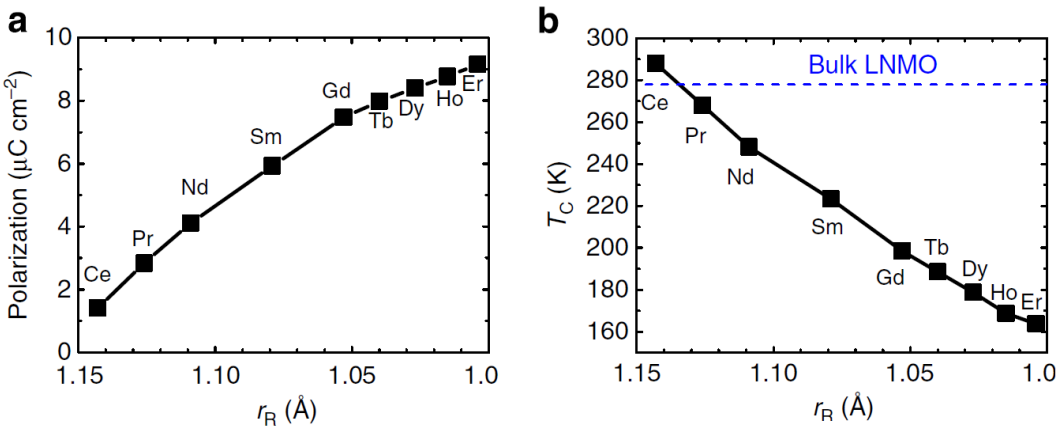

Figure 1. (a) Predicted electrical polarization and (b) magnetic Curie temperature of La_2NiMnO_6/ R_2NiMnO_6 superlattice as a function of the rare-earth ionic radius.

The first kind of superlattice is made by La_2NiMnO_6/R_2NiMnO_6, where R is a rare-earth ion. As shown in Fig. 1a, its electrical polarization increases when decreasing the rare-earth ionic radius. For instance, this polarization is about 9.2 μC/cm^2 at small temperature when R=Er (which is the rare-earth ion having the largest ionic radius). The origin of this polarization is the novel energy term $-K\omega_R\omega_M u$, proposed in Ref. [3], where K is a constant, ω_R and ω_M characterize the in-plane antiphase and out-of-plane in-phase tiltings, respectively, and u is the displacement of the La or R ions with respect to their ideal positions. In both La_2NiMnO_6 and R_2NiMnO_6 bulks, the u of any two neighboring LaO or RO layers cancel each other, therefore making the whole polarization vanishing. On the other hand, in the La_2NiMnO_6/R_2NiMnO_6 superlattices, the u of neighboring LaO and RO layers, while still opposite in direction, are different in magnitude (because their K parameters are different). As a result, the polarization is finite in these superlattices, which naturally explains the so-called hybrid improper ferroelectricity [4-6]. Regarding the magnetic order of these superlattices, the ground state is ferromagnetic with a magnetization being around 2.4 μ_B per 5 atoms (since both La_2NiMnO_6 and R_2NiMnO_6 bulks are

ferromagnetic). As shown in Fig. 1b, the La_2NiMnO_6/Ce_2NiMnO_6 superlattice exhibits a magnetic Curie temperature of 290K, that is very close to room temperature [1], and this magnetic Curie temperature decreases when increasing the rare-earth ionic radius.

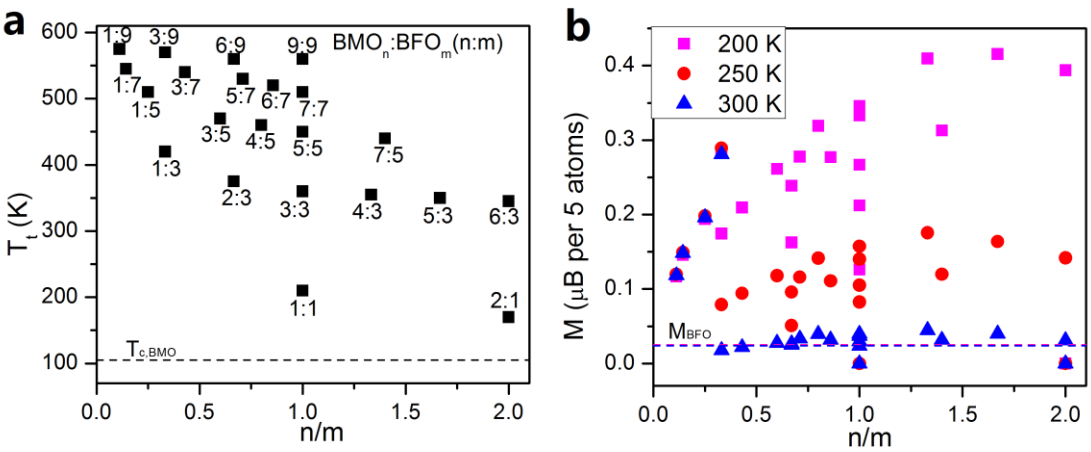

Figure 2. (a): Computed magnetic ordering temperatures for different superlattices studied by Monte Carlo simulations. The results are ordered according to the ratio of *n/m* for each $(BMO)_n/(BFO)_m$ superlattice. (b) Computed magnetization at three different temperatures for these superlattices. The horizontal dashed lines in Panels (a) and (b) show the Curie temperature of pure BMO and the bulk Magnetization of BFO thin film, respectively, for comparison.

The second discovered type of multiferroic materials possessing a large polarization and a strong ferromagnetic order at room-temperature is made of superlattices combining a high Neel temperature anti-ferromagnet and a lower Curie temperature ferromagnet insulator, e.g., $BiMnO_3/BiFeO_3$ (BMO/BFO) superlattices. Indeed, our first-principle calculations show that BMO_n/BFO_m can have an electrical polarization as large as 90 $\mu C/cm^2$ (similar to $BiFeO_3$ bulk) and are also ferromagnetic. The magnetic properties of these superlattices are strongly dependent on the thickness of BMO and BFO (*n* and *m*), as shown in Fig. 2. In particular, the magnetization can reach large values of 0.3 μ_B per five atoms at room temperature in some cases (e.g., BMO_1/BFO_3), which is larger than that of BFO films by at least one order of magnitude. Thus, our works strongly suggest that the most promising commercial application of multiferroics (magneto-electric RAM) is indeed possible [2].

These works are supported by the ONR Grants N00014-11-1-0384 and N00014-08-1-0915, Department of Energy, Office of Basic Energy Sciences, under contract ER-46612, and ARO grant W911NF-12-1-0085. Some computations were also made possible thanks to the ONR grant N00014-07-1-0825 (DURIP), a Challenge grant from the Department of Defense, and the MRI grant 0722625 from NSF.

References:

[1] Hong Jian Zhao, Wei Ren, Yurong Yang, Jorge Iniguez, Xiang Ming Chen and L. Bellaiche, Nature Communications 5, 4021 (2014).
[2] Yurong Yang, L. Bellaiche and Jorge Iniguez, submitted.
[3] L. Bellaiche and Jorge Iniguez, Phys. Rev. B 88, 014104 (2013).
[4] N.A. Benedek and C.J. Fennie, Phys. Rev. Lett. 106, 107204 (2011).
[5] J.M. Rondinelli and C.J. Fennie, Adv. Mater 24, 1961 (2012).
[6] A. Mulder, N A. Benedek, J. M. Rondinelli, and C. J. Fennie, Adv. Funct. Mater. 23, 4810 (2013).

Extrinsic and Intrinsic Charge Trapping at the Graphene/Ferroelectric Interface

M. Humed Yusuf, Bent Nielsen, M. Dawber, and X. Du
Department of Physics and Astronomy, Stony Brook University, Stony Brook, NY 11794-3800, USA

Recently, there have been several studies on integrating graphene with single crystal ferroelectric thin films like $Pb(Zr_x Ti_1 - x)O_3$ (PZT) [1–3] and (Ba,Sr)TiO $_3$ [4], with the aim of fabricating graphene ferroelectric field effect transistors (GFeFETs). Ferroelectric thin films, as a gate dielectric material, have high-κ values that can enhance the graphene channel carrier mobility [5]. Graphene, which acts as a screening material, can be used to read the switching of spontaneous polarization of the ferroelectric gate material, forming the basis for "non-volatile" memory applications [6].

In general, the characteristics of GFeFETs have been affected by anti-hysteresis associated with charge trapping. The cause has been attributed to water molecules [2] and large densities of H^+ and OH^- [1] ions that screen the ferroelectric polarization at the graphene/ferroelectric interface. More recently, the gating of graphene showing proper ferroelectric hysteresis, at room temperature, has been demonstrated by preserving the cleanliness of the graphene/PZT interface [7]. However, the hysteresis depended strongly on the ramping speed of the gate voltage indicating the presence of slow trapping processes, which are associated with surface adsorbates such as water molecules.

In this work [8], the problem of surface adsorbates was tackled by using artificially layered $PbTiO_3/SrTiO_3$ (PTO/STO) superlattices. A schematics of a GFeFET with PTO/STO as the gate dielectric is shown in Fig. 1 (a). The transition temperature and polarization of PTO/STO superlattices can be tuned by changing the PTO volume fraction [9]. Exfoliated graphene was deposited on the superlattice at 250°C, which can effectively decrease the ferroelectric polarization as much as 70%. With ideal superlattice growth conditions and extrinsic adsorbates largely removed, a direct coupling is seen between the graphene channel and the ferroelectric superlattice, as shown in Fig. 1 (b).

Polarization switching, indicated by the peaks of the C-V curve of the superlattice (Fig. 1 (d)), matches with the position of the graphene Dirac peaks as the gate voltage is swept between ±4V. For sub-hertz gate voltage ramping speeds, the dynamics of the Dirac peak positions are virtually unchanged, as shown in Fig. 1 (c). This is indicative of an absence of slow trapping processes, which were commonplace previously [7].

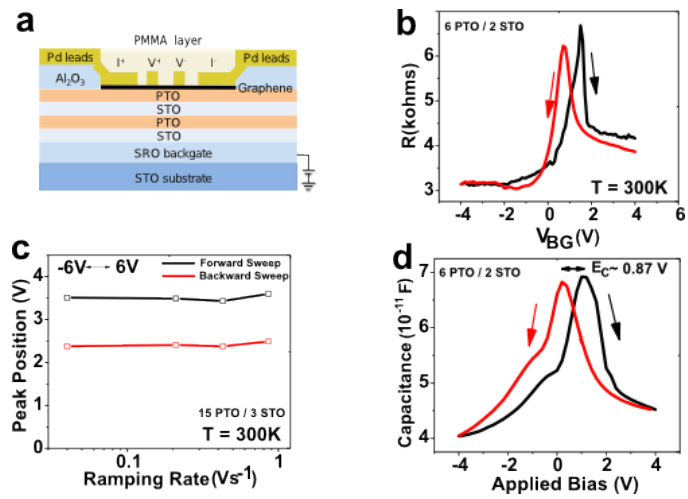

FIG. 1. (a) Schematics of a Graphene Ferroelectric Field Effect Transistor (GFeFET). (b) Graphene channel response due to ferroelectric domain switching at room temperature. (c) For sub-hertz frequencies, the graphene hysteresis is independent of gate ramping speed (d) The capacitance-voltage (C-V) characteristics of the PTO/STO superlattice shows a direct capacitive coupling between graphene and the ferroelectric gate.

With the removal of such extrinsic charge traps, the impact from the "intrinsic" defects of the ferroelectric substrate was revealed. The defects manifested themselves as antihysteresis on the graphene channel. However, this type of antihysteresis has several distinguishing characteristics:

1. The antihysteresis cannot be subdued at cryogenic temperatures (Fig. 2 (a)) as opposed to adsorbate-associated antihysteresis [4];

2. The antihystersis is caused by traps that preferentially trap more electrons than holes from the graphene channel, giving rise to an asymmetric trapping behavior;

3. Compared to the adsorbate-associated traps, the surface defect-associated intrinsic traps show much faster time-response ∼10 μs (Fig. 2 (b)).

A systematic study was carried out to identify the source of such intrinsic charge traps and their impact on the switching behavior of the graphene field effect devices. It was found that the intrinsic traps are largely

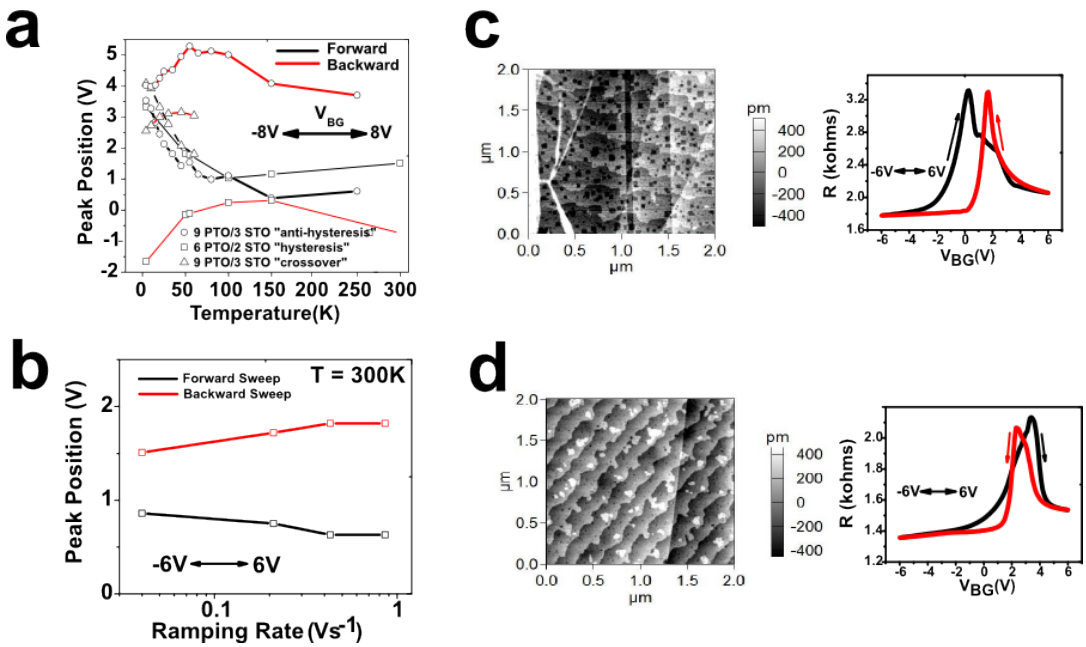

FIG. 2. (a) Dirac point peak position versus temperature for forward and reverse gating for various samples. Remarkably, the forward gate ramping peak positions (black curves) were qualitatively and quantitatively similar for all the devices. This indicates an asymmetry in electron and hole trapping. (b) For sub-hertz frequencies, the anti-hysteresis is robust. This indicates a fast trapping processes. (c) Defects on the ferroelectric surface facilitate charge trapping, and graphene demonstrates"anti-hysteresis". (d) An ideal interface restores ferroelectric switching on the graphene channel.

influenced by the growth parameters of the ferroelectric superlattices. Such intrinsic charge traps, while showing little impact on the C-V characteristics of the superlattice, strongly affect the resistance gating of the graphene channels. Comparing the surface topography of the devices with their gating curves (see Fig. 2 (c) & 2 (d)), the charge trapping centers were attributed to physical defects associated with the dangling bonds on the surface of the superlattice, which cannot be processed or removed simply by making the interface free of adsorbates. These defects manifest themselves as single atom deep, square shaped pits, which may be associated with the 1x6 surface reconstruction of $PbTiO_3$, associated with PbO deficiency [10].

These results are the first successful demonstration of robust, ramping speed independent, room temperature ferroelectric switching in GFeFETs. Through comparison with numerical simulations, a deeper understanding of the graphene-ferroelectric interface was established. This paves the way to reliably study graphene-ferroelectric hybrid devices, and to extend the work to other novel 2D atomic layer systems and ferroelectric systems. This work also established PTO/STO ferroelectric superlattice system as a suitable system for combining two dimensional atomic crystals (2DACs) with ferroelectricity.

ACKNOWLEDGEMENTS

This work was supported by NSF (Grant DMR 1105202). Part of this research was carried out at the Center for Functional Nanomaterials, Brookhaven National Laboratory, which is supported by the U.S. Department of Energy, Office of Basic Energy Sciences, under Contract No. DEAC02-98CH10886. We thank Dong Su and Fernando Camino at CFN for TEM work and assistance with the use of the cryogenic probe station.

[1] X. Hong *et al.*, Appl. Phys. Lett. **97**, 033114 (2010).
[2] E.B. Song *et al.*, Appl. Phys. Lett. **99**, 042109 (2011).
[3] Y. Zheng *et al.*, Epl-Europhys. Lett. **93**, 17002 (2011).
[4] A. Rajapitmahuni *et al.*, Nano. Lett. **13**, 4374 (2013).
[5] X. Hong *et al.*, Solid State Commun. **152**, 1365 (2012).
[6] Y. Zheng *et al.*, Appl. Phys. Lett. **94**, 163505 (2009).
[7] C. Baeumer *et al.*, Nano. Lett. **13**, 1693 (2013).
[8] M.H. Yusuf *et al.*, Nano. Lett.**14**, 5437 (2014).
[9] M. Dawber *et al.*, Adv. Mater. **19**, 4153 (2007).
[10] A. Munkholm *et al.*, Phys. Rev. Lett. **88**, 016101 (2002).

Dopants and Defects

Defects in ferroelectric oxides and at oxide/ferroelectric interfaces

A. V. Kimmel
National Physical Laboratory, Teddington, TW11 0LW, U.K.

In ferroic materials, unwanted changes of the ferroelectric, dielectric, and piezoelectric properties, which either occur spontaneously or accumulate in the course of numerous ferroelectric axis switching events, have been attributed to the presence of defects. Understanding the mechanisms of defect-induced atomic scale processes is, therefore, crucial for not only improving the reliability of existing devices but also for utilizing the defect properties and developing new functionalities.

Oxygen vacancies, being the most abundant defects in oxide materials, are known to induce local perturbation of the lattice, affect dielectric properties, conductivity, polarization, and overall lifetime of ferroelectric devices. In this talk I discuss various mechanisms of Oxygen vacancy defects stabilisation in tetragonal ABO_3 ferroelectric compounds.

From symmetry consideration the oxygen axial sites located along the B-O-B chains, oriented along the tetragonal (polar) axis c, and the oxygen equatorial sites located in the BO_2 planes perpendicular to this axis, are not equivalent. Consequently, the oxygen vacancies at these sites, referred to as axial (V_{ax}) and equatorial (V_{eq}) vacancies, are not iso-energetic and induce strong site-specific lattice relaxation. In particular, the stabilisation may occur via a conventional path of diffusion from metastable to stable configurations. However, an alternative mechanism takes place where the perturbation induced by defect is enough to facilitate the rotation of the polar axis. This mechanism, predicted to dominate in materials with slow oxygen vacancy diffusion and low formation energy of 90° domain walls, can stimulate the formation of domains with their polar axes pinned by the vacancies [1].

We illustrate the material-dependence of these symmetry-conforming properties of defects using a comparative ab initio study of oxygen vacancies in tetragonal phases of $BaTiO_3$, $KNbO_3$ and low energy P4mm phase of solid solution $Pb(Zr_{0.5}Ti_{0.5})O_3$ (PZT). We demonstrated that rotation mechanism is efficient in $BaTiO_3$, while $KNbO_3$ exhibits a preference to the diffusion mechanism. The relative stability of oxygen vacancies in PZT strongly depends on the local chemical environment that stabilises a preferential location of defects in material.

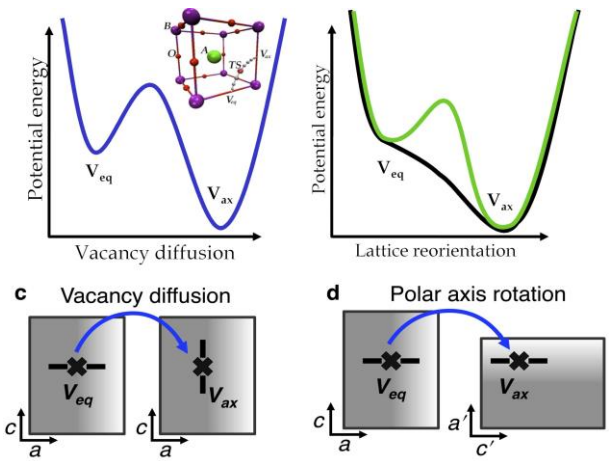

Another example of defect-induced properties is related to oxide/ferroelectric interfaces. Oxide interfaces are known to exhibit properties that are not found in the constituent materials when they are considered separately. At the nanoscale, the properties associated with interfaces often define the properties of entire nano-structures. The materials with new properties and functions can be fabricated by assembling complex hetero-structures, such as epitaxial thin films and core-shell (CS) nanoparticles. CS nanoparticles of $BaTiO_3$ (BTO), in the form of nano-sized (300-500 nm) grains coated with ~5 nm thick silica layer, demonstrated a dielectric constant over 10^5 and quite constant in a wide temperature range. These properties make the BTO-SiO_2 nanoparticles promising for the applications that require high dielectric permittivity, such as solid-state energy storage and random access memory devices.
An atomistic model of $SiO_2/BaTiO_3$ interface was constructed using *ab initio* molecular dynamics. Analysis of its atomistic structure and electronic properties reveals the closure of the band gap at the stoichiometric $SiO_2/BaTiO_3$ interface that is significantly smaller than that of the bulk BTO and SiO_2. We showed that the properties of the interfaces significantly depend on perovskite termination. The interfaces with BaO terminated BTO exhibit stable character of interfacial bonds, while that with TiO_2 terminated BTO shows strong covalent bonds. The structure gives rise to the interface polar region with positive and negative charges localized in the BTO and SiO_2 parts of the interface, respectively. In both cases the formation of the interface facilitates the formation of defects. Thus, the interface contains high concentration of oxygen vacancies in the outermost TiO_2 plane of the $BaTiO_3$. The high dielectric response, observed experimentally in the SiO_2-coated nanoparticles of BTO, was proposed to be due to the electron gas formed in oxygen-deficient BTO and localized in the vicinity of the polar interface [2].

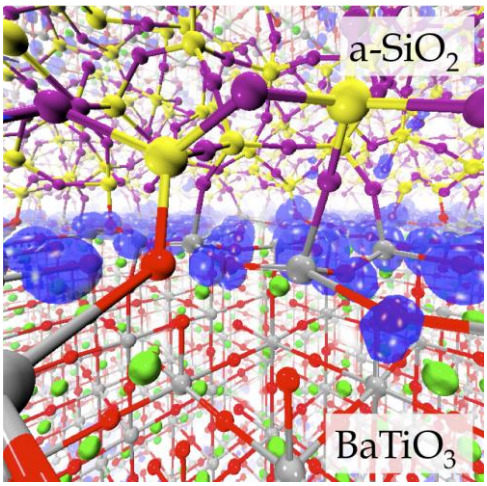

1. A.V. Kimmel, P. Weaver, M.G. Cain, P.V. Sushko Phys. Rev. Lett. 117601, 109 (2012).
2. A.V. Kimmel, J. Íñiguez, M.G. Cain, P.V. Sushko J. Phys. Chem. Lett. 4, 333 (2013).

Point Defects in Lead Titanate : a first-principles study

Charles Paillard[1], Gregory Geneste[2], Brahim Dkhil[1]

[1]Laboratoire SPMS, UMR 8580 CNRS/Ecole Centrale Paris, Grande Voie des Vignes 92 295 Châtenay-Malabry CEDEX, France
[2]CEA, DAM, DIF, F-91297 Arpajon France

Domain Walls have attracted considerable interest recently, for they show enhanced or new properties, such as superconductivity[1] in WO_3, increased conductivity in $BiFeO_3$[2,3], or vortices[4]. Domain walls have also been suggested to trap some point defects. Such property is of crucial interest because it may (i) induce electronic or ionic conductivity in the DW, and (ii) decrease the mobility of the DW. However, these trapping phenomena have not been, to our knowledge, exhaustively investigated in any ferroelectric material. We have chosen $PbTiO_3$ as a prototypical system for modeling the domain walls, and investigated the properties of single vacancies in the domain wall and in the bulk.

In this work, we performed first-principles density-functional calculations, with the ABINIT code, in the Projector-Augmented Wave framework, to simulate Pb, Ti and O vacancies at 180° and 90° domain walls in lead titanate. Here, we focus mainly on 180° DWs, and using the Local Density Approximation in 120-atom (6x2x2) supercells, we show that Pb, Ti and O vacancies preferentially form in the DW, whatever their charge state (formation energies are typically 0.1-0.3 eV lower in the domain wall). Such stabilization is likely to be a consequence of the partial relaxation of the DW elastic energy.

The defect concentration can be tuned by the thermodynamic external conditions (oxygen pressure, Pb and/or Ti chemical potential when the material is formed), and by extrinsic doping (acceptor/donor) to modify the Fermi level. Defect engineering in conjunction with domain engineering could then lead to atomic layer thick 2D conductive pathways, of great interest for new electronic devices.

Acknowledgements

References

[1] E. Salje, *Chemphyschem* **11**, 940, (2010).
[2] J. Seidel, L. Martin, Q. He et al., *Nat. Mat.* **8**, 229, (2009).
[3] S. Farokhipoor, B. Noheda, *Phys.Rev.Lett.* **107**, 127601, (2011).
[4] D. Viehland and E. Salje, *Adv. Phys.* **63**, 267, (2014).

Dopants, defects & domains – Dielectric spectroscopy in $LiNbO_3$

Torsten Granzow[1], Nadège Meyer[1], Guillaume Nataf[1]

[1]Department of Materials Research, Luxembourg Institute of Science and Technology (LIST), L-4422 Belvaux, Luxembourg

Even though the perovskite structure type is often considered to be prototypical for ferroelectric materials, other corner-linked oxygen-octahedral structures are sometimes superior both for the study of fundamental physical properties and the exploitation of these properties in applications. A prime example is the pseudo-ilmenite-structured lithium niobate ($LiNbO_3$, LN). Due to its unique piezolectric, pyroelectric, acoustic, electro-optic and photorefractive properties it has been the subject of intensive studies for many years and has found applications in photorefractive devices, holographic memories, optical frequency converters, etc [1]. There are several remarkable aspects that set $LiNbO_3$ apart from perovskite-structured ferroelectrics: first, it is a uniaxial non-ferroelastic ferroelectric, and only 180° domain wall configurations are possible. Second, it is most often employed in the form of single crystals, in contrast to materials such as lead-based perovskite-structured piezoelectric ceramics, which are more often polycrystalline. The material is usually grown from the melt using the Czochralski technique. Third, its properties are even more defect-dominated than those of most other ferroelectrics. Crystals are most often grown at the congruent melting point, which leads to a high deficiency in Li-ions. In congruently melting LN (c-LN), the concentration of lithium and niobium ions is [Li]/[Li+Nb] = 48.6%. Antisite Nb_{Li} is known to be the most prominent defect. It is generally assumed to be compensated by the creation of either lithium or niobium vacancies, V_{Li} or V_{Nb} [2, 3]. Numerous studies have been performed to elucidate the effect of a large number of dopants in LN. Donor dopants such as iron (Fe) or copper (Cu) increase the photorefractive effect, while magnesium (Mg) reduces the optical damage threshold [1].

Particularly for the last case, the exact defect structure is still under discussion despite numerous publications on the subject. According to a recent study by Yatsenko et al., Mg-doping most probably leads to the formation of defect complexes ($4Mg_{Li} + 4V_{Li}$) [4]. Additionally, there is strong evidence that the local defect structure is decisively influenced by the ferroelectric domain structure, high external electric fields and thermal treatment at moderate temperatures below 200°C [5, 6]. In this context, dielectric spectroscopy is a promising tool to study the interaction between electric fields, intrinsic as well as dopant-induced defects and domain walls at various temperatures. However, these types of measurements have so far been mostly limited to undoped lithium niobate. Only singular measurements show that dielectric relaxation processes can be observed in doped LN, while undoped LN appears to be relaxation-free [7,8].

This presentation will focus on three different types of crystals: single-domain magnesium-doped c-LN, single-domain nominally undoped c-LN and periodically poled (polydomain) nominally undoped c-LN (c-PPLN). The real and imaginary part of the dielectric permittivity in the frequency range between 1 Hz and 1 MHz are measured at various temperatures between -100°C and +200°C. The Mg-doped samples show a very pronounced dielectric relaxation around 100 Hz (see Fig. 1) that irreversibly vanishes when the sample is heated above 140°C. It is suggested to originate from free Mg-donor defects that appear when the Mg_{Li}-V_{Li} defect complexes are destroyed by high-temperature poling. Annealing above 140°C allows the Li-ions to migrate back to their original positions, re-forming the defect complexes and quenching the dielectric relaxation. This interpretation is supported by measurements of the thermally stimulated depolarization current (TSDC) that show an anomalous depolarization current around 140°C during the first heating that is no longer seen in subsequent heating cycles. Similarly, the electrical conductivity is shown to increase drastically in that temperature range; the observed activation energy of ~1eV confirms that the charge transport is due either to lithium vacancies or hydrogen ions.

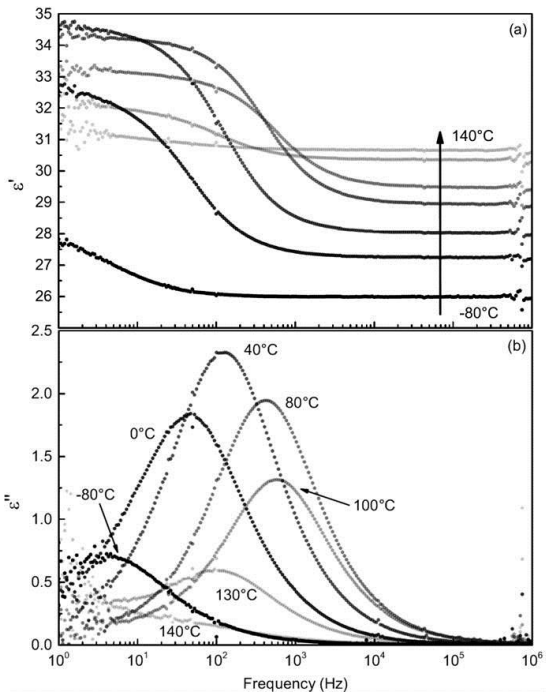

Figure 1 Real (a) and imaginary part (b) of permittivity of c-LN:Mg (5%) at different temperatures.

The behavior is rather different in the nominally undoped single domain c-LN and c-PPLN. Most undoped single-domain samples do not show any dielectric relaxation in the observed frequency range. A relaxation is observed occasionally in nominally undoped single domain c-LN around 10^4 Hz, i.e. at frequencies two orders of magnitude higher than in c-LN:Mg. This type of relaxation is also observed in all the c-PPLN samples examined. Apparently, the samples that are nominally undoped and single-domain still contain some type of defect, either in the form of unintended impurities or domain walls. It is interesting to note that the relaxation at 10^4 Hz again vanishes upon heating beyond 140°C in the single-domain c-LN, but is stable in the c-PPLN. It is tentatively attributed to ionic defects that have been left in an energetically unfavorable position by the high-temperature poling process in the single-domain sample, but are attached to and stabilized by the ferroelectric domain walls in the c-PPLN. The results are discussed with respect to the possibilities of defect- and domain-engineering in $LiNbO_3$ in particular and uniaxial ferroelectrics in general.

Acknowledgements: This work was supported by the 'Fonds National de la Recherche' (FNR) Luxembourg (Projects CO-FERMAT & S-MOD PV)

References

[1] L. Arizmendi, *Phys. status solidi* **201**, 253 (2004).
[2] P. Lerner, C. Legras, and J. Dumas, *J. Cryst. Growth* 3-4, **231** (1968).
[3] S. C. Abrahams and P. Marsh, *Acta Crystallogr. Sect. B Struct. Sci.* **42**, 61 (1986).
[4] A. V. Yatsenko, S. V. Yevdokimov, D. Y. Sugak, and I. M. Solskii, *Funct. Mater.* **21**, 31 (2014).
[5] P. Reichenbach, T. Kämpfe, A. Thiessen, A. Haußmann, T. Woike, and L. M. Eng, *Appl. Phys. Lett.* **105**, 122906 (2014).
[6] P. Reichenbach, T. Kämpfe, A. Thiessen, M. Schröder, A. Haussmann, T. Woike, and L. M. Eng, *J. Appl. Phys.* **115**, 213509 (2014).
[7] A. Mansingh and A. Dhar, *J. Phys. D. - Appl. Phys.* **18**, 2059 (1985).
[8] P. C. Barbosa, J. A. C. de Paiva, J. M. Filho, A. C. Hernandes, J. P. Andreeta, and A. S. B. Sombra, *Phys. Status Solidi* **125**, 723 (1991).

$BiFeO_3$

Spin and lattice dynamics in multiferroic $BiFeO_3$

Guangyong Xu[1], Zhijun Xu[1,2,3], John Schneeloch[1], Jinsheng Wen[1,2,3], Christopher Stock[4], P, M. Gehring[4], M. B. Stone[5], M. Matsuda[5], B. Winn[5], T. Berlijn[1], Wei Ku[1], Genda Gu[1], S. M. Shapiro[1], R. J. Birgeneau[2,3], T. Ushiyama[6], Y. Yanagisawa[6], Y. Yomioka[6], and T. Ito[6]

[1]Condensed Matter Physics and Materials Science Department, Brookhaven National Laboratory, Upton, NY 11973,USA
[2]Physics Department, University of California, Berkeley, California 94720, USA
[3]Materials Science Division, Lawrence Berkeley National Laboratory, Berkeley, California 94720, USA
[4]NIST Center for Neutron Research, National Institute of Standards and Technology, Gaithersburg, Maryland 20899, USA
[5]Quantum Condensed Matter Division, Oak Ridge National Laboratory, Oak Ridge, Tennessee 37831, USA
[6]National Institute of Advanced Industrial Science and Technology (AIST), Tsukuba, Ibaraki 305-8562, Japan

$BiFeO_3$ is a room temperature multiferroic material with great application potentials. The G-type antiferromagnetic (AFM) order in this material is weakly coupled to the ferroelectric polar order, resulting in a cycloid spin structure with long wavelength modulations (~ 62 nm). There has also been growing interest on couplings between the dynamical properties as well. For example, a "magneto-optical" resonance has been proposed theoretically, and extra modes below the lowest lying optic phonon energies have been observed in Raman measurements. A full understanding of both the spin and lattice dynamics in $BiFeO_3$ is highly desired.

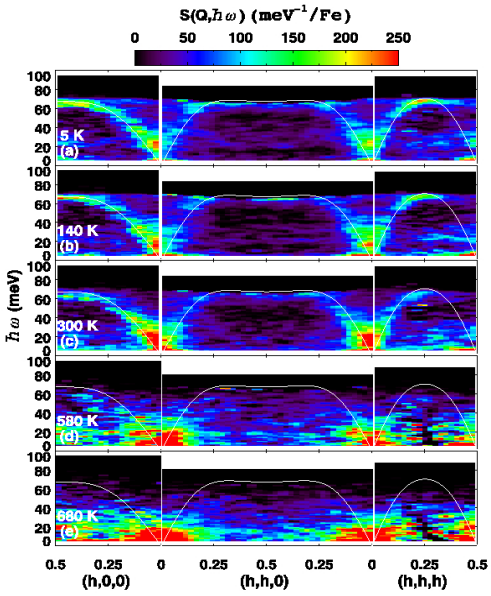

Fig.1 Magnetic excitations measured at 5, 140, 300, 580, and 680 K. The horizontal axis denotes $\mathbf{Q} - \mathbf{Q}_{AF}$. The data shown here are measured with Ei = 120 meV.

With inelastic neutron scattering, we have been able to systematically map out the complete three-dimensional spin-waves in this system. In addition, low energy (~<20 meV) phonons have also been studied. Here we would like to present our work on both the magnetic and lattice dynamics in this system for a large temperature range between 10K and 700K.

The sample being used is a cylindrical single crystal sample which weighs about 3.5 g. The experiments have been performed using ARCS and HYSPEC time-of-flight spectrometers at SNS. The magnetic excitations are measured on ARCS with incident energies of 40 and 120 meV to cover the full dispersion. The low energy phonons are measured on HYSPEC with incident energy of 20 meV.

In Fig.1, magnetic excitations measured along different crystallographic directions are shown. At low temperatures, the spin-waves are well-defined coherent modes. We can use a simple Heisenberg spin Hamiltonian, taking into account the first, second and third nearest neighbor exchange interactions (J_1, J_2, and J_3) to model the spin-waves. The exchange parameters can be obtained from the modeling. Warming up the sample resulting in a reduction of the effective exchange parameter and the life-time of the spin-

wave excitations. When the system is heated above the Neel temperature (T_N=640 K), the spin-waves become heavily damped and broad in space as well. In addition, our analysis on the the magnetic form factor suggests that a strong hybridization between the Fe and O orbitals needs to be taken into account when the magnetic response is considered. Even as a good insulator, the electrons responsible for the magnetic moments are not restricted at the Fe sites, and the local magnetic moment could extend well beyond the typical ionic radius of Fe^{3+} into the adjacent O^{2-} sites.

We were also able to measure low energy phonons in $BiFeO_3$. The phonon excitations in different zones are summarized in Fig.2. The three acoustic phonon modes (TA1, propagating along [010], polarized along [100]; TA2, propagating along [1,-1,0],polarized along [110]; and LA, propagating along [100], polarized along [100]), and the lowest lying optic modes are mapped around a number of Bragg peaks. The measured phonon dispersions and the intensities after removing the Bose-factor do not show any significant variation with temperature within measurement errors. A clear broadening of the transverse acoustic mode is observed near the zone-boundary when heating toward T_N, suggesting a possible coupling between the lattice dynamics and the antiferromagnetic order in the system.

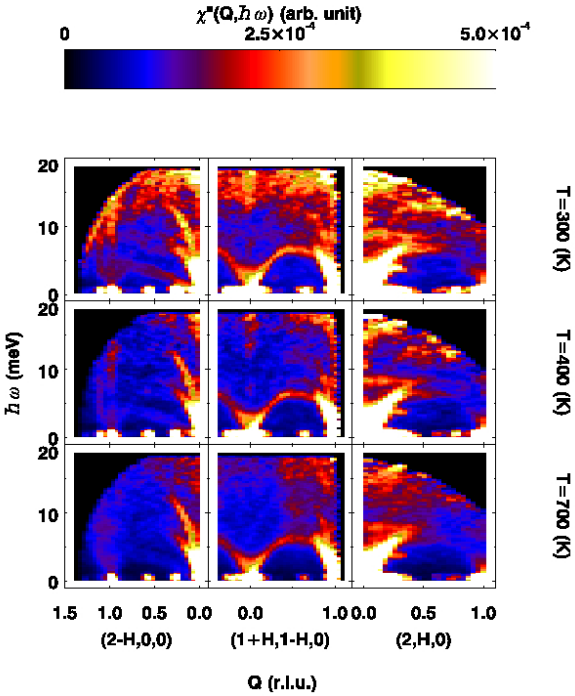

Fig.2 The dynamic response measured from the single crystal BiFeO3 sample, at T=300 K (top row), 500 K (central row), and 700 K (bottom row). The intensities are shown in the (HK0) plane, for q along [100] (left column), [1,-1,0] (central column), and [010] (right column) directions, respectively. The intensities shown near the top of the measurement energy range are spurious intensities when ~! becomes close to the incident energy Ei. These intensities are temperature independent. They only appear to be stronger at 300 K (top frames) in the plot of ″(Q, ~!) because the data here are divided by the Bose factor.

ACKNOWLEDGMENTS

Financial support from Office of Basic Energy Sciences, U.S. Department of Energy under contract No. DE-AC02-98CH10886 and DE-AC02-05CH11231; the Scientific User Facilities Division, Office of Basic Energy Sciences, U.S. Department of Energy; and the Mitsubishi Foundation are acknowledged.

References:

[1] Z. Xu et al., Phys. Rev. B **86**, 174419 (2012).
[2] J. Schneeloch et al., arXiv:1410.2316

Stabilization and switchability of weak ferromagnetism in epitaxially strained $BiFeO_3$

Hemant Dixit[1], Jun Hee Lee[1], Jaron T. Krogel[1], Satoshi Okamoto[1], Valentino R. Cooper[1]

[1] Materials Science and Technology Division, Oak Ridge National Lab, Oak Ridge, TN 37830, USA

The magnetoelectric effect (ME), i.e. controlling ferromagnetism using electric fields, has been a focus of research in multiferroic materials due to potential applications in technologies such as magnetic data storage, spintronics, logic and memory devices[1,2]. Magnetoelectric coupling with substantial magnetic stability and switchability is critical for magnetic information processing with minimal power consumption. In this regard, bismuth ferrite ($BiFeO_3$), has been shown to exhibit coupling between the ferroelectricity and ferromagnetism[3]. Here, we show the stabilization and the swichability of weak ferromagnetism (wFM) under epitaxial strains in $BiFeO_3$ using a first-principles approach and group-theoretic analysis. For this purpose, we perform non-collinear spin-polarized density functional theory (DFT) calculations including spin-orbit couplings under applied compressive and tensile strains. In case of rhombohedral symmetry, we observe that the magnetic ground state is degenerate (refer Figure 1) and is perpendicular to the polarization vector, which is a consequence of isotropic Dzyaloshinskii-Moria interactions. Such degeneracy, however, disappears for the strained phases.

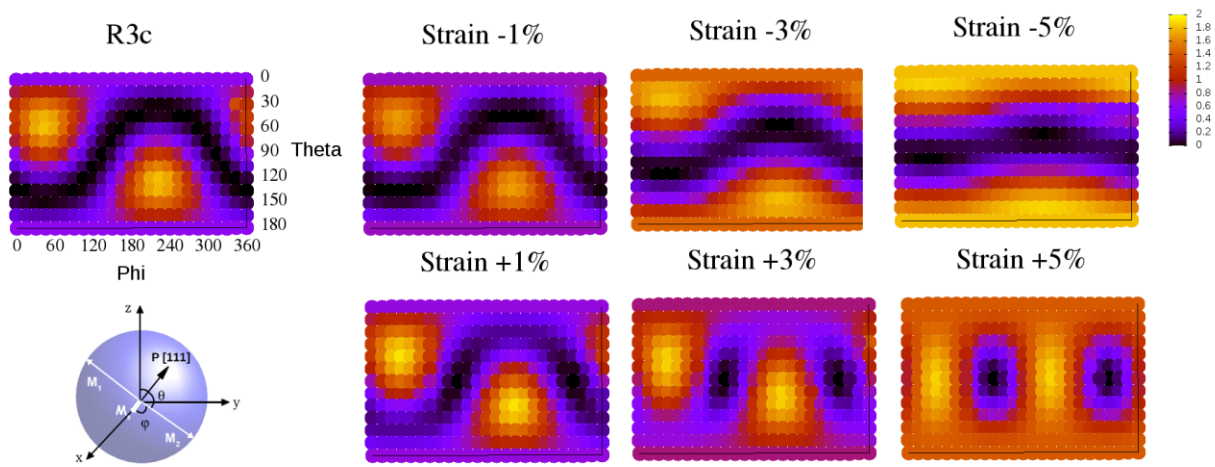

Figure 1. Calculated magnetic energy landscapes showing the energy difference (in meV) between the antiferromagnetic arrangements considered along all the possible orientations in space. The bright spots coincide with the direction of the polarization vector and the dark region represents the magnetic ground state (remains perpendicular to the polarization vector in all the cases).

We find that the tensile strain can be used to stabilize the antiferromagnetic vector along the [1-10] direction due to anisotropic Dzyaloshinskii-Moria interactions in the x-y plane, commensurate with changes in the FeO_6 octahedral tilt pattern. On the other hand, at high enough compressive strains the *C* and *G*-type magnetic ordering are energetically indistinguishable from each other. Furthermore, *C*-type magnetic ordering shows weak antiferromagnetism (wAFM), i.e. the wFM moments are antiferomagnetically ordered in the neighboring planes. Thus it may be possible to switch "on" and "off" the wFM at higher compressive strains.

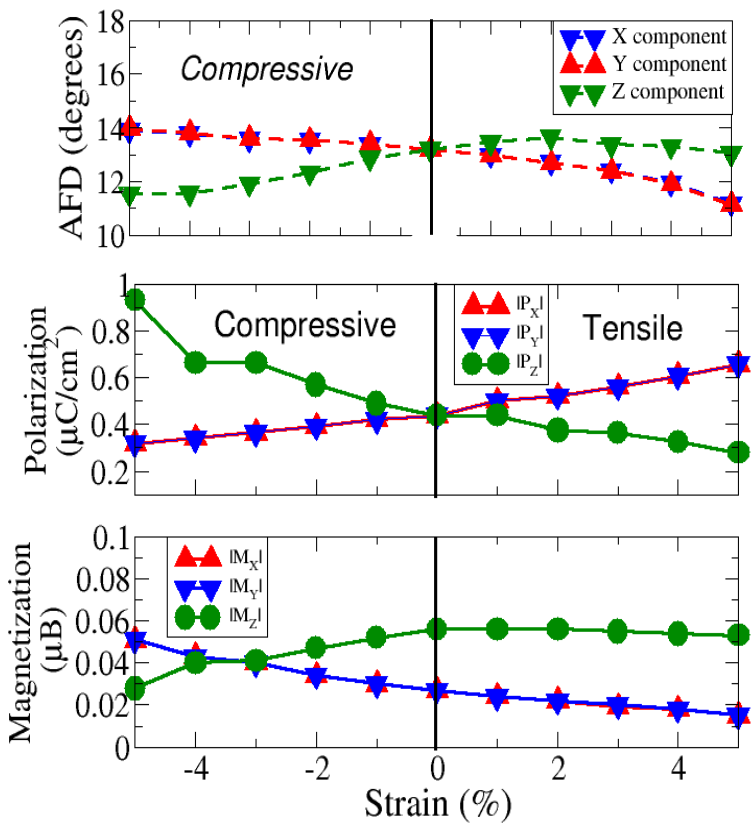

Figure 2. Variation in the in-plane (x-y) and out-plane (z) components of the antiferrodistortive (AFD)rotations polarization (P) and magnetization (M) under applied epitaxial strain.

Finally we summarize the relation between the antiferrodistortive (AFD) rotations and ferroelectric polarization (P) and weak ferromagnetic moment (M) induced via the DM interactions (Figure 2). Our study shows that the wFM is directly linked to the amplitude of AFDs and epitaxial strain is a powerful tool to manipulate the ME coupling in $BiFeO_3$ thin films.

This research was supported by Office of Science of the U.S. Department of Energy, Office of Science Basic Energy Sciences (BES) and Materials Sciences, Engineering Division.

.

References

[1] D. Sando *et. al.*; *Nature materials*, **12**, 641–646, (2013).

[2] Sebastian Neusser and Dirk Grundler; *Advanced Materials*, **21**, 2927–2932 (2009).

[3] Weingart, C., Spaldin, N. & Bousquet, E. *Phys. Rev. B* **86,** 094413 (2012)

Spin-orbit Coupling Effects in Multiferroic Bi_2FeCrO_6

François Vidal[1], Liliana Braescu[1,2], and Alain Pignolet[1]

[1]Institut National de la Recherche Scientifique – Centre Énergie, Matériaux et Télécommunications, Varennes, Québec, Canada
[2]Dept. of Mathematics & Computer Science, Alfaisal University, Riyadh, KSA

For application in integrated sensors or devices, functional materials are used in the form of thin films. Ferroelectricity and many other properties of multiferroic materials, such as the magnetocrystalline anisotropy, are strongly related to the material crystal structure. Because fundamental physics of multiferroic materials is rich, theoretical studies are of great importance, since it is extremely difficult to understand the intrinsic material properties using only experimental data. An example of multiferroic material having the potential to revolutionize electronic industry is the rhombohedral double-perovskite Bi_2FeCrO_6 (BFCO) owing to its good ferroelectric and magnetic properties at room temperature that were both theoretically predicted by ab-initio calculations [1] and experimentally demonstrated on epitaxial thin films [2]. To complement these studies, theoretical investigations have been performed in order to analyze the spin-orbit coupling (SOC) effects on the magnetic and ferroelectric properties of BFCO. Using first-principles density functional theory (DFT) calculations within the VASP package, investigations were performed for both collinear and non-collinear spin structures of BFCO, respectively. Exchange and correlation effects were treated using the local density approximation plus Hubbard potential, on the different possible high spin (HS) and low spin (LS) states of the ferromagnetic (FM) and ferrimagnetic (FiM) spin arrangements.

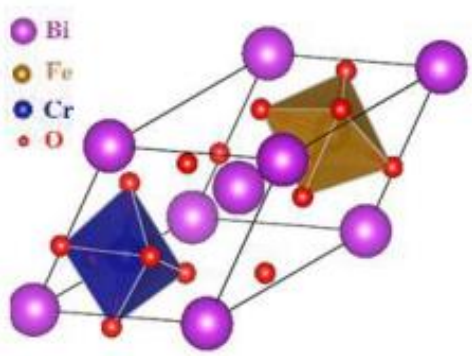

Figure 1 Structure of the BFCO.

In the case of collinear spin calculations without SOC, the existence of four competing phases (FMHS, FMLS, FiMHS and FiMLS) with distinct electronic and magnetic properties was found, in agreement with recent published theoretical results [3]. The FiMHS state was found to be the

most stable, with a total magnetic moment $|M_{BFCO}|$~$2\mu_B$/cell, and a computed spontaneous polarization of P_s=79.1 [μC/cm^2] in agreement with reported data [1]. When SOC was considered, the calculations also showed the existence of the above four stable states, FiMHS remaining the most stable state. It was found that magnetization is somewhat higher, namely $|M_{BFCO}|$=2.005 μ_B/cell, when the total magnetization vector is parallel to the direction (1 1 -2). It was also shown that, the obtained magnetizations does not have a preferred direction in the HS states, but show deviation from the direction (1 1 1) in the LS states, due to structural distortions, with energy minimized in the direction ~(2 1 1). Spontaneous polarizations computed for optimized structures using the Berry-phase method, were found to be slightly higher when SOC is considered, namely P_s~81.5 [μC/cm^2] for FiMHS.

Additionally, comparing the Fe-O and Cr-O bond lengths in the FeO_6 and CrO_6 octahedra, it was found that the Cr-O bonds and Cr^{3+} magnetic moments have non-significant changes (smaller than 0.7% of the bond length) when SOC is considered, while Fe-O bonds and Fe^{3+} magnetic moments exhibit substantial changes (up to 6.9% of the bond length).

References

[1] F. Author, S. Author and T. Author, *J. Sig. Res.* **Vol**, Page, (Year).

[1] P. Baetig, C. Ederer and N. A. Spaldin 2005. First principles study of the multiferroics $BiFeO_3$, Bi_2FeCrO_6, and $BiCrO_3$: Structure, polarization, and magnetic ordering temperature. Phys Rev B 72, 214105 (2005).

[2] R. Nechache, C. Harnagea and A. Pignolet, Multiferroic properties - structure relationships in epitaxial Bi2FeCrO6 thin films: recent developments. J. Phys.: Condensed Matter, 24, 096001 (2012).

[3] M. Goffinet, J. Iniguez, and P. Ghosez, First-principles study of a pressure-induced spin transition in multiferroic Bi_2FeCrO_6. Phys Rev B, 86, 024415 (2012).

Posters

Application of the Wang-Landau Algorithm applied to Ferroelectrics

S. Bin-Omran[1,2], I. Kornev[3], and L. Bellaiche[4]

[1]*King Saud University, Department of Physics and Astronomy, P.O.BOX: 2455, Riyadh 11451, Saudi Arabia*

2 Salman Bin Abdul-Aziz University, Faculty of Science & Humanity Studies, Alkharj 11942, Saudi Arabia

3 Laboratoire SPMS, UMR 8580 du CNRS, Ecole Centrale Paris, 92295 Chatenay-Malabry, France

4 Institute for Nanoscience and Engineering and Physics Department, University of Arkansas, Fayetteville, Arkansas 72701, USA

The conventional description of phase transitions in ferroelectrics is based on canonical thermodynamic functions and always assumes the thermodynamic limit of an infinite system. However, ferroelectrics at nanoscale recently became of high interest due to their potential applications in minuaturized devices. It is this timely and more appropriate to use the microcanonical ensemble when mimicking ferroelectric systems [1,2].

Here, a first-principles-derived scheme, combined with an efficient Monte Carlo microcanonial technique, is used to gain new insight into the paraelectric to ferroelectric phase transition and the effect of the electric field on properties of $BaTiO_3$ systems. More precisely, we use a Wang-Landau algorithm [3]**,** which is an efficient and accurate method for the study of the phase transitions. Since such algorithm computes the density of states, g(E), one can then calculate most thermodynamical quantities for all temperature with one single simulation! Moreover, the free energy (F) and the entropy (S) can be readily calculated, unlike in conventional Monte Carlo Metropolis simulations – which allows the investigation of challenging but important quantities.

In this presentation, we will show the temperature variation of the specific heat for different lattice sizes in $BaTiO_3$ systems. The nature of the phase transition and the behaviour of the specific heat versus the lattice size will be documented. In addition, the effect of the electric field on the character of the phase transitions in BaTiO3 systems will be investigated by showing the free energy (F) versus the internal energy (U) curves. Electrocaloric effects can also be easily computed and will be discussed.

We are confident that our results lead to a deeper understanding of phase transitions in ferroelectrics, in general, and may help in interpreting future experimental data, in particular.

We also hope that it can have an impact in designing new and improved devices for actuators, sensors, optical switches, RF devices and memory storage.

This work is supported by the National Plan for Science, Technology and Innovation under the research project No. NANO-673-2. L.B. thanks the support ONR Grant N00014-12-1-1034.

References:

[1] D. Gross, Microcanonical Thermodynamics: Phase Transitions in "small" Systems, World Scientific lecture notes in physics (World Scientific, 2001), ISBN 9789812798916.

[2] M. Pleimling and H. Behringer, Phase Transitions 78, 787 (2005).

[3] F. Wang and D. P. Landau, Phys. Rev. Lett. 86, 2050 (2001).

Revisiting the phase transition in $SrTiO_3$: type of transition and precursor effects

Annette Bussmann-Holder[1] & Krystian Roleder[2]

[1]Max-Planck-Institute for Solid State Research, Heisenbergstr. 1, D-70569 Stuttgart, Germany

[2]University of Silesia in Katowice, ul. Uniwersytecka 4, 40-007 Katowice, Poland

$SrTiO_3$ is one of the best investigated perovskite oxides and still under intense current research. It is well known that at T_S=105K a structural phase transition from cubic to tetragonal takes place associated with the softening of a transverse acoustic mode. Simultaneously a long wave length transverse optic mode softens reminiscent of a ferroelectric instability. The complete softening is, however, inhibited by quantum fluctuations which lead to the introduction of quantum paraelectricity. Accompanied with the soft optic mode is an enormous increase in the dielectric constant which could be useful for cryogenic applications.

For a long time the structural instability at T_S has been considered to be purely displacive since the transverse acoustic mode softening continues smoothly up to T_S. A certain doubt about this "displacive only" behavior has been raised from EPR measurements where order-disorder dynamics were observed. Thus it clearly appeared that it is impossible to separate different dynamics from each other in an unambiguous way but that coexistence of both dynamics needs to be taken into account where length and time scales differ substantially. In addition, it was shown that the phase transition is preceded by precursor effects which persist up to a certain critical temperature from where on they become manifest and are well detectable. Here we focus on this latter point and provide experimental as well as theoretical evidence for their existence and their implications on the phase transition mechanism.

Experimentally birefringence and elastic constant measurements have been carried through which exhibit pronounced deviations from what would be expected from a Landau free energy expansion (Fig. 1a). Obviously a clear sign of birefringence is seen far above T_S which gets more and more pronounced when approaching T_S. Simultaneously a softening of the elastic constants takes place which is beyond any mean-field approach.

Theoretically, the polarizability model has been employed with focus on the long wave length dynamics. Here pronounced mode-mode coupling takes place which leads to an anomalous acoustic mode dispersion and local mode softening. The length scale of these dynamical clusters increases steadily with decreasing temperature and diverges upon approaching T_S. These additional features are a consequence of strong anharmonicity and anomalous mode-mode coupling which is absent in purely rigid ion models but caused by transition metal d and oxygen ion p dynamical covalency.

Early measurements by Courtens [1] suggested that the birefringence in the ferroelastic phase varied with temperature with a critical exponent for the order parameter of 0.36(2). More recent measurements [2], in which birefringence imaging was used to make sure that a domain-free region of the crystal was measured gave a mean-field exponent close to 0.5. It was suggested that Courten's measurement, which was carried out by averaging over a field of view of the crystal, might have been affected by the presence of domains appearing within the low-temperature phase. More importantly for the purposes of this report, Courtens observed a curious cusp appearing just above the phase transition that he explained in terms of critical fluctuations. Such behavior was not seen in the work [2]. In this report we will show that this cusp can be avoided if only the phase transition is observed at no change in the indicatrix orientation during the structural transformation (Fig 1b). At the same time the temperature behavior of birefringence below T_S is not pointing to a purely displacive transition type. Above Ts the precursor dynamics are present [3] independent on crystal technology and its temperature range is in good agreement with temperature range reported also for micro- and nanoceramics of $SrTiO_3$ by Hehlen et al [4].

1. E. Courtens, Phys. Rev. Letters, 29, No. 20, 1972
2. M. A. Geday and A. M. Glazer, J. Phys.: Condens. Matter 16, 3303–3310, 2004
3. K. Roleder, A. Bussmann-Holder, M. Górny K. Szot and A. M. Glazer, Phase Transitions, 85, No. 11, 939–948, 2012
4. B. Hehlen, A. Al-Zein, C. Bogicevic, P. Gemeiner, and J-M. Kiat, Phys. Rev. B87, 014303 (2013)

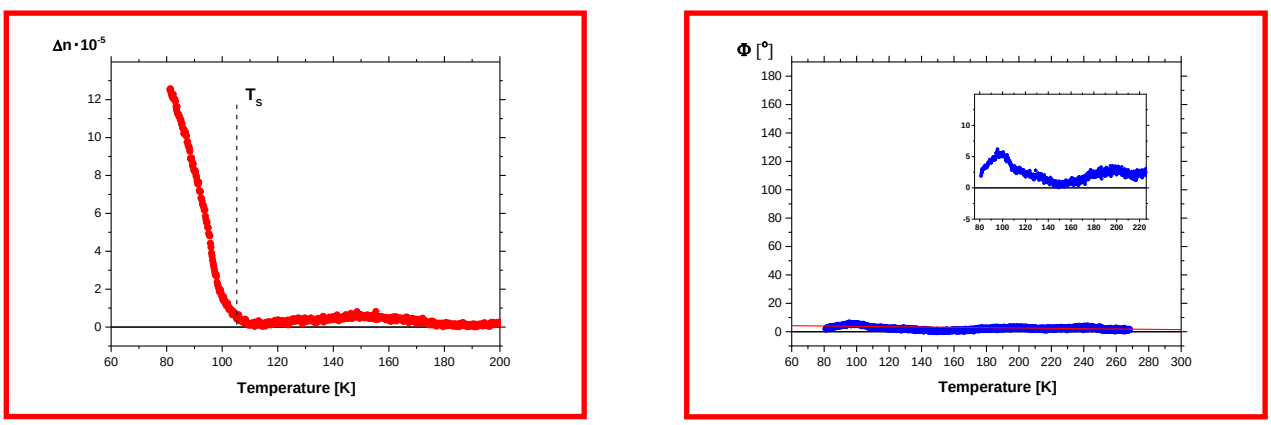

a) b)

Figure 1

Temperature dependence of birefringence for SrTiO3 single crystal (a) at almost constant orientation of optical indicatrix (b). Up to ca. 170K non-zero birefringence is present (a).

Influence of coherent twin grain boundary on domain configuration in PZT

Xiaoxing Cheng[1], Jason Britson[1], Longqing Chen[1]

[1]Department of Materials Science and Engineering,
The Pennsylvania State University, State College, PA, USA

Defects are important for the studying of ferroelectric materials, since they can induce local electric and elastic field. These pinning sites for domain wall migration will further cause the nonlinearity response under electric field. [1] Before diving into the research of switching behavior, it is meaningful to learn what domain pattern is most stable at the presence of a grain boundary, and why such type of configuration is more favorable. Some recent experiment results show domain characterization in vicinity of the grain boundary with great quality. [2] In this work, the simplest type of grain boundary, the coherent twin boundary, was introduced and studied using the time dependent Landau-Ginzburg phase field model. The composition we simulated is Pb(Zr0.2Ti0.8)O3, which has a tetragonal low temperature ferroelectric phase. Three different domain configurations were examined as it is shown in figure 1, exploring the effect of low and high angle, as well as the effect of aligned and unaligned domains. Result shows that the stress state at the grain boundary plays a vital role in stabilizing certain type of bordering domains. For example, due to the asymmetric geometry between partial head to head and partial tail to tail domains at the grain boundary, the previous one is more favored than the latter one.

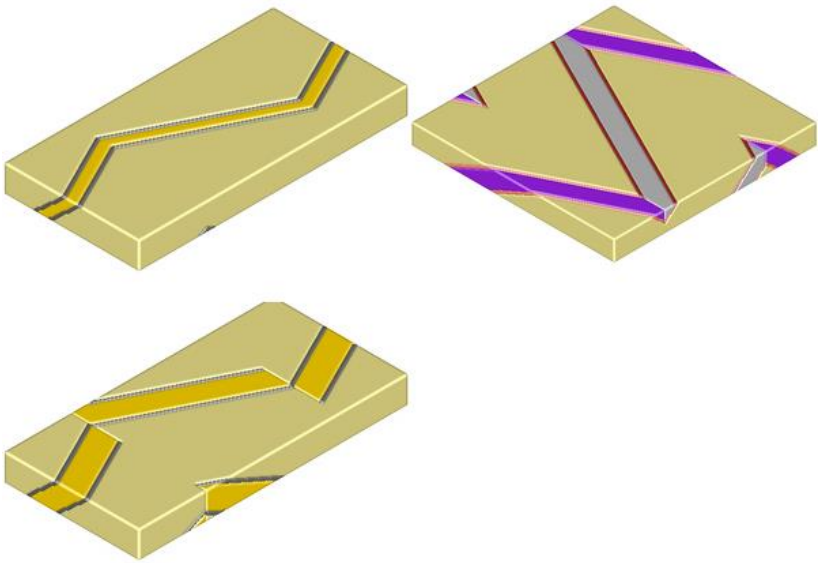

Figure 1 Three initial domain configurations.

References

[1] A. Pramanick, D. Damjanovic, J. Nino, and J. Jones, Journal of the American Ceramic Society **92**, 2291 (2009).

[2] D. Marincel, H. Zhang, A. Kumar, S. Jesse, S. Kalinin, W. Rainforth, I. Reaney, C. Randall, and S. Trolier- McKinstry, Advanced Functional Materials **24**, 1409 (2014).

Structural and Magnetic Properties of the Novel $Sr_{1-x}Ba_xMnO_3$ Multiferroics

Omar Chmaissem[1], Bogdan Dabrowski[1], James Mais[1], Stanislaw Kolesnik[1], Jeffrey W. Lynn[2]

[1]Department of Physics, Northern Illinois University, DeKalb, IL 60115, USA
[2]NIST Center for Neutron Research, National Institute of Standards and Technology, Gaithersburg, MD 20899-6102, USA

The ABO_3 perovskite structure is a very simple cubic construction of octahedral transition metals that offer tremendous opportunities, when coupled with alkaline or rare earth elements, for the creation of diverse materials physics and chemistry and novel phenomena.

$SrMnO_3$ is no exception. Several years ago [1], we have demonstrated the creation of this metastable phase through an elaborate multistep synthesis process that allows the avoidance of its energetically more favorable hexagonal counterpart. $SrMnO_3$ is a cubic room temperature paramagnet with a magnetic transition to the G-type spin configuration at temperatures below ~230 K. Structurally, the spatial symmetry must be broken in response to the magnetic ordering but no clear evidence has been seen in the diffraction data [1]. Nonetheless, examining the structural trends of Ca and Ba substituted SrMnO3 revealed the development of severe local strains as a function of increasing the A-site ionic size that result from the stretching of the Mn-O bonds to values significantly beyond their equilibrium length all while maintaining 180° Mn-O-Mn bond angles, Fig. 1. As shown in the figure, the magnetic transition temperature, T_N, increases continuously from ~120 K of the distorted $CaMnO_3$ structure until it peaks at ~230 K at the cubic $SrMnO_3$ composition. Upon further substitution with the larger Ba ions, the unit cell volume continues to increase linearly but the T_N becomes partially suppressed. In reference, we successfully proposed an empirical equation that describes this T_N behavior in terms of bond-angles and *A*-site ionic size variance. It was clear from that work that local size variations lead to significant tensions and strains coupled with a locally broken spatial symmetry due to a delicate balance of long range magnetic ordering and short range fluctuations.

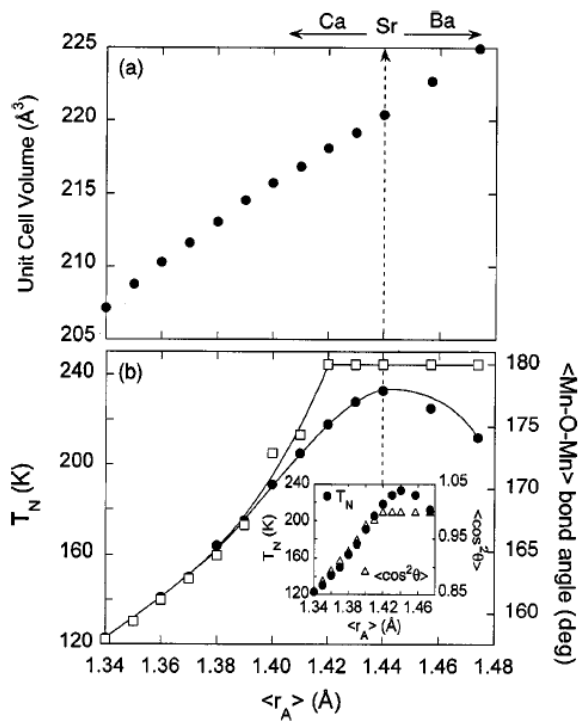

Figure 1 *(a) Room temperature unit-cell volume for $Sr_{1-x}Ca_xMnO_3$ and $Sr_{1-y}Ba_yMnO_3$. (b) T_N (filled circles) and (Mn-O-Mn) bond angle (θ) (open squares) as a function of <r_A>; The inset shows T_N and <$cos^2\theta$> (open triangles) plotted as a function of <r_A>. Figure and caption from ref. [1]*

Recently, Sakai *et al.* [2] demonstrated the successful growth of $Sr_{1-x}Ba_xMnO_3$ single crystals grown under conditions well beyond their thermodynamic equilibrium. Using this method, the Tokura group was able to extend the solubility limit of these materials to x ~ 0.5 but

most importantly they observed high temperature ferroelectric properties (T_E ~350-400 K) and huge polarization values of ~25 μC/m^2 comparable with the best values achieved in $BaTiO_3$ based ferroelectrics. Additionally, these heavily substituted compositions were found to remain antiferromagnetic as expected but with lower T_N's (~200 K). As such, $Sr_{1-x}Ba_xMnO_3$ materials are considered to be unique true multiferroics in which both the ferroelectric and magnetic order parameters occur at the same Mn sublattice. At the same time, a large number of published theoretical papers highlight the high multiferroic potential of pure and substituted $SrMnO_3$ when subjected to large internal or external pressures [see for example refs 3-8].

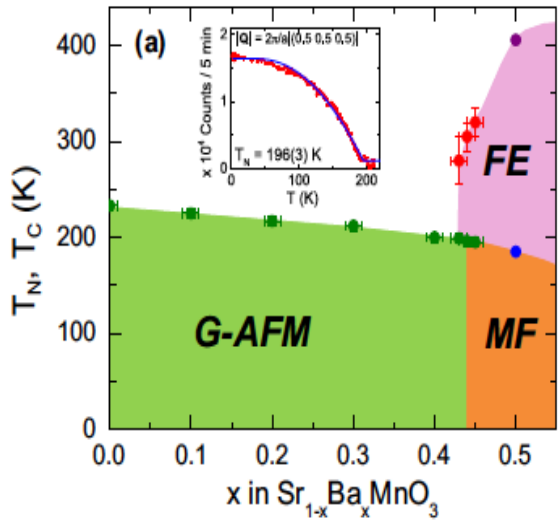

Figure 2 *Phase diagram of $Sr_{1-x}Ba_xMnO_3$ showing extended solubility in which severely strained compositions exhibit multiferroic properties with strongly coupled order parameters. Sakai's data* [2] *also included. Figure from Refs 9-10.*

Recently, we have successfully further developed our synthesis methods and have been able to extend the solubility limit of the $Sr_{1-x}Ba_xMnO_3$ phase diagram in bulk materials [9,10] to approach substitution levels close to those achieved by Sakai's single crystals. Similar ferroelectric and magnetic properties were measured for our compositions with x > 0.43. Preliminary neutron diffraction data collected at POWGEN show a series of structural and magnetic transitions that correlate with T_E and T_N's. Partial or full suppression of the magnetic transition temperature is observed as a function of the Ba content. In this talk, I will present the bulk of our measurements and discuss the materials magnetic and nuclear structures and their correlation to their physical properties.

References

[1] O. Chmaissem, B. Dabrowski, S. Kolesnik, J. Mais, D. E. Brown, R. Kruk, P. Prior, B. Pyles, J. D. Jorgensen, Phys. Rev. B **64**, 134412 (2001)

[2] H. Sakai, J. Fujioka, T. Fukuda, D. Okuyama, D. Hashizume, Kagawa, H. Nakao, Y. Murakami, T. Arima, A. Q. R. Baron, Y. Taguchi, and Y. Tokura, Phys. Rev. Lett. **107**, 137601 (2011)

[3] D. V. Efremov, J. van den Brink, and D. I. Khomskii, Nature Mater. 3, 853-856 (2004)

[4] J. H. Lee and K. M. Rabe, Phys. Rev. Lett. **104**, 207204-1-4 (2010)

[5] S. Kamba, V. Goian, V. Skoromets, J. Hejtmánek, V. Bovtun, M. Kempa, F. Borodavka, P. Vaněk, A. A. Belik, J. H. Lee, O. Pacherová, and K. M. Rabe, Phys. Rev. B **89**, 064308-1-7 (2014)

[6] A. T. Mulder, N. A. Benedek, J. M. Rondinelli, and C. J. Fennie, Adv. Funct. Mater. **23**, 4810–4820 (2013)

[7] H. Sakai, J. Fujioka, T. Fukuda, M. S. Bahramy, D. Okuyama, R. Arita, T. Arima, A. Q. R. Baron, Y. Taguchi, and Y. Tokura, Phys. Rev. B **86**, 104407-1-11 (2012)

[8] Microscopic Origin of Large Negative Magnetoelectric Coupling in $Sr_{1/2}Ba_{1/2}MnO_3$. G. Giovannetti, S. Kumar, C. Ortix, M. Capone, and J. van den Brink, Phys. Rev. Lett. **109**, 107601-1-5 (2012)

[9] D. K. Pratt, J. W. Lynn, J. Mais, O. Chmaissem, D. E. Brown, S. Kolesnik, and B. Dabrowski, Neutron Phys. Rev. B **90**, 140401(R)-1-5 (2014)

[10] J. Mais et al. [*in preparation*].

Multiferroic $Sr_{1-x}Ba_xMnO_3$ Perovskite with a Huge Magnetoelectric Coupling

B. Dabrowski[1], J. Mais[1], O. Chmaissem[1], S. Kolesnik[1], V. Goian[2], S. Kamba[2], D.K. Pratt[3], and J. Lynn[3]
[1]Deptment of Physics, Northern Illinois University, DeKalb, IL, USA,
[2]Institute of Physics, Academy of Sciences of the Czech Republic
[3]NIST Center for Neutron Research, Gaithersburg, MD, USA

e-mail: Dabrowski@anl.gov

It has been recently proposed [1-3] that it should be possible to introduce ferromagnetism and ferroelectricity in $SrMnO_3$ and derivative materials when strains up to 4.9% are achieved, with a computed huge spontaneous polarization $P_s > 54$ mC/cm^2 and $T_C > 92$ K. We have also projected earlier that similar to the d^0 titanates [4,5] strain effects should be observed in the non-d^0 perovskites resulting in a strong ferroelectric-magnetic coupling of the same magnetic ion.[6,7] However, until only recently, it was proven challenging to achieve the displacive ferroelectric distortion in the d^3 manganites because the [Mn^{4+}-O] bonds have not been put under sufficient tension.[8] By advancing elaborate synthesis processes, which are necessary to avoid the more stable hexagonal polymorphs, we were recently able to extended the substitution limit of the large size Ba ion in bulk $Sr_{1-x}Ba_xMnO_3$ samples to $x = 0.45$ with "*in situ*" synthesis in a thermogravimetric furnace in flowing H_2/Ar gas.[9]

Figure 1 demonstrates schematically the idea used to achieve such transition metal $AMO_{3-\delta}$ perovskites by use of "tolerance factor synthesis-properties design rules".[10] Relying on the simple tolerance factor $t(x, T, \delta) = [A–O]/\sqrt{2}[M–O]$ defined as a function of chemical composition, temperature and oxygen nonstoichiometry of the [A–O] and [M–O] interatomic distances, our design rules describe a sequence of synthesis steps necessary to achieve perovskites with nominally t > 1; i.e., with the [M–O] bonds put under severe internal tension.

The achieved perovskite ceramics (x = 0.4-0.45) exhibit ferroelectricity ($T_F > 300$ K) and G-type antiferromagnetism ($T_N \sim 200$ K) originating exclusively from the Mn cations. Similar to $Ba^{2+}Ti^{4+}O_3$, the classical displacive-type ferroelectric phase transition occurs for x > 0.4 when the Mn ions move out of the center of the MnO_6 octahedral units. These materials show on cooling a sequence of transitions from the paramagnetic and paraelectric cubic phase to the paramagnetic and ferroelectric tetragonal P4mm phase and finally to antiferromagnetic and paraelectric P4/mmm phase. The largest known magneto-electric coupling was observed near T_N when ferroelectricity disappears. Because of high conductivity the measurements of complex dielectric permittivity are reliable only below 40 K, where intrinsic permittivity is about 340 and does not change with magnetic field up to 9 T. The antiferromagnetic order parameter has energy

gap of 4.6(5) meV and the top of the magnon band at 43(1) meV. Nearest-neighbor exchange modeling indicates exchange constant of J=4.8(2) meV.

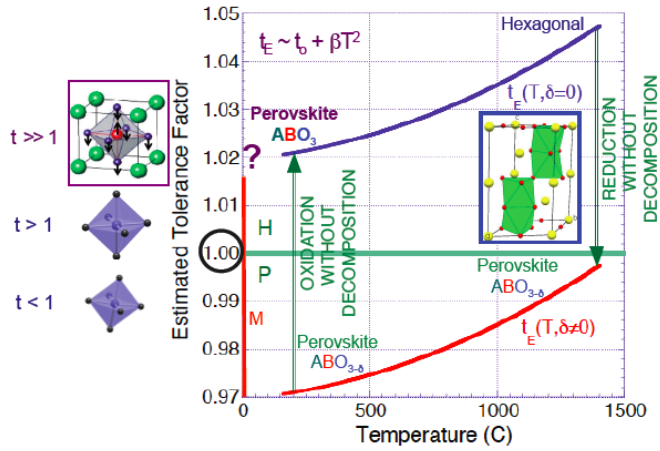

Fig.1 Schematic picture of utilization of properties of tolerance factor $t(x, T, \delta)$ to synthesize perovskites with t > 1 at room temperature.

1. J.H. Lee and K.M. Rabe, Phys. Rev. Lett. 104, 207204-1-4 (2010)
2. S. Bhattacharjee, E. Bousquet, and P. Ghosez, Phys. Rev. Lett. 102, 117602-1-4 (2009)
3. J.M. Rondinelli, A.S. Eidelson, and N.A. Spaldin, Phys. Rev. B 79, 205119-1-6 (2009)
4. V.V. Lemanov, E.P. Smirnova, P.P. Syrnikov, and E.A. Tarakanov, Phys. Rev. B 54, 3151-3157 (1996)
5. M.A. Carpenter, C.J. Howard, K.S. Knight, and Z. Zhang, J. Phys.: Condens. Matter 18 10725–10749 (2006)
6. B. Dabrowski, O. Chmaissem, J. Mais, S. Kolesnik, J.D. Jorgensen, and S. Short, J. Solid State Chem. 170, 154-164 (2003)
7. O. Chmaissem, B. Dabrowski, S. Kolesnik, J. Mais, D.E. Brown, R. Kruk, P. Prior, B. Pyles, J.D. Jorgensen, Phys. Rev. B 64, 134412 (2001)
8. H. Sakai, J. Fujioka, T. Fukuda, D. Okuyama, D. Hashizume, F. Kagawa, H. Nakao, Y. Murakami, T. Arima, A.Q.R. Baron, Y. Taguchi, and Y. Tokura, Phys. Rev. Lett. 107, 137601 (2011)
9. D.K. Pratt, J.W. Lynn, J. Mais, O. Chmaissem, D.E. Brown, S. Kolesnik, and B. Dabrowski, Phys. Rev. B 90, 140401(R) (2014)
10. B. Dabrowski, O. Chmaissem, J. Mais, and S. Kolesnik, Acta Physica Polonica A 105, 45-56 (2004)

Surface polarization, rumpling, and domain ordering of strained ultrathin $BaTiO_3$(001) films with in-plane and out-of-plane polarization

J. Dionot[1], G. Geneste[2], C. Mathieu[1] and N. Barrett[1]

[1]CEA, DSM/IRAMIS/SPEC, F-91191 Gif-sur-Yvette Cedex, France
[2]CEA, DAM, DIF, F-91297 Arpajon, France

At the surface of a ferroelectric material, out-of-plane polarization leaves non-zero surface charge which induces a depolarizing field. Complex screening mechanisms can take place to suppress this field. On the one hand, electrochemical surface charge compensation such as external adsorbates or internal defects can suppress the depolarizing field, stabilizing the polarization. On the other hand, due to the long-range character of the dipole-dipole interactions, the ferroelectric polarization can order into domains of opposite polarization such that the resulting surface charge of each domain screens the depolarizing field of the neighboring domains.

Ultrathin free-standing films (thickness ≈ 1.6 nm – 9 layers) of $BaTiO_3$ with in- and out-of-plane polarization are studied by first-principles calculations [1], with the ABINIT code, by building tetragonal supercells exhibiting alternating up (P^+) and down (P^-) polarization oriented along [001] (Fig. 1a, *c* phase) [2] or orthorhombic supercells with polarization oriented along [110] (Fig. 1a, *aa* phase) [3,4]. The substrate misfit strain is modelled by varying the in-plane lattice constant *a* within a compressive to tensile strain range of ≈ –3.8 to ≈ +1.3% with respect to the LDA lattice constant of cubic $BaTiO_3$ (a = 3.949 Å). Different supercell widths (N = 2, 4 or 6 unit cells along y) allow to investigate the multiplicity of the polarization domains in the *c* phase under periodic boundary conditions. Ferroelectric *c* and *aa* phases are compared to the paraelectric tetragonal centrosymmetric *p* phase. It has been carefully checked that the results are perfectly converged with the vacuum thickness.

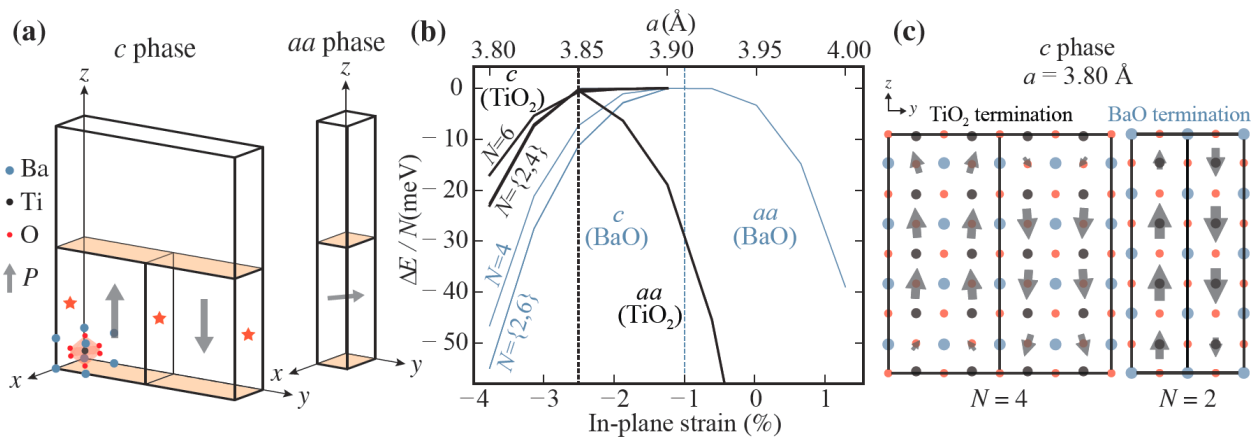

Figure 1. (a) (left) Out-of-plane polarized *c* phase and (right) in-plane polarized *aa* phase configurations. (b) Energy (meV) of the *c* and *aa* phase relative to that of the *p* phase as a function of misfit strain. (c) Polarization pattern in the fundamental state in *c* phase for *a* = 3.80 Å for the (left) TiO_2-terminated and (right) BaO-terminated film.

Out-of-plane polarization (*c* phase) is stabilized under compressive strain whereas in-plane polarization is stabilized under tensile strain, although the strain at the transition between *c* and *aa* depends on the surface termination (≈ –2.5% and ≈ –0.5% for TiO_2 and BaO termination, respectively) (Fig. 1b). This demonstrates a strong surface effect on the value of the lattice constant of the phase transition when compared to that of the bulk (at 0%). The structures of lowest total energy are found with domains 1 to 2 unit cells wide for the TiO_2 termination (Fig. 1c, left) and with domains of 1 unit cell wide for the BaO termination (Fig. 1c, right). Ferroelectric induced displacements at the surface in *c* phase are found to

modify the natural surface rumpling in the corresponding *p* phase, with oxygen atoms outwards and cations inwards in all cases.

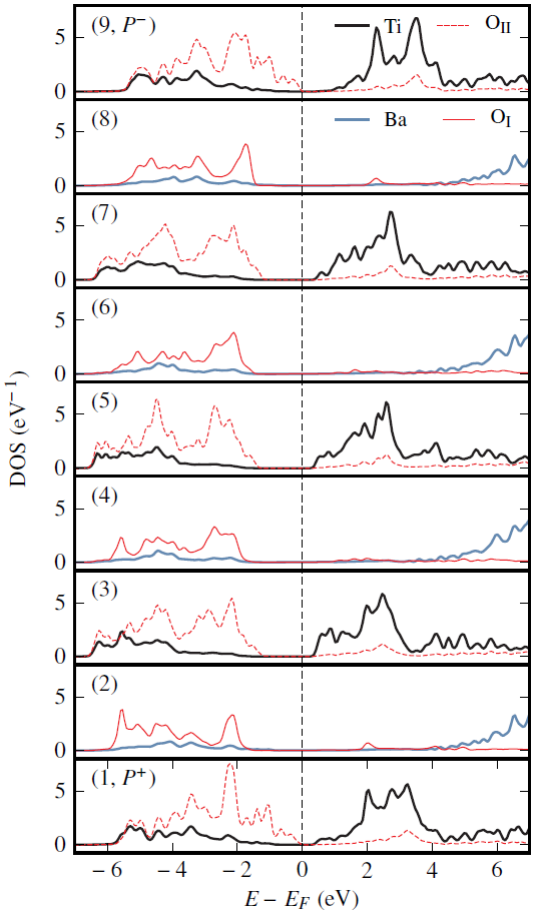

Figure 2. Electronic density of states of the c phase projected on each of the nine atomic layers of one domain of the TiO2-terminated film. $N = 6$, $a = 3.80$ Å.

Electronic density of states (DOS) calculations confirmed the presence of polarization dependent surface states (Fig. 2) that depend on the surface termination. All the surfaces studied are found to be insulating, for both *c* and *aa* phases, even though a strong reduction in the Kohn-Sham band gap (by ≈ 1 eV) is predicted for the TiO_2 surface termination in the *c* phase.

Atom-projected density of states on the (001) atomic planes of a single domain in the case of the TiO_2 termination reveals the combined effects of a microscopic and a macroscopic potential due to the presence of the surface.

Surfaces states are observed at the top of the valence band of both P^+ and P^- (atomic plane numbers 1 and 9, respectively). A clear effect of band bending can also be observed by following the band edges, mostly produced by a difference in the Madelung potential between the oxygen sites at the surface and in the bulk. This microscopic potential is higher in the *c* phase than in the *aa* phase as a consequence of the ferroelectric distortions.

A potential difference of ≈ 0.2 eV between the top of the valence band at P^+ and P^- in the *c* phase is assigned to imperfect screening of the depolarizing field. This is evidenced by the observation of a residual macroscopic potential computed as a double average over (001) atomic planes and then along [001]. Nevertheless, the microscopic Madelung potential at the surface is predicted to play a more prominent role in modifications of the surface electronic structure at this ultrathin film thickness.

This work was performed using the HPC from GENCI-CCRT/CINES (Grant No. 2013-097037). We gratefully acknowledge funding from the Agence Nationale de la Recherche (Project ANR-12-IS04-0001-01 CHEM-SWITCH). Ph. Ghosez is acknowledged for fruitful discussions.

References

[1] J. Dionot, G. Geneste, C. Mathieu and N. Barrett, *Physical Review B* **90**, 014107 (2014)
[2] T. Shimada, S. Tomoda and T. Kitamura, *Physical Review B* **81**, 144116 (2010)
[3] N. A. Pertsev, A. G. Zembilgotov and A. K. Tagantsev, *Physical Review Letters* **80**, 1988 (1998)
[4] B.-K. Lai, I. A. Kornev, L. Bellaiche and G. J. Salamo, *Applied Physics Letters* **86**, 132904 (2005)

Role of interface termination in $SrRuO_3/PbTiO_3/SrRuO_3$ capacitors under epitaxial strain

Simon Divilov[1] and M.-V. Fernández-Serra[1,2]

[1] *Department of Physics and Astronomy, Stony Brook University, Stony Brook, New York 11794-3800, USA*

[2] *Institute for Advanced Computational Sciences, Stony Brook University, Stony Brook, New York 11794-3800, USA*

Ferroelectric devices have seen large advances in terms of speed, density and resistance to degradation allowing them to potentially become a standard for non-volatile memory[1]. A recent study[2] has looked at ultrathin films of SRO/PTO mainly in terms of total energy and Schottky barriers, however we believe not everything is yet fully understood about these systems.

In this work we use density functional theory (DFT) within the local density (LDA) and local spin density with spherically averaged Hubbard U (LSDA+U) approximations using numerical atomic orbitals implemented in the SIESTA[3] code. The systems under consideration are symmetrically terminated SRO/$(PTO)_m$ bulk and SRO/$(PTO)_m$/SRO slabs, where m is an integer. There are two possible geometries, either we have RuO_2-SrO-RuO_2/(PbO-$TiO_2)_m$-PbO/[RuO_2-SrO-RuO_2] or SrO-RuO_2-SrO/TiO_2-(PbO-$TiO_2)_m$/[SrO-RuO_2-SrO], as illustrated in Fig. 1, where the term in the square brackets is absent from the supercell of the bulk system. We varied the amount of PTO unit cells from 2 and 4, the supercell area, A, from 1×1 to $\sqrt{2}\times\sqrt{2}$ and the in-plane lattice constant ($a = b$) from 3.87 Å to 3.67 Å.

For open circuit boundary conditions (OCBC) a dipole moment, for the whole SRO/PTO/SRO system, develops when the lateral lattice constant, a, is 3.67 Å and 3.77 Å for SrO and RuO_2 terminated surfaces, respectively (Fig. 2a). This result can be understood from the fact that when the surface is terminated by RuO_2 rather than SrO, there are twice as many metallic states to provide better screening. The exception to this is RuO_2 terminated surface with parameters $A = \sqrt{2}\times\sqrt{2}$ and $m = 2$, where not only does a polar order appear at increased strain, but also disappears as additional strain is introduced.

For closed circuit boundary conditions (CCBC), we measure Δ_{norm} a parameter that is zero when no polar order is present and unity when the polar order is equal to that of bulk

PTO with the same a. Even with perfect screening the development of polar order with respect to a coincides with OCBC, with interfaces terminated by RuO_2 exhibiting a larger polar order (Fig. 2b). We believe the explanation lies in the interfacial layer, $PbRuO_3$, which plays a role in driving the minimization of the total energy (similar to the anomaly in the OCBC case) due to the fact that it is under the largest compressive strain compared to other layers.

Our analysis also includes the effects of interfaces on structural relaxations, spin polarization, metal-induced gap states and generalized capacitance (a different measure of instabilities due to polar order).

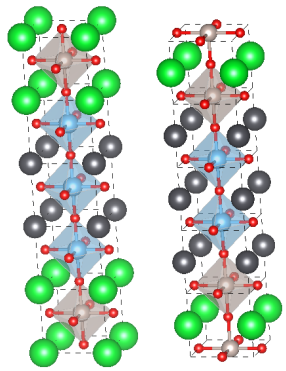

(a) (b)

FIG. 1: Supercell of the slab for SRO/$(PTO)_2$/SRO when the termination plane is either (a) SrO or (b) RuO_2. Green, grey, brown, blue and red correspond to Sr, Pb, Ru, Ti and O, respectively. The images were generated using VESTA[4].

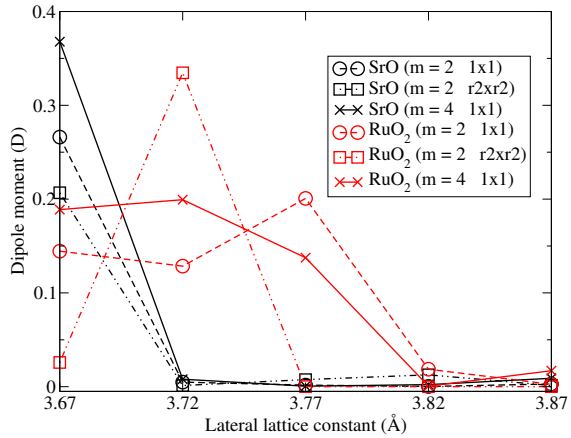

(a)

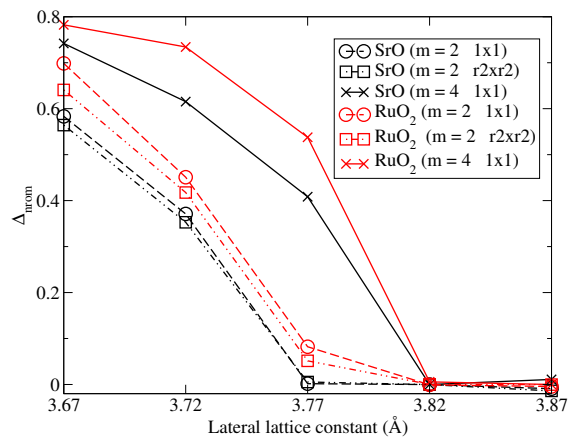

(b)

FIG. 2: Calculations of the polar order in (a) open and (b) closed circuit boundary conditions. Black (Red) refers to SrO (RuO_2) interface terminated.

[1] J. F. Scott and C. A. P. de Araujo, Science **246** (1989), 10.1126/science.246.4936.1400.

[2] Y. Umeno, J. M. Albina, B. Meyer, and C. Elssser, Phys. Rev. B **80** (2009), 10.1103/PhysRevB.80.205122.

[3] J. M. Soler, E. Artacho, J. D. Gale, A. García, J. Junquera, P. Ordejón, and D. Sánchez-Portal, J. Phys. Condens. Matter **14** (2002), 10.1088/0953-8984/14/11/302.

[4] K. Momma and F. Izumi, J. Appl. Crystallogr. **44** (2011), 10.1107/S0021889811038970.

Piezoelectric constants of $KNbO_3$ by molecular dynamics simulations using a shell model

T. Hashimoto[1], H. Moriwake[2]

[1]Nanosystem Research Institute (NRI), National Institute of Advanced Industrial Science and Technology (AIST), Tsukuba Central 2, 1-1-1 Umezono, Tsukuba, Ibaraki 305-8568, Japan
[2]Nanostructures Research Laboratory, Japan Fine Ceramics Center, 2-4-1 Mutsuno, Atsuta-ku, Nagoya, 456-8587, Japan

$KNbO_3$ is an ABO_3 type perovskite whose solid solution with other A site atoms could be a potential candidate for Pb free piezoelectric materials. $KNbO_3$ undergoes phase transitions among, listing from high temperature to low temperature, cubic (C), tetragonal (T), orthorhombic (O), and rhombohedral (R) phases. Despite its importance, the number of the experimental reports on the piezoelectric constants of $KNbO_3$ is small due to the difficulty in the growth of high quality crystals and in the poling treatments, and these reports are limited to room temperatures. In this paper, we predicted the temperature dependence of the piezoelectric coefficients of $KNbO_3$ by molecular dynamics simulations using a shell model[1].

The piezoelectric constants were calculated by[2-4]

$$d_{kij} = \left(\frac{\partial \eta_{ij}}{\partial E_k}\right)_{\sigma,T} = \frac{1}{k_B T} \langle \Delta M_k \Delta \eta_{ij} \rangle .$$

Here, η, $\mathbf{E}$, σ, T, k_B, and $\mathbf{M}$ are the strain tensor, the electric field, the stress, the temperature, the Boltzmann's constant, and the total dipole moment of the MD cell, respectively. ΔX represents X - $\langle X \rangle$, where X is M_k or η_{ij}.

Figure 1 shows the temperature dependence of piezoelectric coefficients d_{ij} for $KNbO_3$ in all three ferroelectric phases. The results were similar to those by the Landau-Ginzburg-Devonshire (LGD) theory[5] and the first-principles calculations for the R phase[6] of $KNbO_3$. The shear and some of the longitudinal piezoelectric constants changed by 200 — 300 % depending on the temperature. This is because the dipole moment deviation from its average value and the strain deviation from its average value are greatly dependent on temperatures. So, it should be difficult to predict the piezoelectric constants by first-principles calculations except for the R phase.

We also predicted the temperature dependence of the longitudinal piezoelectric surface d^*_{33} of $KNbO_3$. The results were also similar to the previous calculations, since the temperature dependence of the piezoelectric constants were similar to them. Near the T-C phase transition temperatures, due to the enhanced d_{33}, d^*_{33} is large along the polar direction. For other temperatures, especially near the phase boundaries, the large shear piezoelectric constants result in the maximum of d^*_{33} along the non-polar directions.

Acknowledgements The computations were carried out on SGI Altix ICE 8400EX at ISSP Supercomputer Center, University of Tokyo, and ASC and AGC in AIST. This work was supported by the Ministry of Education, Culture, Sports, Science and Technology of Japan through the Grant-in-Aid for Scientific Research on Innovative Areas ”Nano Informatics” and Scientific Research C (No. 24560833) from JSPS.

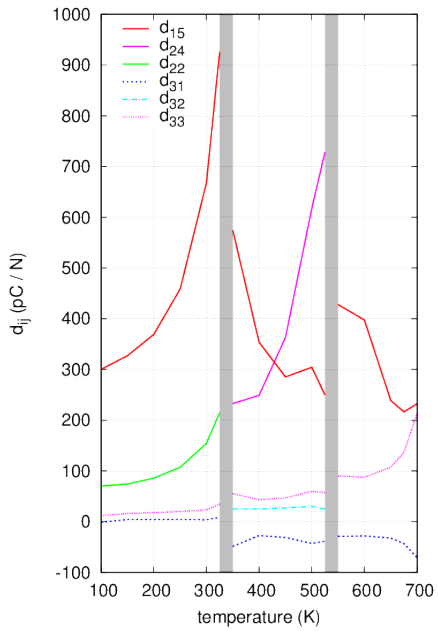

Figure 1. Piezoelectric coefficients for $KNbO_3$.

References

[1] M. Sepliarsky, A. Asthagiri, S. R. Phillpot, M. G. Stachiotti, and R. L. Migoni, Curr. Opin. Solid. St. M. **9**, 107113 (2005).
[2] A. Garcia and D. Vanderbilt, Appl. Phys. Lett. **72**, 2981(1998).
[3] A. Garcia and D. Vanderbilt, First-Principles Calculations for Ferroelectrics: Fifth Williamsburg Workshop, R.E. Cohen, ed. (AIP, Woodbury, New York, 1998) , 53 (1998).
[4] K. M. Rabe and E. Cockayne, First-Principles Calculations for Ferroelectrics: Fifth Williamsburg Workshop, R.E. Cohen, ed. (AIP, Woodbury, New York, 1998) , 61 (1998).
[5] L. Liang, Y. L. Li, S. Y. Hu, L.-Q. Chen, and G.-H. Lu, J. Appl. Phys. **108**, 094111 (2010).
[6] L. F. Wan, T. Nishimatsu, and S. P. Beckman, J. Appl. Phys. **111**, 104107 (2012).

Ab Initio phonon calculations in metallic and insulating VO_2

Christopher Hendriks, Eric J. Walter, Henry Krakauer
Department of Physics, College of William and Mary, Williamsburg, VA 23187, USA

Vanadium dioxide (VO_2) undergoes a first-order metal-insulator transition (MIT) from the high temperature rutile phase (R) to an insulating, low temperature monoclinic phase (M1). Several competing insulating phases exist, with phase boundaries in a narrow temperature and strain range close to the MIT [1, 2]. Recently, novel IR and Raman measurements of micro- and nano-structured VO_2 samples have become increasingly available; this allows the phases to be studied while avoiding many difficulties with bulk samples, such as twinning and cracking on cycling through the MIT. Theoretical calculations of vibrational properties can assist in the interpretation of such experiments [3].

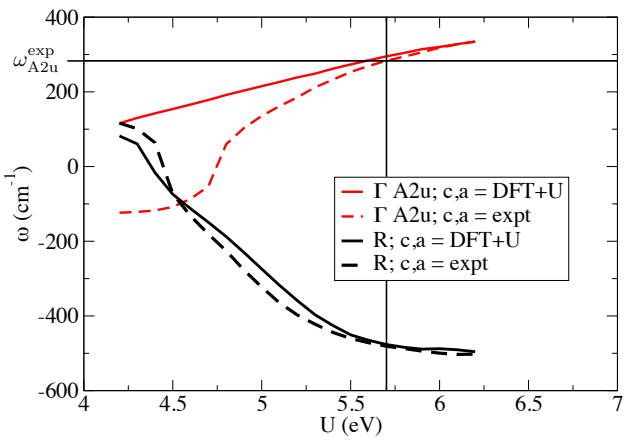

Figure 1: Rutile phonon frequencies vs Hubbard U (J was fixed at 0.8 eV). Calculations were performed using experimental and DFT+U optimized lattice parameters. Vertical line shows $U = 5.7$ eV; horizontal line shows experimental A2u frequency.

We will present first-principles calculations of phonon frequencies for the various phases and compare these to available measurements for the R, M1, M2 and T phases. All calculations were done with the Vienna Ab-initio Simulation Package (VASP) [6]. Phonon frequencies were obtained through computation of force constants via density functional perturbation theory and subsequent analysis using PHONOPY [7]. To describe correlation effects within the V 3d bands, we used the DFT+U extension of standard DFT (= GGA). Calculated results can depend sensitively on the numerical value of the effective on-site electronic interaction parameter, the Hubbard U. A common approach is to tune the value of U in a semi-empirical way, seeking agreement with available experimental measurements of certain properties. One can then use the so determined value to make predictions on other aspects of the behavior of the system of interest. We adopt this approach here.

Experiment	Theory
–	126
201	211
227	232
293	304
340	413
434	446
451	500
648	643
–	667
829	834

Table 1: Comparison of Ag Raman frequencies for M2. Values are in cm^{-1}.

Since the metalic R phase is the parent compound of the various insulating phases that we are interested in studying, we focus on its calculated phonon frequencies and structural instabilities. For example, the M1, M2 and related phases can be traced to harmonically unstable R-point modes. We find the unstable R mode (two-fold degenerate) and the A2u Γ-mode to be most sensitive to the value of U. Figure 1 shows the variation of these phonon modes in rutile VO_2 as a function of the Hubbard parameter U. With $U = 0$ eV, i.e. regular DFT, there is no R-point instability. Adjusting U so that the calculated Γ-point A2u mode frequency agrees with experiment yields $U = 5.7$ eV. Previously, IR phonon calculations in the M1 phase have been reported using a slightly different value of U [3]; the current work yields similarly good agreement with experiment for the R and M1 phase. In addition, our comparison of calculated M2 Raman Ag frequencies with experimental measurement also show good agreement, as shown in Table 1.

Increasingly measurements are being made on micro- and nano-structured VO_2. Such samples facilitate experimental control of applied stress and external

fields to study the properties of the various phases. For example, recent measurements of M1 to M2 phase changes have been reported for VO_2 nano-rods under applied uniaxial strain, showing changes in Raman active phonon frequencies [2]. Theoretical calculations can help interpret these experiments. We will report strain dependent phonon frequencies on the different phases.

Acknowledgments: This work was supported by ONR grant N00014-12-1-1042. Calculations were performed on the SciClone cluster at the College of William and Mary.

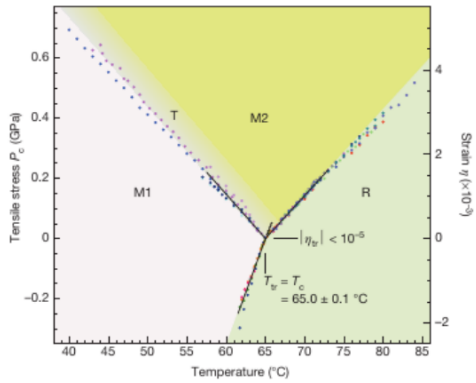

Figure 2: Strain-temperature phase diagram showing the VO_2 triple point.[1]

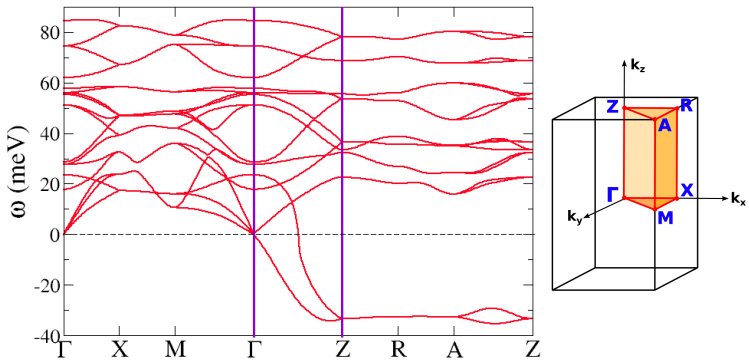

Figure 3: Dispersion curve of rutile VO_2 ($U = 4.2$ eV).

References

[1] J. H. Park, J.M. Coy, T.S. Kasirga, C. Huang, Z. Fei, S. Hunter and D.H. Cobden, *Nature* **500**, 431 (2013).

[2] J. M. Atkin, S. Berweger, E. Chavez, M.B. Raschke, *Phys. Rev. B* **85**, 020101 (2012).

[3] T. J. Huffman, P. Xu, M.M. Qazilbash, E.J. Walter, H. Krakauer, J. Wei, D.H. Cobden, H.A. Becthel, M.C. Martin, G.L. Carr and D.N. Basov, *Phys. Rev. B* **87**, 115121 (2013).

[4] P. Schilbe and D. Maurer, *Mat. Sci. and Eng. A* **370**, 449-452 (2004).

[5] C. Marini, E. Arcangeletti, D. Di Castro, L. Baldassare, A. Perucchi, S. Lupi, L. Malavasi, L. Boeri, E. Pomjakushina, K.Conder and P. Postorino, *Phys. Rev. B* **77**, 235111 (2008).

[6] G. Kresse and J. Furthmüller, *Phys. Rev. B* **54**, 11169 (1996).

[7] A. Togo, F. Oba, and I. Tanaka, *Phys. Rev. B* **78**, 134106 (2008).

Tailored Polarization Reversal and Terahertz Frequency Dynamics in Ferrolectric Nanowires

Ryan Herchig, C.-M. Chang, B. K. Mani, and Inna Ponomareva
Department of Physics, University of South Florida, Tampa, Florida 33620, USA
e-mail: rch@mail.usf.edu

One promising application of ferroelectric nanowires is for use in ferroelectric memory devices which utilize the binary nature of the reversible polarization to store, read, and write a bit of information.[1] However, the field required to reverse the polarization could be quite large for ferroelectrics.[2] In the interest of energy efficiency, it is desirable to reduce this polarization reversal field (PRF). In this work, we propose one way to achieve such a reduction in ferroelectric nanowires. Our approach is to superimpose a subswitching *dc* electric field with a Gaussian-shaped terahertz electric field pulse. The bias field establishes a preferential direction for the polarization, while the THz pulse provides the energy necessary to raise the nanowire's temperature,[3] thus lowering the PRF in the nanowire.

We developed a computational method which uses classical Molecular Dynamics with the force field derived from the first-principles based effective Hamiltonian.[4] Two nanowires made of $PbTiO_3$ and $Pb(Ti_{0.6}Zr_{0.4})O_3$ with square cross-sections of 21.8 nm^2 were simulated. Below the Curie temperature, each nanowire developed polarization along the axial direction under open-circuit boundary conditions. Next the nanowires were subjected to the electric field

$$E\left(t\right) = E_b + E_0 cos(\omega t) e^{-\left(\frac{t-t_0}{\tau}\right)^2}, \tag{1}$$

where E_b is the subswitching *dc* field applied in the direction opposite to the initial polarization vector. The amplitude of the pulse is given by E_0, while $\omega = 2\pi\nu$ is frequency, t_0 is the time at which the Gaussian envelope is centered, and τ is the pulse half-width.

To achieve polarization reversal in the nanowires, it is essential that the frequency of the THz pulse belongs to the range of frequencies associated with the large imaginary part of the complex electric susceptibility, ϵ_2, of the nanowire. To determine this frequency range, we calculated the complex dielectric response in $PbTiO_3$ and $Pb(Ti_{0.6}Zr_{0.4})O_3$ bulk and nanowires both in the absence and in the presence of bias electric fields. In $PbTiO_3$, the soft mode is underdamped and as a result, its ε_2 exhibits a relatively narrow peak centered at the mode characteristic frequency. The data for the characteristic frequency as a function of temperature for the nanowire is shown in Fig. 1(b). For comparison, we also report computational data for bulk $PbTiO_3$. From Fig. 1(b), we see that the $\nu_0\left(T\right)$ for the nanowire are shifted to the left with respect to the branches for bulk $PbTiO_3$. This is due to the decrease in the Curie point for the nanowires. The complex dielectric response of the nanowire is also affected by the presence of the bias field. In Fig. 1(b), we report the characteristic frequencies of the nanowire subjected to a bias field of 450 kV/cm. The effect of the bias field is to shift the $\nu_0\left(T\right)$ branches further to the left if the field is applied in the direction opposite to the polarization. The field also reduces the degree to which the mode-softening occurs. The dependence of the soft-mode dynamics on the size as well as on the applied electric field could be utilized to enhance the tunability of ferroelectric devices. The frequency response determines the band-width of a device, so by applying bias fields of various strengths, the sensitivity of a ferroelectric device can be tuned to a specific frequency.

We investigated the possibility of controllable polarization reversal through tailoring the parameters of the electric field, E_b, E_0, ν, and τ. By varying the parameters we found

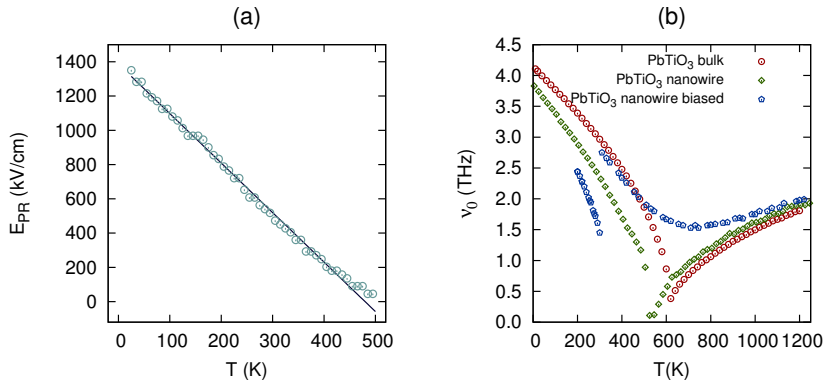

FIG. 1. Panel (a) shows the dependence of the polarization reversal field in the $PbTiO_3$ nanowire on the temperature. Panel (b) summarizes the dependence of the characteristic frequency on the temperature in bulk $PbTiO_3$, biased and unbiased $PbTiO_3$ nanowire. The bias field is 450 kV/cm.

that their certain combinations lead to polarization reversal in the nanowire. Briefly, for polarization reversal to occur, the pulse needs to supply the energy sufficient to elevate the nanowire's temperature by $\Delta T \approx \frac{dT}{dE_{PR}} \left(E_b + E_0 - E_{PR}\left(T_{init}\right)\right)$, where $\frac{dT}{dE_{PR}}$ is the slope in the $T\left(E_{PR}\right)$ dependence in Fig. 1(a), while $E_{PR}\left(T_{init}\right)$ is the PRF associated with the initial temperature. The change in the nanowire's temperature due to the interaction with the THz pulse is given by $\Delta T \approx \sqrt{\frac{\pi}{8}} \frac{\varepsilon_2(\omega)\varepsilon_0 E_0^2 \tau\omega}{C_P}$ [3], where C_P is the heat capacity at constant pressure. Combining these two expressions, we obtain a relationship between the parameters of the electric field associated with polarization reversal in the nanowire

$$\sqrt{\frac{\pi}{8}} \varepsilon_2\left(\omega, T, E_b\right) E_0^2 \tau\omega = C_P\left(E_b + E_0 - E_{PR}\left(T_{init}\right)\right). \tag{2}$$

The set of parameters which satisfies Eq. (2) is expected to reverse the polarization in the nanowire. We tested the validity of Eq. (2) and will report our results for both $PbTiO_3$ and $Pb(Ti_{0.6}Zr_{0.4})O_3$ nanowires.[5]

Acknowledgments: The present work is supported by the Army Research Office under contract 57787-EL (polarization reversal studies) and by the U.S. Department of Energy, Office of Basic Energy Sciences, Division of Materials Sciences and Engineering under award DE-SC0005245 (soft mode dynamics studies).

---

[1] K. Uchino, *Ferroelectric devices* (Marcel Dekker, Inc., New York-Basel, 2000)
[2] S. Kim, V. Gopalan, and A. Gruverman, Applied Physics Letters **80**, 2740 (2002)
[3] R. Herchig, K. Schultz, K. McCash, and I. Ponomareva, Nanotechnology **24**, 045501 (2013)
[4] B. K. Mani, C.-M. Chang, and I. Ponomareva, Phys. Rev. B **88**, 064306 (2013)
[5] R. Herchig, C.-M. Chang, B. K. Mani, and I. Ponomareva, Applied Physics Letters **105**, 012907 (2014)

Direct band gaps in multiferroic h-$LuFeO_3$

B. S. Holinsworth, D. Mazumdar, C. M. Brooks, J. A. Mundy, H. Das, J. G. Cherian, S. A. McGill, C. J. Fennie, D. G. Schlom, and J. L. Musfeldt

Abstract :
We measured the optical properties of epitaxial thin films of the metastable hexagonal polymorph of LuFeO3 by absorption spectroscopy, magnetic circular dichroism, and photoconductivity. Comparison with complementary electronic structure calculations reveals a 1.1 eV direct gap involving hybridized Fe $3d_z^2$ + O $2p_z$ to Fe *d* excitations at the Γ and A points, with a higher energy direct gap at 2.0 eV. Both charge gaps nicely overlap the solar spectrum.

Electrical Transport and Magnetic Properties of $PbTiO_3/SrRuO_3$ superlattices

H.C. Hsing, S.J. Callori, J. Gabel, S. Divilov, P. Kumaravadivel, X. Du, M.V. Fernandez-Serra

and M. Dawber

Department of Physics and Astronomy, Stony Brook University, Stony Brook, NY 11790, USA

Artificially structured oxides present exciting opportunities to design materials with specified or novel properties [1,2]. With advanced epitaxial growth techniques, multicomponent perovskite heterostructure with desired dielectric, ferroelectric and magnetic behavior can be achieved experimentally. Currently, we have successfully fabricated $PbTiO_3/SrRuO_3$ (PTO/SRO) superlattices with ultra thin $SrRuO_3$ layers through RF magnetron off-axis sputtering [3]. The superlattice thin films (100nm) with top and bottom $SrRuO_3$ electrodes were deposit on a TiO_2 terminated $SrTiO_3$ substrate. The structure and quality of the films were examined through transmission electron microscope (HRTEM), X-ray diffraction (XRD) and atomic force microscopy (AFM). In addition, the electrical properties were obtained using a home-built probe station, and the magnetocapacitance measurement of the samples is done with a superconducting magnet system.

Here, our samples show a large anisotropy in their electrical resistvity, which can be tuned by changing the $PbTiO_3$ layer thickness. Along the out of plane direction, the samples demonstrate ferroelectricity and tunneling current characteristics that confirm the metallicity of the $SrRuO_3$ layers but can also act as a novel dielectric component. From the HRTEM cross-sectional image, Figure 1(a), we show evidence of thin SRO layers within the superlattice and that good quality is achieved throughout the sample. One important characteristic of our superlattices is the compositional breaking of inversion symmetry. The superlattice system of $PbTiO_3/SrRuO_3$ has both A site and B site variation that can break the inversion symmetry, as seen in Figure 1(b), resulting in a preference for a particular polarization direction. Perovskite-oxide superlattice systems demonstrating broken inversion symmetry have been both theoretically and experimentally studied in recent years. However, experimentally the systems are mostly deposited with three different materials to achieved symmetry breaking [4]. Figure 2(a) shows the calculated double well potential for LDA (local density approximation). To compare structures with a different composition, the energy is plotted in energy per unit cell instead of total energy. When the PTO layer is around 7 unit cells or less, the potential double-well is asymmetric and indicates a favored polarization state. Once the PTO layer increases to 9 unit cells and above, the PTO becomes the dominant phase and the system is not affected by the breaking of inversion symmetry, so the potential double-well remains symmetric.

In this work, we studied the impact of the compositionally broken inversion symmetry and magnetic field on the capacitance-voltage characteristic of our superlattices. As seen in Figure 2(b), the 5/1 and 7/1 PTO/SRO samples, the effect of the compositional inversion symmetry breaking is significant and the two peaks in the dielectric constant butterfly loop shifts to the right. Once the PTO layer thickness increases to 9 unit cells or more, the PTO becomes dominant and the system is a conventional ferroelectric material with the butterfly loop centered close to 0V. To investigate potential magnetoelectric coupling, we have applied a magnetic field to our samples at low temperature while measuring the dielectric constant. Acknowledgement: This work was funded by NSF DMR1334867.

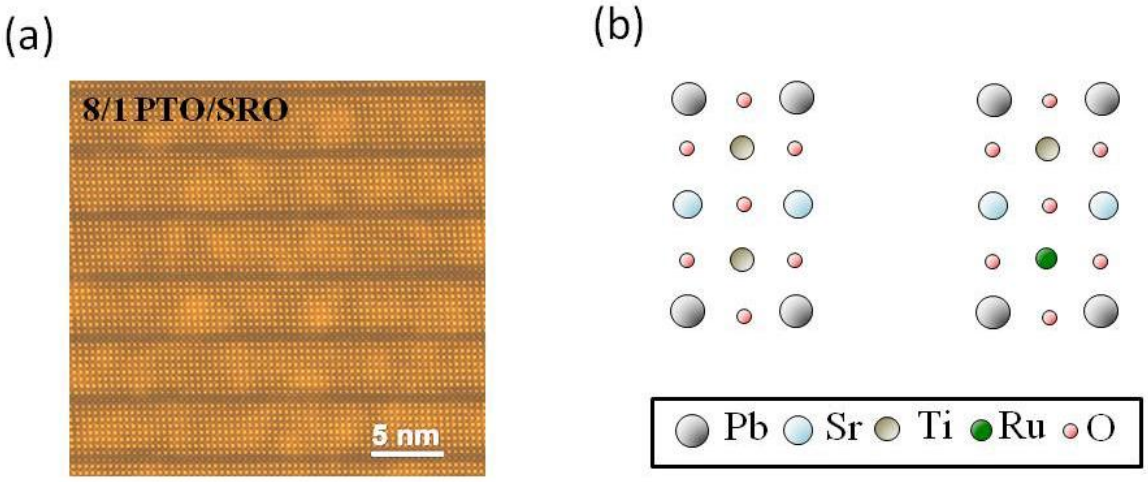

Figure 1. (a) HRTEM cross-sectional image of 8/1 PTO/SRO superlattice. (b)Superlattice interface of only A site changes (left) and where both the A and B site changes (right) resulting in the breaking of inversion symmetry.

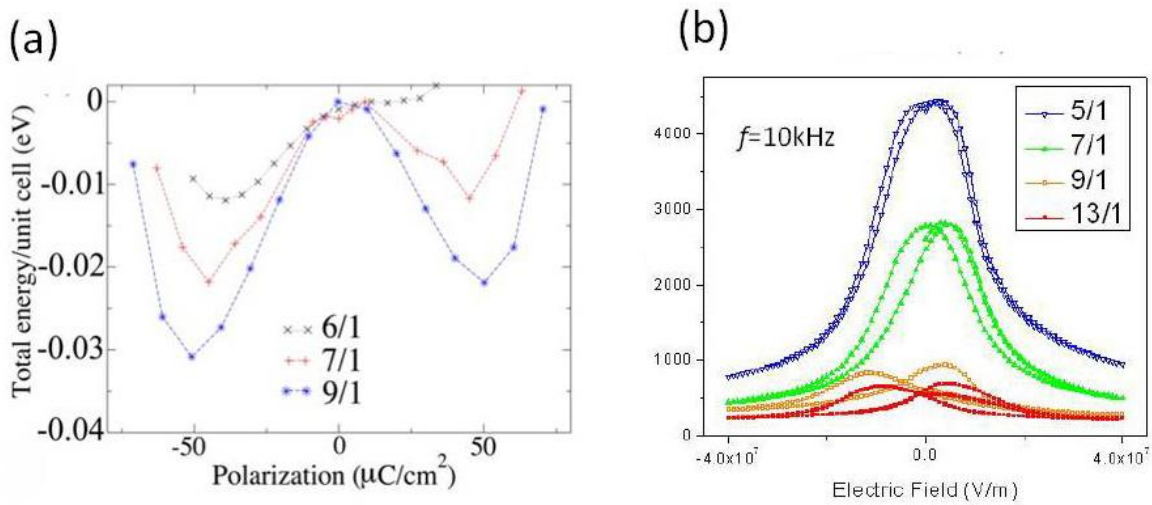

Figure 2. (a)) Total energy of several PbTiO3/SrRuo3 superlattices plotted as a function of polarization. (b) Comparison of dielectric constant between different PTO/SRO superlattices.

Reference

[1] C. H. Ahn, K. M. Rabe and J.-M. Triscone, "Ferroelectricity at the Nanoscale: Local Polarization in Oxide Thin Films and Heterostructures," *Science* **303**, 488 (2004).
[2] M. Dawber, K. M. Rabe and J. F. Scott, "Physics of thin-film ferroelectric oxides," *Rev. Mod. Phys.* **77**, 1083 (2005).

[3] S.J. Callori, J. Gabel, D. Su, J. Sinsheimer, M.V. Fernandez-Serra and M. Dawber, "Ferroelectric *PbTiO*3/*SrRuO*3 Superlattices with Broken Inversion Symmetry," *Phys. Rev. Lett.***109**, 067601 (2012).

[4]H.N. Lee, H.M. Christen, M.F. Chisholm, C.M. Rouleau and D.H. Lowndes, "Strong polarization enhancement in asymmetric three-component ferroelectric superlattices," *Nature* **433**, 395 (2005).

Purely electric-field-driven perpendicular magnetization reversal

Jia-Mian Hu[1]*, Tiannan Yang[1], Jianjun Wang[2], Houbing Huang[1], Ce-Wen Nan[2], and Long-Qing Chen[1]

[1]Department of Materials Science and Engineering, Pennsylvania State University,
University Park, Pennsylvania 16802, USA
[2]School of Materials Science and Engineering, and State Key Lab of New Ceramics and Fine Processing,
Tsinghua University, Beijing 100084, China

Magnetization reversal purely with an electric field, if achieved, has the potential to revolutionize the spintronic devices that currently utilize power-dissipating currents. However, all existing proposals involve the use of a magnetic field. Here we use phase-field simulations to study the piezoelectric and magnetoelectric responses in a three-dimensional multiferroic nanostructure consisting of a perpendicularly magnetized nanomagnet with an in-plane long axis and a juxtaposed ferroelectric nanoisland. We demonstrate, for the first time, a full reversal of perpendicular magnetization via successive precession and damping, driven purely by a perpendicular electric-field pulse of certain pulse duration across the nanoferorroelectric. We discuss the materials selection and size dependence of both nanoferroelctrics and nanomagnets for experimental verification. These results offer new inspiration to the design of spintronic devices that simultaneously possess high density, high thermal stability, and high reliability.

*E-mail: juh34@psu.edu

Ferroelectric phase transitions in stressed $SrTiO_3$ thin films

A. I. Lebedev

Physics Department, Moscow State University, Moscow, 119991, Russia

The strain engineering is a widely used technique in modern electronics. When searching for new applications of ferroelectrics, the first-principles studies of the strain effects are usually performed using the fixed-strain boundary conditions. At the same time, for studying the strain effects in substrate-free thin films or thick films, the using of *fixed-stress* boundary conditions seems more preferable. In this work, we use the first-principles density functional theory to study the ferroelectric instability in stressed strontium titanate thin films, calculate the phase diagram of this system, and discuss possible application of the bistability revealed in the ferroelectric properties of this system.

The calculations of the equilibrium lattice parameters and atomic coordinates of thin films of $SrTiO_3$ subjected to biaxial tensile or compressive stress were performed within the first-principles density functional theory using the ABINIT program. The film was relaxed in the direction normal to its surface. The exchange-correlation interaction was described in the local density approximation. The pseudopotentials of atoms were constructed following the RKKJ scheme. The cut-off energy was 30 Ha. The integration over the Brillouin zone was performed on the 8×8×8 Monkhorst–Pack meshes for the cubic cell or meshes with equivalent density of *k*-points for lower-symmetry phases. To obtain the ground-state structure for each in-plane stress, the phonon spectrum and elastic tensor were calculated for all possible phases and it was checked whether the frequencies of all optical phonons at all points of the Brillouin zone are positive and if the determinant and all principal minors constructed of the elastic tensor components are positive (the stability criterion).

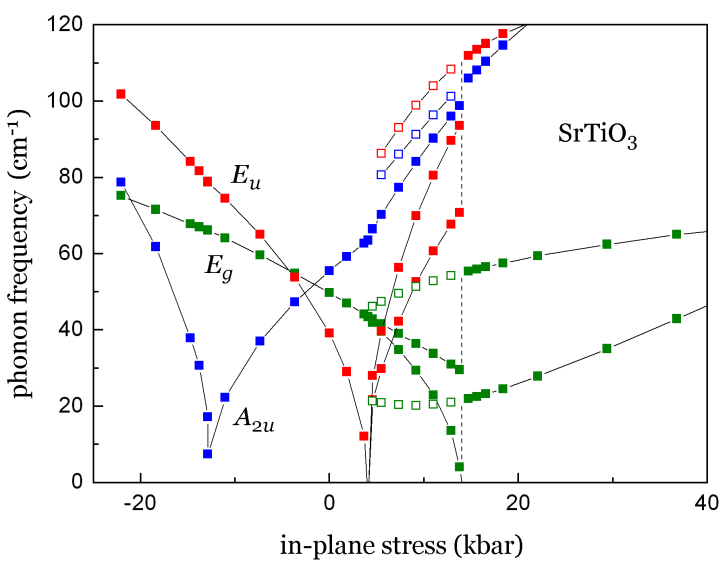

Fig. 1. The frequencies of the phonon spectrum in the ground-state structures of stressed $SrTiO_3$ thin film at different in-plane stresses.

Under the biaxial stress, the structure of high-temperature cubic phase of $SrTiO_3$ is reduced to tetragonal (*P*4/*mmm* space group), and the *I*4/*mcm* phase is the ground state in the pressure range from $p = -13$ kbar to $p = +4.1$ kbar (Fig. 1). The existence region of this phase is limited by the softening of the ferroelectric A_{2u} mode (under the compressive conditions) and of the E_u one (under tensile conditions). When crossing these limits, the structure of the ground state changes to *I*4*cm* or *Ima*2, respectively. An analysis of the behavior of the A_{2u} soft mode at the *I*4/*mcm*–*I*4*cm* phase transition shows that the magnitudes of the mechanical stresses at which the frequency of this mode vanishes on both sides of the boundary differ by 0.74 kbar. This means that the *I*4/*mcm*–*I*4*cm* phase transition is actually a first-order one.

Since the E_u mode is doubly degenerate, to find the ground-state structure at $p > 4.1$ kbar we considered two structures described by the two-component order parameters of $(P_x,0)$ and (P_x,P_x), and chose among them the one that has a lower enthalpy. Under the biaxial stress, the enthalpy is calculated using the formula $H = E_{tot} + pV(u_{11} + u_{22})$, where E_{tot} is the total energy, p is the stress, V is the unit cell volume, and u_{11} and u_{22} are the in-plane components of the strain tensor. Among two possible solutions with space groups *Fmm*2 and *Ima*2, the latter phase had the lower enthalpy.

Much more interesting phenomena are observed in the case of tensile stress. In the *I*4/*mcm* phase not only the E_u mode is softened with increasing tensile stress, but also the E_g mode, which splits into two components upon the transition to the *Ima*2 phase, and the frequency of one of its components becomes zero at a pressure of +13.8 kbar (Fig. 1). This triggers another phase transition into a phase with the same space group (denoted below as *Ima*2(II)), which has a different picture of octahedra rotations. Because the E_g mode is genetically derived from the R_{25} mode of cubic $SrTiO_3$, the cause of this phase transition is the structural instability. At this phase transition the direction of the rotation axis abruptly changes from the direction normal to the film plane to the direction along the polar axis.

An interesting feature of the *Ima*2(II) phase is the behavior of the soft mode as a function of stress. At the isostructural *Ima*2–*Ima*2(II) phase transition, the frequency of many modes changes abruptly (dashed lines in Fig. 1) and the frequency of the soft mode in the *Ima*2(II) phase does not vanish when approaching the phase boundary. This means that this phase transition is of the first order. This is also clearly evidenced by the possibility to preserve the stability of the *Ima*2(II) phase when gradually decreasing tensile stress (open circles in Fig. 1)—up to a pressure of about 4 kbar, when the enthalpies of the *I*4/*mcm* and *Ima*2(II) phases become equal and the *Ima*2(II) phase transforms to the *I*4/*mcm* one. Thus, a large hysteresis loop occurs on the phase diagram at the stresses between +4.1 and +13.8 kbar. The comparison of the enthalpies of two phases shows that in the hysteresis region the ground state (which corresponds to the minimum enthalpy) is the *Ima*2(II) phase, whereas the *Ima*2 phase is metastable (for both phases the above criterion of stability is fulfilled).

The specific feature of the considered system is that the ferroelectric phase transition around 4 kbar goes from the non-polar to *metastable polar* phase, which transforms into the stable polar phase only at higher pressure. The properties of two polar phases coexisting in the hysteresis region are significantly different. For example, the values of spontaneous polarization in these phases at +11 kbar are 0.128 C/m^2 in the *Ima*2 phase and 0.182 C/m^2 in the *Ima*2(II) phase. The difference of the band gaps in the two phases is 61 meV.

The phase sequence revealed in stressed $SrTiO_3$ films suggests another possible application of ferroelectrics—in phase change memory devices. Indeed, after the transition to the ferroelectric *Ima*2 phase induced by an applied stress at low temperatures, the film is in a uniform metastable state in which regions of stable *Ima*2(II) phase can be created by the local optical heating. Because the system is bistable, both states can coexist at low temperatures, and the contrast in the optical properties of the two phases can be used for nondestructive read-out of the stored information. Erasing of information can be achieved simply by reducing the applied stress. Such a device can work only at low temperatures because at high temperatures the system will transform from the *I*4/*mcm* phase to the thermodynamically stable *Ima*2(II) phase with increasing stress.

One should add that the described bistability is not specific to $SrTiO_3$ but is possible in other systems with competing instabilities.

Acknowledgments. This work was supported by the Russian Foundation for Basic Research, projects 11-02-01317 and 13-02-00724.

Magnetoelectric properties of ferrite-PZT multilayer thin films

You Jeong Eum[1], Chang Young Koo[1], Jungho Ryu[2], Hee Young Lee[1]

[1]School of Mateterials Science and Engineering, Yeungnam University, Gyeongsan, Korea
[2]Functional Ceramics Research Group, Korea Institute of Materials Science, Changwon, Korea

Lamellar type 2-2 composite structure of various ferrite films deposited onto either rhombohedral Pb(Zr0.52Ti0.48)O3 or tetragonal Pb(Zr0.3Ti0.7)O3 thin film was prepared in an attempt to investigate the magnetoelectric properties of magnetic-piezoelectric composite materials.[1-5] PZT films were spin-coated on (111)-oriented Pt/Ti/SiO2/Si<100> substrate utilizing the wet sol-gel technique. The ferrite films studied included CuFe2O4, CoFe2O4, and (Ni,Zn)Fe2O4, which possessed varying values of magnetic susceptibility and magnetostriction coefficients. A thin Pt layer, which was deposited by ion beam sputtering method, was inserted between the magnetic and the piezoelectric layers in order to suppress diffusion at high processing temperatures and thereby to prevent possible interfacial reactions between magnetic and piezoelectric layers. Ferrite layer was then deposited using pulsed laser deposition method (PLD). The resulting film structure is tri-layered type, where the bottom PZT layer covered the whole substrate, while Pt and ferrite layers were deposited through circular shadow masks to measure ferroelectric and magnetoelectric properties. The structural properties of the films were investigated by X-ray diffraction (XRD) and field-emission scanning electron microscopy (FE-SEM). Ferroelectric and magnetic behaviors were analyzed by measuring polarization and magnetization – electric and magnetic field hysteresis, utilizing the ferroelectric test system and the vibrating sample magnetometer. The possible effect of annealing on the film microstructure and multiferroic properties was then investigated using thin film stacks heat-treated at temperatures ranging from 550 to 650C. Magnetoelectric coefficients were calculated by measuring magnetoelectric voltages using magnetoelectric measurement system. Both the magnetoelectric properties and the coupling effect of ferrite/Pt/PZT films on magnetic and magnetoelectric properties are discussed as a function of heat-treatment temperature. In this paper, the effect of annealing temperature on the magnetoelectric coupling in various ferrite/Pt/PZT multilayer thin film is discussed in detail.

References

[1] S.-O. Hwang, Y.J. Eum, C.Y. Koo, H.Y. Lee, J.M. Park and J. Ryu, *J. Korean Phys. Soc.*, **Vol**. 65, 229, (2014).
[2] Y.J. Eum, S.-O. Hwang, C.Y. Koo, J.-Y. Lee, H.Y. Lee, J. Ryu and J.M. Park, *J. Korean Phys. Soc.*, **Vol**. 65, 342, (2014).
[3] Y. J. Eum, S.-O. Hwang, J. Ryu, J.-W. Kim, C. Y. Koo, J.-Y. Lee and H. Y. Lee, *Ferroelectrics*, **Vol**. 465, 76, (2014).
[4] S.-O. Hwang, Y.J. Eum, J.-W. Kim, J. Ryu, C.Y. Koo, J.-Y. Lee and H.Y. Lee, *Ferroelectrics*, **Vol**. 465, 83, (2014).
[5] S.-O. Hwang, Y.J. Eum, J.-W. Kim, J. Ryu, C.Y. Koo, J.-Y. Lee and H.Y. Lee, *Integr. Ferroelectr.*, **Vol**. 157, 57, (2014).

Growth control of metal-insulator transition and oxygen stoichiometry in VO_{2-x} epitaxial thin films

Shinbuhm Lee, Tricia L. Meyer, and Ho Nyung Lee

Materials Science and Technology Division, Oak Ridge National Laboratory, Oak Ridge, Tennessee 37831, United States

Metal-insulator transition (MIT) in strongly correlated electron oxides (CEOs) is one of the most fascinating research topics in condensed matter physics, but is still far from fully understood.[1–3] Among CEOs, VO_2 has attracted great attention since it undergoes the MIT near room temperature (~340 K). Due to the multivalent nature of vanadium oxides,[4–12] *i.e.* $V_2^{+3}O_3$, $V^{+4}O_2$, and $V_2^{+5}O_5$, the oxidation state and oxygen stoichiometry play an important role for determining the structural and electronic properties. For example, Jeong *et al.* recently demonstrated suppression of the MIT in VO_2 by electric field-induced oxygen vacancies.[13] In addition, due to the lack of a good understanding on growth control of the oxidation state, stabilization of phase pure vanadium oxides with a single oxidation state is extremely challenging. Therefore, precise control of the chemical valence or oxidation state of vanadium in vanadium oxide thin films is highly desirable for not only fundamental research, but also technological applications

In this study, we precisely mapped out the optimal growth window of vanadium oxides with different oxidation states by the state-of-the-art pulsed laser epitaxy technique for providing a guideline to grow high quality thin films. As shown in Fig. 1, a well-pronounced MIT was only observed in VO_2 films grown in a very narrow range of oxygen partial pressure (10~25 mTorr). On the other hand, thin films grown either in lower (<10 mTorr) or higher (>25 mTorr) oxygen partial pressure resulted in the formation of V_2O_3 and V_2O_5 phases, respectively, as well as the suppression of the MIT for both cases. We have also found that the resistivity ratio before and after the MIT of VO_2 thin films can be further enhanced by one order of magnitude when the films are further oxidized by post-annealing at a well-controlled oxidizing ambient. This result indicates that stabilizing vanadium into a single valence state has to compromise with insufficient oxidation of an as grown thin film and, thereby, a subsequent oxidation is requisite for an improved MIT behavior.

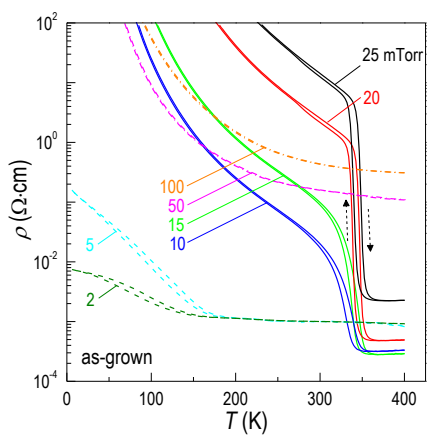

Figure 1 Resistivity $\rho(T)$ curves of as grown vanadium oxide films deposited at various oxygen partial pressure $P(O_2)$. Dashed, solid, and dash-dotted lines represent three vanadium oxide phases, *i.e.* V_2O_3, VO_2, and V_2O_5, respectively.

Our result ultimately stresses the importance of oxygen content in VO_2 that plays a critical role in the sharpness and resistivity ratio of the MIT. VO_2 thin films easily absorbed oxygen as low as 300 ^oC, implying that VO_2 can be regarded as an oxygen sponge.

Acknowledgements
This work was supported by the U.S. Department of Energy, Office of Science, Basic Energy Sciences, Materials Sciences and Engineering Division.

References

[1] M. Imada, A. Fujimori, and Y. Tokura, Rev. Mod. Phys. **70,** 1039 (1998).
[2] D. N. Basov, R. D. Averitt, D. van der Marel, M. Dressel, and K. Haule, Rev. Mod. Phys. **83,** 471 (2011).
[3] E. Morosan, D. Natelson, A. H. Nevidomskyy, and Q. Si, Adv. Mater. **24,** 4896 (2012).
[4] S. Lupi *et al.*, Nat. Commun. **1,** 105 (2010).
[5] J. S. Brockman, L. Gao, B. Hughes, C. T. Rettner, M. G. Samant, K. P. Roche, and S. S. P. Parkin, Nature Nanotech. **9,** 453 (2014).
[6] M. M. Qazilbash *et al.*, Science **318,** 1750 (2007).
[7] T. Driscoll, H.-T. Kim, B.-G. Chae, B.-J. Kim, Y.-W. Lee, N. M. Jokerst, S. Palit, D. R. Smith, M. Di Ventra, and D. N. Basov, Science **325,** 1518 (2009).
[8] V. Pardo and W. E. Pickett, Phys. Rev. Lett. **102,** 166803 (2009).
[9] N. B. Aetukuri *et al.*, Nature Phys. **9,** 661 (2013).
[10] Y. Wang and G. Cao, Chem. Mater. **18,** 2787 (2006).
[11] N. A. Chernova, M. Roppolo, A. C. Dillon, and M. S. Whittingham, J. Mater. Chem. **19,** 2526 (2009).
[12] G. Gu, M. Schmid, P.-W. Chiu, A. Minett, J. Fraysse, G.-T. Kim, S. Roth, M. Kozlov, E. Muñoz, and R. H. Baughman, Nature Mater. **2,** 316 (2003).
[13] J. Jeong, N. Aetukuri, T. Graf, T. D. Schladt, M. G. Samant, and S. S. P. Parkin, Science **339,** 1402 (2013).

Structural and dielectric properties of the Ruddlesden-Popper Ba_2ZrO_4 structure from first-principles

Lydie Louis and Serge M. Nakhmanson
*Department of Materials Science & Engineering, and Institute of Materials Science, University of Connecticut, Storrs, Connecticut 06269, USA**

Layered variations of the ABO_3 perovskite structures have gained widespread interest of technological and fundamental importance in view of their inherent properties and functionalities [1–4]. Well-known homologous series of layered oxides based on slabs with (001) perovskite surfaces include Ruddlesden-Popper (RP; structural formula $A_{n+1}B_nO_{3n+1}$), Aurivillius and Dion-Jacobson compounds [3, 4]. Numerous fundamental investigations of their structural, electronic and dielectric properties have led to insights on how to design and tune functional behavior of these materials through strain and interface engineering. Utilizing first-principles-based computational techniques, we have already predicted intriguing behavior in layered-perovskite compounds of the RP type. Specifically, we showed that Goldstone-like states (collective, close to zero frequency excitations, requiring practically no consumption of energy) can be induced in a $PbSr_2Ti_2O_7$ RP superlattice as easy rotations of the in-plane polarization vector [5]. Furthermore, examination of an (as of now, fictitious) epitaxial Ba_2TiO_4 RP compound demonstrated that it exhibits an assortment of competing incommensurate distortions, including ones that promote polarization [6].

Here we focus on exploring the properties of the RP Ba_2ZrO_4 structure that displays a yet poorly understood tendency to absorb and desorb small molecules, such as water and CO_2 [1, 2, 7] (see Figure 1). Therefore, acquiring a greater insight into the physical underpinnings of the behavior of this compound can result in emergence of useful materials templates for the design of new functional-oxide membranes. This, in turn, will greatly reduce the high energy costs associated with the process of CO_2 capture and storage [8], thus contributing to the already substantial efforts aimed at developing more advanced technologies for the CO_2 sequestration.

We have employed a first-principles method based on density-functional theory (DFT) to investigate electronic, vibrational and dielectric properties of the RP Ba_2ZrO_4 structure, as well as its phase transformations under applied biaxial strain emulating epitaxial thin-film environment.

The phase space for the system can be separated into four main regions according to the values of $\varepsilon_s = (a - a_0)/a_0$, where a_0 is the in-plane lattice parameter of the free standing Ba_2ZrO_4 structure with all the normal stress tensor components relaxed to small values: (I) high compressions of above 0.8–1.0%, dominated by incommensurate (IC) distortions; (II) moderate compressions and tensions, where the nonpolar $I4/mmm$ structure is stable; (III) intermediate tensions ranging from 0.5 to ∼3.0%, dominated by combinations of antiferrodistortive (AFD) instabilities; (IV) high tensions of above 3.0–3.5%, with polar distortions being of similar or greater strength than the AFD ones. In comparison, the previously

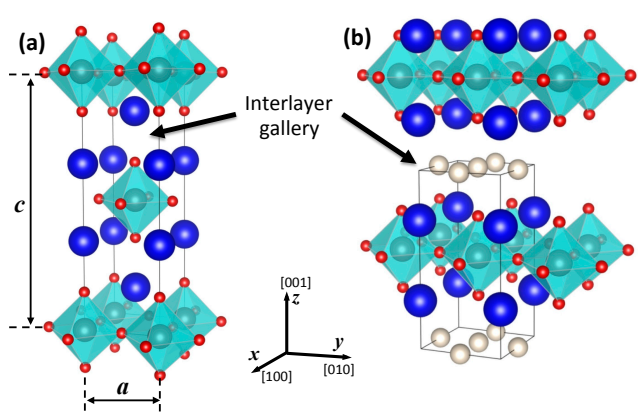

FIG. 1. Molecular intercalation between perovskite-oxide layers. **(a)** A RP A_2BO_4 structure with an empty interlayer gallery (space between the two AO layers) marked by a thick arrow. In-plane and out-of plane lattice parameters a and c of the typical tetragonal unit cell are also shown. **(b)** Attachment sites for small molecules inside the interlayer gallery of the A_2BO_4 structure are indicated by ivory spheres. Notice the difference in layer stackings of the structures depicted in **(a)** and **(b)** due to a "layer slide" phase transition.

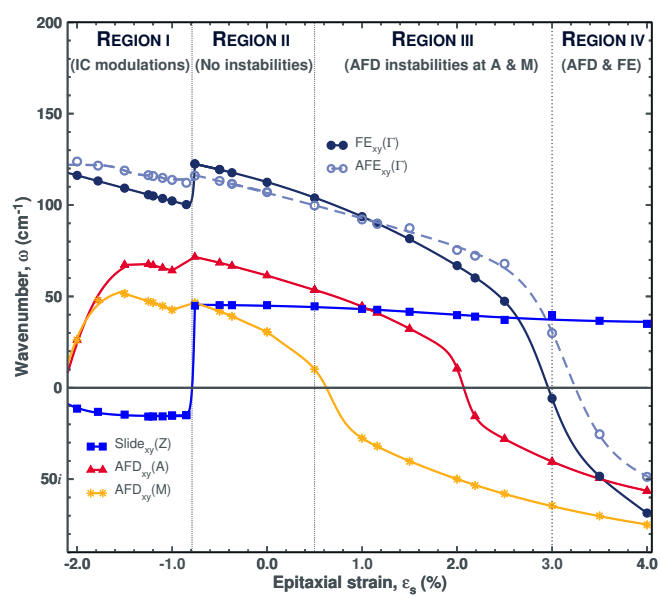

FIG. 2. Soft vibrational modes frequencies ω at Γ and various BZ-boundary $\mathbf{q}$ points as functions of epitaxial strain ε_s for Ba_2ZrO_4.

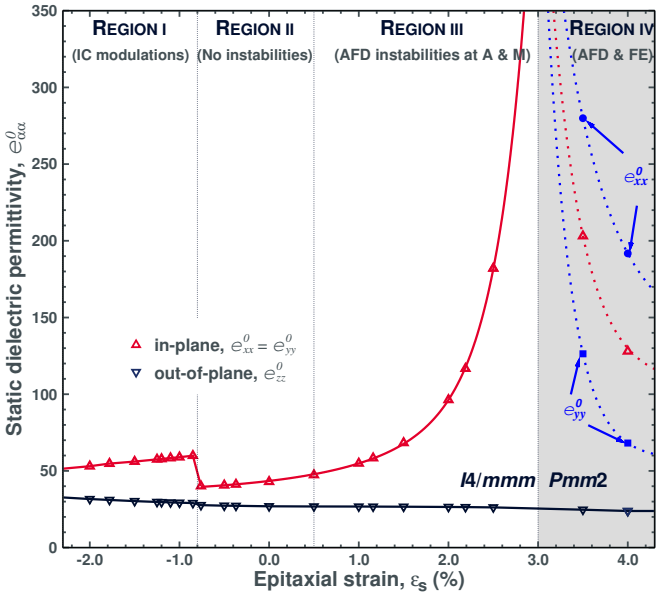

FIG. 3. In- and out-of-plane components of the static dielectric permittivity tensor $\epsilon^0_{\alpha\alpha}$ computed for the RP Ba_2ZrO_4 structure with respect to varying biaxial strain ε_s. For all compressions and for tensions of less than 3.0% dielectric tensors are computed for the non-polar $I4/mmm$ configuration, while for larger tensions they are computed for the polar $Pmm2$ configuration (where ϵ^0_{xx} and ϵ^0_{yy} are no longer equal by symmetry). Connecting lines are used to guide the eye.

studied case of the RP Ba_2TiO_4 [6] is of greater complexity, with IC distortions persisting throughout the whole interval of considered strains and different kinds of IC distortions being possible, as well as their mixing with polar distortions.

In Figure 3 we present the calculated in-plane and out-of-plane components of the static dielectric permittivity tensor $\epsilon^0_{\alpha\beta}$. For all the considered compressions and for tensions of less than 3.0% it was done for the non-polar $I4/mmm$ configuration, while for larger tensions the polar $Pmm2$ configuration was used. The plot clearly shows the divergence of the in-plane component of the dielectric permittivity tensor at the non-polar to polar phase transition on the boundary between regions III and IV, as well as another minor anomaly upon the lock-in of the IC phase on the boundary between regions I and II. The out-of-plane component of the dielectric permittivity tensor remains approximately the same throughout the region of all the considered epitaxial strains.

Remarkably, though, even after the transition into the polar $Pmm2$ state the in-plane dielectric permittivity remains unusually high (on the order of 300). We attribute that to the presence of a Goldstone-like excitation [9, 10] in this system, as shown in Figure 4. Although the circular groove in the energy landscape is not as pronounced here as in the case of $PbSr_2Ti_2O_7$ RP superlattice [5], we can still observe shallow energy minima that are extended in the direction perpendicular to [100] (and other crystallographic directions related by the fourfold rotational symmetry) that allow for easy rotation of polarization. The nature of this excitation in the RP Ba_2ZrO_4 structure — which, unlike the previously studied one, does not contain lead or other lone-pair active ions — is yet unclear and the work to elucidate its origins is currently underway.

* lydie.louis@uconn.edu

[1] P. R. Slater and R. K. B. Gover, J. Mater. Chem. **11**, 2035 (2001).
[2] P. R. Slater and R. K. B. Gover, J. Mater. Chem. **12**, 291 (2002).
[3] K. Aleksandrov and V. Beznosikov, Phys. Solid State **39**, 695 (1997).
[4] R. Mitchell, *Perovskites: Modern and Ancient* (Almaz Press, 2002).
[5] S. M. Nakhmanson and I. Naumov, Phys. Rev. Lett. **104**, 097601 (2010).
[6] W. D. Parker and S. M. Nakhmanson, Phys. Rev. B **88**, 035203 (2013).
[7] R. V. Shpanchenko, E. V. Antipov, and L. M. Kovba, Zh. Neorg. Khim. **38**, 599 (1993).
[8] D. M. D'Alessandro, B. Smit, and J. R. Long, Angew. Chem. Int. Ed. **49**, 6058 (2010).
[9] I. Muševič, R. Blinc, and B. Žekš, *The Physics of Ferroelectric and Antiferroelectric Liquid Crystals* (World Scientific, Singapore, 2000).
[10] A. D. Bruce and R. A. Cowley, *Structural phase transitions* (Taylor and Francis Ltd., London, 1981).

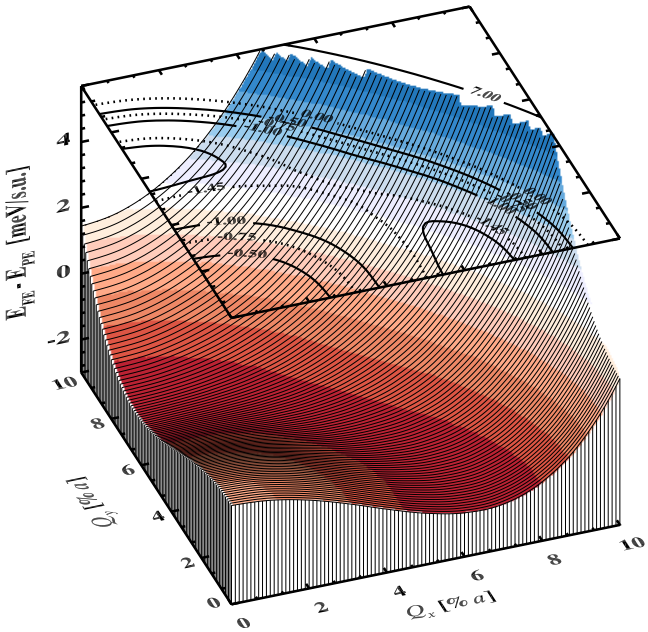

FIG. 4. Energy landscape for the epitaxially strained at $\varepsilon_s = 3.5\%$ RP Ba_2ZrO_4 structure with frozen-in doubly degenerate FE_{xy} distortions (space group $Pmm2$). Q_x and Q_y are the amplitudes of the FE mode eigenvectors polarized along the x- and y- axes, respectively. The energy of the paraelectric $I4/mmm$ phase is taken as zero and a is the value of the in-plane lattice parameter.

Enhanced piezoelectric response near the morphotropic phase-boundary in lead-free $(Na,Bi)TiO_3$-$BaTiO_3$

Chengtao Luo[1], Olivier Delaire[2], Haosu Luo[3], Barry Winn[2], Dwight Viehland[1]

1 Department of Materials Science and Engineering, Virginia Tech, Blacksburg, Virginia 24061, USA
2 Oak Ridge Natl Lab, Div Mat Sci & Technol, Oak Ridge, TN 37831 USA
3 Shanghai Institute of Ceramics, Chinese Academy of Sciences, Shanghai 201800, P.R. China

Lead-free $Na_{1/2}Bi_{1/2}TiO_3$ (NBT) piezoelectrics have received much attention due to environmental concerns associated with traditional lead-containing piezoelectric compounds [1-5]. Structural investigations by x-ray diffraction (XRD) and neutron diffraction have revealed a morphotropic phase boundary (MPB) in the NBT-x%BaTiO3 (NBT-x %BT) solid solution for 6<x< 7, where piezoelectric coefficients as high as 480 pC/N have been reported [6]. The behavior as function of composition (x) and temperature is summarized in the phase-diagram of figure 1. The NBT-BT system exhibits a MPB around x=6%, between the R and T phases. This overall behavior is reminiscent of that seen in lead-containing compounds such as $Pb(Mg_{1/3}Nb_{2/3})O_3 – PbTiO_3$ (PMN-PT) and $Pb(Zn_{1/3}Nb_{2/3})O_3 – PbTiO_3$ (PZN-PT), which have been thoroughly studied owing to their good piezoelectric properties. However, the fundamental properties and microscopic mechanisms leading to the large piezoelectric response of NBT-BT have been much less studied. In addition, *there is a fundamental difference between the lead-based compounds, in which cation disorder is on the B-site of the ABO_3 perovskite structure, while the lead-free NBT-BT exhibits cation disorder in the A-site*. The impact of this fundamental difference on the lattice dynamics and the ferroelectric properties are currently not well understood.

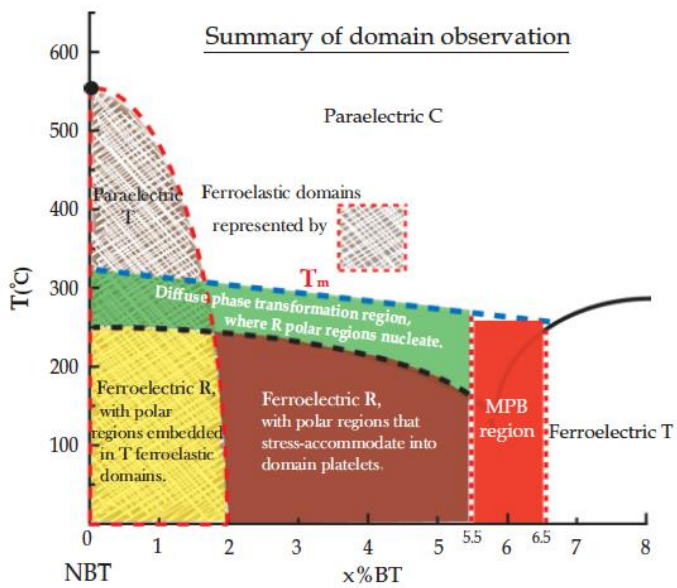

Figure 1 Phase-diagram of NBT-x %BT (from [5]).

Neutron diffuse scattering and inelastic scattering measurements are powerful techniques to unravel the microstructure and mechanisms underpinning the bulk piezoelectric behavior [7,8]. A recent study of neutron diffuse scattering comparing NBT and PMN reported both similarities and differences in the geometry of the diffuse scattering and the morphology of polar nanoregions [7]. This study found prominent ridges in the elastic diffuse scattering intensity contours that extend along <110>, with the same zone dependence as in PMN and other lead-based relaxors. These ridges disappear gradually on heating above the cubic-to-tetragonal phase transition temperature, T_{CT} = 523°C. It was concluded that <110>-oriented ridges are a relaxor-specific property. In addition, further ridges were also identified, which are perhaps more related to those seen in $BaTiO_3$ and $KNbO_3$, and could be related to either correlated off-centerings or anisotropic transverse acoustic phonons. This latter point remains to be elucidated.

In this experiment, which will start on Dec 15, we will focus on compositions x=4% and 6%, corresponding to the ferroelectric R phase and the MPB region, respectively (Fig. 1).

We propose to measure the phonon dispersions in single-crystals of NBT-x%BT across the morphotropic phase boundary, and correlate our results with diffuse scattering measurements, as well as piezo-force and electron microscopy measurements, to identify changes in lattice dynamics associated with the large piezoelectric response at the MPB.

We will focus on low-energy optic and acoustic phonons, which are the dominant contributors to the diffuse scattering signal. Specifically, we will map the TA and TO branches. The TO ferroelectric mode is expected to dip to very low energies at the zone center, although it can be quite steep. For this reason, we plan to use two incident energies Ei=27meV and Ei=15meV, which are both free of prompt-pulse contamination on HYSPEC, and have favorable neutron flux. The higher Ei will enable us to access phonon dispersions in Brillouin zones (0,0,2), (1,1,1), and (2,2,0), while the lower Ei will enable high resolution in (1,1,1).

References:

[1] T. Takenaka, K. Maruyama, and K. Sakata, Jpn. J. Appl. Phys. 30, 2236 (1991).

[2] Y. M. Chiang, G.W. Farrey, and A. N. Soukhojak, Appl. Phys. Lett. 73, 3683 (1998).

[3] B. J. Chu, D. R. Chen, G. R. Li, and Q. R. Yin, J. Eur. Ceram. Soc. 22, 2115 (2002).

[4] G. Smolenskii, V. Isupov, A. Agranovskaya, and N. Kainik, Sov. Phys. Solid State 2, 2651 (1961).

[5] Jianjun Yao, Li Yan, Wenwei Ge, Liang Luo, Jiefang Li, and D. Viehland, Phys. Rev. B 83, 054107 (2011).

[6] J. Zvirgzds, P. Kapostins, J. Zvirgzde, and T. Kruzina, Ferroelectrics 40, 75 (1982).

[7] Wenwei Ge, C. P. Devreugd, D. Phelan, Qinhui Zhang, M. Ahart, Jiefang Li, Haosu Luo, L. A. Boatner, D. Viehland, and P. M. Gehring, Phys. Rev. B 88, 174115 (2013).

[8] D. Phelan, C. Stock, J. A. Rodriguez-Rivera, *et al.*, Proc. Nat. Acad. Sci. USA 111, 1754-1759 (2014).

Many body effects on the formal charge of 3*d* - Transition Metal Doped $BaTiO_3$

Subhasish Mandal[1, 2], R. E. Cohen[2, 3], K. Haule[4]

[1]Department of Applied Physics, Yale University, New Haven, Connecticut, USA
[2] Geophysical Laboratory, Carnegie Institution of Washington, Washington D.C, USA
[3] Department of Earth Sciences, University College London, London, UK,
[4] Department of Physics, Rutgers University, Piscataway, New Jersey, USA

One route to magnetoelectric materials, which couple magnetism and ferroelectricity, is to dope ferroelectrics with magnetic ions. Such materials are of interest for electronics that can integrate data processing and memory operation in a single device [1-4]. In addition, most commercial transducer materials have added Mn impurity to improve piezoelectric properties, mechanical quality factor, and coercive field, and to decrease electrical conductivity. To find the role of the impurity atom in these materials, one important task is to understand the charge transfer process. The first order problem is to finding an accurate charge state and 3*d* occupation of the magnetic impurity, and therefore it needs a detail understanding of atomic nature of the impurity in a crystal.

Using density functional theory (DFT) in combination with dynamical mean field theory (DMFT) in Mn doped $BaTiO_3$, we find a different charge state and 3*d*- orbital occupations than obtained from either DFT or DFT+U. We find that the explicit treatment of many-body effects induced by the Hund's rule coupling in Mn shows a donor charge state of Mn^{2+}, instead of usual acceptor charge state of Mn^{4+} as is found in both DFT and DFT+U. The differences in electron density reveal that charge transfer due to strong Hubbard interactions is not sufficient to describe the electron correlations in transition metal doped ferroelectrics.

In the DFT-DMFT method, the self-energy, sampling all Feynman diagrams local to the impurity Mn ion, is added to the DFT Kohn-Sham Hamiltonian [5, 6]. This implementation is fully self-consistent and all-electron [5, 6]. The computations are converged with respect to charge density, impurity level, chemical potential, self-energy, lattice, and impurity Green's functions. The lattice is represented using the full potential linear augmented plane wave method, implemented in the WIEN2K [7] package in its generalized gradient approximation [Wu-Cohen GGA]. The continuous time quantum Monte Carlo method is used to solve the quantum impurity problem and to obtain the local self-energy due to the correlated Mn 3d orbitals. A unit cell containing 40 atoms including one Mn ion (at Ti site) is used for our simulations. 40,000000 Monte Carlo steps are used for each iteration.

We show the density of states obtained from DFT, DFT+U, and DFT+DMFT methods and charge density difference plot between each method. To quantify the probability of finding an Mn atom in the solid in one of the atomic states, we will present atomic histogram and its dependence on U and J. We will show how Hund's rule coupling affects the 3*d*-orbital occupancy in this material.

Acknowledgements:
This work is supported by ONR grants N00014-12-1-1038 and N00014-14-1-0561, by the ERC Advanced grant ToMCaT, and by the Carnegie Institution.

References

[1] D. V. Efremov, J. V. D. Brink, and D. I. Khomskii, Nature Mat. **3**, 853 (2004).

[2] C. Ederer and N. A. Spaldin, Nature Mat. **3**, 849 (2004).
[3] Y. Shauai *et al.* J. Appl. Phys. **109**, 084105 (2011)
[4] X. Tong, Y-H Lin, S. Zhang, Y. Wang, and C. -W. Nan, J. Appl. Phys. **104**, 066108 (2008).
[5] G. Kotliar, S. Y. Savrasov, K. Haule, V. S. Oudovenko, O. Parcollet, and C. A.Marianetti, Rev. Mod. Phys. **78**, 865 (2006).
[6] K. Haule, C.-H. Yee, and K. Kim, Phys. Rev. B 81, 195107 (2010).
[7] P. Blaha, K. Schwarz, G. Madsen, D. Kvasnicka, and J. Luitz, in An Augmented Plane Wave Plus Local Orbitals Program for Calculating Crystal Properties, edited by K. Schwarz (Vienna University of Technology, Austria, 2001).

Skyrmionic state in ferroelectric nanocomposites

Y. Nahas, S. Prokhorenko, L. Bellaiche, L. Louis, Z. Gui
Physics Department and Institute for Nanoscience and Engineering,
University of Arkansas, Fayetteville, AR 72701, USA

The topological invariance of nontrivial textures such as vortices and skyrmionic configurations against fluctuations and deformations triggers considerable interest for device applications [1–3]. Many advances have been achieved in predicting their formation and characterizing the new order they subtend in *magnetic* systems [4–6]. Whereas vortex configurations have already been revealed in ferroelectrics within nanoscale geometries [7–11], the search for a spontaneous formation of skyrmionic textures in *ferroelectrics* was somewhat hindered by the absence of chiral interactions that are known to stabilize such configurations in magnetic systems [12–14]. We here show that the anisotropy emanating from such interactions can be compensated for by that of confined geometries which can readily become the locus of thermodynamically stable skyrmionic configuration of polarization.

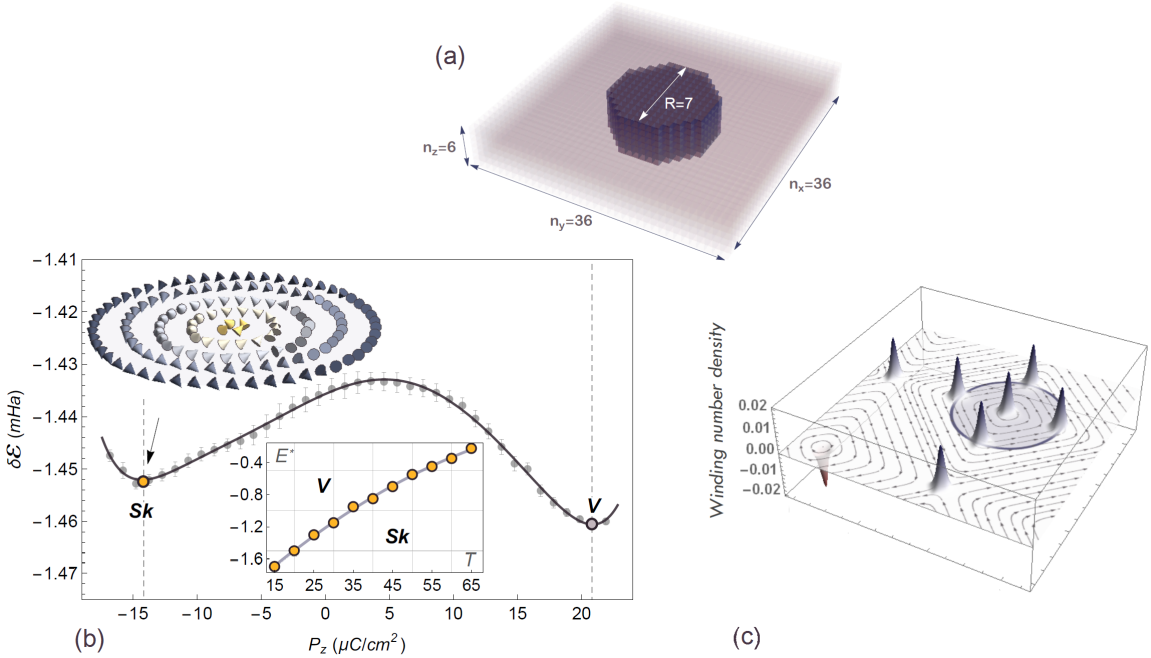

FIG. 1: (a) Schematic representation of the periodic supercell under study. The structure consists of a cylindrical $BaTiO_3$ nanowire embedded in a $Ba_{0.15}Sr_{0.85}TiO_3$ matrix. (b) Dependence of the internal energy on the P_z component of polarization showing the crossover between two stable minima: the one corresponding to the vortex configuration (V) and the one associated with the skyrmionic texture (Sk). Bottom inset provides the temperature dependence of the estimated threshold external electric field E^* needed to drive the system towards the skyrmion state. Pictorial inset depicts the polarization configuration within the skyrmionic state as obtained at 15 K. (c) Density of the winding number in an arbitrary z-plane of the shifted perdiodic supercell, showing the breaking of the skyrmion into fractions located at the junctions of domain walls. The location of the nanowire is indicated by a circle.

The considered structure is schematized in Fig.1(a). It consists of a cylindrical $BaTiO_3$ nanowire with a radius of 2.7 nm (7 lattice constant units) embedded in a $Ba_{0.15}Sr_{0.85}TiO_3$ matrix. We study this structure under periodic boundary conditions using Monte Carlo simulations of the first-principle-based effective Hamiltonian scheme of [11, 15], which has been shown to accurately

reproduce various properties of (Ba,Sr)TiO_3 systems [15].

The procedure for getting a skyrmionic configuration involves the following steps. Firstly, we perform a temperature annealing under an electric field $E_{[001]}=10^8$ V/m. Secondly, we set the field to zero and further relax the priorly obtained 15 K configuration into a local minimum. The resulting configuration has been formerly observed [11]. It features a spontaneous polarization along the z direction coexisting with a flux-closure four-domain pattern formed by the components of polarization lying in the plane perpendicular to the wire axis. Within the wire, the in-plane components form a vortex occurring in order to reduce the depolarizing field stemming from the difference in polarizability between the wire and the matrix, while the matrix exhibits an additional vortex at mid-way between second-nearest neighbor wires and two anti-vortices at mid-way between first-nearest neighbor wires of the periodic supercell. These in-plane punctual topological defects all occur at the intersection of P_x and P_y domains and yield a zero net topological charge for the P_x and P_y component of polarization. Thirdly, we subject the obtained relaxed configuration under zero-field to a gradually increasing $E_{[00\bar{1}]}$ electric field. At a certain threshold value E^* of the field, the configuration is such that the P_z component of the matrix is anti-parallel to that of the wire, yielding a Bloch-like [16] skyrmionic configuration of polarization (pictorial inset of Fig.1(b)). Collecting the internal energies during this partial switching process enables us to access the internal-energy landscape as a function of P_z at 15 K (Fig.1(b)). The profile indicates the (meta)stability of the skyrmion state and reveals that the barrier's height is equivalent to approximately 6 K. Bottom inset of Fig.1(b) provides the temperature dependence of the estimated threshold external electric field E^* needed to drive the system towards the skyrmion state. Figure 1(c) provides the winding number density $\vec{P}_{ijk}.(\partial_x\vec{P}_{ijk}\times\partial_y\vec{P}_{ijk})$ where $\{ijk\}$ runs over the nodes of the lattice. The integration of the density over the supercell yields a winding number of 1 and it is thus seen that the skyrmion is broken into fractions located at the junctions of (P_x and P_y), (P_z and P_x) and (P_z and P_y) domain walls, as a genuine consequence of the considered nanocomposite structure.

This work is supported by the ARO grant W911NF-12-1–0085.

[1] K. Yamada, S. Kasai, Y. Nakatani, K. Kobayashi, H. Kohno, A. Thiaville, and T. Ono, Nature Mater. 6, 269273 (2007).

[2] X.Z. Yu, N. Kanazawa, W.Z. Zhang, T. Nagai, T. Hara, K. Kimoto, Y. Matsui, Y. Onose, and Y. Tokura, Nature Commun. 3, 988 (2012).

[3] J. Sampaio, V. Cros, S. Rohart, A. Thiaville, and A. Fert, Nature Nanotech. 8, 839844 (2013).

[4] T. Shinjo, T. Okuno, R. Hassdorf, K. Shigeto, and T. Ono, Science 289, 930932 (2000).

[5] S. Muhlbauer, B. Binz, F. Jonietz, C. Pfleiderer, A. Rosch, A. Neubauer, R. Georgii, and P. Boni, Science 323, 915919 (2009).

[6] X.Z. Yu, Y. Onose, N. Kanazawa, J.H. Park, J.H. Han, Y. Matsui, N. Nagaosa, and Y. Tokura, Nature 465, 901904 (2010)

[7] I.I. Naumov, L. Bellaiche, and H. Fu, Nature 432, 737 (2004).

[8] J. Scott, Nature Materials 4, 13-14 (2005).

[9] S. Prosandeev, I.A. Kornev, and L. Bellaiche, Phys. Rev. Lett. 107, 117602 (2011).

[10] N. Balke, B. Winchester, W. Ren, Y.H. Chu, A.N. Morozovska, E.A. Eliseev, M. Huijben, R.K. Vasudevan, P. Maksymovych, J. Britson, S. Jesse, I.A. Kornev, R. Ramesh, L. Bellaiche, L.Q. Chen, and S.V. Kalinin, Nature Physics 8, 8188 (2012).

[11] L. Louis, I.A. Kornev, G. Geneste, B. Dkhil, and L. Bellaiche, J.Phys.: Condens. Matter 24, 402201 (2012).

[12] I.E. Dzyaloshinskii, J. Phys. Chem. Solids 4, 241255 (1958)

[13] T. Moriya, Phys. Rev. 120, 9198 (1960).

[14] U. K. Rossler, A.N. Bogdanov and C. Pfleiderer, Nature 442, 797801 (2006).

[15] L. Walizer, S. Lisenkov and L. Bellaiche, Phys. Rev. B 73, 144105 (2006).

[16] R. Tomasello, E. Martinez, R. Zivieri, L. Torres, M. Carpentieri, and G. Finocchio, Sci. Rep 4, 6784 (2014).

Tuning the physical properties in strontium iridate heterostructures

John Nichols[1], Tricia Meyer[1], Ho Nyung Lee[1]

[1]Material Science and Technology Division, Oak Ridge National Laboratory, Oak Ridge, Tennessee 37831, USA

Iridium based transition metal oxides (iridates) were originally anticipated to be governed by paramagnetic metallic ground states because their 5*d* electrons are more spatially extended than in their 3*d* and 4*d* counterparts, resulting in a reduced on-site Coulomb interaction. However, recent studies have revealed novel ground states in these compounds due to the interaction strength of spin-orbit coupling being comparable with both the Coulomb interaction and crystal fields. The comparable energy scales of these fundamental physical interactions results in Sr_2IrO_4, the prototypical material exhibiting such behavior, being an antiferromagnetic insulator (T_N = 240 K)[1,2] with a novel J_{eff} = 1/2 ground state[3]. This discovery has generated enormous interest recently including several theoretical efforts predicting exotic phases of matter in these compounds such as unconventional superconductivity[4] and topologically protected states[5]. Experimental studies on bulk crystals of Sr_2IrO_4 have revealed metallic states by electrochemical substitution[6,7], but the insulating state has proven to be quite robust under hydrostatic pressure as high as 40 GPa[8].

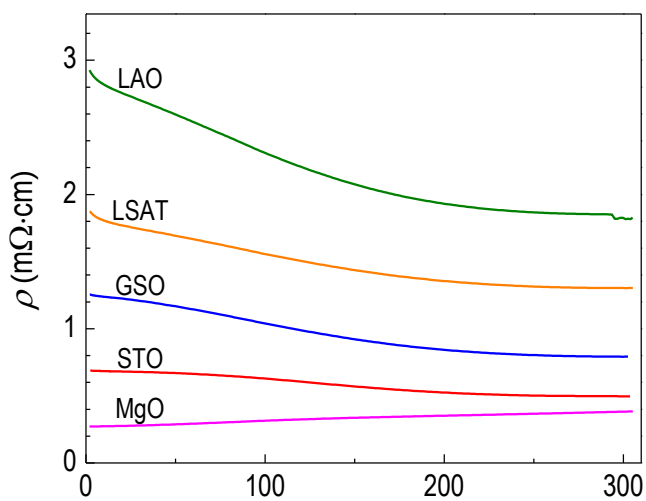

Figure 1 Temperature dependent resistivity of $SrIrO_3$ thin films grown on various substrates.

Thin films and heterostructures of iridates provide a unique playground to tune the physical properties of these materials to exhibit the predicted properties discussed above through strain, electrochemical doping, electron confinement, dimensionality, and interfacial coupling. Since strontium iridate has lattice parameters similar to many commercially available single crystal substrates, samples with various strain states can be realized. It has been shown that increasing strain in Sr_2IrO_4 enhances both the electronic bandwidth and effective correlation energy, maintaining a strain independent gap energy[9], as well as the magnetic ordering temperature[10]. Conversely, increasing strain in $SrIrO_3$ induces a metal-insulator transition (Fig. 1). Although possible to manipulate the physical properties of strontium iridate via epitaxial strain, it appears unlikely that the novel states discussed above will be realized solely through applied strain. However, heterostructuring strontium iridate with other materials creates a new platform for investigating these materials.

We have successfully synthesized thin film heterostructures, $SrIrO_3/AMO_3$ (A = Sr, La; B = Ti, Mn, Rh), that were grown layer-by-layer by a pulsed laser deposition system equipped with reflective high energy electron diffraction. We have investigated the physical properties of these samples with x-ray diffraction, *dc* transport, SQUID magnetometry, and will present that they depend strongly on epitaxial strain and spatial confinement.

Acknowledgements This work was supported by the U. S. Department of Energy, Office of Science, Basic Energy Sciences, Materials Science and Engineering Division.

References

[1] G. Cao, J. Bolivar, S. McCall, J. E. Crow, and R. P. Guertin, *Physical Review B* **57,** 11039 (1998).

[2] B. J. Kim, H. Ohsumi, T. Komesu, S. Sakai, T. Morita, H. Takagi, and T. Arima, *Science* **323,** 1329 (2009).

[3] B. J. Kim, H. Jin, S. J. Moon, J. Y. Kim, B. G. Park, C. S. Leem, J. Yu, T. W. Noh, C. Kim, S. J. Oh, J. H. Park, V. Durairaj, G. Cao, and E. Rotenberg, *Physical Review Letters* **101,** 076402 (2008).

[4] F. Wang, and T. Senthil, *Physical Review Letters* **106,** 136402 (2011).

[5] D. Pesin, and L. Balents, *Nature Physics* **6,** 376 (2010).

[6] M. Ge, T. F. Qi, O. B. Korneta, D. E. De Long, P. Schlottmann, W. P. Crummett, and G. Cao, *Physical Review B* **84,** 100402 (2011).

[7] O. B. Korneta, T. Qi, S. Chikara, S. Parkin, L. E. De Long, P. Schlottmann, and G. Cao, *Physical Review B* **82,** 115117 (2010).

[8] D. Haskel, G. Fabbris, M. Zhernenkov, P. P. Kong, C. Q. Jin, G. Cao, and M. van Veenendaal, *Physical Review Letters* **109,** 027204 (2012).

[9] J. Nichols, J. Terzic, E. G. Bittle, O. B. Korneta, L. E. De Long, J. W. Brill, G. Cao, and S. S. A. Seo, *Applied Physics Letters* **102,** 141908 (2013).

[10] A. Lupascu, J. P. Clancy, H. Gretarsson, Z. Nie, J. Nichols, J. Terzic, G. Cao, S. S. A. Seo, Z. Islam, M. H. Upton, J. Kim, D. Casa, T. Gog, A. H. Said, V. M. Katukuri, H. Stoll, L. Hozoi, J. van den Brink, and Y.-J. Kim, *Physical Review Letters* **112,** 147201 (2014).

Direct molecular dynamics simulation of thermal conductivity in ferroelectrics

Takeshi Nishimatsu[1], Umesh V. Waghmare[2]

[1]Institute for Materials Research (IMR), Tohoku University, Sendai 980-8577, Japan

[2]Theoretical Sciences Unit, Jawaharlal Nehru Centre for Advanced Scientific Research, Bangalore 560 064, India

From the point of view of fundamental physics, thermal conductivity in ferroelectric materials with phase transitions may be interesting to understand. Here, we present a method to calculate the thermal conductivity directly by molecular dynamics (MD) simulations.

The effective Hamiltonian, constructed from first-principles calculations, and used in the present MD simulations is essentially the same as that in Refs. [1, 2]

$$H^{\mathrm{eff}} = \frac{M^*_{\mathrm{dipole}}}{2}\sum_{\boldsymbol{R},\alpha}\dot{u}^2_\alpha(\boldsymbol{R}) + \frac{M^*_{\mathrm{acoustic}}}{2}\sum_{\boldsymbol{R},\alpha}\dot{w}^2_\alpha(\boldsymbol{R}) + V^{\mathrm{self}}(\{\boldsymbol{u}\}) + V^{\mathrm{dpl}}(\{\boldsymbol{u}\}) + V^{\mathrm{short}}(\{\boldsymbol{u}\})$$
$$+ V^{\mathrm{elas,\,homo}}(\eta_1,\ldots,\eta_6) + V^{\mathrm{elas,\,inho}}(\{\boldsymbol{w}\}) + V^{\mathrm{coup,\,homo}}(\{\boldsymbol{u}\},\eta_1,\ldots,\eta_6) + V^{\mathrm{coup,\,inho}}(\{\boldsymbol{u}\},\{\boldsymbol{w}\}). \quad (1)$$

The true atomic structure has properties determined by the complex chemical bonding between the atoms, but in the model system the complexity is reduced; the collective atomic motion is coarse-grained by local soft mode vectors, $\boldsymbol{u}(\boldsymbol{R})$, and local acoustic displacement vectors, $\boldsymbol{w}(\boldsymbol{R})$, of each unit cell located at $\boldsymbol{R}$ in a simulation supercell. Each term in the Hamiltonian is described in Ref. [2].

In Fig. 1, the supercell used in MD simulations is schematically illustrated. The procedure to estimate thermal conductivity involves two steps: First, constant-temperature MD is performed in the canonical ensemble using the velocity-scaling thermostat. Next, constant-energy MD using the leapfrog method is performed with adding energy Δe at each MD step into a single layer at $z = \frac{1}{4}L_z$ and removing the same amount of energy at $z = \frac{3}{4}L_z$. Temperature gradient and consequently heat flows appear between the energy source and sink. Typical time-averaged layer-by-layer temperature profile used to compute the thermal conductivity is shown in Fig. 2. MD simulations are performed with our original `feram` software. `feram` is distributed freely under the GNU General Public License (GPL) and can be found at `http://loto.sourceforge.net/feram/` .

References

[1] U. V. Waghmare and K. M. Rabe, Phys. Rev. B **55**, 6161 (1997).

[2] T. Nishimatsu, U. V. Waghmare, Y. Kawazoe, and D. Vanderbilt, Phys. Rev. B **78**, 104104 (2008).

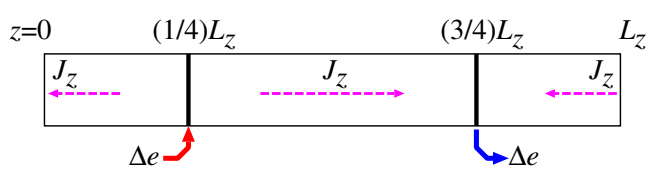

Figure 1: Schematic illustration of supercell used in MD simulations. The supercell of size of $L_x \times L_y \times L_z$ unit cells is placed in the periodic boundary condition. Energy Δe is pushed into the system through the $L_x \times L_y = 24 \times 24$ dipoles in a single layer at $z = \frac{1}{4}L_z$. Same amount of energy is pulled out from the system at $z = \frac{3}{4}L_z$. The heat flows J_z is indicated with dashed lines.

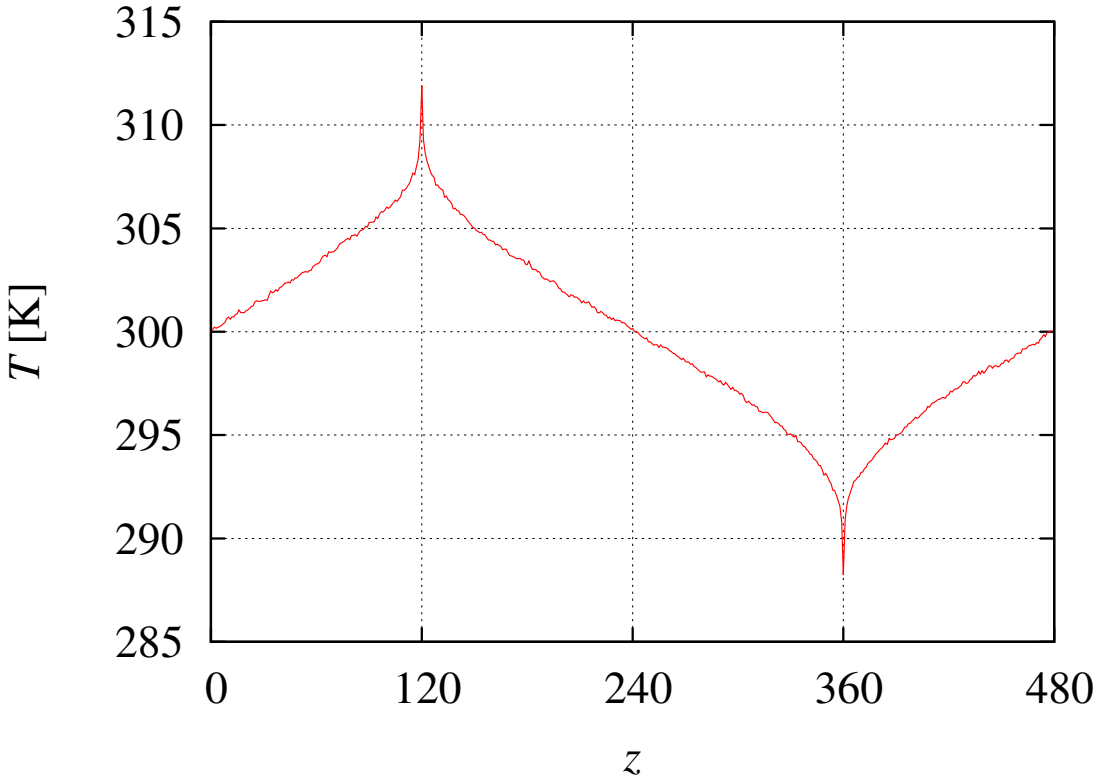

Figure 2: Typical temperature profile for a $48 \times 48 \times 480$ system at an average temperature of 300 K.

Effects of Mn Addition and Compensating Oxygen Vacancies on the Ferroelectric Properties of $BaTiO_3$

J. F. Nossa[1], I.I. Naumov[1], and R.E. Cohen[1,2]

[1]Geophysical Laboratory, CIW, 5251 Broad Branch Road, Washington, D.C. 20015, USA
[2]Department of Earth Sciences, University College London, Gower Street, WC1E 6BT, London, United Kingdom

The Mn dopant has been intensively used to improve the electromechanical properties of perovskite oxides. It increases coercive fields, quality factors and dielectric constants [1,2], reduces dielectric losses and hysteretic fatigues[3], stabilizes domain structures[4] among other effects. Since Mn is magnetic and multivalent, its behavior in polar materials is quite complex [5,6] and has been poorly understood from the electronic point of view. It has been discovered in recent experiments on spin-electric couplings in Mn defects in ZnO that the Mn^{2+} spin Hamiltonian is extremely sensitive to an external electric field [7]. In the presence of an electric field, ions are displaced and, as a result, the dimension of the crystal change. This change in the strain is known as piezoelectricity and has a vast range of applications. It has been proposed, however, that this effect can be increased in aged $BaTiO_3$ (BTO) [8]. Although this could extend the frame of conventional multiferroicity and give new perspective for studies of the phenomenon and potential applications, there has been limited first-principles theoretical study of defects on ferroelectrics and piezoelectricity.

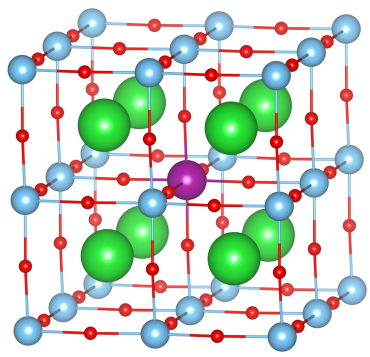

Fig 1. 2x2x2 Mn-doped $BaTiO_3$ supercell. Red, blue, green and purple balls correspond to Oxygen, Titanium, Barium and Manganese atoms, respectively.

Using density functional theory, we have investigated the equilibrium geometry and electronic properties of Mn ion on *A* or *B* sites of BTO perovskite structure, and with compensating oxygen vacancies, V_O. We have used a 40- and 39-atom supercell with a single Mn and Mn-V_O complex, respectively (See Fig. 1). In our studies, we have used both GGA (Wu-Cohen) and GGA+U with U=8 and J=0.8 eV. Our calculations have been carried out with ABINIT code using PAWs. We have studied the change in the oxidation state of Mn occupying *B* site in respond to local environment changes, such as the presence of oxygen vacancies. We also have investigated the role of the oxygen vacancies around Mn impurity in order to engineer reversible domain switching in aged samples. Mn ions go in the *B* site (Ti^{4+}) rather than *A* site (Pb^{2+} or Ba^{2+}) in that the radius of Mn is closer to that of *B* atom [9]. This phenomena causes oxygen vacancies in the lattice, which would boost the electric conductance. Thus, understanding the role of defects in the O vacancy formation and transducer ageing would be a key to design reversible switching devices.

We have found that the Mn ion, in the presence of an oxygen vacancy, in the BTO is in a more centered position than the original Ti^{4+} (see Fig. 2). This shift modifies the ferroelectric properties of BTO. We have used the modern theory of polarization implemented in Quantum espresso code to calculate the polarization of Mn-doped BTO. Table 1 shows the change in the polarization for different structures considered in this work. We find that the polarization of BTO:Mn in a 40 atom supercell with a single

Mn, with Mn on the B site, is 0.077 C/m^2, is lower that un-doped BTO. It can, however, be increased to 0.092 C/m^2 when considering Mn-V_O defects. Although this value is smaller than that found in un-doped BTO, 0.33 C/m^2, it is still larger than most multiferroics.

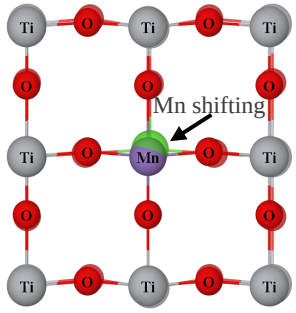

Fig. 2. After fully relaxation, Mn ion is shifted to a more centered position when an oxygen vacancy is present.

We also compare our findings with previous work in V-doped BTO and co-substitution of N and F for oxygen in $BTO_{2.8}N_{0.1}F_{0.1}$, where the polarization has also been found to decrease because the doping [10,11]. In order to analyze the consequences of the changes in the electronic and ferroelectric properties of the Mn-doped, V_O vacancy and BTO perovskite, we also calculate the effective charges and dielectric constants for our structures. As a final remark, we also investigate the effect of an external electric field on the polarization. This effect is a key point in the achievement of recoverable electro-strain without using external force. Understanding the effect of a perpendicular external electric field on the polarization of BTO:Mn-V_O is a necessary key to exploit the idea of reversible domain switching.

Structure	P(C/m^2)
BTO	0.335
BTO:Mn	0.077
BTO:Mn-V_O	0.092

Table 1. Polarizations in C/m^2.

Acknowledgements
This work has been supported by This work was supported by the Center the Office of Naval Research (ONR) under ONR Grant No. N00014-12-1-1038.

References
[1] E. Perez-Delfin, J.E.G.a., D. A. Ochoa, R. Perez, F. Guerrero, and J. A. Eiras. J. Appl. Phys. 110, 034106 (2011).
[2] J.-H. Park, J.P., J.-G. Park, B.-K. Kim, and Y. Kim. J. Eur. Cer. Soc,21, 1383 (2001).
[3] S. Wu, S.W., L. Chen, and X. Wang. J. Mater. Sci: Mater. Electron, 19, 505-508 (2008).
[4] M. A. Hentati, M.G., H. Dammak, H. Khemakhem and M. P. Thi. J. Appl. Phys. 107, 064108 (2010).
[5] Kvyatkovskii, O.E. Physics of the Solid State, 51, 982 (2009).
[6] Kvyatkovskii, O.E. Physics of the Solid State, 54, 1397 (2012).
[7] Richard E. George, James P. Edwards, and Arzhang Ardavan. Phys. Rev. Lett. 110, 027601 (2013).
[8] Ren, X., Nature Materials, 3, 91 (2004).
[9] Xiang Wang , Min Gu , Bin Yang , Shining Zhu , Wenwu Cao. Microelectronic Engineering 66, 855–859 (2003).
[10] Hirak Kumar Chandra, Kapil Gupta, Ashis Kumar Nandy, and Priya Mahadevan. Phys. Rev. B 87, 214110 (2013).
[11] Nitesh Kumar, Jaysree Pan, N Aysha, Umesh V Waghmare, A Sundaresan and C N R Rao. J. Phys.: Condens. Matter 25 345901 (2013).

Tuning the electron-skyrmion interaction: topological Hall effect and beyond

Charles Paillard[1,6], Bertrand Dupé[2,3], Ritwik Mondal[4], Marco Berritta[4], Zhigang Gui[5,6], Surendra Singh[5],Brahim Dkhil[1], Peter M. Oppeneer[4] and Laurent Bellaiche[5,6]

[1]Laboratoire SPMS, UMR 8580 CNRS/Ecole Centrale Paris, Grande Voie des Vignes 92 295 Châtenay-Malabry CEDEX, France
[2]Institute of Theoretical Physics, Christian-Albrechts Universität zu Kiel, Germany
[3]Peter Grünberg Institute and Institute for Advanced Simulation, Forschungzentrum Jülich and JARA, D-52425 Jülich, Germany
[4]Dept. of Physics and Astronomy, Uppsala University, P.O. Box 516, SE-75120 Uppsala, Sweden
[5]Physics Department, University of Arkansas, 72701 Fayetteville, AR, USA
[6]Institute for Nanoscience and Engineering, University of Arkansas, 72701 Fayetteville, AR, USA

Topological solitons such as skyrmions hold great promise to build ultra-high density magnetic racetrack memory because they can be reduced down to the nanoscale[1] and be moved with low-density current[2]. Achieving such a device can only be realized by a deep understanding of the interaction between the skyrmion and electrons. So far these interactions, such as the topological Hall effect (THE), have only been described in the complex framework of the Berry phase theory. Recently, a new energy term coupling the angular momentum of light with a magnetic moment has been shown to be able to re-derive complex magneto-electric effects such as the spin current model[3] in multiferroics, the anomalous Hall effect[4], inverse Rashba-Edelstein effect[5], anisotropic magnetoresistance and planar Hall effects[6]. However, no rigourous proof of this Angular MagnetoElectric (AME) coupling was given.
In this work, we demonstrate the existence of this coupling starting from the Dirac equation, and are able to re-derive the THE.
In addition, we are able to show that, under the application of electric fields, the force applied on the skyrmion could be finely tuned. Furthermore, the direct relationship between the transverse Hall conductivity and the skyrmion radius could allow the study of dynamical excitation of the skyrmion such as e.g., breathing modes. The AME coupling also allows for the prediction of novel magnetoelectric effects in metals hosting skyrmions.

Acknowledgements We thank Huaxiang Fu for insightful discussions. We acknowledge the Department of Energy, Office of Basic Energy Sciences, under contract ER-46612, for personnel support of C.P. during his visit to Fayetteville, and ARO Grant No. W911NF-12-1-0085 for personnel support of Z.G. R.M., M.B. and P.M.O. acknowledge support by the European Community's Seventh Framework Programme (FP7/2007-2013) under Grant Agreement No. 281043, ``FemtoSpin''.

References

[1] S. Heinze, K. von Bergmann, M. Menzel et al., *Nat. Phys.* **7**, 713, (2011).
[2] A. Fert, V. Cros, J. Sampaio, *Nat. Nano.* **8**, 152, (2013).
[3] A. Raeliarijaona, S. Singh, H. Fu, L. Bellaiche *Phys .Rev. Lett.* **110**, 137205, (2013).
[4] L. Bellaiche, S. Singh, *Phys. Rev. B.* **88**, 161102, (2013).
[5] S. Bhattacharjee, S. Singh, D. Wang, M. Viret, L. Bellaiche, *J. Phys.: Cond. Mat.* **26**, 315008, (2014).
[6] R. Walter, M. Viret, S. Singh, L. Bellaiche, *J. Phys.: Cond. Mat.* **26**, 432201, (2014).

Strain control of electronic structure in epitaxial $LaNiO_3$

J. R. Petrie[1], V. R. Cooper[1], S. Okamoto[1], J. W. Freeland[2], and H. N. Lee[1].

[1]Materials Science & Technology Division, Oak Ridge National Laboratory, Oak Ridge, TN, USA
[2]Advanced Photon Source, Argonne National Laboratory, Argonne, IL, USA

Perovskites that are conducting at room temperature have found a significant niche as electrodes for functional oxide devices. One such oxide is $LaNiO_3$, which exhibits a unique paramagnetic metallic behavior. While other strongly correlated oxides in the d^7 *Re*NiO_3 (*Re* = trivalent rare earth ion) system display a metal-to-insulator (MIT) transition due to the more compressed Ni-O bond associated with smaller *Re* ions, bulk $LaNiO_3$ shows no such transition[1]. The larger La^{3+} ion results in a rhombohedral structure that remains metallic down to low temperatures as a more linear Ni-O-Ni bond angle closest to 180º substantiates increased Ni hybridization with the O (2*p*) states. However, structural modifications due to a lattice-mismatch across an interface can result in significant changes in NiO_6 octahedral bond lengths and rotations, resulting in novel electronic properties as the band structure of this e_g^1 system is altered. Recent theoretical work has postulated that by confining the e_g electron to the in-plane d_{x2-y2} orbitals, one could approach the high-Tc superconductivity seen in cuprates[2]. Other work has emphasized the importance of the d_{z2} orbitals in surface catalysis[3].

To systematically explore how we could use structural modifications to control the electrical transport and orbital polarization, we have taken advantage of the unique stoichiometric and thickness control offered by pulsed laser epitaxy to deposit $LaNiO_3$ thin films on different substrates. The resulting high quality (001)-oriented films were coherently grown, as confirmed by x-ray diffraction, and, at 10 nm, were thick enough to minimize the effects of dimensionality due to weak localization and polar disruption associated with films under 2 nm[4]. As the biaxial strain was swept from 2.7% to -1.3%, the tetragonality, as measured by the *c/a* ratio, increased from 0.96 to 1.04 with increasing levels of compressive strain. Likewise, the in-plane conductivity, as measured via the van der Pauw technique, was enhanced by compressive strain. Average polarized X-ray absorbance spectroscopy (XAS) measurements verified in all cases the 3+ oxidation state of the Ni ion and its d^7 occupancy. As seen in Figure 1, X-ray linear dichroism (XLD) studies showed that all strain resulted in orbital splitting while compressive (tensile) strain tended to orbitally polarize the e_g^1 electron towards the d_{z2} (d_{x2-y2}) orbital, an effect correspondingly observed in other thin films[5].

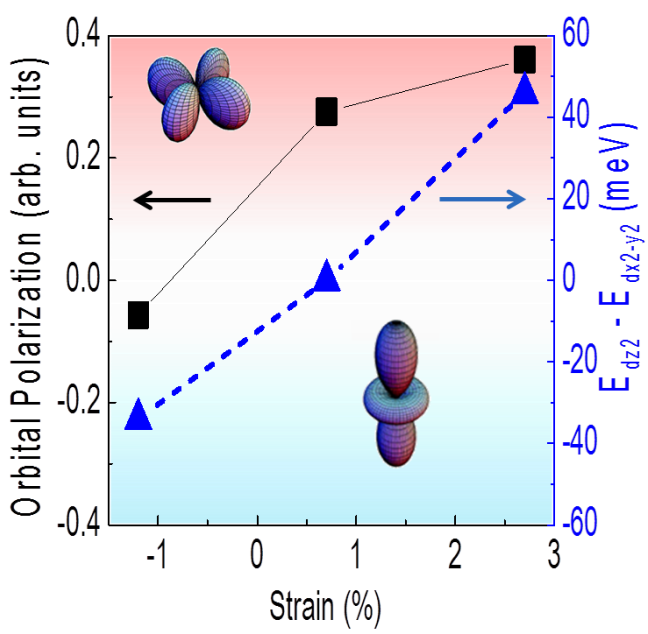

Figure 1 Orbital polarization and splitting as a function of strain, as captured by the $d_{z2} - d_{x2-y2}$ differences in either XLD area or peak position of polarized X-rays, respectively.

Density functional theory calculations were able to correlate the increased tetragonality with compressive strain. We found such strain resulted in a larger Ni-O-Ni bond angle as a result of decreased octahedral rotation around the [110] direction, which led to increases in conductivity. In addition, calculated changes in the Ni-O bond length provided a structural basis for the observed orbital splitting and polarization. As determined in this study, compressive strain

leads to greater hybridization between Ni and O(2p), yielding a greater out-of-plane orbital polarization, whereas the tensile strain follows the opposite trend. Strain control of these properties thus provides a possible mechanism towards tuning electrical and catalytic properties.

The work was supported by the U.S. Department of Energy, Office of Science, Basic Energy Sciences, Materials Sciences and Engineering Division (synthesis) and by the LDRD Program of ORNL (theory and electrochemical testing). Use of the Advanced Photon Source was supported by the U. S. Department of Energy, Office of Science, under Contract No.DE-AC02-06CH11357.

References

[1] J.M. Rondinelli, S.J. May, and J.W. Freeland, *MRS Bulletin* **37** (03), 261 (2012).
[2] J. Chaloupka, and G. Khaliullin, *Phy.Rev. Lett.* **100** (1), 016404 (2008).
[3] J.Suntivich, H.A. Gasteiger, N. Yabuuchi, H. Nakanishi, J.B. Goodenough, and Y. Shao-Horn, *Nat Chem* **3** (7), 546 (2011).
[4] D.P. Kumah, A. Malashevich, A.S. Disa, D.A. Arena, F.J. Walker, S. Ismail-Beigi, and C.H. Ahn, *Phys. Rev. App.* **2** (5), 054004 (2014).
[5] D. Pesquera, G. Herranz, A. Barla, E. Pellegrin, F. Bondino, E. Magnano, F. Sánchez, and J. Fontcuberta, *Nat Commun* **3**, 1189 (2012).

Revisiting the structural evolution in powders and single crystals of PMN-xPT

D. Phelan[1,2], E.E. Rodriguez[2,3], J. Gao[4], Y. Bing[4], Z.-G. Ye[4], Q. Huang[2], J. Wen[5], G. Xu[6], C. Stock[7], M. Matsuura[8], and P.M. Gehring[2]

[1]Materials Science Division, Argonne National Laboratory, Argonne, USA
[2]NIST Center for Neutron Research, National Institute of Standards and Technology, Gaithersburg, USA
[3]Department of Chemistry and Biochemistry, University of Maryland, College Park, USA
[4]Department of Chemistry, Simon Fraser University, Burnaby, Canada
[5]School of Physics, Nanjing University, Nanjing, China
[6]Condensed Matter Physics and Materials Science Dept., Brookhaven National Laboratory, Upton, USA
[7]School of Physics and Astronomy, University of Edinburgh, Edinburgh, United Kingdom
[8]Institute for Materials Research, Tohoku University, Sendai, Japan

The intimate connection between electromechanical properties and structure mandates that determination and understanding of the crystal structure is prominently important for interpreting piezoelectric properties. Indeed, it is well-known that the best piezoelectric properties in Pb-based ferroelectric relaxors, such as (1-*x*)$PbMg_{1/3}Nb_{2/3}O_3$-*x*$PbTiO_3$ (PMN-*x*PT), occur at morphotropic phase boundaries (MPBs) that separate different ferroelectric symmetries, in particular pseudorhombohedral and tetragonal symmetries. Nevertheless, the phase diagrams of such systems are complicated by a variety of factors: (i) powder diffraction patterns can be well fit by a number of structures, and the use of a higher or lower symmetry is often a non-trivial choice; (ii) there is a significant amount of local atomic disorder such that the local structure differs from the average structure; (iii) there are discrepancies between single crystal and powder diffraction measurements [1]; (iv) differing line-shapes have been observed from the same crystal depending on the X-ray wavelengths [2]. (iii) and (iv) can be understood as a consequence of a skin effect such that the skin or surface layer of the single crystal possesses a different structure than the bulk interior, though this remains a controversial subject [3]. We have reinvestigated the phase diagram of PMN-*x*PT using powder neutron diffraction on two sets of powders (*x*=0.1, 0.2, 0.3, and 0.4), with one set annealed after grinding to promote oxygen stoichiometry and to relieve grinding-induced strain, in order to determine how such strain might affect the crystal structure and perhaps have led to ambiguity in the phase diagram. Furthermore, we directly compare the profiles of Bragg reflections measured on these powders with measurements of single-crystals.

Briefly, we found that polycrystalline samples of all compositions studied ($0.1 \leq x \leq 0.4$) possess a ferroelectric ground-state. Consistent with the work of Singh *et al.* [4], our refinements favored a monoclinic (s.g. *Cm*) structure on the Ti-poor side of the MPB, though such a conclusion is based on the quality of agreement factors in Rietveld refinements rather than the observation of a splitting not allowed by the rhombohedral (*R3m*) symmetry. Regardless of whether the refinement was carried out in monoclinic or rhombohedral symmetry, a slightly smaller ferroelectric distortion was consistently obtained for the set of samples annealed after grinding to reduce strain and promote oxygen stoichiometry as compared to the as-grown samples. The notion of strained crystals having a larger distortion would be consistent with a skin effect in single crystals, provided that the surface layer of the crystals was significantly more strained than the interior. Nevertheless, the subtlety of this effect in our polycrystalline samples suggests that external, mechanical sources of strain, such as grinding or polishing, are unlikely to account for the differences between powders and single crystals that have been attributed to a skin effect.

Direct comparisons between the observed lineshapes of select Bragg reflections show that our polycrystalline samples are inconsistent with measurements of single crystals on the Ti-poor side of the MPB. We argue that the polycrystalline grains are essentially entirely composed of “skin” and attribute the different lineshapes of single crystals and powders to a skin effect. Interestingly, on the Ti-rich (tetragonal) side of the MPB, we find that the structures of the polycrystalline and single crystal samples

become consistent with one another. The cross-over from a regime where there is a skin-effect to one where the skin-effect disappears occurs around the MPB at a composition $x \leq 0.40$. We have constructed a phase diagram that illustrates the evolution of both polycrystalline and single crystal ground-states. We suggest that the disappearance of the skin effect is related to the relative strengths of the ferroelectric distortion and random electric fields. An expanded discussion can be found in [5].

Acknowledgements

The authors acknowledge the support of the National Institute of Standards and Technology, U. S. Department of Commerce, in providing the neutron research facilities used in this work. The work at Simon Fraser University was supported by the United States Office of Naval Research (ONR, Grant No. N00014-12-1-1045) and the Natural Sciences and Engineering Research Council of Canada (NSERC, Grant No. 203772). Work in the Materials Science Division at Argonne National Laboratory is supported by the U.S. Department of Energy, Office of Science, Basic Energy Sciences, Materials Science and Engineering Division under Contract No. DE-AC02-06CH11357. GX acknowledges support from the Office of Basic Energy Sciences, U.S. Department of Energy under Contract No. DE-AC02-98CH10886, while CS acknowledges the Carnegie Trust for the Universities of Scotland and the Royal Society.

References

[1] P.M. Gehring *et al*., *J. Phys.: Condens. Matter* **16**, 7113 (2004).
[2] G. Xu *et al*., *Phys. Rev. B* **67**, 104102 (2003).
[3] E.H. Kisi and J.S. Forrester, *J. Phys.: Condens. Matter* **17**, L381 (2005).
[4] A. K. Singh *et al*., *Phys. Rev. B* **74**, 024101 (2006).
[5] D. Phelan *et al*., *Phase Transitions* (in press, DOI: 10.1080/01411594.2014.989226).

Vortex lines at the intersection of domain walls in ferroelectrics

Sergei Prokhorenko,* Yousra Nahas, and L. Bellaiche
Physics Department and Institute for Nanoscience and Engineering,
University of Arkansas, Fayetteville, Arkansas 72701, USA

In this study we qualitatively investigate the geometric properties of intersecting ferroelectric domain walls. Such intersections, being the locus of two vanishing polarization components, represent topological defects of reduced dimensionality [1] as compared to the domain walls themselves, and therefore can posses advanced functionalities for the design and implementation of novel electronic devices [2, 3]. However, despite the considerable interest in nontrivial ferroelectric domain patterns [2–5], the full topological classification of inhomogeneous polarization structures in the vicinity of the domain walls intersection lines has not been fully developed. For instance, the description of the intersection of two domain walls has been thoroughly investigated in the sole case of ferroelectric systems described by two-component order parameter [7]. Herein, we attempt to advance the methodology described in Ref. [7] to the three dimensional case.

Our discussion is limited to intersecting domain walls that do not carry any bound electric charge density [9]. Without any loss of generality, we choose the line at the intersection of the domain walls as being along the z-axis, and the domain walls coinciding with the xz and yz coordinate planes. Since $\nabla \cdot P = 0$, only P_x (P_y) and P_z components of polarization can change upon crossing the xz (yz) plane. Two simple illustrative cases under study are presented in Fig.1. In the first case (Fig.1(a.1)), only P_x and P_y components change across the xz and yz planes, respectively. The presented configuration corresponds to a flux-closure pattern of polarization for the P_x and P_y components, while additionally featuring a nonzero constant P_z component. Notably, similar polarization structures have been predicted from first-principles calculations in (Ba,Sr)TiO_3 nanocomposites [5]. One instructive topological characteristic of this configuration can be obtained by mapping the flux of polarization through a contour in real space to the flux in the order parameter space. The topological flux in real space can be defined as $\Phi = \int_S n \cdot (\partial_x n \times \partial_y n)$ [8], where n represents the normalized polarization vector field, and S denotes a specific simply connected region in real space. In the case under study, topological flux represents a characteristic of particular importance. Indeed, the translational invariance of the considered polarization distributions along the domains intersection line makes the system effectively two-dimensional, allowing to keep Φ well defined. Practically, the first step of the calculation of topological flux generated by the intersection line (its topological charge), is achieved by defining a closed contour in the xy plane enclosing the intersection line (blue circle in Fig.1(a.3)). Secondly, one maps the orientation of the dipoles along this path onto the unit sphere. In our case this yields a square whose nodes (red dots in Fig.1(a.2) and (a.3)) intercept the sphere at the latitude defined by P_z. The topological flux is equal to the area of the spherical cap with cut edges (Fig.1(a.2)) obtained by projection of the obtained square on the sphere surface. As one can immediately see, the obtained topological charge monotonically increases upon decreasing $|P_z|$, however showing a discontinuity at $P_z = 0$. Indeed, in contrast to magnetic systems, for which the magnitude of individual spins can be assumed constant, Φ is equal to zero at $P_z = 0$, while having a limit of $\pi/2$ at $P_z \to 0$. The existence of such limiting point configuration would correspond to a ferroelectric analogue of the so-called Bloch-line in magnetic materials. Finally, it is worthwhile noticing that in this domains configuration, the variation of P_x and P_y along the path are encompassed in the cross product term $\partial_x n \times \partial_y n$ appearing in the chiral charge definition. Hence, considering these two components only, yields a vortex singularity in the xy plane, thereby enabling the identification of the intersection line with a vortex line.

The second case is concerned with the domain walls intersection for which only P_z and P_x components change across the yz and xz planes, respectively (Fig.1(b.1)). This configuration is assumed to have a constant P_y component. The mapping of the flux in real space to the order

*Electronic address: prokhorenko.s@gmail.com

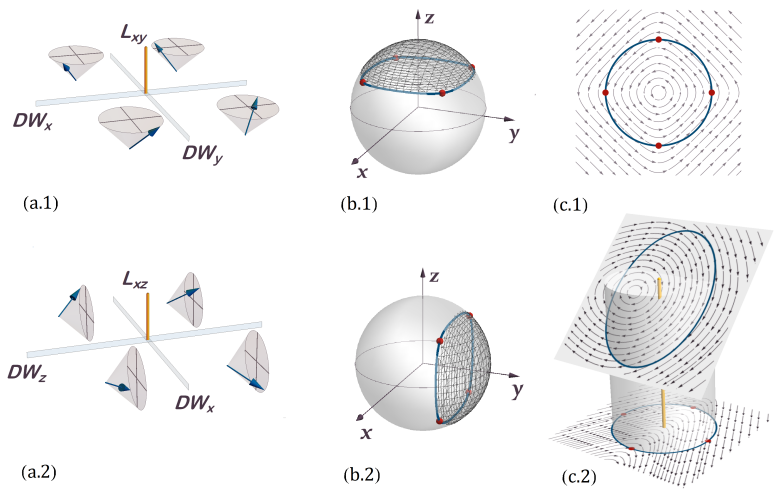

FIG. 1: (a) Dipolar structure in the vicinity of intersecting domain walls. In (a.1) is displayed the case of intersecting P_x and P_y domain walls (denoted by DW_x and DW_y), while (a.2) corresponds to the case of intersecting P_x and P_z domain walls (DW_x and DW_z). In both cases, the intersection line is along the z-axis (L_{xy} in (a.1) and L_{xz} in (a.2)). (b) Mapping of the polarization orientation onto the unit sphere when circulating along a closed path in xy-plane enclosing L_{xy} (b.1) and L_{xz} (b.2). (c) Projection of polarization field depicted in (a.1) on xy plane (c.1). Projection of polarization distribution (b.1) on two differently oriented planes. In the inclined plane, the projection of the vector field reveals its vortex singularity.

parameter space yields the same result as in the former case, however having the truncated spherical cap revolving around the y-axis, in accordance with the constant P_y component. Notably, one does not observe the vortex singularity in the xz plane, but rather an Ising domain profile, which in our case corresponds to the stacking of the vortices in xz plane along the intersection line contained within this plane. Later can be verified by projecting the polarization vector field on xy plane rotated around x axis by the angle ϕ gradually approaching $\pi/2$. The projection corresponding to $\phi = \pi/4$ is depicted in Fig.1(b.3), for which the vortex nature of the intersection line is retrieved. At $\phi \to \pi/2$ the distance between the core of the projected vortex observed in Fig.1(b.3) and the domain walls intersection line tends to zero along with the elongation of the vortex projection along the rotated y axis. Moreover, the vortex nature of the intersection line can be confirmed by the existence of a global transformation of the vector field corresponding to a passive coordinate rotation around x axis by an angle of $\pi/2$ which conserves the topological flux.

Finally, we show, that realistic patterns of polarization field yielding an integer topological flux can be allowed in ferroelectric systems thereby allowing to predict dipolar configurations analogous to magnetic skyrmionic structures.

This work is supported by the ARO grant W911NF-12-1–0085.

---

[1] T. C. Proctor, D. A. Garanin, and E. M. Chudnovsky, *Phys. Rev. Lett.*, 112, 097201 (2014)
[2] N. Balke, B. Winchester, W. Ren, Y.H. Chu, A.N. Morozovska, E.A. Eliseev, M. Huijben, R.K. Vasudevan, P. Maksymovych, J. Britson, S. Jesse, I.A. Kornev, R. Ramesh, L. Bellaiche, L.Q. Chen, and S.V. Kalinin, *Nature Physics*, 8, 8188 (2012)
[3] T. Choi, Y. Horibe, H. T. Yi, Y. J. Choi, Weida Wu, and S.-W. Cheong, *Nature Mat.*, 9, 253 (2010)
[4] Jia, C. L. , K. W. Urban , M. Alexe , D. Hesse , and I. Vrejoiu *Science*, 331, 1420 (2011)
[5] L. Louis, I. Kornev, G. Geneste, B. Dkhil, and L. Bellaiche, *J. Phys.: Condens. Matter*, 24, 402201 (2012)
[6] S. Prosandeev, A. Malashevich, Z. Gui, L. Louis, R. Walter, I. Souza, and L. Bellaiche, *Phys. Rev. B*, 87, 195111 (2013)
[7] E. B. Sonin, and A. K. Tagantsev, *Sov. Phys. JETP*, 67, 396 (1988)
[8] N.D. Mermin, *Rev. Mod. Phys.*, 51, 591 (1979)
[9] P. Marton, I. Rychetsky, and J. Hlinka, *Phys. Rev. B*, 81, 144125 2010

Influence of vacancies on polarization and polarization switching from first-principles.

Aldo Raeliarijaona and Huaxiang Fu
Department of Physics, University of Arkansas, Fayetteville, AR 72701, USA

We investigate the influence of vacancies on polarization and polarization switching in ferroelectric $BaTiO_3$ using first-principles calculations. Our study demonstrates that $BaTiO_3$ with V_{O1}^{2+}, V_{Ti}^{4-} and V_{Ba}^{2-} are insulators with nonzero electric polarization. Interestingly, we find that vacancy species have little effect on the polarization of $BaTiO_3$ as they produce polarizations comparable to that in perfect crystal. Furthermore, a new switching mechanism is proposed to reverse the polarization when vacancy is present. We show that the switching barrier in the presence of V_{O1}^{2+} is small with $\Delta E = 6$ meV per formula cell.

ONR's Research Program on Acoustic Transduction Materials and Devices

Harold C. Robinson, Wallace A. Smith and Carl C.M. Wu
Office of Naval Research
Materials Division, ONR 332
875 North Randolph Street
Arlington, Virginia 22203-1995

Research on innovative materials and device structures is sought that enhances the performance of electro-mechanical transducers used by the Department of Navy to generate, detect and suppress undersea sound waves. The present Office of Naval Research program has two thrusts. The first aims to devise and validate first-principles quantum-mechanical methods to evaluate the properties of materials with structural phase transitions; this will enable the exploration of the properties of new materials in advance of their synthesis. The second focuses on the new high coupling, high-strain relaxor piezoelectric single crystals. Efforts underway aim to produce and characterize these piezocrystals and to design, fabricate and test innovative transducers from them for Navy SONAR systems.

Interfacial Structure in Epitaxial Perovskite Oxides on (001) Ge Crystal

Xuan Shen,[1,2] K. Ahmadi-Majlan,[3] Joseph H. Ngai,[3] Di Wu,[2] and Dong Su[1]

[1]Center for Functional Nanomaterials, Brookhaven National Laboratory, Upton, NY 11973, USA
[2]National Laboratory of Solid State Microstructures and Department of Materials Science and Engineering, Nanjing University, Nanjing, 210093, China
[3]Department of Physics, University of Texas at Arlington, 502 Yates Street, Arlington, TX 76019, USA

Abstract

Perovskite oxides films have attracted much attention due to their intriguing electrical, magnetic, and optical properties. In the hetero-epitaxial thin film system, as the film grows up to a certain thickness, interfacial dislocations are expected to form to relax the strain. Intensive transmission electron microscopy (TEM) work has been performed for perovskite-on-perovskite systems, e.g., PZT/$SrTiO_3$,[1] $SrTiO_3$/$LaAlO_3$,[2] *et al*. It is well recognized that the interfacial dislocations are crucial for some physical properties of the thin film.[3,4] Very recently, high-quality epitaxial perovskite thin films on semiconductor wafers have been achieved. However the nature of interfacial dislocations in this perovskite-on-diamond system has never been reported.

We investigated the interfacial structure of perovskite ($SrZr_{0.68}Ti_{0.32}O_3$, SZTO) thin film on (001) Ge single crystal, using various TEM techniques. In contrast to the most found dislocations with Burgers vectors of ***a*** <100> in perovskite heterostructures (cubic-on-cubic system), we observed dislocation-loop with a Burgers vector of ½***a*** <111>. We also found the dislocation reaction from two partial dislocations to one perfect dislocation ½***a*** $[1\bar{1}1]$ + ½***a*** $[11\bar{1}]$ = ***a*** [100], which leads to the formation of threading dislocation with Burgers vector of ***a*** [100]. In addition, we found the coupling of dislocation half-loop with anti-phase boundary (APB, shift vector of ½***a*** <111>) induced by lattice terrace of Ge and they can decouple after annealing. The possible models based on the half-loop theory are also proposed for the dislocation reactions and the coupling behavior.

Our findings on the interfacial dislocations, which are for the first time reported in perovskite-on-diamond system, describe the nature of the interface between semiconductors and perovskite, and give valuable insights on how the misfit strain is relaxed. It will help the researchers who investigate and develop the semiconductor-based functional oxide devices, to optimize their design and growth techniques.

Acknowledgements
Electron microscopy studies were performed at the Center for Functional Nanomaterials, Brookhaven National Laboratory supported by the U.S. Department of Energy, Office of Basic Energy Sciences, under contract no. DEAC02-98CH10886. X. S. is grateful for the financial support of the China Scholarship Council and Brookhaven National Laboratory for his exchange program. K. A. -M. and J. H. N. acknowledge the support of The University of Texas at Arlington. D. W. thanks National Key Basic Research Program of China (2015CB921203) for support. We thank Dr. Woodhead for the proof reading.

References
[1] M. –W. Chu, I. Szafraniak, R. Scholz, C. Harnagea, D. Hesse, M. Alexe, and U. Gösele, Nature Materials **3,** 87 (2004)
[2] D. Su, T. Yamada, V. O. Sherman, A. K. Tagantsev, P. Muralt, and N. Setter, J. Appl. Phys. **101,** 064102 (2007)
[3] R. Ramesh, and Nicola A. Spaldin, Nature Materials **6,** 21 (2007)
[4] J. H. Lee, *et al.*, Nature **466,** 954 (2010)

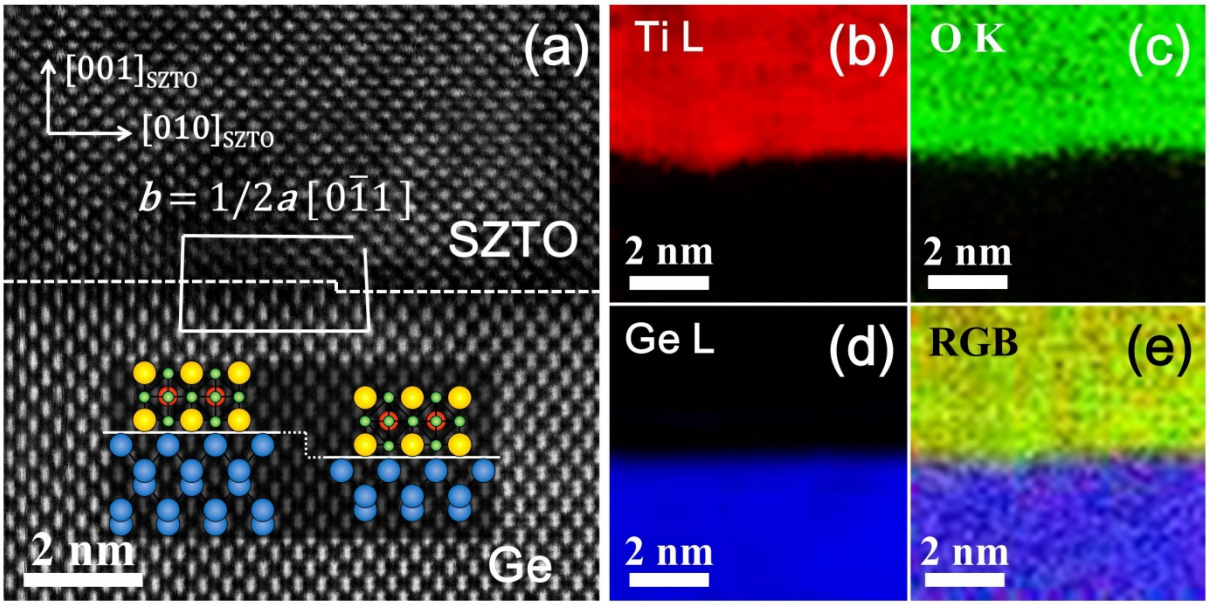

Figure 1. (a) Cross-sectional STEM image with Burgers vector along [0$\bar{1}$1] direction. The Burgers circuit is drawn around the dislocation core. Schematic diagram of step and terrace structure is shown in the inset. Elemental maps (50 pixels by 50 pixels) from STEM EELS of Ti (red), O (green), Ge (blue) and their RGB mixture are shown in (b), (c), (d), and (e), respectively.

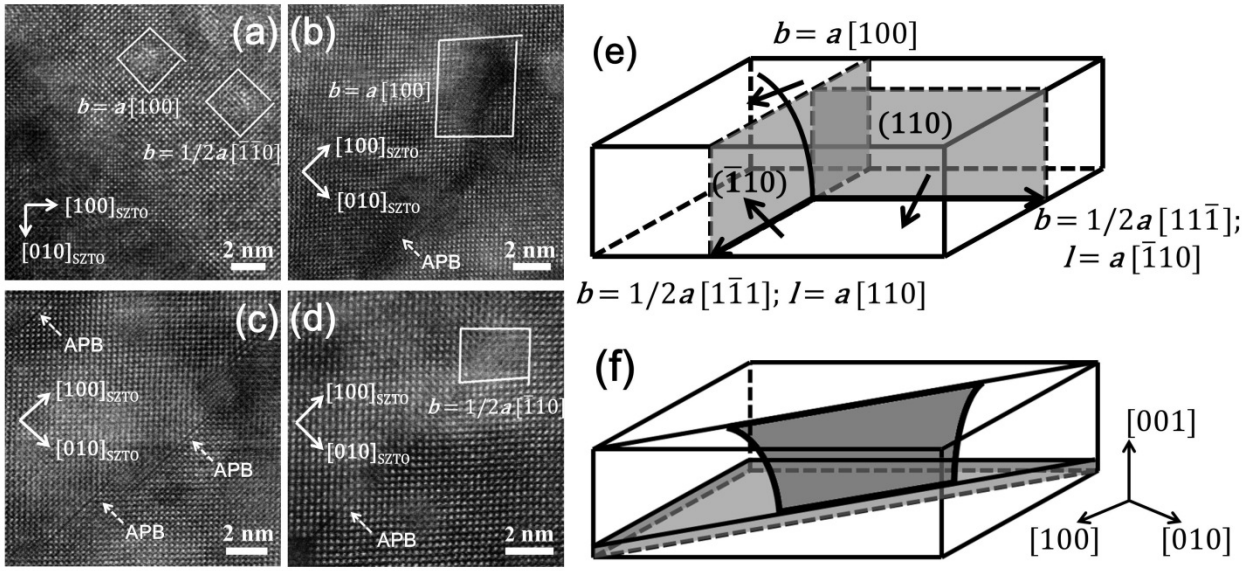

Figure 2. (a) Plane-view HRTEM image of SZTO thin films. HR-STEM images of the plane view are shown in (b), (c), and (d). The APBs are indicated by white dashed arrows. Schematic diagrams of dislocation dissociation and coupling behavior between APBs and dislocations are shown in (e) and (f), respectively.

Local structure and oxidation state of Ni impurity in $SrTiO_3$, $BaTiO_3$, and $PbTiO_3$

I. A. Sluchinskaya and A. I. Lebedev

Physics Department, Moscow State University, Moscow, 119991, Russia

In recent years, doped ferroelectric perovskite oxides have attracted attention because of developing a new type of solar energy converters based on the photovoltaic effect. Recent theoretical studies have shown that the substitution of Ti at the *B* site of $PbTiO_3$ by vacancy-compensated divalent impurities with the d^8 electron configuration (Ni, Pd, Pt) reduces the band gap to the levels optimal for effective energy conversion [1]. As an 3*d* impurity may occupy different sites in $SrTiO_3$, $BaTiO_3$, and $PbTiO_3$ and have different oxidation states [2], the aim of this work was to use XAFS spectroscopy to determine the structural position and oxidation state of nickel in $SrTiO_3$, $BaTiO_3$, and $PbTiO_3$ and to compare the obtained results with results of first-principles calculations.

Samples of $SrTiO_3$, $BaTiO_3$, and $PbTiO_3$ with Ni concentration of 2–3% were prepared by the solid-state reaction method at 1100–1500°C. Since the doping with 3*d* elements results in the formation of the hexagonal phase of $BaTiO_3$, in addition to doped hexagonal samples of $BaTiO_3$, samples with the cubic structure obtained by substituting 20% of Ba atoms by Sr atoms were investigated. Doping was performed by adding nickel acetate in the case of $SrTiO_3$ and $BaTiO_3$ and by adding $NiNb_2O_6$ columbite phase in the case of $PbTiO_3$. The quality of the samples was controlled by X-ray diffraction. Spectra of fluorescent EXAFS and XANES were recorded at the KMC-2 station of the BESSY synchrotron radiation source at the Ni *K*-edge in the fluorescence mode at 300 K. The calculations were performed in the LDA+*U* approximation for supercells containing Ni atoms in the oxidation state determined from the XANES data.

All the samples were single-phase with the cubic, tetragonal, or hexagonal perovskite structures at 300 K. To determine the oxidation state of the Ni impurity, the position of the absorption edge in XANES spectra was compared with those of the reference compounds (Fig. 1). It is seen that in $SrTiO_3$ nickel is in the 4+ oxidation state [3], whereas in $BaTiO_3$, $Ba_{0.8}Sr_{0.2}TiO_3$, and $PbTiO_3$ it is in the 2+ oxidation state.

To determine the local structure of the Ni impurity, EXAFS spectra were analyzed. According to the EXAFS data, in $SrTiO_3$ the Ni^{4+} ions are located at the *B* sites and are on-center ($R_{Ni\text{-}O}$ = 1.925 Å, $R_{Ni\text{-}Sr}$ = 3.36 Å, $R_{Ni\text{-}Ti}$ = 3.89 Å) [3]. The calculated distances for this structural model ($R_{Ni\text{-}O}$ = 1.923 Å, $R_{Ni\text{-}Sr}$ = 3.376 Å, $R_{Ni\text{-}Ti}$ = 3.935 Å) were in good agreement with experiment.

For cubic $Ba_{0.8}Sr_{0.2}TiO_3$ the satisfactory agreement between the experimental and calculated spectra was obtained in the model in which the impurity atom forms the complex with the oxygen vacancy and is shifted from the Ti site ($R_{Ni\text{-}O}$ = 2.07 Å). However, as was shown in the first-principles calculation for this impurity complex, the Ni^{2+} ion forms a typical square-planar coordination with the Ni-O distance of 1.940 Å which is 0.13 Å shorter than the experimental one. So, this model disagrees with the experimental data. In order to improve the agreement, other Ni impurity complexes were modeled and it was shown that to retain large Ni-O distance observed in the experiment, the local environment of Ni should be perfect (six oxygen atoms). So we think that the oxygen vacancy that compensate the ionic charge of Ni at the Ti site is distant from the impurity atom. For this models, we get the $R_{Ni\text{-}O}$ distance of 2.064–2.079 Å, close the experimental one.

For tetragonal $PbTiO_3$, the distances to the closest atoms determined from the EXAFS data analysis were $R_{Ni\,O}$ = 2.04 Å and $R_{Ni\text{-}Ti(Ni)}$ = 2.95–2.99 Å. To construct the structural model of the local environment of Ni atom in $PbTiO_3$, three first-principles models were analyzed. First, we used the model proposed in [1] in which the Ni^{2+} atom at the *B* site is surrounded by five oxygen atoms and one oxygen vacancy. Second, we analyzed the model with Ni^{2+} at the *B* site and a distant oxygen vacancy (two configurations). And the last, we analyzed the model with off-center Ni^{2+} ion at the *A* site. Unfortunately, none of these models agrees with

the experiment. The first and third models give the Ni^{2+}-O distance of 1.905 Å and 1.896 Å, respectively, which are typical of square-planar Ni coordination and are inconsistent with experiment. The Fourier transforms of the EXAFS spectra for all studied samples and $NiTiO_3$ reference compound are shown in Fig. 2. The most intriguing feature of the Fourier transforms for $PbTiO_3$(Ni) is the appearance of an extra peak corresponding to the light (Ti or Ni) atom in the second shell. This distance is absent in three above-mentioned models of $PbTiO_3$(Ni). We suppose that Ni atoms in $PbTiO_3$ form some complexes, whose structure is resembling the $NiTiO_3$ structure in which the octahedra are edge-sharing. At the same time, no traces of $NiTiO_3$ and $NiNb_2O_6$ phases are present in EXAFS and X-ray data.

It should be noted that the color of the samples depends on the local structure of the Ni impurity: the color is nearly black for $SrTiO_3$ and $BaSrTiO_3$ in which Ni is at the *B* site and dark-yellow for $PbTiO_3$ in which Ni forms a complex with a structure different from the perovskite structure.

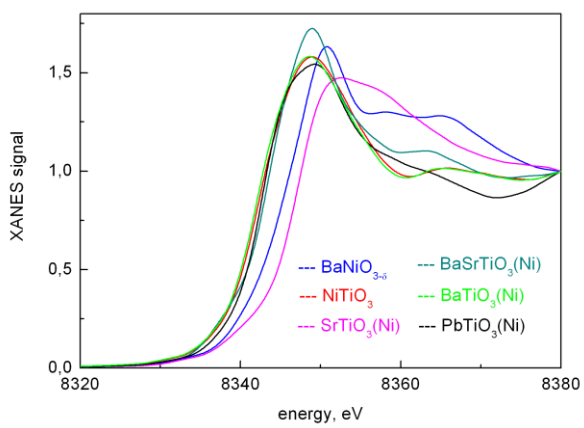

Fig. 1. XANES spectra of $SrTiO_3$(Ni), $BaTiO_3$(Ni), $Ba_{0.8}Sr_{0.2}TiO_3$(Ni), and $PbTiO_3$(Ni) samples and of $BaNiO_{3-\delta}$ ($\delta\approx0.4$) and $NiTiO_3$ reference compounds recorded at the Ni *K*-edge at 300 K.

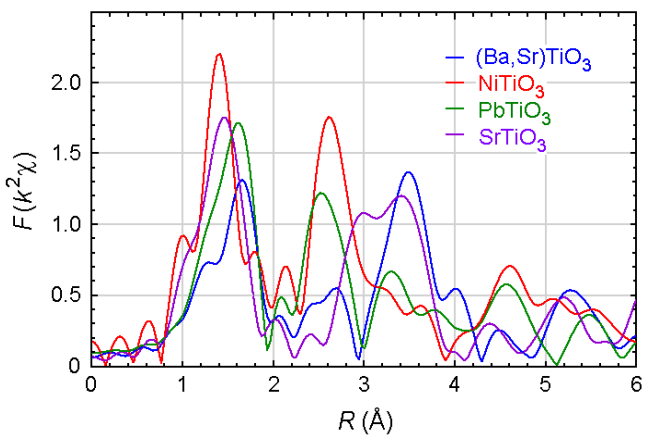

Fig. 2. Fourier transforms of the EXAFS spectra of $SrTiO_3$(Ni), $Ba_{0.8}Sr_{0.2}TiO_3$(Ni), and $PbTiO_3$(Ni) samples and of $NiTiO_3$ reference compound.

Acknowledgment. This work was supported by RFBR Grant No. 13-02-00724. The authors are grateful to the Russian-German laboratory of BESSY for fruitful collaboration.

References

[1] W. Bennett, I. Grinberg, A.M. Rappe. *J. Am. Chem. Soc.* **130**, 17409 (2008).
[2] A.I. Lebedev, I.A. Sluchinskaya, A. Erko, V.F. Kozlovskii. *JETP Lett.* **89**, 457 (2009).
[3] I.A. Sluchinskaya, A.I. Lebedev, A. Erko. *Phys. Solid State* **56**, 442 (2014).

Electron Transport Properties of Composite Ferroelectrics

Oleg Udalov[1], N.M. Chtchelkatchev[2], A. Glatz[3], I.S. Beloborodov[1]

[1] Department of Physics and Astronomy, California State University Northridge, Northridge, CA 91330, USA
[2] Institute for Physics of Microstructures, Russian Academy of Science, Nizhny Novgorod, 603950, Russia
[3]Argonne National Laboratory, Argonne, Illinois 60439, USA

In the past years, composite materials, consisting of conductive grains embedded into some insulating matrix, have attracted continuously increasing attention due to the possibility to combine different, and sometimes competing physical phenomena in a single material and observe new fundamental effects[1,2]. The possible range of observable behaviors is very broad and the following examples are by no means exhaustive: granular metals can show the insulator-superconductor transition[3] due to an interplay of superconductivity and Coulomb blockade, giant magnetoresistance effects appear in granular ferromagnets[4] because of the spin dependent tunneling of current carriers between grains, or the combination of ferroelectric and ferromagnetic materials allows to produce a strain mediated magnetoelectric coupling[5].

We investigated theoretically electron transport in granular ferroelectrics (GFE) consisting of metallic nano grains embedded into a ferroelectric matrix and show that depending on the external electric field and temperature three transport regimes are possible: 1) multiple electron cotunneling, 2) sequential tunneling, and 3) metallic transport[6,7,8]. We showed that the crossover between different regimes can be studied by changing the temperature or the external electric field leading to a strongly non-linear conductivity behavior and large conductivity jumps. The microscopic reason for the crossover between different regimes is the changing of the Coulomb gap due to the variation of dielectric permittivity of the ferroelectric (FE) matrix under the influence of temperature or electric field.

For temperatures approaching the paraelectric-ferroelectric transition point the dielectric permittivity of the FE matrix increases leading to a decrease of the Coulomb gap. This leads to occurrence of insulator-metal transition for temperatures close to the ferroelectric Curie temperature and weak applied electric fields (see Fig. 1(a)). The conductivity of GFE increases three orders of magnitude in a rather narrow temperature range. This is an unexpected result because usually conductivity decreases in the vicinity of a phase transition due to scattering of electrons on fluctuations of the order parameter. This behavior can be utilized to built a GFE thermometer for precise temperature measurements. It is worth to mention that this non-trivial behavior is a peculiarity of granular ferroelectrics and cannot be observed in the tunnel junctions with ferroelectric barrier.

Another peculiarity of electron transport in composite ferroelectrics occurs due to the hysteretic behavior of the ferroelectric matrix. The hysteresis leads to the existence of two different intermediate states with different average electrical polarization and correlation function of microscopic electric field and microscopic polarization. The conductivities in these states can be several order of magnitude different. This occurs since the two states of FE matrix corresponds to different transport regimes of the whole GFE, namely insulating and metal. The effect can be utilized in memory applications. It provides the reading mechanism based on the current measurement.

We calculated conductivity of granular metal film placed above FE substrate (see Fig. 1(b)). FE substrate state strongly influences the conductivity of granular film. The state of FE substrate can be controlled

with a gate electrode placed below FE substrate. Due to above mentioned effect conductivity shows hysteresis behavior.

We showed that our theory is in qualitative agreement with recent experiments on transport properties of granular ferroelectrics.

In addition, we show that the main parameters determining the transport in composite ferroelectrics are: 1) the correlation function of intrinsic microscopic field and the local electric polarization and 2) the dielectric permittivity of the ferroelectric matrix.

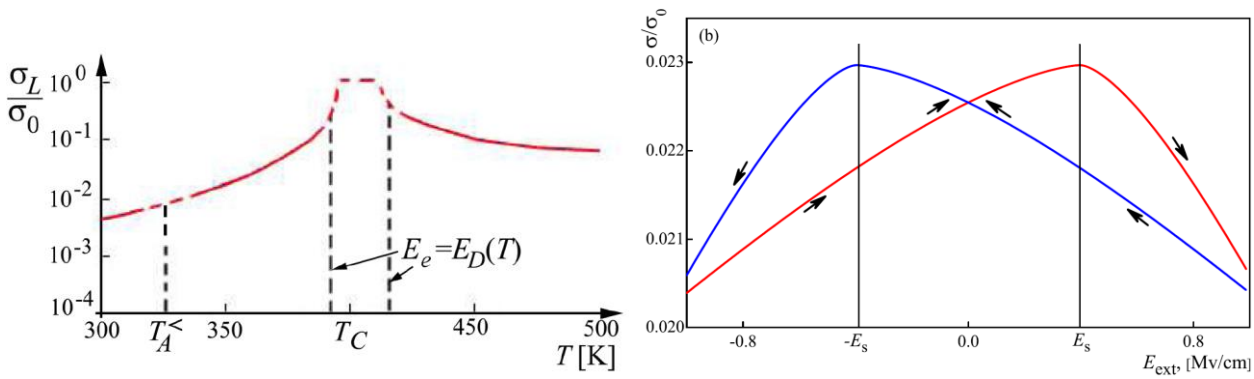

Figure 1. (a) Conductivity as a function of temperature for granular FE in which metal grains embedded into FE matrix. T_C is the FE Curie temperature. (b) Conductivity as a function of gate voltage for a field effect transistor with FE placed in between the channel and a gate electrode. Channel is made of granular metal film. E_s is the FE switching field.

Acknowledgements A.G. was supported by the U.S. Department of Energy Office of Science under the Contract No. DE-AC02-06CH11357. I. B. was supported by NSF under Cooperative Agreement Award EEC-1160504.

References

[1] M. Dawber, K. M. Rabe, and J. F. Scott, *Rev. Mod. Phys.* **77**, 1083 (2005).
[2] I. S. Beloborodov, A. V. Lopatin, V. M. Vinokur, and K. B. Efetov, *Rev. Mod. Phys.* **79**, 469 (2007).
[3] Y. Shapira and G. Deutscher, *Phys. Rev. B* **27**, 4463 (1983).
[4] M. Salvato, M. Lucci, I. Ottaviani, M. Cirillo, E. Tamburri, S. Orlanducci, M. L. Terranova, M. Notarianni, C. C. Young, N. Behabtu, and M. Pasquali, *Phys. Rev. B* **86**, 115117 (2012).
[5] H. Ryu, P. Murugavel, J. H. Lee, S. C. Chae, T. W. Noh, Y. S. Oh, H. J. Kim, K. H. Kim, J. H. Jang,M.Kim,C.Bae, and J.-G. Park, *Appl. Phys. Lett.* **89**, 102907 (2006).
[6] O. G. Udalov, A. Glatz, and I. S. Beloborodov, *Europhys. Lett.* **104**, 47004 (2013).
[7] O. G. Udalov, N. M. Chtchelkatchev, A. Glatz, and I. S. Beloborodov, *Phys. Rev. B* **89**, 054203
[8] O. G. Udalov, N. M. Chtchelkatchev, and I. S. Beloborodov, *Phys. Rev. B* **90**, 054201

High pressure synthesis and characterization of predicted oxynitride perovskite: Yttrium Silicon Oxynitride ($YSiO_2N$)

Rajasekarakumar Vadapoo,[1] Muhtar Ahart,[1] M. Somayazulu,[1] and R. E. Cohen[1,2]

[1]Geophysical laboratory, Carnegie institution of Washington, Washington, DC 20015 USA
[2]Department of Earth Sciences, University College London, WC1E 6BT, London, UK

New stable polar oxynitride perovskites were predicted from first principle calculations.[1] These structures were derived by replacing an oxygen atom by nitrogen in the perovskite structure and also the cations of divalent and trivalent as shown in figure 1. Among the combination of oxynitrides, Yttrium Silicon Oxynitride ($YSiO_2N$) and Yttrium Germanium Oxynitride ($YGeO_2N$) were found to be dynamically stable polar insulators. $YSiO_2N$ was predicted to have a giant effective spontaneous polarization of 130 μC/cm^2, which is one of the largest polarization predicted so far. It has the polar structures with P4mm symmetry as shown in figure 1. The predicted large spontaneous polarization and the nonlinear optical properties of this material have the potential for the futuristic piezoelectric, nonlinear dielectric, high energy x-ray and neutron generator applications.[2, 3]

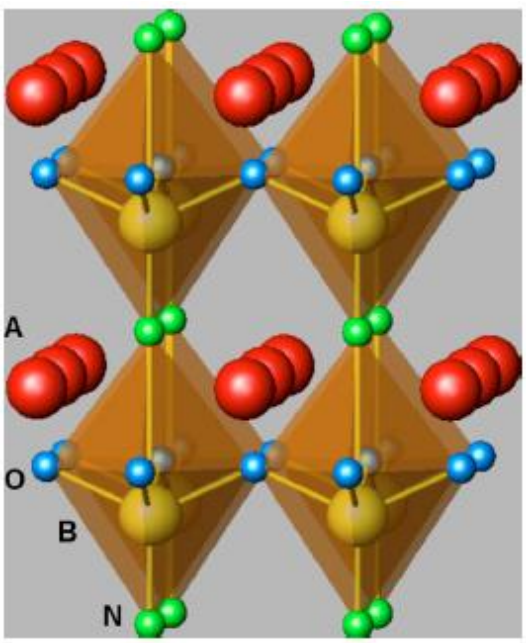

Figure 1. P4mm polar structure of the ordered ABO_2N oxynitride perovskites.[1] Here, A represent Yttrium (Y) and B represent Silicon (Si) atoms.

The theoretical prediction of these improved properties of oxynitride perovskites motivated us to synthesize these novel materials. We prepared the $YSiO_2N$ starting from a mixture of Yttrium nitride (YN) and amorphous Silicon dioxide (SiO_2). We prepared the $YSiO_2N$ sample under high pressure (12GPa) and high temperature (1200 ^{o}C) by using a combination of diamond anvil cell and laser heating technique. Note that YN must be handled in a glove box as it reacts with air and water.

We characterized the run products by x-ray diffraction and Raman spectroscopy for their phase and structural properties. The x-ray diffraction experiments were carried out at sector 16 (0.41 Å) at the Advanced Photon Source, Argonne National laboratory. The x-ray diffraction pattern shows the phase formation of $YSiO_2N$ and matches with the diffraction pattern (shown in red lines at the bottom of the scale) derived from

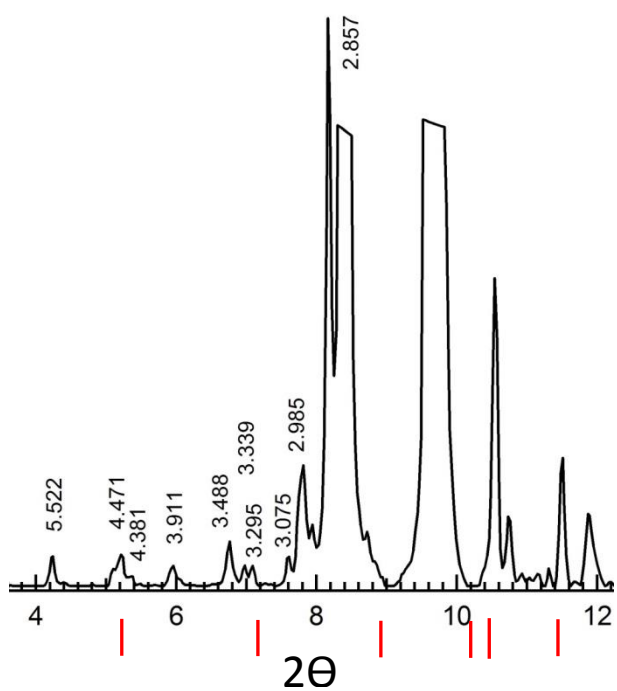

Figure 2. X-Ray diffraction pattern of the high pressure synthesized $YSiO_2N$ compared with the theoritical predicted patterns at the bottom of the scale (in red).

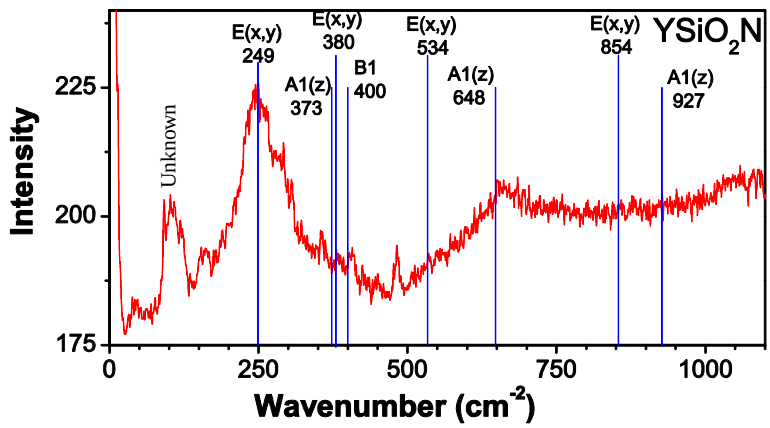

Figure 3. Raman spectra of the $YSiO_2N$ synthesized at high pressure along with the theoretically predicted modes shown with blue reference lines.

the first principle predicted lattice parameters and atomic positions as shown in figure 2. The predicted structure for $YSiO_2N$ in P4mm space group with the lattice parameters of a = 3.228 Å, c = 4.435 Å and with the Wyckoff positions of 1b (0.5 0.5 z), 1a (0 0 z), 2(0.5 0 z) and 1a (0 0 z) for the Y, Si, O, and N atoms respectively.[1] From figure 2, it is clear that the sample is not a single phase oxynitride perovskite, and the sample is not yet well crystallized. The dominant broad peaks at 2Θ correspond to 8.4 and 9.7 match the starting material YN. In addition, a new unassigned dominant peak at d = 2.857 Å is also observed. This indicates the co-existence of other unknown phases. Further effort is in progress to optimize the formation of pure oxynitride phase.

Experiment	Theory[1]
357	A1(z) 373
652	648
Weak 927	927
402	B1 400
246	E(x,y) 249
381	380
Weak 535	534
Weak 859	854

Table 1. The experimental and theoretical Raman modes observed for $YSiO_2N$.

Raman spectroscopy confirms the phase formation of $YSiO_2N$. The comparison of Raman spectra for the synthesized structure with the Raman active modes predicted by theoretical calculations can be seen from figure 3 and table 1. We can observe that most of the theoretically predicted modes are in agreement with the experimentally observed Raman modes. While the predominant 246 cm^{-1} is in excellent agreement some modes show a small shift. Moreover, we observed a strong unassigned peak at 105 cm^{-1} and emergent peaks like at 161 cm^{-1}. Also, the peaks at 534, 854 and 927 cm^{-1} are extremely weak. These evident the formation of oxynitride perovskite along with the coexistence of other phases as confirmed by X-ray diffraction results.

In summary, we have successfully synthesized the stable oxynitride perovskite of $YSiO_2N$ by high energy-high pressure method. The structural characterization confirms the formation of the first principle predicted oxynitride perovskite phase. However unpredicted mixed and, or high pressure induced phases also coexist.

Acknowledgements

This work is supported by ONR grants N00014-12-1-1038 and N00014-14-1-0561, by the ERC Advanced grant ToMCaT, by CDAC-NNSA (DE-NA- 000006).

References

[1] Razvan Caracas, R. E. Cohen, Appl. Phys. Lett. **91**, 092902 (2007).

[2] Piezoelectric transducers and applications, edited by A. Arnau Springer, Heidelberg, 2004.

[3] B. Naranjo, J. K. Gimzewski, and S. putterman, Nature (London) **4343**, 1115 (2005).

Revisiting Galvanomagnetic Effects in Conducting Ferromagnets Through Electromagnetic Field Angular Momentum Density and Magnetic Moment Coupling

R. Walter[1,2,3], M. Viret[4], S. Singh[1], L. Bellaiche[1,2]

[1]Physics Department, University of Arkansas, Fayetteville, Arkansas 72701, USA
[2]Institute for Nanoscience and Engineering, University of Arkansas, Fayetteville, Arkansas 72701, USA
[3]Department of Mathematical Sciences, University of Arkansas, Fayetteville, Arkansas 72701, USA
[4]Service de Physique de l'Etat Condense, CEA Saclay, DSM/IRAMIS/SPEC, URA CNRS 2464, 91191 Gif-Sur-Yvette Cedex, France

This poster presentation discusses the recently proposed coupling between electromagnetic field angular momentum density and magnetic moments [1], with an overview of the different physical phenomena readily explained by this coupling [1-4] and emphasis on various galvanomagnetic effects [2] – anisotropic magnetoresistance and the planar Hall effect.

It is known that reversing the vector resulting from the cross product of electric and magnetic fields reverses the sense of rotation of magnetic vortices, through the coupling of the magnetic toroidal moment with this cross product [5-4]. By appropriately transforming this coupling energy, Ref. [1] demonstrated that the electromagnetic field angular momentum density can directly couple with magnetic moments to produce a physical energy. In that setting, this coupling reproduced the spin-current model in multiferroics and characterized a novel antiferroelectricity-driven magnetic anisotropy [1]. In conducting ferromagnets, it can explain the intrinsic anomalous Hall effect (AHE) and predict a novel Hall effect [3] as well as explain the anisotropic magnetoresistance (AMR) and the planar Hall effect (PHE) [2]. This energy also led to the prediction of novel spintronic effects [4] that bear resemblance to the so-called inverse Rashba-Edelstein effect. It may also be applicable to additional magneto-optical and spintronic phenomena.

Except for the phenomena discussed in Refs. [1] and [4], the proposed coupling has derived these effects according to a simple common method. The relevant electric and magnetic fields are first identified: for galvanomagnetic effects [2], an applied homogeneous electric field is used for the electric field and the Weiss field (proportional to magnetization) is used for the (homogeneous) magnetic field [9]. The coupling energy of a single conduction electron is taken as proportional to minus the scalar product of the field angular momentum and the magnetic moment of the electron, with some material dependent coupling constant as the proportionality coefficient. In this treatment of AMR and PHE, we are seeking anisotropy in longitudinal and transverse resistivity, so the electric field may adopt general Cartesian components along the longitudinal and transverse directions. Derivation of the appropriate expressions for AHE, AMR, and PHE then follows the standard derivation of the Hall effect in a Drude model. The equation of motion including the Lorentz force and the coupling force is considered component-wise in steady state; multiplying by the appropriate factor and summing over all electrons allows the component-wise equations to be expressed in terms of magnetization and current density. In steady state and with appropriate boundary conditions, the transverse applied electric field components cancel out the transverse current density, leaving only the longitudinal component of current density. Solving one of these resulting equations yields an expression for AHE. Solving for the longitudinal and transverse resistivities, the known expressions for AMR and PHE are recovered readily.

This derivation of galvanomagnetic effects has several advantages. One, as far as the authors are aware, it provides the first unified explanation for AHE together with AMR and PHE. Moreover, provided the material dependent coupling constant and the proportionality coefficient between the Weiss field and magnetization are each linear in spin-orbit interaction, our model reproduces the respective first- and second-order dependencies of AHE and AMR on spin-orbit interaction. Second, since in our model the difference between the resistivities for magnetization parallel and perpendicular to the current is proportional to the material dependent coupling constant; if this constant is negative in some materials, the phenomenon of so-called negative AMR naturally

results. Third, the derivation for AHE worked as well in semiclassical electron dynamics and this allowed the coupling constant there to be expressed in terms of Berry-phase curvature [3]; if this can be shown to work for AMR, then a novel Berry-phase curvature theory of AMR may be possible. Fourth, if materials can be engineered to achieve a particular coupling constant, this could lead to design of novel electronic devices.

We thank C Paillard for valuable discussions. R Walter acknowledges this material is based upon work supported by the National Science Foundation Graduate Research Fellowship Program under Grant No. DGE-0957325. Furthermore he acknowledges support from a University of Arkansas Distinguished Doctoral Fellowship in Mathematics and Physics. This work is financially supported by ARO Grant W911NF-12-1-0085.

References

[1] A. Raeliarijaona, S. Singh, H. Fu, and L. Bellaiche, *Phys. Rev. Lett.* **110**, 137205 (2013).

[2] R. Walter, M. Viret, Surendra Singh and L. Bellaiche, *J. Phys.: Condens. Matter* **26**, 432201 (2014).

[3] L. Bellaiche, Wei Ren and Surendra Singh, *Phys. Rev. B* **88**, 161102(R) (2013).

[4] S. Bhattacharjee, S. Singh, D. Wang, M. Viret and L. Bellaiche, *J. Phys.: Condens. Matter* **26**, 315008 (2014).

[5] H. Schmid, *Ferroelectrics* 252, 41 (2001).

[6] C. Ederer and N.A. Spaldin, *Phys. Rev. B* **76**, 214404 (2007).

[7] V. M. Dubovik and V. V. Tugushev, *Physics Reports* **187**, 145 (1990).

[8] A. A. Gorbatsevich, Yu.V. Kopaev, and V.V. Tugushev, Zh. Eksp. Teor. Fiz. **85**, 1107 (1983) [Sov. Phys. JETP 58, 643 (1983)].

[9] NW Ashcroft and ND Mermin, *Solid State Physics,* (Philadelphia, PA: Saunders 1976).

Finite-temperature Properties of Rare-Earth-Substituted $BiFeO_3$ Multiferroic Solid Solutions and Superlattices

Bin Xu[1], Dawei Wang[2], Jorge Íñiguez[3], Laurent Bellaiche[1]

[1]Physics Department and Institute for Nanoscience and Engineering, University of Arkansas, Fayetteville, Arkansas 72701, USA
[2]Electronic Materials Research Laboratory-Key Laboratory of the Ministry of Education and International Center for Dielectric Research,
Xi'an Jiaotong University, Xi'an 710049, China
[3]Institut de Ciència de Materials de Barcelona (ICMAB-CSIC), Campus UAB, 08193 Bellaterra, Spain

Multiferroics form an important class of materials that possess coupled long-range-ordered electric and magnetic degrees of freedom.[1] Such magneto-electric coupling is promising for designing new devices taking advantage of the control of magnetic properties by the application of an electric field; or vise versa. The most studied multiferroic to date is bismuth ferrite ($BiFeO_3$ or BFO) because it exhibits ferroelectricity at a high Curie temperature ($T_C \approx 1100$ K) as well as possesses a magnetic ordering (which consists of a G-type based cycloid in the bulk) with a Néel temperature $T_N \approx 640$ K, therefore rendering it a room-temperature multiferroic having a large spontaneous polarization (~90 μC/cm^2).

However, BFO has several drawbacks, such as large coercive fields and high leakage currents,[2] which can be detrimental for some applications. Such drawbacks can be resolved by alloying BFO with $RFeO_3$ materials for which *R* is a rare-earth element.[2–5] Recent investigations on the $(Bi_{1-x}R_x)FeO_3$ solid solutions revealed striking behaviors. Examples include modulated phases observed in the compositional range bridging the well-known ferroelectric *R3c* state (for low *R* concentrations) and the well-determined antipolar *Pnma* phase (for higher *R* compositions). Interestingly, the precise structure and atomic characteristics of these bridging phases are not fully resolved.[2-8] In particular, the nature and role of oxygen octahedral tiltings and antipolar motions in these phases are subject to debate. These bridging phases are further believed to be associated with an enhancement of the piezoelectric responses,[3] whose precise origin remains to be confirmed. Another example of striking behaviors in $(Bi_{1-x}R_x)FeO_3$ is the strong decrease of the ferroelectric Curie temperature, T_C, at which the *R3c* state disappears versus the weak dependency of the magnetic Néel temperature, T_N, when increasing the *R* composition, which can therefore lead to the interesting possibility of T_C being equal to T_N (and thus to the optimization of magneto-electricity) for some concentration. Moreover, applying an electric field in the *Pnma* state of *R*-doped BFO systems can lead to an antiferroelectric-to-ferroelectric phase transition (since *Pnma* is antipolar in nature and is close in energy to the

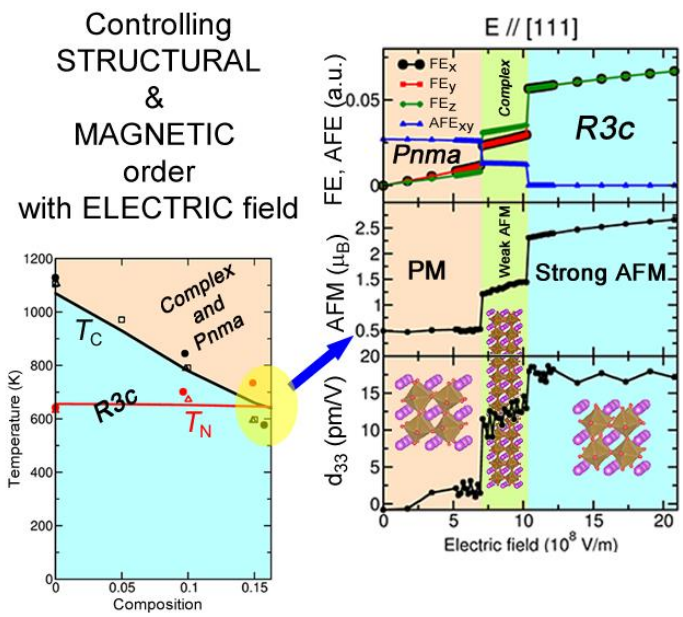

Figure 1 At the composition that $T_C \approx T_N$ and the temperature slightly above T_C, the application of an electric field can induce simultaneously structural and magnetic transitions.

ferroelectric *R3c* state in these compounds) that has the potential to be utilized in antiferroelectric capacitors and thus holds promise for energy storage devices.[9]

An atomistic scheme that accurately mimics $(Bi_{1-x}R_x)FeO_3$ solid solutions at finite temperature is therefore highly desirable in order to understand their unusual properties at a microscopic level as well as to guide the design of efficient devices. We are not aware that such scheme exists, likely due to the formidable challenge in treating well the finite-temperature and alloying effects on the subtle magnetic and structural properties of large supercells made of doped BFO compounds. Here we demonstrate that it is possible to develop such scheme, and apply it to study finite-temperature properties of disordered $Bi_{1-x}Nd_xFeO_3$ (BNFO) as representative of rare-earth-doped BFO systems (note that the choice of *R*=Nd is also motivated by the fact that numerous measurements have been conducted on this particular system,[3,4,10–12] which will therefore allow us to ground our predictions). Remarkably, this scheme can 1) reproduce very well observed properties, 2) resolve aforementioned issues, and 3) even predict novel and useful features in this important material [13].

This original numerical scheme can also be applied to ordered BNFO systems, e.g., 1/1 BFO/NFO layered superlattice for which each (001) layer has a *Pnma* structure. This latter system can therefore exhibit the so-called hybrid-improper-type ferroelectricity (HIF) [14]. The use of our developed atomistic technique allows to determine the effect of temperature and applied electric field on the polarization and its switching [15] as well as on the dielectric response associated with HIF. These numerical results can be further analyzed and understood within a Landau-type model.

Acknowledgements This work is financially supported by the Department of Energy, Office of Basic Energy Sciences, under contract ER-46612 (B.X. and L.B.) and by NSF Grant No. DMR-1066158 (D.W.). D.W also acknowledges the support from the NSFC grant 51390472 and the 111 Project (B14040). J.I. was financially supported by MINECO-Spain (Grant No. MAT2013-40581-P).

References

[1] G. Catalan and J. F. Scott, Adv. Mater. **21**, 2463 (2009).
[2] S. Emery, C.-J. Cheng, D. Kan, F. Rueckert, S. Alpay, V. Nagarajan, I. Takeuchi, and B. Wells, Appl. Phys. Lett. **97**, 152902 (2010).
[3] D. Kan, L. Pálová, V. Anbusathaiah, C. J. Cheng, S. Fujino, V. Nagarajan, K. M. Rabe, and I. Takeuchi, Adv. Funct. Mater. **20**, 1108 (2010).
[4] I. Levin, S. Karimi, V. Provenzano, C. L. Dennis, H. Wu, T. P. Comyn, T. J. Stevenson, R. I. Smith, and I. M. Reaney, Phys. Rev. B **81**, 020103 (2010).
[5] W. Chen, W. Ren, L. You, Y. Yang, Z. Chen, Y. Qi, X. Zou, J. Wang, T. Sritharan, P. Yang, et al., Appl. Phys. Lett. **99**, 222904 (2011).
[6] C.-J. Cheng, D. Kan, S.-H. Lim, W. R. McKenzie, P. R. Munroe, L. G. Salamanca-Riba, R. L. Withers, I. Takeuchi, and V. Nagarajan, Phys. Rev. B **80**, 014109 (2009).
[7] C.-J. Cheng, D. Kan, V. Anbusathaiah, I. Takeuchi, V. Nagarajan, Appl. Phys. Lett. **97**, 212905 (2010).
[8] A. Y. Borisevich, E. A. Eliseev, A. N. Morozovska, C. J. Cheng, J. Y. Lin, Y. H. Chu, D. Kan, I. Takeuchi, V. Nagarajan, S. V. Kalinin, Nat. Commun. **3**, 775 (2012).
[9] X. Tan, C. Ma, J. Frederick, S. Beckman, K. G. Webber, J. Am. Ceram. Soc. **94**, 4091 (2011).
[10] I. Levin, M. G. Tucker, H. Wu, V. Provenzano, C. L. Dennis, S. Karimi, T. Comyn, T. Stevenson, R. I. Smith, I. M. Reaney, Chem. Mater. **23**, 2166 (2011).
[11] S. Karimi, I. M. Reaney, Y. Han, J. Pokorny, I. Sterianou, J. Mater. Sci. **44**, 5102 (2009).
[12] S. Karimi, I. M. Reaney, I. Levin, I. Sterianou, Appl. Phys. Lett. **94**, 112903 (2009).
[13] B. Xu, D. Wang, J. Íñiguez and L. Bellaiche, Adv. Funct. Mater., in press (2014).
[14] J. Rondinelli and C. J. Fennie, Adv. Mater. **24**, 1961 (2012).
[15] Z. Zanolli, J. C.Wojdeł, J. Íñiguez, and P. Ghosez, Phys. Rev. B **88**, 060102 (2013)

Phase-field modeling on the elastically coupled magnetic and ferroelectric domains

T.N. Yang[1], J.M. Hu[1], C.W. Nan[2], and L.Q. Chen[1,2]

[1]*Department of Materials Science and Engineering, the Pennsylvania State University, University Park, Pennsylvania 16802*

[2]*Department of Materials Science and Engineering, Tsinghua University, Beijing 100084, China*

The scaling law for ferroics[1,2] indicates that the domain width of magnets and ferroelectrics become comparable only when the thickness of ferroelectrics is much larger. Indeed, it has been recently demonstrated in multiferroic layered heterostructures with magnetic thin films directly grown on ferroelectric (FE) $BaTiO_3$ substrates[3-7] that the domains in an as-grown magnetic thin film have not only the same width but also a surprising collinear alignment with the contacted FE domains. This further enables a precise control over the magnetic domain wall motion by electrically driving its elastically coupled FE domain wall[8,9]. Such one-to-one match between magnetic and FE domains offers new opportunities for the creation of periodic magnetic domain patterns used for magnonic devices, and particularly, the low-power spintronic devices based on electro-strain-driven magnetic domain orientation or domain wall propagation.

In the present work, a phase-field model is developed to study the dynamics of such local elastic coupling between magnetic and FE domains in multiferroic heterostructures. Taking a CoFe film grown on a $BaTiO_3$ single crystal substrate as an example, we simulate the evolution of both types of domains upon applying an electric field, including field-driven changes in domain morphology and domain wall velocity.

Ferroelectric stripe domains are directly imprinted onto the overlaying magnetic domains through elastic coupling in the as-grown multiferroic heterostructure. By driving the elastically coupled ferroelectric domains with a vertical AC electric field, repeated writing and erasure of the magnetic stripe domains are achieved. An alternating occurrence of coherent local magnetization rotation and magnetic domain wall motion coupled to ferroelectric domain walls is observed during an electric field loop. Studies on the dynamics of electric-field manipulation of magnetic domain evolution reveal closely coupled domain wall motions of magnetic and ferroelectric domain walls with almost identical velocities.

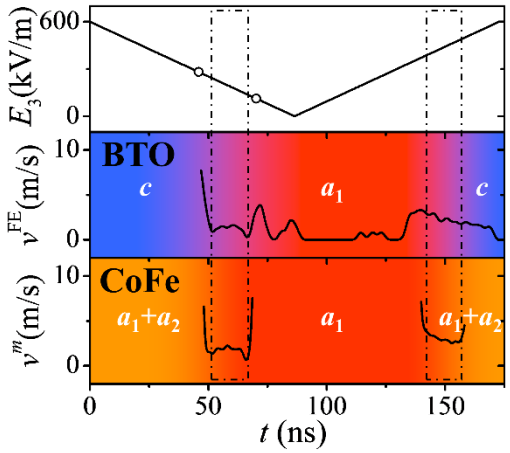

FIG. 1. Time sequence of the applied vertical electric field E and the resultant velocity of FE (v^{FE}) and magnetic (v^m) domain wall motion, in FE a_1/c domain and mixed a_1 and a_1/a_2 magnetic domain configurations, respectively. The background colors indicate the dominant FE or magnetic domains at different stages.

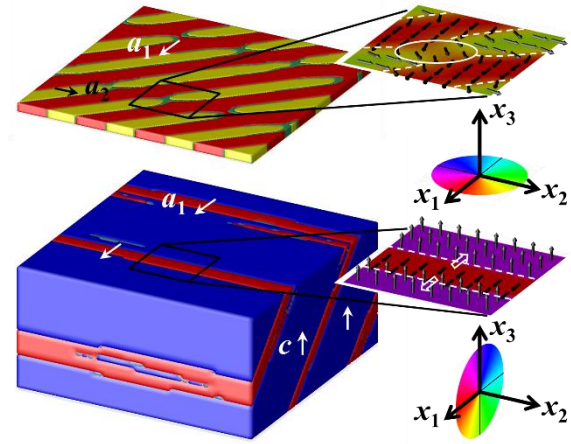

FIG. 2. Magnetic and FE domain structures at E_3=280 kV/m in a downhill electric-field cycle. (Right column) close-up vector plots of the polarization and magnetization configuration within the selected areas; the white dashed lines and the hollow arrows indicate the domain wall and the direction of the domain wall motion, respectively.

References

[1] A. Schilling, T. B. Adams, R. M. Bowman, J. M. Gregg, G. Catalan, and J. F. Scott, Phys. Rev. B **74,** 024115 (2006).
[2] G. Catalan, J. F. Scott, A. Schilling, and J. M. Gregg, J. Phys.: Condens. Matter **19,** 022201 (2007).
[3] T. H. E. Lahtinen, J. O. Tuomi, and S. van Dijken, Adv. Mater. **23,** 3187-3191 (2011).
[4] R. V. Chopdekar, V. K. Malik, A. Fraile Rodríguez, L. Le Guyader, Y. Takamura, A. Scholl, D. Stender, C. W. Schneider, C. Bernhard, F. Nolting, and L. J. Heyderman, Phys. Rev. B **86,** 014408 (2012).
[5] R. Streubel, D. Köhler, R. Schäfer, and L. M. Eng, Phys. Rev. B **87,** 054410 (2013).
[6] S. Geprägs, M. Opel, S. T. B. Goennenwein, and R. Gross, Phys. Rev. B **86,** 134432 (2012).
[7] K. J. A. Franke, D. L. González, S. J. Hämäläinen, and S. van Dijken, Phys. Rev. Lett. **112**, 017201 (2014).
[8] K. J. A. Franke, T. H. E. Lahtinen, and S. van Dijken, Phys. Rev. B **85,** 094423 (2012).
[9] H. T. Chen, Y. Ni, and A. K. Soh, J. Appl. Phys. **113,** 134102 (2013).

Magnetic charge and the magnetoelectricity in hexagonal manganites RMnO$_3$ and ferrites RFeO$_3$

Meng Ye* and David Vanderbilt
Department of Physics and Astronomy, Rutgers University, Piscataway, New Jersey 08854-8019, USA

The magnetoelectric (ME) effect is the phenomenon in which polarization $\mathbf{P}$ is induced by a magnetic field $\mathbf{H}$ or magnetization $\mathbf{M}$ is induced by an electric field $\boldsymbol{\mathcal{E}}$. The ME coupling (MEC) between magnetic and electric properties has motivated intense experimental and theoretical investigations in bulk single crystals, thin films, composite layers and organic-inorganic hybrid materials in recent years[1].

The linear ME effect α is defined as

$$\alpha_{\beta\nu} = \frac{\partial P_\beta}{\partial H_\nu}\Big|_{\boldsymbol{\mathcal{E}}} = \mu_0 \frac{\partial M_\nu}{\partial \mathcal{E}_\beta}\Big|_{\mathbf{H}}, \tag{1}$$

where indices β and ν denote the Cartesian directions and μ_0 is the vacuum permeability. From a theoretical point of view, the linear ME effect can be decomposed into electronic (frozen-ion), ionic (lattice-mediated), and strain-mediated responses [2]. Each term can be further subdivided into spin and orbital contributions based on the origin of the induced magnetization. As the orbital moment is largely quenched on transition-metal sites, most phenomenological and first-principles studies focus on the spin-electronic [6] and the spin-lattice [3, 4] contributions. Following [5], the latter can be written as

$$\alpha^{\rm latt} \propto Z^{\rm e} \cdot K^{-1} \cdot Z^{\rm m}, \tag{2}$$

i.e., as a matrix product of the dynamical Born electric charge $Z^{\rm e}$, the inverse force-constant matrix K^{-1}, and the dynamical magnetic charge $Z^{\rm m}$,

$$Z^{\rm m}_{m\nu} = \Omega_0 \frac{\partial M_\nu}{\partial u_m}\Big|_{\mathcal{E},\mathbf{H},\eta} = \mu_0^{-1} \frac{\partial F_m}{\partial H_\nu}\Big|_{\mathcal{E},\eta}, \tag{3}$$

which is the magnetic analog of the Born charge. Here m is a composite labels for atom and displacement direction, u_m is the internal displacement, F_m is the atomic force, Ω_0 is the unit cell volume and η is a homogeneous strain. Our previous first-principles study has shown that exchange striction acting on noncollinear spin structures induces much larger magnetic charges than when $Z^{\rm m}$ is driven by spin-orbit coupling (SOC), providing a promising mechanism for large MECs [7].

The hexagonal manganites RMnO$_3$ and ferrites RFeO$_3$ (R=Sc, Y, In, Ho-Lu) shown in Fig. 1 exhibit strong couplings between electric, magnetic and structural degrees of freedom. The transition-metal ions in the basal plane are antiferromagnetically coupled through superexchange so as to form a 120° spin arrangement. There are two types of magnetic orders in Mn^{3+} that allow a linear MEC to be present, the A$_1$ phase (P6$_3$cm) and the A$_2$ phase (P6$_3$c′m′), shown in Fig. 2. In this work, we use first-principles density functional methods to study the transverse magnetic charges, and the spin-lattice and spin-electronic MECs, in hexagonal HoMnO$_3$, ErMnO$_3$, YbMnO$_3$, LuMnO$_3$ and LuFeO$_3$, in the A$_1$ and A$_2$ phases, clarifying the conditions under which exchange striction leads to enhanced magnetic charges and anomalously large in-plane spin-lattice ME effects.

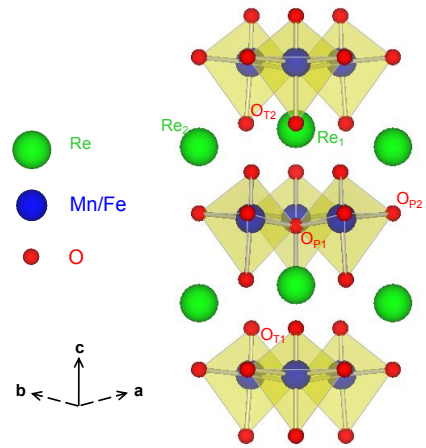

FIG. 1. Structure of ferroelectric hexagonal RMnO$_3$ and RFeO$_3$.

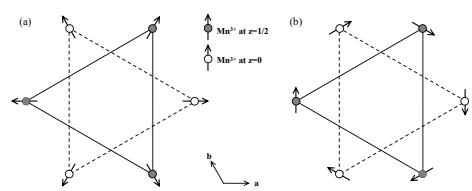

FIG. 2. The magnetic phases of hexagonal RMnO$_3$ and RFeO$_3$. (a) The A$_2$ phase has spins on the two Mn^{3+} layers pointing outward (inward) as a magnetic monopole. (b) The A$_1$ phase has the Mn^{3+} spins pointing in the tangential direction, forming a magnetic vortex pattern. The A$_1$ and A$_2$ phases only differ by a 90° global rotation of the spins.

As the spins are non-collinearly aligned in the basal plane, the transverse magnetic charges are driven by both SOC and exchange striction. As the exchange-striction strength can exceed the SOC by orders of magnitude in some materials, it is worthwhile to understand the effect of SOC, compared with exchange striction, in RMnO$_3$ and RFeO$_3$. In Table I, we present a selection of our results on the transverse magnetic charges induced with

TABLE I. Transverse magnetic charge components Z^{m} ($10^{-2}\mu_{\mathrm{B}}/\mathrm{Å}$), without SOC and total including SOC, for $ErMnO_3$ in the A_2 phase and $HoMnO_3$ in the A_1 phase.

	A_2 phase $ErMnO_3$			A_1 phase $HoMnO_3$	
	No SOC	Total		No SOC	Total
$Z^{\mathrm{m}}_{xx}(\mathrm{R}_1)$	-21.74	-21.02	$Z^{\mathrm{m}}_{yx}\mathrm{Ho}_1$	-27.83	-24.45
$Z^{\mathrm{m}}_{xx}(\mathrm{R}_2)$	2.98	5.85	$Z^{\mathrm{m}}_{xx}\mathrm{Ho}_2$	-18.14	-14.70
$Z^{\mathrm{m}}_{yx}(\mathrm{R}_2)$	11.96	11.27	$Z^{\mathrm{m}}_{yx}\mathrm{Ho}_2$	2.87	-0.81
$Z^{\mathrm{m}}_{xx}(\mathrm{Mn})$	-9.79	-6.92	$Z^{\mathrm{m}}_{yx}\mathrm{Mn}$	53.47	92.07
$Z^{\mathrm{m}}_{zx}(\mathrm{Mn})$	-21.79	-38.43	$Z^{\mathrm{m}}_{xy}\mathrm{Mn}$	1.80	-9.79
$Z^{\mathrm{m}}_{yy}(\mathrm{Mn})$	32.36	-7.35	$Z^{\mathrm{m}}_{zy}\mathrm{Mn}$	47.72	41.08
$Z^{\mathrm{m}}_{xx}(\mathrm{O_{T1}})$	6.07	5.84	$Z^{\mathrm{m}}_{yx}\mathrm{O_{T1}}$	27.64	22.46
$Z^{\mathrm{m}}_{zx}(\mathrm{O_{T1}})$	154.04	149.71	$Z^{\mathrm{m}}_{xy}\mathrm{O_{T1}}$	-6.86	-7.34
$Z^{\mathrm{m}}_{yy}(\mathrm{O_{T1}})$	21.72	21.49	$Z^{\mathrm{m}}_{zy}\mathrm{O_{T1}}$	-229.85	-187.73
$Z^{\mathrm{m}}_{xx}(\mathrm{O_{T2}})$	18.45	15.80	$Z^{\mathrm{m}}_{yx}\mathrm{O_{T2}}$	-66.85	-57.11
$Z^{\mathrm{m}}_{zx}(\mathrm{O_{T2}})$	160.49	139.70	$Z^{\mathrm{m}}_{xy}\mathrm{O_{T2}}$	-25.70	-19.56
$Z^{\mathrm{m}}_{yy}(\mathrm{O_{T2}})$	-46.09	-47.67	$Z^{\mathrm{m}}_{zy}\mathrm{O_{T2}}$	-231.43	-192.11
$Z^{\mathrm{m}}_{xx}(\mathrm{O_{P1}})$	-421.57	-391.56	$Z^{\mathrm{m}}_{yx}\mathrm{O_{P1}}$	-551.22	-483.14
$Z^{\mathrm{m}}_{xx}(\mathrm{O_{P2}})$	201.65	214.54	$Z^{\mathrm{m}}_{xx}\mathrm{O_{P2}}$	461.15	394.63
$Z^{\mathrm{m}}_{yx}(\mathrm{O_{P2}})$	-354.57	-334.71	$Z^{\mathrm{m}}_{yx}\mathrm{O_{P2}}$	252.87	183.98

and without SOC, focusing on $ErMnO_3$ in the A_2 phase and $HoMnO_3$ in the A_1 phase. It is obvious that the SOC contributions are an order of magnitude smaller for many transverse components.

We then calculate the spin-lattice MEC from Eq. (2) using our computed Born charges, force-constant matrices and magnetic charges. The spin-electronic MECs are calculated using the definition in Eq. (1) with the lattice degrees of freedom frozen. In Fig. 3, we show the transverse MECs α_{xx} for $R\mathrm{MnO_3}$ and $LuFeO_3$ in the A_2 phase. In Fig. 3(a), the spin-lattice ME response is one order of magnitude stronger than the SOC induced ME

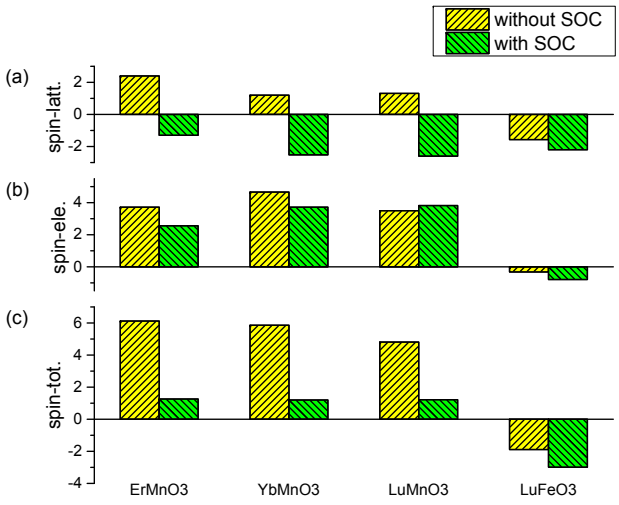

FIG. 3. The spin-lattice, spin-electronic and the total spin ME constants α_{xx} of $R\mathrm{MnO_3}$ and $LuFeO_3$ in the A_2 phase.

TABLE II. Transverse ME constants α_{xy} (in ps/m) without SOC, and total including SOC, for the A_1 phase $HoMnO_3$.

	No SOC	Total
Spin-lattice	−4.88	−9.55
Spin-electronic	−5.35	−5.24
Total spin	−10.23	−14.79

in Cr_2O_3 [8], as a result of the exchange-striction mechanism. Surprisingly, the effect of SOC on the spin-lattice MECs is comparable to the effect of exchange striction, although the SOC acts only as a perturbation to most of the Z^{m}. The underlying reason is that the spin-lattice MEC is smaller than expected as a result of a large degree of cancellation between the contributions from different infrared-active modes. Thus, small perturbations to the magnetic charges can lead to large relative changes in the MEC result. From Fig. 3(b) it can be seen that the spin-electronic contribution is not negligible, and it counteracts the ME effect from the spin-lattice channel in $R\mathrm{MnO_3}$. The total transverse ME effect is summarized in Fig. 3(c). Because of the large SOC effect and the cancellation between the lattice and electronic contributions, the total spin MEC α_{xx} is ~ 1.2 ps/m in the A_2 phase. In $LuFeO_3$, the spin-lattice and the spin-electronic terms are all smaller than in $R\mathrm{MnO_3}$. However, as the exchange-striction induced spin-lattice MEC term has the opposite sign compared to $R\mathrm{MnO_3}$, the cancellation induced by the SOC perturbation and the spin-electronic contribution is avoided, so that $LuFeO_3$ has the largest total spin MEC of ~ -3 ps/m in the A_2 phase.

For the A_1 phase, we present the MECs for $HoMnO_3$ in Table II. Unlike the MECs in the A_2 phase $R\mathrm{MnO_3}$, the spin-lattice, spin-electronic and SOC contributions all have the same sign. As each term contributes ~ -5 ps/m, the spin-total MEC α_{xy} reaches to ~ -15 ps/m, which is the largest in all of the $R\mathrm{MnO_3}$ and $LuMnO_3$ materials we studied.

* mengye@physics.rutgers.edu

[1] M. Fiebig, J. Phys. D **38**, R123 (2005).
[2] T. Birol, N. A. Benedek, H. Das, A. L. Wysocki, A. T. Mulder, B. M. Abbett, E. H. Smith, S. Ghosh, and C. J. Fennie, Curr. Opin. Solid State Mater. Sci. **16**, 227 (2012).
[3] J. C. Wojdel and J. Íñiguez, Phys. Rev. Lett. **103**, 267205 (2009).
[4] H. Das, A. L. Wysocki, Y. Geng, W. Wu and C. J. Fennie, Nat. Commun. **5**, 2998 (2014)
[5] J. Íñiguez, Phys. Rev. Lett. **101**, 117201 (2008).
[6] E. Bousquet, N. A. Spaldin, and K. T. Delaney, Phys. Rev. Lett. **106**, 107202 (2011).
[7] M. Ye and D. Vanderbilt, Phys. Rev. B **89**, 064301 (2014).
[8] A. Malashevich, S. Coh, I. Souza and D. Vanderbilt, Phys. Rev. B **86**, 094430 (2012).

Magnetoelectric coupling in Ni_3TeO_6

Michael Yokosuk[1], Dipanjan Mazumdar[1], Peng Chen[1], Kenneth O'Neal[1], Amal al-Wahish[1],Sergey Artyukhin[2], Steve McGill[3], Kristjan Haule[2], David Vanderbilt[2], Sang-Wook Cheong[2,4,5], and Janice Musfeldt[1]

[1]Department of Chemistry, University of Tennessee, Knoxville, Tennessee, USA
[2]Department of Physics and Astronomy, Rutgers University, Piscataway, New Jersey, USA
[3]National High Magnetic Field Laboratory, 1800 East Paul Dirac Drive, Tallahassee, Florida, USA
[4]Laboratory for Pohang Emergent Materials and Department of Physics, Pohang University of Science and Technology, Pohang, Korea
[5]Rutgers Center for Emergent Materials, Rutgers University, Piscataway, New Jersey, USA

We measured the optical and magneto-optical properties of Ni_3TeO_6 and combined our findings with complementary electronic structure calculations to understand magnetoelectric coupling in a system with strong spin-orbit coupling. We find striking changes in the polarized optical response through the 9 T spin flop transition that we understand in terms of microscopic nature of the excitations and the development of a substantial polarization. Precursor effects on approach to the spin flop as well as evidence for short range ordering above the 54 K Neel temperature are also observed. The high field response of Ni_3TeO_6 continues to change beyond 9 T, evidence that another magnetically-driven transition is likely to occur at fields higher than 35 T. These findings advance the understanding of magnetoelectric coupling in 4*d*-containing materials.

Oxygen vacancy diffusion in bulk SrTiO3 from density functional theory

Lipeng Zhang[1], Bin Liu[1], Houlong Zhuang[2], Paul R. Kent[2], Valentino R. Cooper [3], Panchapakesan Ganesh[2], Haixuan Xu [1,*]

[1]Department of Material Science and Engineering, The University of Tennessee, Knoxville, Tennessee 37996 USA
[2]Center for Nanophase Materials Science, Oak Ridge National Laboratory, Bethel Valley Road, Oak Ridge, Tennessee 37831, USA
[3]Materials Science and Technology Division, Oak Ridge National Laboratory, Bethel Valley Road, Oak Ridge, Tennessee 37831, USA

The migration energy of oxygen vacancy diffusion in $SrTiO_3$ (STO) is one of the critical characteristic parameters that could potentially influence many aspects of its physical properties [1,2]. Thus it is imperative to obtain an accurate value of the energy barrier. However, the existing data [3-7] determined using either experimental or theoretical techniques varies significantly. In this study, the isolated neutral and charged oxygen vacancy diffusion energy barriers in n × n × n STO supercells (n increased from 2 to 5) have been obtained using density functional theory (DFT) in combination with nudged elastic band (NEB) method. The effects of several factors that can potentially influence the results have been examined. These factors include supercell sizes, spin, octahedral rotation induced by the oxygen vacancy, charge state of oxygen vacancy, the type of the chosen exchange and correlation functionals, e.g. PBE and PBEsol and the effects of +U. Surprisingly, the results show that oxygen octahedral rotation cooperating with boundary condition of STO supercell significantly affects the oxygen vacancy diffusion energy barrier. The effects of charge states of oxygen vacancy and exchange-correlation functionals on the energy barrier are found to be diminishing as the size of STO supercell increases. Moreover, within a sufficiently large supercell (5x5x5), DFT underestimates the migration energy barrier, regardless of which functionals or whether the DFT+U has been employed. This work offers a comprehensive picture of oxygen vacancy diffusion in bulk STO using DFT calculations and provides fundamental insights on how to accurately simulate defect transport in other perovskite oxide compounds.

Acknowledge This research is sponsored by the University of Tennessee Science Alliance Joint Directed Research and Development Program and UT/ORNL Joint Institute of Advanced Materials, the Laboratory Directed Research and Development Program of Oak Ridge National Laboratory, managed by UT-Battelle, LLC, for the US Department of Energy (VRC, HZ, PG, PRCK) and (HX) this research used resources of the National Energy Research Scientific Computing Center, which is supported by the Office of Science of the US Department of Energy under Contract No. DE-AC02-05CH11231

References

[1] David A. Muller, Naoyuki Nakagawa, Akira Ohtomo, John L. Grazul, Harold Y. Hwang; *Nature* **430**, 657-661, (2004).

[2] Minseok Choi, Fumiyasu Oba, Yu Kumagai, Isao Tanaka; *Advanced Materials* **25**, 86-90, (2013).

[3] T. Mizoguchi, N. Takahashi, and H. Lee; *Appl. Phys. Lett.* **98**, 091909, (2011).

[4] A. Walsh, C. R. A. Catlow, A. G. H. Smith, A. A. Sokol, and S. M. Wood- ley; *Phys. Rev. B* **83**, 220301, (2011).

[5] J. Carrasco, F. Illas, N. Lopez, E. A. Kotomin, Y. F. Zhukovskii, R. A. Evarestov, Y. A. Mastrikov, S. Piskunov, and J. Maier; *Phys. Rev. B* **73**, 064106, (2006).

[6] R. A. da Souza and V. Metlenko; *Phys. Rev. B* **85**, 174109, (2012).

[7] Do Duc Cuong, Bora Lee, Kyeong Mi Choi, Hyo-Shin Ahn, Seungwu Han, and Jaichan Lee; *PRL* **98**, 115503, (2007).

First-principles calculation of bulk photovoltaic effect in $CH_3NH_3PbI_3$ and $CH_3NH_3PbI_{3-x}Cl_x$

Fan Zheng[1], Hiroyuki Takenaka[1], Fenggong Wang[1], Nathan Z. Koocher[1], Andrew M. Rappe[1]

[1]The Makineni Theoretical Laboratories, Department of Chemistry, University of Pennsylvania, Philadelphia, PA 19104, United States

The power conversion efficiency (PCE) of organometallic halide perovskites photovoltaic has soared from around 9% to 20% within two years.[1,2] A great deal of studies have been done to understand the reason of such high efficiency. Methylammonium lead halide perovskite ($MAPbI_3$) as the one with relatively high PCE has been studied intensively. This material has the perovskite structure ABX_3 (X=Cl, Br, I) with corner-sharing PbI_3 octahedral cages forming the inorganic frame. Small organic molecule methylammonium (MA) occupies A site to balance the charge. Besides its outstanding properties such as appropriate band gap, high light absorption coefficient, fast electron-hole pair generation and long carrier life time, $MAPbI_3$ shows very high open-circuit voltage.[3] Various I/V hysteresis loops are also observed. Since bulk photovoltaic effect (BPVE) can provide high open-circuit voltage, it is possible that the ferroelectricity and BPVE in this material play an important role. In this work, we focus on its ferroelectric properties induced by different orientations of organic molecules. Shift current as the dominant mechanism for BPVE has been calculated for this material. By using Density Function Theory, we found that for the configurations with dipole moments aligned in parallel, the inorganic PbI_3 frame are more significantly distorted than configurations with near net zero dipole. And this distorted configuration also yields a larger shift current response. This can further explain the measured high open-circuit voltage as well as I/V hysteresis. Furthermore, we explore the effect of Cl substitution of I, as $MAPbI_{3-x}Cl_x$ has been observed to have the highest PCE. We find that Cl substitution at the equatorial site induces a larger response than does substitution at the apical site. But its effect to the total polarization becomes less significant.

Acknowledgements

The authors were supported by the Department of Energy Office of Basic Energy Sciences, the Office of Naval Research, the Roy & Diana Vagelos Scholars Program in the Molecular Life Sciences, and the National Science Foundation. Computational support was provided by the High-Performance Computing Modernization Office of the Department of Defense and the National Energy Research Scientific Computing Center.

References

[1] H.-S. Kim, C.-R. Lee, J.-H. Im, K.-B. Lee, T. Moehl, A. Marchioro, S.-J. Moon, R. Humphry-Baker, J.-H. Yum, J. E. Moser, M. Gratzel and N. G Park, *Sci. Rep.* **2**, 591, (2012).

[2] H. Zhou, Q. Chen, G. Li, S. Luo, T.-b. Song, H.-S. Duan, Z. Hong, J. You, Y. Liu and Y. Yang, *Science* **345**, 542, (2014).

[3] J. Ponseca, S. Carlito, T. J. Savenije, M. Abdellah, K. Zheng, A. Yartsev, T. Pascher, T. Harlang, P. Chabera, T. Pullerits, A. Stepanov, J.-P. Wolf and V. Sundström, *J. Am. Chem. Soc.* **136**, 5189, (2014).

Metal-insulator transition in nanostructured $SrTiO_3/LaAlO_3$

Houlong L. Zhuang,[1] Valentino R. Cooper,[2] Haixuan Xu,[3] P. R. C. Kent,[4, 1] and P. Ganesh[1]

[1]Center for Nanophase Materials Sciences, Oak Ridge National Laboratory, Bethel Valley Road, Oak Ridge, Tennessee 37831, USA

[2]Materials Science and Technology Division, Oak Ridge National Laboratory, Bethel Valley Road, Oak Ridge, Tennessee 37831, USA

[3]Department of Materials Science and Engineering, The University of Tennessee, Knoxville, Tennessee 37996, USA

[4]Computer Science and Mathematics Division, Oak Ridge National Laboratory, Bethel Valley Road, Oak Ridge, Tennessee 37831, USA

$SrTiO_3$(STO)/$LaAlO_3$(LAO) heterostructures have attracted significant attention as they exhibit a wealth of intriguing properties such as electric [1], magnetic [2], and superconducting [3] that are absent in their bulk constituents. Among these properties is the presence of a high-mobility two dimensional electron gas (2DEG) when the thickness of the LAO epitaxial layers reaches a critical number of four layers [4]. The requirement of this particular number can be understood by the polar catastrophe" model illustrated in [5], which describes that a minimum number of four LAO layers is needed to accumulate a sufficiently large electric field to enable the transfer of electrons from LAO to the interface [6].

The desired properties of STO/LAO heterostructures depend heavily on novel designs of their atomic structures. For example, nanowire-like STO/LAO heterostructures obtained by the standard photo-lithography technique exhibit a conducting one-dimensional channel [7]. Inspired by this experimental study, we design overlayer heterostructure model formed by combining a LAO overlayer and a regular STO (001) substrate. The stepped LAO surface can be regarded as consisting of an alternating pattern of one and two LAO layers. Therefore, we henceforth refer to this interface as the 1+2 overlayer heterostructure. Figure 1(a) shows a supercell of a the 1+2 STO/LAO overlayer het-erostructure, and Figure 1(b) illustrates the atomic configurations after geometry optimizations. At a regular STO/LAO heterostructure [8], atoms are relaxed primarily along the z direction, whereas at

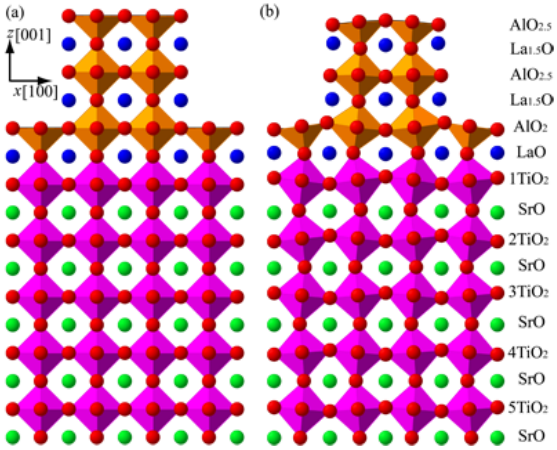

Figure 1. (a) Unrelaxed and (b) relaxed 1+2 STO/LAO overlayer heterostructure. Only one half of the atoms in each supercell are shown. Lanthanum, strontium, and oxygen atoms are illustrated by blue, green, and red balls, respectively. Ti and Al-centered octahedra are represented by magenta and orange polyhedra, respectively. The numbers before the TiO_2 notations denote the order by distance of a TiO_2 layer in STO from the interface.

the overlayer heterostructure, one prominent feature is the rotations of the Ti- and Al-centered octahedra.

In this work, we aim to gain insights on how the peculiar structure, i.e. a STO/LAO overlayer heterostructure affects its electronic properties. Interestingly, we find that metallic states can as well appear at the over-layer heterostructure despite the maximum number of LAO layers is below the aforementioned threshold number. Furthermore, band structures (e.g., see Figure 2) of the overlayer heterostructures show that the metallic states behave as a 2DEG. To this end, we propose a modified polar catastrophe model to understand the occurrence of 2DEGs in these overlayer heterostructures.

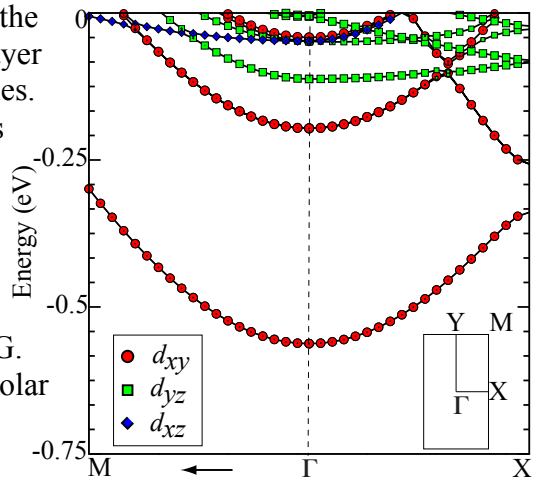

Figure 2. Orbital-resolved band structure of the 1+2 STO/LAO overlayer heterostructure.

Acknowledgements Research sponsored by the Laboratory Directed Research and Development Program of Oak Ridge National Laboratory, managed by UT-Battelle, LLC, for the U. S. Department of Energy, and (HX) The University of Tennessee (UT) Science Alliance Joint Directed Research and Development Program (JDRD) and UT/ORNL Joint Institute of Advanced Materials (JIAM). This research used resources of the National Energy Research Scientific Computing Center, which is supported by the Office of Science of the U.S. Department of Energy under Contract No. DE-AC02-05CH11231.

References

[1] A. Ohtomo and H. Hwang, Nature, **427**, 423 (2004).
[2] A. Brinkman, M. Huijben, M. van Zalk, J. Huijben, U. Zeitler, J. C. Maan, W. G. van der Wiel, G. Rijnders, D. H. A. Blank, and H. Hilgenkamp, Nature materials, **6**, 493 (2007).
[3] N. Reyren, S. Thiel, A. D. Caviglia, L. F. Kourkoutis, G. Hammerl, C. Richter, C. W. Schneider, T. Kopp, A.-S. Retschi, D. Jaccard, M. Gabay, D. A. Muller, J.-M. Triscone, and J. Mannhart, Science, **317**, 1196 (2007).
[4] S. Thiel, G. Hammerl, A. Schmehl, C. W. Schneider, and J. Mannhart, Science, **313,** 1942 (2006).
[5] N. Nakagawa, H. Y. Hwang, and D. A. Muller, Nature materials, **5,** 204 (2006).
[6] J. Mannhart and D. G. Schlom, Science, **327,** 1607 (2010).
[7] A. Ron and Y. Dagan, Phys. Rev. Lett., **112,** 136801 (2014).
[8] R. Pentcheva and W. E. Pickett, Phys. Rev. Lett., **102,** 107602 (2009).